SCUOLA INTERNAZIONALE SUPERIORE DI STUDI AVANZATI
INTERNATIONAL SCHOOL FOR ADVANCED STUDIES

Physics Area
Astrophysics Sector

Dust production in Thermally Pulsing Asymptotic Giant Branch Stars

Thesis submitted for the degree of
Doctor Philosophiæ

SUPERVISORS:
Prof. Alessandro Bressan
Dr. Paola Marigo

CANDIDATE:
Ambra Nanni

October 2013

To my family

Abstract

In this thesis I discuss the dust chemistry and growth in the circumstellar envelopes (CSEs) of Thermally Pulsing Asymptotic Giant Branch (TP-AGB) stars computed with the `COLIBRI` code at different initial metallicities ($Z = 0.001$, 0.008, 0.02, 0.04, 0.06) and stellar masses.

I adopt a formalism of dust growth coupled with a stationary wind for both M and C-stars CSEs. In the original version of this formalism, the most efficient destruction process of silicate dust in M-giants is chemisputtering by H_2 molecules. For these stars I find that dust grains can only form at relatively large radial distances ($r \sim 5\,R_*$), where they cannot be efficiently accelerated, in agreement with other investigations.

In the light of recent laboratory results, I also consider the alternative case that the condensation temperature of silicates is determined only by the competition between growth and free evaporation processes (i.e. no chemisputtering). With this latter approach I obtain dust condensation temperatures that are significantly higher (up to $T_{\rm cond}$ ~1400 K) than those found when chemisputtering is included ($T_{\rm cond}$ ~900 K), and in better agreement with condensation experiments. As a consequence, silicate grains remain stable closer to the stellar photosphere ($r \sim 2\,R_*$), where they rapidly grow and are efficiently accelerated. With this modification, the models nicely reproduce the observed trend between terminal velocities and mass-loss rates of Galactic M-giants.

For C-stars the formalism is based on the homogeneous growth scheme where the key role is played by the carbon over oxygen excess. The models reproduce fairly well the terminal velocities of Galactic stars and there is no need to invoke changes in the standard assumptions. At decreasing metallicity the carbon excess becomes more pronounced and the efficiency of dust formation increases. This trend could be in tension with recent observational evidence in favour of a decreasing efficiency, at decreasing metallicity. If confirmed by more observational data, it would indicate that either the amount of the carbon excess, determined by the complex interplay between mass loss, third dredge-up and hot bottom burning, or the dust growth scheme should be revised.

This comparison also shows that the properties of TP-AGB CSEs are important diagnostic tools that may be profitably added to the traditional calibrators for setting further constraints on this complex phase of stellar evolution.

I first compute the dust ejecta integrated along the all TP-AGB phase at solar and sub-solar metallicities ($Z = 0.001$, 0.008, 0.02) comparing the results obtained with the two formalisms (with and without chemisputtering) and with other results in the literature. I find that, in spite of the differences in the expected dust stratification, for a given set of TP-AGB models, the ejecta are only weakly sensitive to the specific assumption. On the other hand, the results highly depend on the adopted TP-AGB models.

I thus extend this formalism to the case of super-solar metallicity stars considering the preferred scheme for dust growth: for M-stars, I neglect chemisputtering by H_2 molecules and, for C-stars, I assume the homogeneous growth scheme.

At super-solar metallicity, dust forms more efficiently than in the solar and sub-solar cases and silicates tend to form at significantly inner radii, and thus at higher temperatures and densities, than at solar and sub-solar metallicity values.

In such conditions, the hypothesis of thermal decoupling between gas and dust becomes questionable and dust heating due to collisions become important. This heating mechanism delays dust condensation to slightly outer regions in the circumstellar envelope.

By calculating the dust ejecta at super-solar metallicities I find that the main dust products metallicities are silicates.

I finally present the total dust-to-gas ejecta for different values of the stellar initial masses and for all the metallicity values considered: $Z = 0.001, 0.008, 0.02, 0.04, 0.06$, finding that the total dust-to-gas ejecta of intermediate-mass stars are much less dependent on the metallicity than what is usually assumed.

Contents

List of Figures

List of Tables

Chapter 1

Introduction

1.1 The general framework

During the Thermally Pulsing Asymptotic Giant Branch (TP-AGB) phase, stars with initial masses in the range $0.8 < M_* < 6 - 8\ \mathrm{M}_\odot$ lose their envelopes at typical rates between $10^{-8}\ \mathrm{M}_\odot\ \mathrm{yr}^{-1}$ and few $10^{-5}\ \mathrm{M}_\odot\ \mathrm{yr}^{-1}$, polluting the Interstellar Medium (ISM) with metals, partially condensed into dust.

The term "dust" refers to small particles with size (radius) of the order of $0.1\ \mu$m with different chemical composition according to the initial abundances in the atmosphere of the star (Sargent et al., 2010; Norris et al., 2012). In this respect, TP-AGB stars are classified on the basis of their surface C/O number ratio in two main classes. If $\mathrm{C/O} < 1$ the star is classified as M-star while, if $\mathrm{C/O} > 1$, the star is classified as "Carbon-star" (C-star). In M-stars ($\mathrm{C/O} < 1$) the main dust species are amorphous silicates, as well as forsterite (Mg_2SiO_4) and enstatite ($MgSiO_3$), quartz (SiO_2) and corundum (Al_2O_3) (Tielens et al., 1998; Ossenkopf et al., 1992). Amorphous silicates are particularly abundant and observations indicate that their grains are Mg-rich with an Fe-content of $< 10\%$. On the other hand, in C-stars ($\mathrm{C/O} > 1$) the dust produced is predominantly amorphous carbon and silicon carbide (SiC) (Groenewegen et al., 1998).

As it will be extensively explained in the following sections, the C/O ratio depends on the physical processes experienced by the star during its evolution and its value at the stellar surface depends on the initial mass and composition.

Direct estimates of the amount of dust and its mineralogy are provided by mid- and far-infrared (MIR, FIR) observations of TP-AGB stars, both in our galaxy and in the nearby ones (Knapp, 1985; Matsuura et al., 2009, 2012).

Comparing the dust mass-loss rates derived from FIR observations with the gas mass-loss rates obtained from CO observations of Galactic TP-AGB stars, Knapp (1985) have found typical dust-to-gas ratios of $\sim 6 \times 10^{-3}$ for oxygen-rich (M-stars), mainly in the form of amorphous silicates, and $\sim 10^{-3}$ for carbon-rich (C-stars), mainly as amorphous carbon. In particular they have estimated that, at solar metallicity, a large fraction of the silicon should condense into dust in the circumstellar envelopes (CSEs) of these stars.

TP-AGB stars have soon been recognized as the main stellar dust producers, compared to other sources like Supernovae (SNe), Red Supergiant and Wolf-Rayet stars (Gehrz, 1989). This picture becomes more complex considering that, once dust is injected into the ISM, it is subject to many processes that can significantly alter its abundance and composition (Draine, 2003).

Moving beyond the Galactic context, it is now well established that the stellar dust has a far-reaching relevance, being a critical element in the interpretation of extragalactic observations up to the far Universe. The study of the Spectral Energy Distribution (SED) of galaxies and quasars at high redshifts shows that even very young objects possess large dust reservoirs (Lilly et al., 1999; Eales et al., 2000; Bertoldi et al., 2003; Robson et al., 2004; Beelen et al., 2006; Dwek & Cherchneff, 2011). On the theoretical side, many efforts have been made in order to model dust evolution in local galaxies (Dwek, 1998; Calura et al., 2008; Zhukovska et al., 2008; Piovan et al., 2011a,b), and to explain the presence of large amounts of dust at early epochs, when the dust and chemical enrichment time-scale was only a fraction of a Gyr (Dwek et al., 2007; Valiante et al., 2009; Mattsson, 2011; Valiante et al., 2011; Dwek & Cherchneff, 2011; Gall et al., 2011; Pipino et al., 2011; Pipino & Matteucci, 2011; Michałowski et al., 2010,b; Yamasawa et al., 2011). Several authors suggest that at high redshifts the major dust contributors should be SNe because of their short lifetimes with respect to those of TP-AGB stars (Maiolino et al., 2004; Marchenko, 2006). However, SNe play also an important role in dust destruction since they produce shocks and high energy particles, so that their contribution is still controversial (Todini & Ferrara, 2001; Nozawa et al., 2003; Sugerman et al., 2006). In fact, recent studies have concluded that the observed dust at these redshifts should be ascribed to the ejecta of TP-AGB stars more massive than 3 $M_{\odot}$, with SNe confined to a secondary contribution (Dwek et al., 2007; Valiante et al., 2009; Dwek & Cherchneff, 2011). In this framework, it is therefore crucial to know how stellar dust ejecta, and in particular those of intermediate-mass stars, depend on metallicity since, at least in the early phases of galaxy evolution, the environmental conditions were rather different from those of the present local Universe. Once the dust is injected in the ISM it can subsequently evolve and dust accretion in the ISM can also be relevant (Draine, 2009).

Another important effect of dusty CSEs is that they affect the MIR colours of TP-AGB stars and thus the interpretation of their colour-magnitude diagrams. This is particularly important for the calibration of the uncertain parameters that are commonly used in stellar evolution calculations, such as the efficiency of mass-loss. It is now well established that the MIR colours of TP-AGB stars critically depend on the mass-loss rates and, while stellar isochrones in MIR bands have already been obtained (Bressan et al., 1998; Marigo et al., 2008), these studies do not rely on direct calculations of dust properties in the CSEs. The aim of this work is to predict all the basic quantities needed for stellar population studies in the MIR, i.e. dust ejecta, dust-to-gas ratio, composition, and outflow velocity, as a function of stellar parameters, for the sets of TP-AGB presented by our group (Marigo et al., 2013).

Detailed modeling of dust formation within CSEs of TP-AGB stars has already been carried out by several authors. The most advanced models describe the complex interaction between radiation and dust grains by means of full hydrodynamical computations, coupling radiative transfer with pulsations-induced shocks (Bowen & Willson, 1991; Fleischer et al., 1991; Lodders & Fegley, 1999; Cherchneff, 2000; Winters et al., 2000; Elitzur & Ivezić, 2001; Jeong et al., 2003; Höfner et al., 2003; Höfner, 2008b). These models require a significant computational effort and are not yet applicable to the analysis of large data sets. A simpler approach is that of describing the dust growth in an expanding envelope, under the stationary-wind approximation, as done by Ferrarotti & Gail (2006)(hereafter FG06) and Gail & Sedlmayr (1999) (GS99). The latter approach is not as fully self-consistent as the former one, since, for example, it cannot predict the mass-loss rate as a function of stellar parameters. However, at the present time this simplified method is the only feasible way to couple dust formation with stellar evolution calculations that, especially for the TP-AGB phase, involve a large number of models. Moreover, this method can be useful for testing the effects of some critical assumptions discussed later.

As a matter of fact, there are still several uncertainties that affect the theory of dust for-

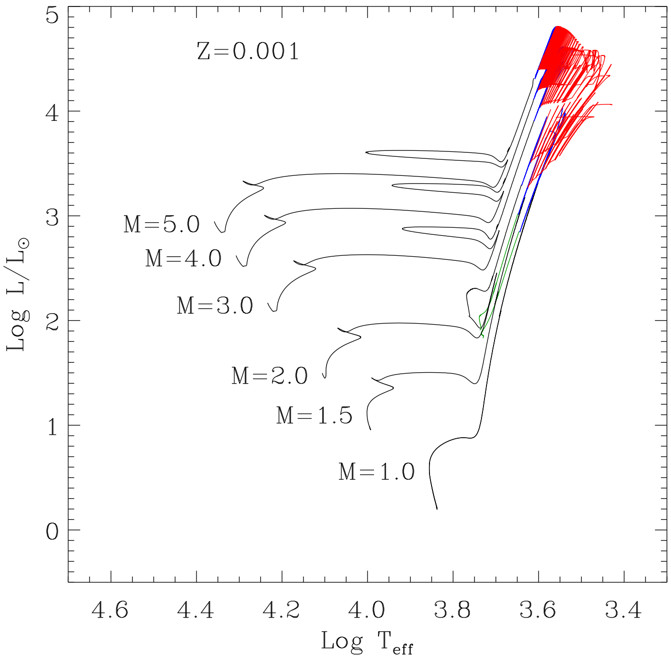

Figure 1.1: Evolutionary tracks for stars with $Z = 0.001$ and initial masses $M_* = 1, 1.5, 2, 3, 4, 5\ \mathrm{M}_\odot$. The tracks are computed by means of `PARSEC` code up to the TP-AGB phase, and by means of `COLIBRI` until the entire envelope of the star is lost by stellar winds. The thermal pulses developed when $\mathrm{C/O} < 1$ are plotted with blue lines. On the other hand, the thermal pulses plotted in red correspond to $\mathrm{C/O} > 1$. The He-burning phase of low-mass stars is plotted in green color.

mation. In particular the dust condensation temperature of silicates obtained from the original and widely used models by GS99 and FG06, $T_{\rm cond} \leq 1000$ K, is significantly lower than the one measured in more recent laboratory experiments, $T_{\rm cond} \sim 1350$ K (Nagahara et al., 2009) which depends, moreover, on the gas pressure. This may affect significantly the results of the dust formation models.

In this work I will opt for the more agile approach of FG06 because the TP-AGB tracks by Marigo et al. (2013) span a wide range of masses and metallicities and comprehend thousands of models. The flexibility of this method also allows a thorough investigation of the effects of changing some of the basic assumptions of the dust formation scheme used by FG06. In particular, I will compare my predictions with the expansion velocities observed in Galactic TP-AGB stars outflows, and analyze the impact of the different assumptions on the resulting dust ejecta.

1.2 Stellar evolution

1.2.1 Stellar evolution overview

In this section I briefly summarize the main properties of low- and intermediate-mass stars, from the beginning of the hydrogen-burning phases to the end of the TP-AGB phase, which can be considered as the end of their nuclear life.

Examples of stellar evolutionary tracks of low- and intermediate-mass stars are shown in

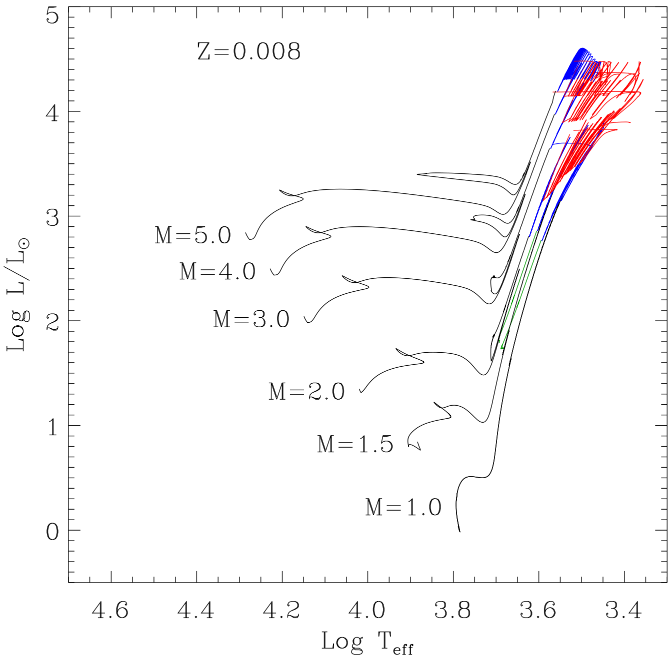

Figure 1.2: The same as in Fig. 1.1, but for $Z = 0.008$.

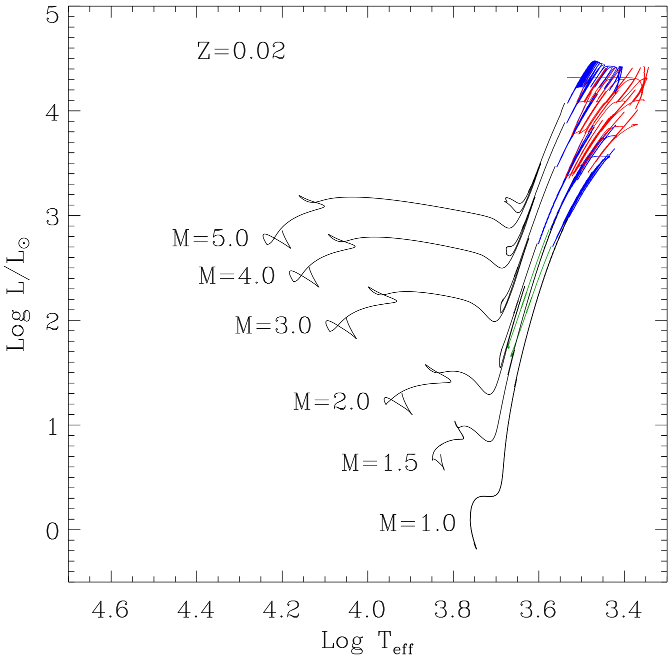

Figure 1.3: The same as in Fig. 1.1, but for $Z = 0.02$.

Figs. 1.1, 1.2 and 1.3, for different choices of the initial metallicity, $Z = 0.001$, 0.008 and 0.02 adopting solar-scaled chemical composition and the He over Z enrichment law $Y = 0.2485 + 1.78\,Z$, derived in `PARSEC`. The evolutionary tracks are computed by means of `PARSEC` code, from the pre-main sequence phase (not shown in figures) up to the TP-AGB phase. The TP-AGB phase is instead followed by means of the `COLIBRI` code until the entire envelope is lost by stellar winds. The characteristic quantities at the first thermal pulse, obtained from `PARSEC`, are fed as initial conditions into `COLIBRI`.

The main characteristics of these two codes will be outlined in Sections 1.2.2 and 1.2.3.

If I exclude the low temperature (and generally less energetically important) reactions that happen during the pre-main sequence (PMS) phase, the nuclear life of a star begins when hydrogen is stably converted into helium, in its core. This phase is the longest one in the star life, lasting until the hydrogen fuel in the core is completely exhausted.

Stars with initial masses $M_{*} \lesssim 1$ $\mathrm{M}_{\odot}$ burn hydrogen through the P-P cycle, in a radiative core, as depicted in Fig. 1.4. Hydrogen is not burnt homogeneously within the core, because the thermonuclear reactions are more efficient in the central regions, where the temperature is higher. In these conditions, hydrogen diminishes more rapidly in the central parts leaving a composition profile toward the more external regions. during this phase the core smoothly contracts and the star moves towards higher luminosities and effective temperatures, maintaining almost the same radius (Figs. 1.1, 1.2 and 1.3).

On the other hand in stars more massive than about 1 $\mathrm{M}_{\odot}$ the CNO cycle is more efficient than the P-P one and, because of the much more concentrated nuclear energy generation rate, the stars develop a convective core, Fig. 1.4. The hydrogen abundance within the core is kept constant by convective mixing. In stars less massive than about $M_{*} = 10$ $\mathrm{M}_{\odot}$ the convective core recedes during the evolution in such a way that they also develop an internal chemical profile. Actually the existence of a larger homogenous core from the beginning of H-burning, makes the star to evolve at decreasing temperature (Figs. 1.1, 1.2 and 1.3). However the structure at the end of central H-burning phase is not very different from that of the less massive stars without central convection.

When central hydrogen is exhausted the thermonuclear reactions do not provide the pressure gradient needed in order to sustain the star against gravity. In these conditions the stellar core contracts (more markedly in stars with convective cores), and H-burning proceeds in a nearby shell, in this case always through the CNO cycle. When the stellar core contracts the stars move rapidly towards higher luminosities and lower effective temperatures, approaching the Hayashi track, where a deep convective envelope develops.

Stars with initial mass below a critical value, M_{HeF} that depends on the chemical composition and on the efficiency of the central mixing (overshoot or rotation) undergo central electron degeneracy, their contraction becomes very slow and, on nuclear timescales, they climb the so called Red Giant Branch (RGB) as shown in Figs. 1.1, 1.2 and 1.3. These stars, called low-mass stars, will ignite helium in a strongly electron degenerate core, producing the so called “helium-flash” that corresponds to the most luminous point of the RGB. The run of M_{HeF} as a function of the metallicity and for different efficiencies of core convective mixing into the underlying stable regions, an effect called convective overshoot, is shown in Fig. 1.4. The RGB phase is characterized by the conversion of hydrogen into helium occurring in a circumnuclear shell. During this phase, the star moves towards higher luminosity and the mass of the core progressively accretes the newly-produced helium. As the mass of the core increases, its central temperature also rises, until it is high enough to ignite helium.

Stars more massive than M_{HeF}, named intermediate-mass stars, ignite central helium before encountering the strong electron degeneracy. A noticeable difference in this case is that the

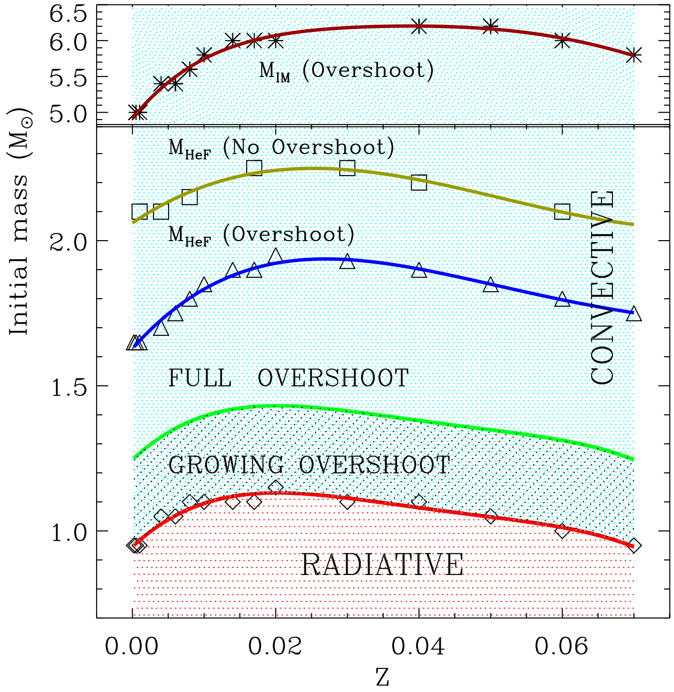

Figure 1.4: The behaviour of a few critical masses as a function of metallicity. From bottom to top: the minimum mass that maintains a persistent convective core during H-burning, M_{O1}; the mass above which core overshoot is taken at the maximum efficiency M_{O2}; the minimum mass for a model to ignite central helium non degenerately, M_{HeF} for both the overshoot and the no-overshoot cases; finally, in the upper panel, the minimum mass of the stars that ignite C in a non electron degenerate core, M_{IM}. The typical resolution in determining these mass limits is 0.05 $M_\odot$ for M_{O1} and M_{HeF}, and 0.2 $M_\odot$ for M_{IM}. The curves are polynomial fits to the corresponding values. The figure is taken from Bressan et al. (2012).

contraction toward central helium ignition is relatively rapid, the typical lifetime being Kelvin-Helmholtz timescale. The star does not posses a real RGB but only a red tip.

In both cases, the convective envelope can reach previously processed regions deep in the star, dredging the products up to the surface. This process is known as “first dredge-up”.

After the He-flash, the evolution of low-mass stars continues with the central helium-burning. During the RGB phase low-mass stars may experience a significant mass-loss at a rate of about 10^{-8}-10^{-7} $M_\odot$ yr^{-1}. As a consequence, these stars lose part of their envelopes and their mass may be even significantly less than the initial mass (by even about 20%). The core is no more degenerate and the star sits on the so called Horizontal Branch, typical of Globular Clusters, or in a red luminous clump, typical of younger and/or more metal rich systems like Old Open Clusters or metal rich Globular Clusters.

In Figs. 1.1, 1.2 and 1.3, the He-burning phase of low-mass stars is plotted in green color. The He-flash is not followed in these stars. Instead the models are evolved from a Zero Age Horizontal Branch sequence representing the initial steady He-burning phase.

After quiescent helium ignition, intermediate-mass stars descend their red branch until contraction moves them away from the Hayashi track, where they describe the so-called “blue loop”. By comparing Figs. 1.1, 1.2 and 1.3 it is clear that the blue loop is particularly well developed at low metallicity for stars with initial masses between 3 and 5 $M_\odot$. As initial metallicity increases, the blue loop amplitude is reduced.

The burning of the helium in the core of low and intermediate-mass stars produces ^{12}C, ^{16}O and also ^{20}Ne, through the 3α and α-capture reactions. A core mainly made of C and O is built up during central He-burning.

After central helium exhaustion, the evolution of both low- and intermediate-massive stars is the same. The star begins to burn helium in a shell that surrounds the C-O core and the energy released by this process makes the envelope expand and cool down. The hydrogen shell is switched off and the envelope becomes convective again. The star again moves toward lower effective temperatures and higher luminosities as shown in Figs. 1.1, 1.2 and 1.3 toward the RGB phase, but never reaching it (or its prolongation in intermediate-mass stars). This phase of the stellar evolution is known as “Asymptotic Giant Branch” (AGB) phase.

If the star is massive enough, the convective envelope can possibly reach regions in which hydrogen has already been exhausted, dredging up previously CNO processed material. The process is known as “second dredge-up”. In this first phase in which the helium-shell provides most of the stellar luminosity, the AGB phase is named “Early AGB” (EAGB). During this phase neutrino production increases and actually may becomes so important that the neutrino luminosity may balance the gravitational energy release due to the contraction of the C-O core. Lacking this only heating engine, the temperature rise becomes much less significant than the density rise and the star enters again the region of strong electron degeneracy. At this stage the core contraction stops and the He-burning shell moves rapidly toward the hydrogen discontinuity. When the latter is reached, the H-shell re-ignites and the star enters the double shell phase better known as the Thermally Pulsing AGB (TP-AGB) phase, because of periodic thermal pulses (nuclear flashes) of the He-burning shell. At this point, the H-shell produces newly synthesized helium that accumulates above the degenerate C-O core. When this helium pocket reaches a critical mass of about 10^{-3} $M_\odot$ for a C-O core mass of 0.8 $M_\odot$, helium ignites and a thermonuclear runaway occurs, producing a helium-flash. Most of the energy released by the He-flash heats up the above layers, expanding them and switching off the H-shell. The huge amount of energy suddenly released produces an intermediate convective zone extending from the He-burning shell up to the hydrogen-helium discontinuity, as shown in Fig. 1.5. Convection can pollute the intermediate regions with elements processed in the stellar interior, as carbon. Moreover, due to the expansion, the stellar envelope becomes strongly convective, and the H-burning shell quenches off. In sufficiently massive intermediate-mass stars the external convection can penetrate regions already polluted by the intermediate convection initiated by the helium-flash. This process is known as “third-dredge up” and it enriches the photosphere of the star with newly produced elements such as helium and carbon. After this strong expansion, the H-burning shell ignites again and a quiescent phase of H-burning is initiated until another pocket of helium is built up again for another helium-flash to occur. The He-flash occurs cyclically every time that the critical mass is reached. This cycle is known as “thermal pulse”. The amplitude of the pulse progressively increases at each cycle until an asymptotic regime is reached. During the inter-pulse period, the efficiency of the H-shell is essentially determined by the mass of the helium-exhausted core. Therefore, a relation between the mass of this core and the luminosity holds (core-mass luminosity relation, CMLR).

At each thermal pulse a new third dredge-up episode can occur enriching the stellar atmosphere with the products of the nuclear burning inside the star. This process changes abundances of the stellar atmosphere at each episode. In particular, the C/O number ratio may even become greater than one and the TP-AGB stars show typical photospheric abundances of C-stars.

The efficiency of the third-dredge up is determined by various factors. The general trend is that the dredge-up efficiency increases at decreasing metallicities and at increasing stellar masses. During the TP-AGB phase, the efficiency rises until it reaches a maximum value after a certain number of thermal pulses. Below a critical envelope mass of 0.2 $\mathrm{M}_{\odot}$ the third dredge-up does not occur. Both the maximum efficiency value of the third dredge-up and the number of pulses after which this value is reached, depends on the stellar mass and composition.

In more massive TP-AGB stars, with $M_{*} \gtrsim 4\ \mathrm{M}_{\odot}$, another physical process can occur. At the bottom of the convective envelope the temperature can be so high ($T \sim 8 \times 10^{7}$ K) that significant H-burning through the CNO cycle can occur (Renzini & Voli, 1981; Boothroyd & Sackmann, 1992). This process is known as “hot-bottom burning” (HBB). The consequences of this nuclear burning are basically two. First of all, the surface luminosity is higher than expected from the CMLR. In addition, the carbon that has been previously dredged-up is partially converted into nitrogen through the CNO cycle and the formation of C-stars can be prevented. As a consequence of a very efficient HBB, the C/O ratio may become larger than unity because of the activation of the ON cycle that causes the destruction of oxygen in favour of nitrogen.

In Figs. 1.1, 1.2 and 1.3 the thermal pulses developed when $\mathrm{C/O} < 1$ are plotted with blue lines. On the other hand, the thermal pulses plotted in red corresponds to the phases with $\mathrm{C/O} > 1$. From these figures one can see that, at $Z = 0.001$, all the stars considered experience many more thermal pulses as C-stars, than at higher metallicities.

This depends on different factors. First of all, consider that the oxygen in the stellar atmosphere has approximately the same partition (number or mass ratio between the element and the metallicity) at the beginning of the TP-AGB phase. As a consequence, the lower the metallicity is, the lower will be the abundance of oxygen in the atmosphere and the carbon needed to have that $\mathrm{C/O} > 1$. Furthermore, the third dredge-up tends to be more efficient at low metallicity, favoring even more the production of C-stars. At $Z = 0.008$ and 0.02, stars with masses above 4 $M_{\odot}$ tend to develop only few pulses as C-stars.

The complex interplay between the dredge-up and HBB for different initial stellar masses and metallicity values will be discussed in Section 1.3.

As already mentioned, during the TP-AGB phase, the star increasingly loses mass. Though the details of the mass-loss mechanism are still unknown, there is a general agreement on the fact that the strong pulsations experienced by the star in this phase, levitate the gas up to a few

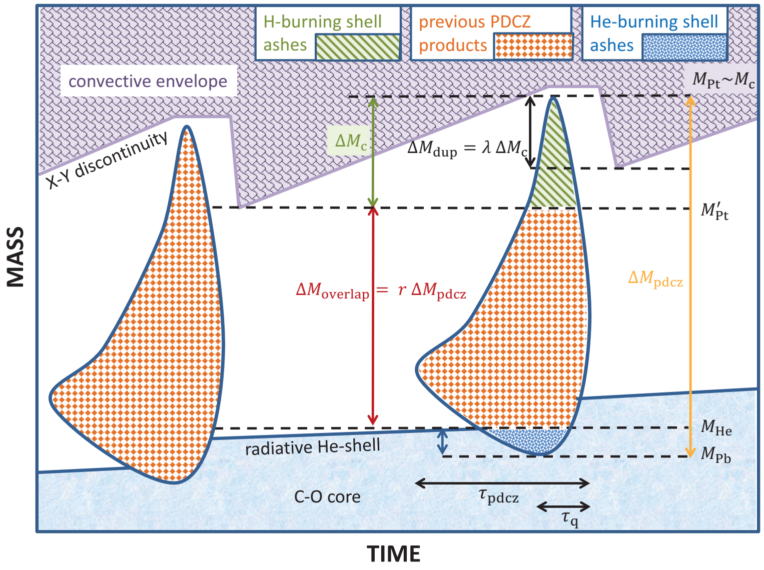

Figure 1.5: Evolution of the inner layers of a TP-AGB star during and between two consecutive thermal pulses. Mass boundaries and relevant quantities are indicated. Note that mass and time coordinates are not on real scales, for graphical clarity. The hatched areas over the later pulse-driven convective zone (PDCZ) correspond to the three-zone stratification of the material, containing from top to bottom: the ashes left by the H-burning shell, the products of the previous PDCZ and the ashes left by the He-burning shell. On the abscissa, the lifetime of the convective pulse τ_{PDCZ} and the quenching time τ_{q}. The figure is taken from Marigo et al. (2013).

stellar radii, where dust is able to condense and may produce a radiation-driven wind, triggered by the interaction between the photons coming from the stellar surface and the dust particles (see Chapter 2).

The evolution of the star proceeds from semiregular (SR) to Mira and eventually to IR star, with mass-loss rates increasing from 10^{-6} $\mathrm{M}_{\odot}$ yr^{-1} for Miras, to about 10^{-4} $\mathrm{M}_{\odot}$ yr^{-1} for IR stars (Zijlstra et al., 2009). The latter class of stars is characterized by strong self-obscuration by the dust produced in the CSE. If the star is O-rich and OH maser emission is detected the star is classified as OH/IR. The details of the computation of the mass-loss rate are explained in Section 1.3.

1.2.2 PARSEC: stellar tracks with the PAdova and TRieste Stellar Evolution Code

The stellar evolutionary code PARSEC computes the stellar tracks in a range of masses between 0.1 and 12 $\mathrm{M}_{\odot}$, with a resolution of 0.05 $\mathrm{M}_{\odot}$ in the range of low-mass stars and of 0.2 $\mathrm{M}_{\odot}$ for intermediate-mass stars. The evolutionary tracks follow the evolution of the stars from the pre-main sequence up to the first well developed thermal pulses of the AGB.

The basic assumptions of the input physics of the stellar evolutionary code are summarized below.

- *The solar distribution of the heavy elements.*

For each element heavier than ^{4}He, a fractional abundance relative to the solar metallicity is specified as a reference distribution ($X_{i,\odot}/Z_{\odot}$). The solar distribution is assigned for 90 chemical elements from Li to U with abundances from Grevesse & Sauval (1998) except for a subset of species for which the revised abundances of Caffau et al. (2011) are adopted. According to these abundances the present-day metallicity of the Sun is $Z_\odot = 0.01524$.

• *Opacities.*

The absorption properties of the matter in the gas phase are evaluated by means of pre-computed Rosseland mean opacities $\kappa_R(\rho, T)$. The opacity is a function of the temperature and density, and has been computed for combinations of temperatures and densities that describe different conditions of the matter in the stellar structure.

In addition to that, the opacity also depends on the gas chemical composition specified by the hydrogen and helium abundances X and Y and by the distribution of the heavy elements. Different programmes have been used in the different temperature ranges for the computations of the opacity tables.

At high temperatures, $4.2 \leq \log(T/K) \leq 8.7$, the opacities adopted are the ones provided by the Opacity Project At Livermore (OPAL) (Iglesias & Rogers, 1996). The computation in this case is performed after specifying the abundances of 19 heavy elements (C, N, O, Ne, Na, Mg, Al, Si, P, S, Cl, Ar, K, Ca, Ti, Cr, Mn, Fe and Ni).

At low temperatures, $3.2 \leq \log(T/K) \leq 4.1$, opacities have been evaluated by ÆSOPUS for any set of chemical abundances for 92 elements from H to U (Marigo & Aringer, 2009). The opacity computations performed by ÆSOPUS account for many continuum and discrete sources, including atomic opacities, molecular absorption and collision-induced absorption.

In the transition region of temperatures between $4.1 \leq \log(T/K) \leq 4.2$ a linear interpolation between the opacities obtained by OPAL and ÆSOPUS is adopted.

Given the distribution of the heavy elements, two distinct sets of tables are generated: the H-rich and H-free one ($X = 0$). This second set is generated to specifically describe the opacities for the He-burning regions.

• *Convection.*

Extended mixing *across* a convective border (overshoot) is formalized in two distinct ways, for the convective core and the external convective shell(s), by means of the mean free-path of fluid elements (mixing length) which is set proportional to the local pressure scale height, H_p:

$$H_\mathrm{p} = \frac{Pr^2}{Gm_r\rho}, \tag{1.1}$$

where P is the pressure, r the distance from the centre of the star, G the gravitational constant, m_r the mass within the radius r and ρ the density.

The efficiency of convection is still uncertain and the mixing length is current calibrated on the Sun.

- *Convective core.*

  In the convective core the value of the overshoot parameter, Λ_C, is chosen accordingly to the stellar mass.

  A variable overshoot parameter is adopted to describe the transition between the stars with radiative and convective cores:

  1. Λ_C is zero below a threshold mass M_O1;
  2. a linear increase of the overshoot efficiency with the mass is adopted between M_O1 and M_O2 up to a maximum value $\Lambda_\mathrm{max} = 0.5$ (Bertelli et al., 1994; Girardi et al., 2000).
  3. for stars more massive than M_O2 the overshoot is assumed to be fully efficient $\Lambda_\mathrm{C} = \Lambda_\mathrm{max}$.

The stellar masses M_{O1} and M_{O2} are not fixed, but are assumed to depend on the initial chemical composition (Fig. 1.4). For the He-burning phases, the overshoot is always fully efficient.

- *Overshoot of the convective envelope*.
  The original prescriptions for the overshoot efficiency in the convective envelope by Alongi et al. (1991) and Bressan et al. (1993) are adopted. The values assumed are $\Lambda_e = 0.05$ in the envelope of stars of $M_* < M_{O1}$ and $\Lambda_e = 0.7$ for $M_* > M_{O2}$. A smooth transition between the two efficiencies is adopted similarly to the case of the convective core.

The overshoot parameters, Λ_C and Λ_e are determined on the base of some observational proprierties of the Hertzsprung-Russel diagram.

1.2.3 Evolution of Thermally Pulsing Asymptotic Giant Branch Stars. The `COLIBRI` Code.

The TP-AGB evolutionary models are computed with `COLIBRI` code, described in Marigo et al. (2013) to which the reader should refer for all the details. For each combination of initial stellar mass (M_*) and initial metallicity (Z), the characteristic quantities at the first thermal pulse, obtained from the `PARSEC` database of full stellar models (Bressan et al., 2012), summarized in Section 1.2.2, are fed as initial conditions into `COLIBRI`, that calculates the whole TP-AGB evolution until the entire envelope is lost by stellar winds.

It is worth emphasizing that, compared to purely synthetic TP-AGB codes, `COLIBRI` relaxes a significant part of their previous analytic formalism in favour of detailed physics applied to a complete envelope model, in which the stellar structure equations are integrated from the atmosphere down to the bottom of the H-burning shell. As a consequence, both the HBB energetics and nucleosynthesis, as well as the basic changes in envelope structure, including effective temperature and radius, can be followed with the same richness of detail as in full models, and even more accurately. The initial mass of the H-exhausted core is taken from the stellar model obtained by `PARSEC` and its growth is followed by evaluating the H-burning rate of the radiative part of the H-shell.

A unique feature of `COLIBRI`, which is of particular importance for the present work, is the first *on-the-fly* computation ever with the `ÆSOPUS` code (Marigo & Aringer, 2009) of: i) the chemistry for roughly 300 atoms and 500 molecular species and ii) gas opacities throughout the atmosphere and the deep envelope at each time step during the TP-AGB phase. This technique assures a consistent coupling of the envelope structure with its chemical composition, that may significantly change due to the third dredge-up and HBB processes.

In particular, with `COLIBRI` it is possible to follow in detail the evolution of the surface C/O ratio, which is known to produce a dramatic impact on molecular chemistry, opacity, and effective temperature every time it crosses the critical region around unity (Marigo, 2002; Marigo & Aringer, 2009). In turn, the C/O ratio plays a paramount role in determining the chemical and physical properties of the dust, as will be discussed in this thesis.

The TP-AGB models used are based on specific prescriptions for the third dredge-up, HBB and mass-loss rate which are outlined below.

• *The third dredge-up*.
The occurrence of the third dredge-up during the TP-AGB phase is estabilished as explained in Wood & Zarro (1981); Marigo et al. (1999) and is a function of the current mass and chemical composition of the star.

After the He-flash the He-shell is pushed out and it cools down to its minimum temperature over the flashcycle, $T_{\rm N}^{\rm min}$. As the thermal pulses reach the full-amplitude regime, a limiting characteristic value of $T_{\rm N}^{\rm min}$ is approached, $\log(T_{\rm N}^{\rm min}) = 6.5 - 6.7$ (Boothroyd & Sackmann, 1992; Karakas et al., 2002). The exact value of $T_{\rm N}^{\rm min}$ is only weakly dependent on chemical composition and core mass. At the same time at which post-flash luminosity maximum is reached, the envelope convection extends to its maximum inward penetration (in mass fraction) and the maximum base temperature, $T_{\rm bce}^{\rm max}$. Hence, it is reasonable to assume that the third dredge-up takes place if, at the stage of post-flash luminosity maximum, the condition $T_{\rm bce}^{\rm max} > T_{\rm N}^{\rm min}$ is satisfied. In particular, in the `COLIBRI` code the condition for the onset of the third dredge-up is established to be $T_{\rm bce}^{\rm max} > T_{\rm dup}$, where $T_{\rm dup}$ is assumed to be a free parameter ($\log T_{\rm dup} = 6.4$ for the present calculations). The rather low value of the temperature parameter favours an earlier occurrence of the third dredge-up episodes.

The third dredge-up is instead modeled by means of two characteristic quantities:

- $M_{\rm C}^{\rm min}$: the minimum core mass for the occurrence of the third dredge-up;
- the dredge-up efficiency described by $\lambda_{\rm du}$:

$$\lambda_{\rm du} = \frac{\Delta {\rm M}_{\rm dup}}{\Delta {\rm M}_{\rm c,tpc}}, \tag{1.2}$$

  where $\Delta{\rm M}_{\rm dup}$ is the dredged-up mass at a given thermal pulse and $\Delta{\rm M}_{\rm c,tpc}$ is the core mass growth over one interpulse period.

The efficiency $\lambda_{\rm du}$ is expected to increase with stellar mass M_*, such that TP-AGB stars with initial masses $M_* > 3\,{\rm M}_\odot$ are predicted to reach $\lambda_{\rm du} \sim 1$, which implies no, or very little, core mass growth. For lower values of the metallicity an earlier onset of the third dredge-up and a larger efficiency is favoured. This implies that low-mass carbon stars are more easily formed as shown in Figs. 1.1, 1.2 and 1.3.

The determination of the parameters $M_{\rm C}^{\rm min}$ and $\lambda_{\rm du}$ is still affected by uncertainties and their values vary considerably from author to author for the same combination of initial stellar mass and metallicity. The adopted approach in the `COLIBRI` code is that of taking $\lambda_{\rm du}$ and $M_{\rm C}^{\rm min}$ as free parameters, and to calibrate them with the largest possible set of observations.

The chemical composition of the dredged-up material (mainly in terms of ^{4}He, ^{12}C, ^{16}O, ^{22}Ne and ^{23}Na) is obtained with the aid of a full nuclear network applied to a model for the pulse-driven convection zone.

• *Hot bottom burning*.
Both the break-down of the CMLR and the rich nucleosynthesis of HBB (via the CNO, NeNa and MgAl cycles) are followed in detail, solving a complete nuclear network coupled to a diffusive description of mixing, at each mesh throughout the convective envelope.

The occurrence of HBB is expected to produce the break-down of the CMLR (Renzini & Voli, 1981; Bloecker & Schoenberner, 1991; Karakas et al., 2002), the `COLIBRI` sequences with $M_* > 4\,{\rm M}_\odot$ exhibit a steep luminosity increase at almost constant core mass as $\lambda_{\rm du} \sim 1$. After reaching a maximum, the luminosity starts to decline quickly from pulse to pulse until the CMLR is recovered again. This is due to the fact that the efficiency of the HBB, and therefore the excess in luminosity with respect to the CMLR, depends on the envelope mass that is rapidly reduced by the onset of the super-wind phase. The peculiar bell-shaped luminosity evolution of massive TP-AGB stars with HBB is shown in Figs. 1.6, 1.7 and 1.8.

- *Mass-loss.*

It has been included under the hypothesis that it is driven by two main mechanisms, dominating at different stages. Initially, before radiation pressure on dust grains becomes the main agent of stellar winds, mass-loss is described with the semi-empirical relation by Schröder & Cuntz (2005), which essentially assumes that the stellar wind originates from magneto-acoustic waves operating below the stellar chromosphere. The corresponding mass-loss rates are indicated with $\dot{M}_{\rm pre-dust}$.

Later on the TP-AGB the star enters the dust-driven wind regime, which is treated with an approach similar to that developed by Bedijn (1988), and recently adopted by Girardi et al. (2010).

Assuming that the wind mechanism is the combined effect of two processes, i.e., radial pulsation and radiation pressure on the dust grains in the outermost atmospheric layers, a functional form of the kind $\dot{M} \propto \exp(M_*^{\alpha} R_*^{\beta})$, as a function of the current stellar mass and radius, is adopted. This expression synthesizes the results of numerical computations of periodically-shocked atmospheres (Bedijn, 1988). The free parameters α and β have been calibrated on a sample of Galactic long-period variables with measured mass-loss rates, pulsation periods, stellar masses, radii, and effective temperatures. The corresponding mass-loss rates are denoted with $\dot{M}_{\rm dust}$. At any time during the TP-AGB calculations the actual mass-loss rate is taken as the maximum between $\dot{M}_{\rm pre-dust}$ and $\dot{M}_{\rm dust}$.

The sample used for the calibration of the mass-loss is composed of about 40 O-rich Mira stars with pulsation periods (fundamental modes) between P ~100 and P ~800 days. The stellar luminosities are derived from the period-luminosity relation. The radii are inferred from interferometric measures, when available, or from the Stephan-Boltzmann relation if the luminosity and effective temperature are known. The stellar masses are calculated using the relation between pulsation, mass and radius (Wood, 1990). Data of the stellar parameters are taken from Le Bertre & Winters (1998) and the mass-loss rates are taken from Loup et al. (1993). The results of the current calibration are preliminary and will be extended to C-stars when the relation between the pulsation period, mass and radius will be available also for these objects.

The key feature of this formalism is that it predicts an exponential increase of the mass-loss rates as the evolution proceeds along the TP-AGB, until typical superwind values, around $10^{-5} - 10^{-4}\ M_{\odot}{\rm yr}^{-1}$, are eventually reached (see bottom panels of Figs. 1.6, 1.7 and 1.8).

Following the results of Marigo et al. (2013) the evolution of the surface C/O ratio is essentially governed by the competition between the third dredge-up occurring at thermal pulses, and HBB taking place during the quiescent interpulse periods. Of great importance are also the stages of onset and quenching of the two processes, that normally do not coincide.

The resulting picture is quite complex as transitions through C/O = 1 may happen at different stages during the TP-AGB evolution and with different characteristics.

1.3 TP-AGB models adopted in this thesis

Figures 1.6, 1.7 and 1.8 show the time evolution of C/O ratio, effective temperature, luminosity, and mass-loss rate for a few TP-AGB stellar models with selected values of the initial mass ($M_* = 1, 2, 3, 4, 5\ {\rm M}_{\odot}$) and metallicity ($Z = 0.001, 0.008, 0.02$). Together with the C/O ratio the carbon excess, defined as the difference between the number of carbon and oxygen atoms, normalized to that of hydrogen atoms, $\epsilon_{\rm C}$-$\epsilon_{\rm O}$=$N_{\rm C}/N_{\rm H} - N_{\rm O}/N_{\rm H}$, is also plotted. This quantity is even more meaningful than the C/O ratio, as it defines approximately the number of carbon atoms not locked into the CO molecule, and thus available for the formation of the

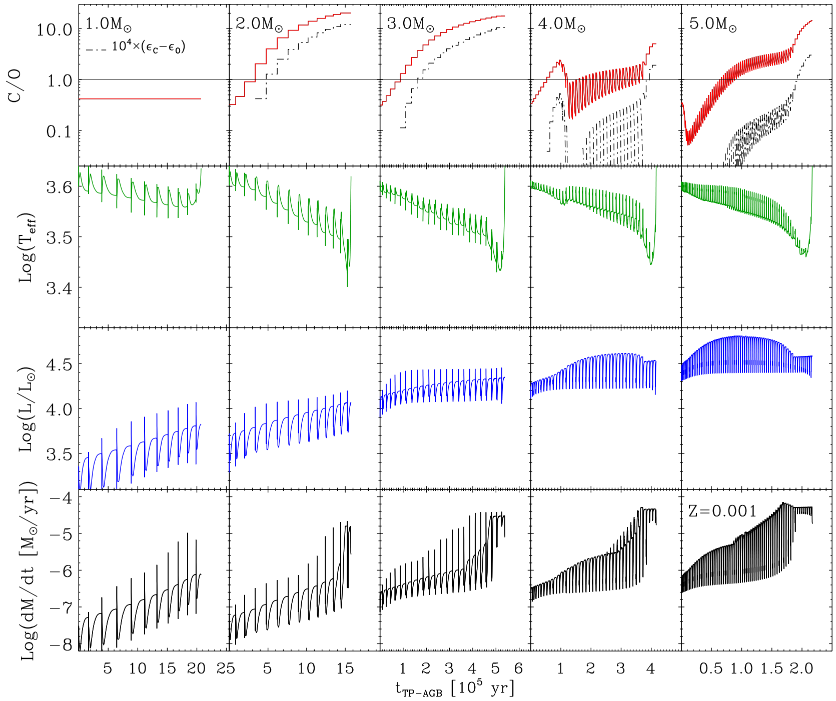

Figure 1.6: Evolution of surface C/O, carbon excess ϵ_C-ϵ_O (only when positive), effective temperature, luminosity, and mass-loss rate during the whole TP-AGB phase of a few selected models with initial metallicity $Z = 0.001$, computed with the `COLIBRI` code (Marigo et al., 2013). These quantities are the key input stellar parameters for the dust growth model. Time is counted from the first thermal pulse. Note that effective temperature and luminosity are obtained from the solution of the full set of the stellar structure equations, and not from fitting relations as usually done in synthetic TP-AGB models. The trends of the C/O ratio and carbon excess reflect the occurrence of the third dredge-up and HBB in TP-AGB stars with different masses and metallicities. Particularly interesting is the case of the $M_* = 4\ \mathrm{M}_\odot$, $Z = 0.001$ model, that undergoes several crossings through C/O = 1. See the text for more details.

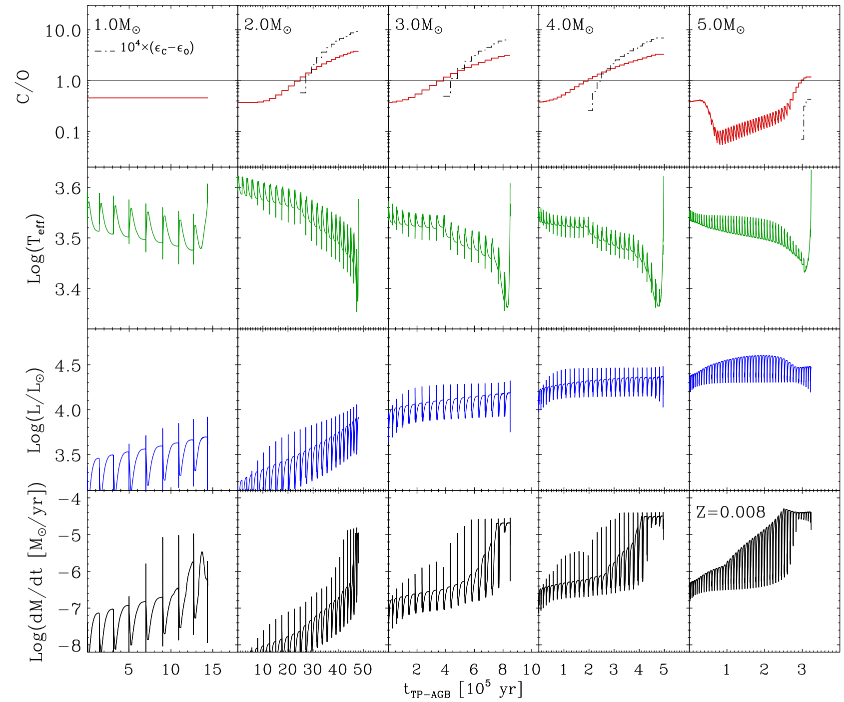

Figure 1.7: The same as in Fig. 1.6, but for initial metallicity $Z = 0.008$.

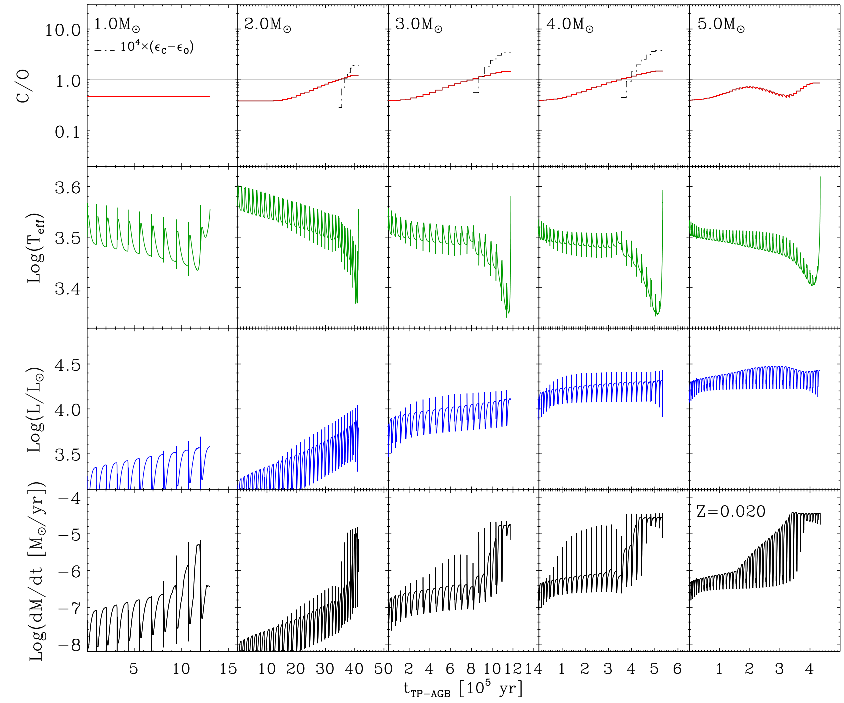

Figure 1.8: The same as in Fig. 1.6, but for initial metallicity $Z = 0.02$.

carbonaceous dust. From inspection of Figs. 1.6, 1.7 and 1.8 a few representative cases of the C/O evolution during the TP-AGB phase, that are relevant for the interpretation of the results presented in this work, are extracted.

a) C/O $<$ 1 during the whole TP-AGB evolution. This is typical of low-mass stars ($M_* \sim 1\,M_\odot$), but the actual minimum mass for a star to become a carbon star, $M_{\rm C}^{\rm min}$, is expected to depend critically on the metallicity, increasing at larger Z.

b) C/O $<$ 1 $\rightarrow$ C/O $>$ 1 as a consequence of the carbon enrichment due to the third dredge-up at thermal pulses. This explains the existence of carbon stars with typical masses of $\sim 2-3\,M_\odot$ depending on metallicity and model details. In these models the rise of the C/O ratio begins at the beginning of the third dredge-up and it is not inhibited by the HBB. Notice that, in these cases, the excess carbon becomes larger and larger at decreasing initial metallicity. Thus at decreasing metallicity, not only the carbon abundance reaches the oxygen abundance more easily but also the amount of primary carbon production is larger. The transition to C/O $>$ 1 may be also experienced by the brightest mass-losing objects (e.g. $M_* > 5M_\odot$ and $Z = 0.008$), that become carbon rich in their last evolutionary stages when HBB is extinguished, while a few more third dredge-up episodes may still take place.

c) C/O $<$ 1 $\rightarrow$ C/O $>$ 1 as a consequence of a very efficient HBB, mainly in quite massive TP-AGB stars, $M_* \gtrsim 5M_\odot$, at very low metallicities, $Z = 0.001$. Differently from the standard channel of carbon star formation, illustrated in the former examples, in this case the C/O ratio becomes larger than unity because of the activation of the ON cycle that causes the destruction of oxygen in favour of nitrogen.

d) C/O $>$ 1 $\rightarrow$ C/O $<$ 1 may take place in relatively massive TP-AGB stars in which HBB develops after the transition to the carbon star regime. In these cases the CN cycle becomes efficient enough to bring the star back to the M spectral type (see the crossing of C/O in the model of 4 $\mathrm{M}_\odot$ and $Z = 0.001$, at time $t_{\rm TP-AGB} \simeq 1.2 \times 10^5$ yr).

e) C/O $<$ 1 $\rightleftarrows$ C/O $>$ 1: multiple transitions across C/O = 1 may take place under particular conditions. The sawtooth trend of the C/O ratio around unity occurs for a significant part of the TP-AGB evolution of the $M_* = 4\ \mathrm{M}_\odot$, $Z = 0.001$ model. This peculiar phase is characterized by quasi-periodic transitions across C/O = 1 from both below and above unity, caused by the alternating effects of the third dredge-up (C/O $\uparrow$) and HBB (C/O $\downarrow$), so that two crossings may be experienced within a single thermal pulse cycle.

Various tests indicate that the present version of TP-AGB models already yields a fairly good description of the TP-AGB phase. Compared to previously calibrated sets (Marigo & Girardi, 2007; Marigo et al., 2008; Girardi et al., 2010) the TP-AGB models yield somewhat shorter, but still comparable, TP-AGB lifetimes, and they successfully recover various observational constraints dealing with e.g. the Galactic initial-final mass relation, spectro-interferometric determinations of TP-AGB stellar parameters (Klotz et al., 2013), the correlations between mass-loss rates and pulsation periods, and the trends of the effective temperature with the C/O ratio observed in Galactic M, S and C-stars.

As it will be discussed in this thesis, further important support comes from the results of the dust growth model applied to the TP-AGB tracks, which are found to nicely reproduce other independent sets of observations, i.e. the correlation between expansion velocities and mass-loss rates of Galactic AGB stars (see Chapter 6).

Chapter 2

Dust-driven wind model

Stellar winds are a phenomenon that induces mass-loss during the lifetime of a star. For TP-AGB stars the characteristic mass-loss rates caused by the wind can reach very high values, up to 10^{-4} $M_\odot$ yr^{-1}, compared with the typical present mass-loss rate of the sun, $2{\times}10^{-14}$ $M_\odot$ yr^{-1}.

Stellar winds can be distinguished on the basis of their driving mechanism as "pressure-driven wind" and "radiation-driven wind". In the former case, the wind is caused by the dissipation of mechanical energy provided by the convection zones, stellar pulsation, and shock waves in the outer regions of the stellar atmosphere. In the radiation driven wind, the acceleration is caused by the transfer of the radiative momentum to dust particles or ions in hot massive stars. The momentum acquired by the dust grains or ions from the photons is finally transferred to the gas by collisions.

In particular, the wind in TP-AGB stars is generated by a combination of the two mechanisms and can be ideally divided in two phases. First, shock waves generated by pulsations are able to lift the gas up to the dust condensation zone, then, when dust is condensed, the outflow is accelerated by the radiation-driven mechanism (Höfner, 2009). The first mechanism has a crucial role, because the temperatures at the photosphere of TP-AGB stars are typically between 2000 and 3000 K, by far too high for the condensation of even the most refractory dust species. Therefore, a mechanism able to lift the gas in regions of lower temperatures is necessary for the onset of a dust-driven wind. The schematic view of dust formation and wind acceleration in TP-AGB is shown in Fig. 2.1.

In this thesis, only the mechanism of dust-driven wind is modeled, assuming that pulsations can levitate the gas up to a few stellar radii. Before the dust condensation region is reached, I assume that the gas moves outwards at fixed initial velocity.

In the models considered in this thesis, the input parameters of TP-AGB evolutionary models necessary to determine the structure of the expanding CSE at each time step are computed with `COLIBRI` code. In particular, `COLIBRI` provides the effective temperature ($T_{\rm eff}$), luminosity (L_*), current mass (M_*), mass-loss rate ($\dot{M}$) and photospheric mass fraction of the element j, X_j.

In the following, the set of differential equations adopted to study the dust formation coupled with a stationary and spherically symmetric wind is summarized. Some of the additional equations needed in the computations are also described.

2.1 Wind dynamics

The initial abundance in the gas phase of a certain atomic or molecular species is calculated starting from the quantity X_j. It is convenient to express the abundances as the number of

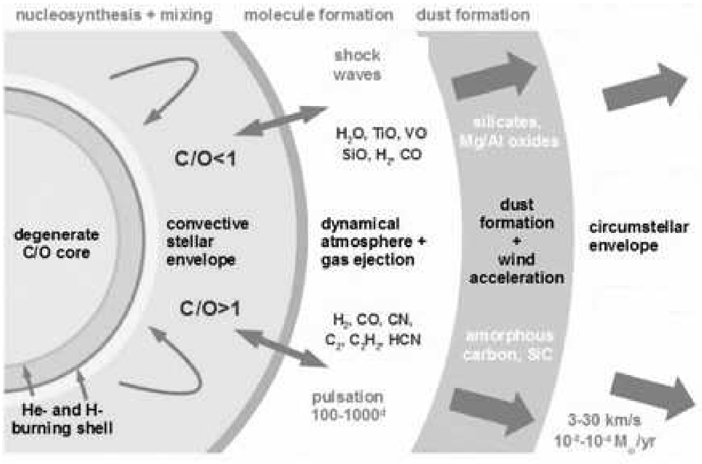

Figure 2.1: A schematic picture of dust-driven wind initiated by shock waves that lift the gas up to the condensation radius (few stellar radii).

atoms or molecules over the number of hydrogen atoms, ϵ_j. The number of hydrogen atoms is calculated starting from the quantity $X_{\rm H}$ provided by the `COLIBRI` code. The quantity ϵ_j along the TP-AGB track is therefore computed as

$$\epsilon_j = \frac{X_j}{m_j} / \frac{X_{\rm H}}{m_{\rm H}} \tag{2.1}$$

where m_j and $m_{\rm H}$ are the mass of the species j and of hydrogen, respectively. The quantity X_j/m_j is the number of the gas species j per gram. Therefore, by dividing by the term $X_{\rm H}/m_{\rm H}$ the quantity obtained is a pure number that gives the ratio between the number density of the species j normalized by the number density of hydrogen.

Following FG06, the momentum equation of a stationary and spherically symmetric outflow is

$$v\frac{dv}{dr} = -\frac{1}{\rho}\frac{dP}{dr} - \frac{GM_*}{r^2}(1-\Gamma)\,, \tag{2.2}$$

where ρ is the gas density, P is the gas pressure, M_* is the actual mass of the star and Γ is the ratio between the radiative and the gravitational accelerations:

$$\Gamma = \frac{L_*}{4\pi c G M_*}\,\kappa, \tag{2.3}$$

where L_* is the actual stellar luminosity, c is the speed of light, G is the gravitational constant and κ is an average quantity expressed as mean absorption coefficient per unit mass [cm^2 g^{-1}]. The mean opacity κ is thus assumed to be independent of the wavelength (grey atmophere approximation). Equation 2.2 is valid for both the dust and the gas components if they are coupled, which means that all the momentum that dust grains receive from the radiation field is rapidly transmitted to the gas. Under this approximation, gas and dust are treated as one-fluid component with no drift velocity between them.

Equation 2.2 has a critical point when the velocity of The sonic radius is located just before Γ becomes larger than one. At this point, the wind becomes supersonic and the contribution of the pressure becomes negligible. As the quantity Γ rapidly increases after that dust is formed, it is possible to assume that the dust condensation radius is approximately equal to the sonic radius (Lamers & Cassinelli, 1999).

In the following I consider the approximation introduced by Lamers & Cassinelli (1999) that considered only the supersonic portion of the outflow in the momentum equation. In such approximation the pressure of the gas is neglected and the momentum equation is

$$v\frac{dv}{dr} = -\frac{GM_*}{r^2}(1 - \Gamma). \tag{2.4}$$

Note that Γ is a function of the stellar parameters which change along the TP-AGB phase. The outflow is more easily accelerated for high luminosity, L_*, and low stellar masses, M_*, for which the gravitational pull is lower, and large values of κ. The initial velocity of the outflow is kept constant up to the point in which $\Gamma > 1$ and its initial value is chosen to be lower than the speed of sound computed along the CSE.

As previously mentioned, the sonic radius approximately coincides with the point in which the outflow is accelerated. The speed of sound at the sonic point is between ~1.5 and ~2.5 km s^{-1} and thus it is safely assumed that the initial velocity of the outflow is 0.5 km s^{-1}.

From Eqs. 2.4 and 2.3 it follows that the outflow is accelerated if the opacity reaches a certain critical value such that the condition $\Gamma > 1$ is satisfied. This value corresponds to

$$\kappa_{\mathrm{cr}} > \frac{4\pi c G M_*}{L_*}. \tag{2.5}$$

In addition to that, from Eq. 2.4 it turns out that the acceleration is higher if the condition $\Gamma > 1$ is satisfied at shorter radial distances, as it is proportional to r^{-2}.

The condition for which $\Gamma > 1$ is necessary but not sufficient in order to produce an efficient outflow. In fact, the expansion velocity should be larger than the escape velocity at some radial distance.

The escape velocity profile is given by

$$v_{\mathrm{esc}} = \sqrt{\frac{2GM_*}{r}}. \tag{2.6}$$

The proportionality between the escape velocity and the actual stellar mass M_*, indicates that the dust-driven wind tends to be more efficient in the final phases of TP-AGB as the stellar mass progressively decreases because of mass-loss.

The final fate of the outflows can always be distinguished in three cases (Höfner, 2009):

1. not being accelerated at all. This happens for $\kappa < \kappa_{\mathrm{cr}}$, or equivalently $\Gamma < 1$;
2. first accelerate, but then decelerate again at some radial distance. This happens when $\kappa > \kappa_{\mathrm{cr}}$, but the acceleration term is not sufficiently high to get that $v_{\mathrm{exp}} > v_{\mathrm{esc}}$.
3. being accelerated away from the star. This happens when $\kappa > \kappa_{\mathrm{cr}}$ and $v_{\mathrm{exp}} > v_{\mathrm{esc}}$.

The quantity κ is provided by the sum of the gas opacity, κ_{gas}, plus all the opacities of the various dust species (see Chapter 3).

Briefly, the opacity of each dust species is computed for a given grain size distribution in a range of dust sizes between a_{min} and a_{max} and averaged over the incident radiation energy density. This last computation is performed by first considering two limiting regimes: the optically thin one, when only a tiny amount of dust is formed, and the optically thick one, that holds when the bulk of dust has been produced.

In the optically thick regime the local thermodynamical equilibrium (LTE) and the diffusion approximation (DA) of the radiative transport equation are valid. Indeed, both the LTE and the

DA are met when the photon mean free path is is much shorter than the typical scale length (R_*). In these conditions, for the grey atmosphere approximation, the frequency-independent opacity is suitable described by the Rosseland mean opacity $\kappa_{\mathrm{R},i}$.

On the other hand, when the medium is optically thin, the photon mean free path is so long that the DA breaks down and the Rosseland mean opacity approximation is no longer valid. In these conditions, the most suitable approximation is the Planck mean opacity, indicated by $\kappa_{\mathrm{P},i}$. Both $\kappa_{\mathrm{R},i}$ and $\kappa_{\mathrm{P},i}$ vary along the CSE.

The computation is performed for a complete condensation of the key-elements ($f_i = 1$) of the various dust species. The key-elements for the solar partition abundances are listed in Table 2.1. Following FG06, the key-element of a given dust species is the least abundant element among those involved in its formation:

$$\epsilon_{k,i} = \min\{\epsilon_{j,i}\}, \tag{2.7}$$

where I indicate with $\epsilon_{j,i}$ the quantities defined by Eq. 2.1 involved in the formation of the dust species i.

The final opacities are proportional to the condensation fractions of the key-elements into the dust grains of the species under consideration, f_i. Therefore, each opacity $\kappa_{\mathrm{P},i}$ or $\kappa_{\mathrm{R},i}$ computed for the complete condensation ($f_i = 1$), has to be multiplied by the fraction effectively condensed into dust.

The condensation fraction can be written as,

$$f_i = n_{k,i} \frac{4\pi(a_i^3 - a_0^3)\rho_{d,i}}{3m_{d,i}\epsilon_{k,i}} \epsilon_s, \tag{2.8}$$

where $n_{k,i}$ is the number of atoms of the key-element present in one monomer of the dust species i; $m_{d,i}$ is the mass of the monomer; a_i denotes the grain size (radius) and a_0 the initial grain size; $\rho_{d,i}$ is the dust density of the grain; $\epsilon_{k,i}$, ϵ_s are the number densities of the key-element, and of the initial number of dust grains (seed nuclei) normalized to the number density of Hydrogen, respectively.

The total Rosseland, κ_{R}, and Planck, κ_{P}, opacities are obtained by summing the contribution of all the dust species $\kappa_{\mathrm{R},i}$ and $\kappa_{\mathrm{P},i}$.

The final opacity is evaluated by weighting the two contributions,

$$\kappa_{\mathrm{av}} = \kappa_{\mathrm{gas}} + \kappa_{\mathrm{P}} \exp(-\tau_d) + \kappa_{\mathrm{R}}(1 - \exp(-\tau_d)]. \tag{2.9}$$

The quantity τ_d is a suitable weighting factor, computed by integrating from the dust condensation radius (R_c) outwards

$$\tau_d = \int_{R_c}^{r} \rho \kappa_{av} dr'. \tag{2.10}$$

The quantity κ_{av} is finally used in Eq. 2.3 in the presented calculations.

The density profile $\rho(r)$ is determined by the continuity equation:

$$\rho(r) = \frac{\dot{M}}{4\pi r^2 v}\,. \tag{2.11}$$

This quantity is directly proportional to the mass-loss rate, that can vary along the TP-AGB by more than three orders of magnitude (from 10^{-8} to $>10^{-5}$ $\mathrm{M}_\odot$ yr^{-1}). For a constant initial velocity, the density profile initially decreases with the distance (as $\propto r^{-2}$) but, when the outflow is accelerated, the density drops more steeply.

A useful quantity is the number density of Hydrogen atoms, N_H. hydrogen is not present in form of single atoms at the typical temperatures of the CSEs, however N_H is computed as if all the hydrogen present in the gas phase were present in this form.

N_H is directly provided by Eq. 2.11 assuming that the gas is made up by hydrogen molecules (H_2) and helium atoms (He)

$$N_H = \frac{\rho}{(1+4\epsilon_{He})m_H}. \tag{2.12}$$

The temperature structure $T(r)$ is described by means of the approximation for a grey and spherically symmetric extended atmosphere in radiative equilibrium $J = B$, where J is the integrated mean intensity and $B = \sigma {T_{eff}}^4/\pi$ is the integrated Planck function (Lucy, 1971, 1976)

$$T(r)^4 = {T_{eff}}^4\Big[W(r) + \frac{3}{4}\tau\Big], \tag{2.13}$$

where

$$W(r) = \frac{1}{2}\Big[1 - \sqrt{1-\Big(\frac{R_*}{r}\Big)^2}\Big] \tag{2.14}$$

is the dilution factor, R_* is the photospheric radius, and τ is the optical depth that obeys the differential equation

$$\frac{d\tau}{dr} = -\rho\kappa\frac{R_*^2}{r^2}, \tag{2.15}$$

with the boundary condition

$$\lim_{r\to\infty} \tau = 0. \tag{2.16}$$

For each dust species i the growth of dust grains is assumed to start from first refractory and stable compounds, called seed nuclei, not necessary of the same chemical composition as the final fully-grown grains. The subsequent addition of molecules or atoms on these first aggregates is called “accretion” (see Chapter 4).

The accretion rate of dust grains is described by a specific differential equation which takes into account the balance between the growth rate J_i^{gr}, and the decomposition rate, J_i^{dec} of the grain. The differential equation describing the dust growth is usually expressed in terms of the variation of the grain radius, a_i, which is obtained from the variation of the grain volume, V_i

$$\frac{dV_i}{dt} = 4\pi a_i^2 V_{0,i}(J_i^{gr} - J_i^{dec}), \tag{2.17}$$

where J_i^{gr} and J_i^{dec} are the growth and decomposition rates expressed per unit time and per unit surface, and $V_{0,i}$ is the volume of the nominal monomer of dust, obtained by the relation

$$V_{0,i} = \frac{m_{d,i}}{\rho_{d,i}}. \tag{2.18}$$

By differentiating $V_i = (4/3)\pi a_i^3$ in Eq. 2.17 one finally obtains

$$\frac{da_i}{dt} = \Big(\frac{da_i}{dt}\Big)^{gr} - \Big(\frac{da_i}{dt}\Big)^{dec} = V_{0,i}(J_i^{gr} - J_i^{dec}), \tag{2.19}$$

The dust species assumed to form in CSEs of M- and C-stars and the correspondent abbreviations used in the text are listed in Table 2.1. For each dust species i one differential equation of the form 2.19 is integrated.

Here I briefly remind that the term J_i^{gr} is essentially evaluated by computing the minimum between the fluxes of the incident molecules or atoms needed to form the dust species, i:

$$J_{i,j}^{gr} = \alpha_i n_{j,g} v_{th,j}(T_{gas}), \tag{2.20}$$

where $n_{j,g}$ is the number density of the particle j, $v_{th,j}(T_{\rm gas})$ is the mean velocity of the particles moving towards the surface of the grain and and α_i is the so called “sticking coefficient” that takes into account the probability for a particle to stick on the grain surface.

The initial abundances of the molecules and atoms in the gas phase are defined by Eq. 2.1 and they change along the CSE because they are depleted from the gas phase when dust is formed. The actual abundances in the gas phase are indicated as $\epsilon_{j,g}$.

The corresponding number densities of the molecules and atoms in the gas phase $n_{j,g}$ are computed as the product between $\epsilon_{j,g}$ and $N_{\rm H}$ (given by Eq. 2.12):

$$n_{j,g} = \epsilon_{j,g} N_{\rm H}. \tag{2.21}$$

This means that the number density of the species j is affected by the variation of $N_{\rm H}$ that changes with the density profile (Eq. 2.12). In particular, the density is affected by the velocity and therefore by the wind dynamics (Eq. 2.11). Moreover, the density also depends directly on the mass-loss rate, which changes by orders of magnitude during the TP-AGB evolution (from 10^{-8} to 10^{-5} $M_\odot$ yr^{-1}).

For olivine and pyroxene there are two differential equations describing the fractional content of magnesium in grains, $x_{\rm ol}$ and $x_{\rm py}$, respectively. In the corresponding stoichiometric formulae these two quantities are the number of sites occupied by Mg atoms over the total number of sites occupied by Mg plus Fe atoms.

The fractional abundances $x_{\rm ol}$ and $x_{\rm py}$ range from 0 to 1, where 1 corresponds to the case known as “iron-free” silicates. In all the intermediate cases the silicates are named “dirty”.

For the case $x_i = 1$ olivine dust species is known as *forsterite* (fo) and pyroxene as *enstatite* (en), on the other hand for $x_i = 0$ the two species are called *fayalite* (fa) and *ferrosilite* (fer), respectively.

The quantities $x_{\rm ol}$ and $x_{\rm py}$ change with time according to two distinct differential equations describing the variation of the fractional abundance of magnesium due to possible exchange with Fe atoms in the gas phase and due to the dust growth process.

- Olivine.

$$\frac{dx_{\rm ol}}{dt} = \frac{3V_{0,\rm ol}}{a}[(x_g - x_{\rm ol})J^{\rm gr}_{\rm ol} + \frac{1}{2}(J^{\rm ex}_{+,\rm ol} - J^{\rm ex}_{-,\rm ol})], \tag{2.22}$$

- Pyroxene.

$$\frac{dx_{\rm py}}{dt} = \frac{3V_{0,\rm py}}{a}[(x_g - x_{\rm py})J^{\rm gr}_{\rm py} + (J^{\rm ex}_{+,\rm py} - J^{\rm ex}_{-,\rm py})]. \tag{2.23}$$

where the quantities $J^{\rm ex}_{+,i}$ are the exchange rates between Mg atoms in the dust grain and Fe atoms in the gas phase, and $J^{\rm ex}_{-,i}$ are the correspondent inverse rates. These quantities will be specified in Chapter 4. Here I just remind that the term $J^{\rm ex}_{+,i}$ is evaluated similarly to $J^{\rm gr}_i$ taking into account the flux of incident Mg atoms multiplied by a factor that takes into account the probability that an exchange between Mg and Fe can occur.

2.2 Method of solution and initial conditions

The system of differential equations describing the dust evolution is given by Eqs. 2.4, 2.15 and an equation like 2.19 for each dust species listed in Table 2.1.

Table 2.1: Chemical composition of the dust species in CSEs for M- and C-star CSEs. The corresponding molecules and atoms in the gas phase involved in the formation of the specific dust species and the key-element are also listed. The key-element is selected for each model along the TP-AGB evolution. I here indicate the usual key-element for the solar partition of the metallicity (See Table 2.2).

Species	Abbreviation	Stoichiometric formula	key-element
M-stars			
Olivine	ol	$Mg_{2x_{ol}}Fe_{2(1-x_{ol})}SiO_4$	Si
Pyroxene	py	$Mg_{x_{py}}Fe_{(1-x_{py})}SiO_3$	Si
Quartz	qu	SiO_2	Si
Periclase	pe	MgO	Mg
Corundum	co	Al_2O_3	Al
Iron	ir	Fe	Fe
C-stars			
Amorphous Carbon	C(s)	C	C
Silicon Carbide	SiC	SiC	Si
Iron	Fe(s)	Fe	Fe

Table 2.2: Abundances of various elements provided by Anders & Grevesse (1989).

Element	ϵ_i
He	9.77×10^{-2}
C	3.63×10^{-4}
O	8.51×10^{-4}
Mg	3.80×10^{-5}
Fe	4.68×10^{-5}
Si	3.55×10^{-5}
S	1.62×10^{-5}
Al	2.95×10^{-6}
Ti	9.77×10^{-8}

Finally I add the Eq. 2.10 to compute the weighting factor for the opacity. The independent variable of the system is the radial distance r, whereas the dependent variables are the velocity, v, the optical depth, τ, the grain size for each dust species, a_i, the quantities $x_{\rm ol}$ and $x_{\rm py}$ and the radial optical depth, τ_d. The quantities that determine the wind structure are the gas temperature and the density profiles, $T(r)$ and $\rho(r)$, the total opacity, κ, the dust condensation fraction, f_i, and Γ.

Since the boundary condition on τ (Eq. 2.16) is at infinity, but all the other conditions are at the inner radius, I solve the system by means of the following shooting method. I begin the integration with a guess value of τ_i at a suitable inner radius $r_i \geq R_*$ chosen so that the gas temperature is high enough to inhibit the formation of any type of dust. I then integrate outward all the equations until $r = 1000\ R_*$. The latter condition is set because, at these large distances from the photosphere, the density is so low that dust cannot grow any more and the acceleration term is negligible. As the integration moves outward, all the dependent variables but τ are reset to their initial values, until dust begins to condense. In this way I avoid that, for example, the velocity drops to zero before dust condenses, which corresponds to the assumption that pulsations are able to drive the medium into the condensation region. I iterate on τ_i until the condition $\tau \leq \epsilon \times \tau_i$ is met at the end of the integration. This condition actually replaces Eq. 2.16 and the accuracy has been chosen to be $\epsilon = 10^{-4}$ in order to provide stable solutions and to avoid excessive computational time, at once.

The value of initial velocity of the wind is chosen to be lower than the speed of sound, 0.5 km s^{-1}. If the outflow is not finally accelerated, I assume that it proceeds at least at this initial velocity. This assumption tends to overestimate the fraction of dust that can condense but, since it corresponds to phases where the mass-loss rate is relatively low, it does not significantly affect the total dust ejecta.

The initial grain size is assumed to be the one of the first stable seed nuclei, $a_0 = 10^{-3}\ \mu$m corresponding to clusters of about 100 atoms.

The reactions assumed for dust formation are discussed in Chapter 4. The adopted opacities are described in Chapter 3.

Chapter 3

Opacity

As mentioned in Chapter 2, dust opacity is a crucial ingredient as far as the wind dynamics is concerned because it provides the momentum coupling between radiation and matter.

In this Chapter I describe the details of the opacity calculations used in this thesis, given by Eq. 2.9.

3.1 Dust opacities from the scattering, absorption and radiation pressure cross sections

When a light ray passes through a medium, it is partially scattered and partially absorbed. In this process, part of its momentum is transferred to the medium.

In the case of a single dust grain of size a, the momentum transmitted to the dust particle by the incident light is evaluated from its radiation pressure cross-section (in cm^2), $C_{\rm rp}$, that is a function of the grain size and of the wavelength of the incident radiation. This term is evaluated from the scattering and the absorption cross-sections of the dust grains, indicated respectively by $C_{\rm sca}$ and $C_{\rm abs}$ (Hoyle & Wickramasinghe, 1991).

The relation linking $C_{\rm rp}$ to $C_{\rm sca}$ and $C_{\rm abs}$ is

$$C_{\rm rp}(\lambda, a) = C_{\rm abs}(\lambda, a) + C_{\rm sca}(\lambda, a)(1- < \cos\theta >), \tag{3.1}$$

where θ is the scattering angle shown in Fig. 3.1 and $< \cos\theta >$ is the average value of the scattered light component with the same direction of the incoming light beam.

Another useful quantity is the extinction cross-section, $C_{\rm ext}$, that is a measure of how much light has been subtracted from the incident beam after it has passed through a medium:

$$C_{\rm ext} = C_{\rm abs} + C_{\rm sca}. \tag{3.2}$$

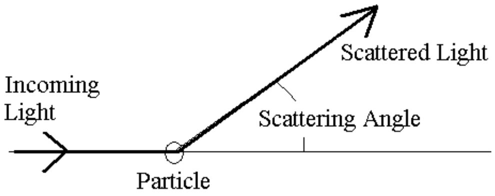

Figure 3.1: Schematic representation of the scattering process.

For the computations that follow, it is useful to define the adimensional quantity known as "radiation-pressure efficiency", $Q_{\rm rp}$

$$Q_{\rm rp} = \frac{C_{\rm rp}}{\pi a^2}. \tag{3.3}$$

Similarly, it is possible to define the absorption, the scattering and the extinction efficiencies as

$$Q_{\rm abs} = \frac{C_{\rm abs}}{\pi a^2}, \tag{3.4}$$

$$Q_{\rm sca} = \frac{C_{\rm sca}}{\pi a^2}, \tag{3.5}$$

and

$$Q_{\rm ext} = \frac{C_{\rm ext}}{\pi a^2}. \tag{3.6}$$

For an ideal ensemble of dust grains of the same size, the total radiation pressure opacity (in cm^2 g^{-1}) is obtained by multiplying the cross-section of a single grain by the total number of dust grains per unit of mass. If n_{gr} is the number density of the grains and ρ the medium average density, for each dust species i one gets

$$\kappa_{i,\lambda} = \frac{n_{gr}}{\rho} C_{\rm rp}(a, \lambda), \tag{3.7}$$

where n_{gr}/ρ gives the total number of grains per unit mass.

By expressing Eq. 3.7 in terms of $Q_{\rm rp}$ by means of Eq. 3.3, and after multiplying and dividing by a, one gets

$$\kappa_{i,\lambda} = \frac{n_{gr}}{\rho} \pi a^3 \frac{Q_{\rm rp}(a, \lambda)}{a}. \tag{3.8}$$

From this equation, it follows immediately that $\kappa_{i,\lambda}$ is proportional to the volume occupied by all the dust grains ($\propto n_{gr}\pi a^3$) that depends essentially on the abundance of the key-element. Therefore, the behaviour of the opacity, given the initial gas abundance, depends on the term $Q_{\rm rp}/a$.

As this term is a function of the incident radiation, the opacity will be mostly influenced by those wavelengths at which the stellar radiation peaks. The stellar emission is, at first approximation, the one of a Black Body at the star's effective temperature. The radiative power density of black body emission in [erg s^{-1} cm^{-2} sr^{-2} μm^{-1}] is expressed as a function of the wavelength as

$$B_\lambda(T) = \frac{2h\pi c^2}{\lambda^5} \frac{1}{\exp[hc/(\lambda k_b T)] - 1}, \tag{3.9}$$

where h is the Planck constant, k_b the Boltzmann constant, λ the wavelength and T the black body temperature. For TP-AGB stars the effective temperatures are typically between $T_{\rm eff}$ = 2000 and 3000 K. As the temperature decreases, the peak in the emission is shifted toward longer wavelengths. Note that, at these temperatures, the peak of the stellar radiation is around 1 μm.

For the cases in which the incident radiation peaks at wavelength much longer than the typical grain size ($\lambda >> a$) the evaluation of the quantities $Q_{\rm rp}/a$, $Q_{\rm abs}/a$ and $Q_{\rm sca}/a$ can be performed by means of the Rayleigh limit approximation and the quantity $Q_{\rm rp}/a$ is independent of the grain size. However, at the typical wavelength (1 μm) at which the stellar energy density peaks, this approximation is not valid, because λ and a are comparable. In this regime, the quantity $Q_{\rm rp}/a$ critically depends on the grain size, and the computation needs to be performed by means of the Mie theory starting from the complex refractive index $m = n - ik$, where n and k are the refractive and absorptive indexes, respectively.

In the Mie theory, the basic assumption is that the particles have a regular, spherical shape, so that the problem of studying the interaction between dust particles and the electromagnetic waves is reduced to the classical problem of finding the solution for the Maxwell's equations with the boundary condition for a sphere.

The solutions of this problem are implemented in numerical form in several textbooks. I use here the formulae implemented by Christian Mätzler[1] for `MATLAB`. These routines make it possible to evaluate the quantities $Q_{\rm sca}$, $Q_{\rm sca} < \cos\theta >$, $Q_{\rm ext}$ from the optical constants (n, k) as follows:

$$Q_{\rm sca} = \frac{2}{x^2}\sum_{n=1}^{\infty}(2n+1)(|a_n|^2 + |b_n|^2), \tag{3.10}$$

$$Q_{\rm sca} < \cos\theta >= \frac{4}{x^2}\Big\{\sum_{n=1}^{\infty}\frac{n(n+2)}{n+1}Re(a_n a^*_{n+1} + b_n b^*_{n+1}) + \sum_{n=1}^{\infty}\frac{2n+1}{n(n+1)Re(a_n b^*_n)}\Big\}. \tag{3.11}$$

$$Q_{\rm ext} = \frac{2}{x^2}\sum_{n=1}^{\infty}(2n+1)Re(a_n + b_n). \tag{3.12}$$

From Eqs. 3.10 and 3.12 it is possible to compute $Q_{\rm abs}$ by using Eqs. 3.2, 3.4, 3.5 and 3.6. From Eqs. 3.10 and 3.11 and from $Q_{\rm abs}$ I can compute $Q_{\rm rp}$ by using Eqs. 3.1, 3.3, 3.4 and 3.5.

The quantities a_n and b_n are given by

$$a_n = \frac{m^2 j_n(mx)[x j_n(x)]' - j_n(x)[mx j_n(mx)]'}{m^2 j_n(mx)[x h_n^{(1)}(x)]' - h_n^{(1)}(x)[mx j_n(mx)]'}, \tag{3.13}$$

$$b_n = \frac{j_n(mx)[x j_n(x)]' - j_n(x)[mx j_n(mx)]'}{j_n(mx)[x h_n^{(1)}(x)]' - h_n^{(1)}(x)[mx j_n(mx)]'}, \tag{3.14}$$

where $j_n(z)$, $h_n^{(1)} = j_n(z) + iy_n(z)$ are spherical Bessel functions of order n ($n = 1, 2, \ldots$) and arguments $z = x$ or mx, where $x = 2\pi a/\lambda$ and primes mean derivatives with respect to the argument.

Figure 3.2 shows the behaviour of $Q_{\rm rp}/a$ (black line), $Q_{\rm abs}/a$ (red line) and $Q_{\rm sca}/a$ (blue line) as a function of the wavelength of the incident radiation for three different amorphous dust species: carbon (Hanner, 1988) (upper panel), iron-bearing (dirty) oxygen-rich silicates (Ossenkopf et al., 1992) (middle panel) and iron-free silicates (Jäger et al., 2003) (lower panel). The lines are drawn for different choices of the grain size (0.01, 0.05, 0.1 and 0.3 μm). The range of wavelength shown is between 0.5 and 50 μm.

For all the species considered, $Q_{\rm rp}/a$, $Q_{\rm abs}/a$, $Q_{\rm sca}/a$ show a dramatic rise in the region around the peak of the stellar radiation (1 μm) for increasing grain sizes, while for $\lambda >> a$ $Q_{\rm rp}/a$ and $Q_{\rm abs}/a$ show the same asymptotic behaviour for all the grain sizes. Also the relative contribution of absorption and scattering to the radiation pressure term changes according to the grain size.

When initially dust starts to form, the grains are small ($a \sim 0.01$ μm), $Q_{\rm rp}/a$ is almost entirely provided by the absorption term, and scattering is negligible. Once the dust has grown significantly, the terms $Q_{\rm rp}/a$, $Q_{\rm abs}/a$, $Q_{\rm sca}/a$ increase and become strongly dependent on the

---

[1] The routine is available at http://omlc.ogi.edu/software/mie/

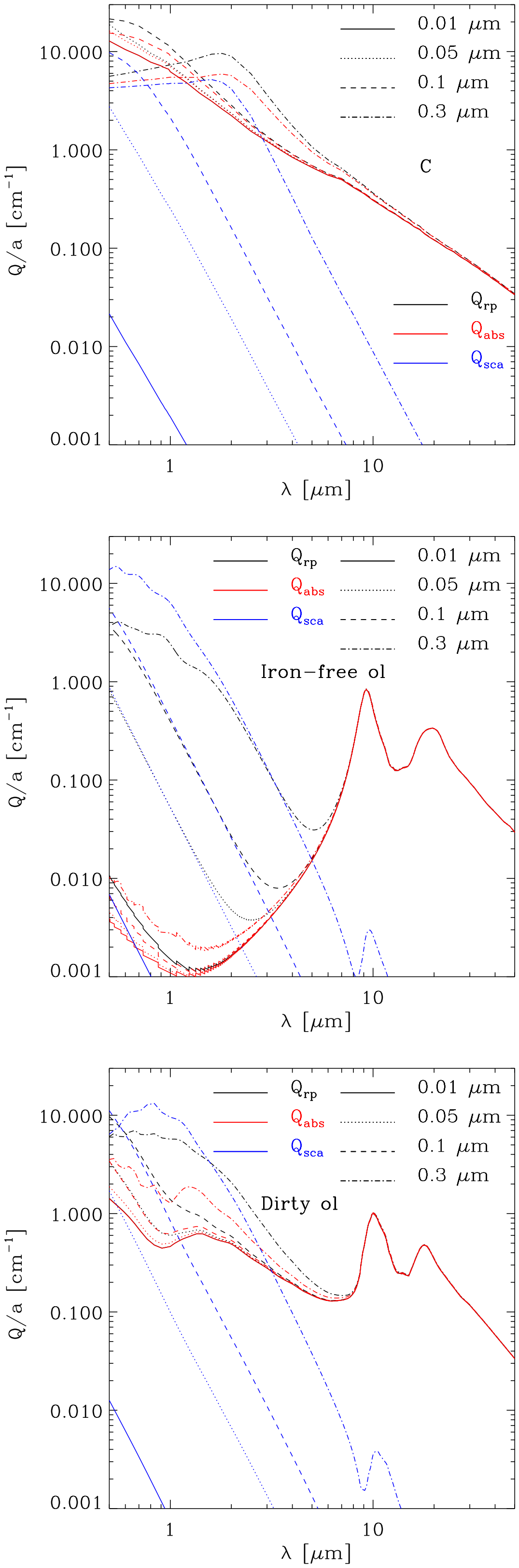

Figure 3.2: $Q_{\rm rp}/a$ (black lines), $Q_{\rm sca}/a$ (blue lines) and $Q_{\rm abs}/a$ (red lines) as a function of the wavelength for amorphous carbon (Hanner, 1988) (upper panel), dirty silicates (Ossenkopf et al., 1992) (middle panel) and iron-free silicates (Jäger et al., 2003) (lower panel). The lines drawn correspond to different grain sizes: 0.01 (solid), 0.05 (dotted), 0.1 (dashed) and 0.3 μm (dotted-dashed).

size in a way that varies with the dust species. For amorphous carbon, the dominant term is absorption for all the sizes considered in the plotted range of wavelength. For dirty silicates, the scattering term becomes dominant for $a > 0.1\ \mu$m below $\lambda \sim 1\ \mu m$. For iron-free silicates, $Q_{\rm rp}/a$ is very low for grain sizes below $a \sim 0.01\ \mu$m and it is relevant only when the scattering becomes dominant ($a > 0.05\ \mu$m below $\lambda \sim 2\ \mu$m).

At fixed grain size, the three dust species show different behaviours: around 1 μm the radiation pressure opacity of carbon dust is always higher than that of silicates because this species is more opaque to the stellar radiation at those wavelengths (the absorption term is higher). Iron-free silicates are always less opaque than the dirty silicates due to their high transparency to radiation (low $Q_{\rm abs}/a$) and the value of $Q_{\rm rp}/a$ becomes comparable to the one of dirty silicates only for large grain sizes ($a \sim 0.3\ \mu$m), when the scattering is by far dominant compared to absorption.

Silicates also show the characteristic absorption double peaks at 9.8 and 18 μm for which their absorption is greater than the one of amorphous carbon.

3.2 The opacity for a grain size distribution

In the general case the opacity is computed by integrating the radiation pressure cross-section over a grain size distribution, for each species. This corresponds to an extension of the relation 3.8 under the assumption that the grains formed are not of the same size. Considering for example the average of $Q_{\rm rp}/a$ computed over the grain size distribution one gets

$$\kappa_{i,\lambda} = \frac{\pi}{m_{\rm H}} \int_{a_{\rm min}}^{a_{\rm max}} a^3 \frac{Q_{\rm rp}(a,\lambda)}{a} \frac{d\epsilon_i}{da} da, \tag{3.15}$$

where $d\epsilon_i/da$ per μm is normalized for the number density of the hydrogens, $m_{\rm H}$ is the Hydrogen mass and $a_{\rm max}$, $a_{\rm min}$ are the maximum and the minimum grain size of the distribution, respectively.

To start with, I consider the power-law grain size distribution assumed for the ISM (Mathis et al., 1977) for each dust species i

$$\frac{d\epsilon_i}{da} = A_i a^{-x_g}, \tag{3.16}$$

where the size a is normalized to 1 μm, A_i is the normalization constant and the slope, x_g, is assumed to be the same for all the dust species. The quantity A_i is computed for the case of complete condensation of the key-element into the dust species i. It is evaluated by considering that the total mass of dust can be expressed either as

$$M_i = \frac{\epsilon_{k,i}}{n_{k,i}} m_{d,i} N_{\rm H}, \tag{3.17}$$

or, after integrating the grain size distribution, as

$$M_i = \rho_{d,i} N_{\rm H} \int_{a_{\rm min}}^{a_{\rm max}} \frac{4\pi a^3}{3} \frac{d\epsilon_i}{da} da. \tag{3.18}$$

The quantities $n_{k,i}$ and $m_{d,i}$ have been introduced in Chapter 2. By means of Eq. 3.16 I get

$$M_i = \rho_{d,i} N_{\rm H} \int_{a_{\rm min}}^{a_{\rm max}} \frac{4\pi a^3}{3} A_i a^{-x_g} da. \tag{3.19}$$

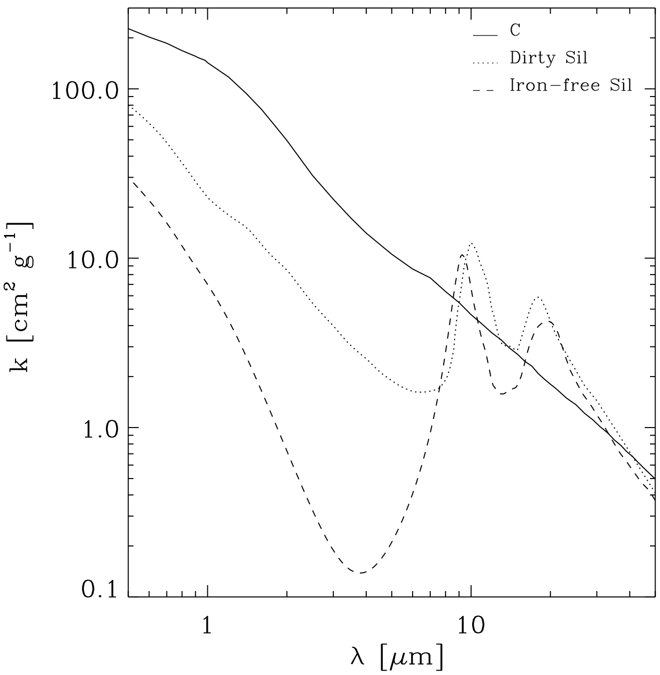

Figure 3.3: Opacities of different dust species (Carbon, solid line; dirty silicates, dotted line and iron-free silicates, dashed line) as a function of the wavelength, averaged over the grain size distribution given by Eq. 3.16 and $a_{\min} = 0.005$ and $a_{\max} = 0.25$ μm. The normalizations are the ones for the abundances of Anders & Grevesse (1989) and are computed through Eq. 3.20.

By equating Eqs. 3.17 and 3.19 the normalization constant reads

$$A_i = \frac{3\epsilon_{k,i} m_{d,i}(4 - x_g)}{n_{k,i} 4\pi\rho_{d,i}(a_{\max}^{4-x_g} - a_{\min}^{4-x_g})}. \tag{3.20}$$

This quantity, and therefore the total opacity, scales with the abundance of the key-element (proportional to the metallicity).

Figure 3.3 shows the radiation pressure opacity obtained by integrating Eq. 3.15 over the grain size distribution 3.16 for the three dust species considered in the previous section (carbon, dirty and iron-free silicates). The resulting opacity provides the total cross-section of a grain distribution. The total mass of dust is fixed by the abundance of the key-element, $\epsilon_{k,i}$, according to Eq. 3.17. The key-elements are assumed to be the ones listed in Table 2.1 and their abundances, taken from Anders & Grevesse (1989) can be found in Table 2.2.

The normalization constant is computed according to the Eq. 3.20 for the solar abundances of Anders & Grevesse (1989) and the range of grain sizes is between $a_{\min} = 0.005$ and $a_{\max} = 0.25$ μm.

Carbon dust (solid line) shows the highest opacity in the range of wavelength from 0.5 up to 8 μm. Above these wavelengths, the silicate features at 9.8 and 11.2 μm increase their opacities above the carbon one. Iron-free silicates show the lowest opacity up to 8 μm, whereas the presence of iron in silicate dust more than doubles its opacity around 1 μm. This fact points out the critical dependence of the opacity on the chemical composition of the silicates.

From Eqs. 3.8 and 3.15 it follows that the total opacity depends on the term $Q_{\rm rp}/a$ as a function of the grain size once the key-element abundance is fixed. In particular, if the grain size distribution is shifted toward large grains, the final opacity is expected to be larger than the one obtained from a size distribution in which most of the grains are small.

In this regard it is important to remember that it is established from observations that dust grains formed in the CSEs of TP-AGB stars tend to be larger than the ones of the observed distribution in the ISM. This is mainly due to the fact that dust grains produced in the CSEs can undergo a subsequent evolution in the ISM once they are injected in the surrounding medium (Draine, 2003).

Since the size distribution of dust grains formed in the CSEs is not easily predictable and tends to be higher than the one found in the ISM, it is worth testing how the opacity changes for different choices of the grain size distributions and for different ranges of grain sizes.

In Fig. 3.4 the effects of the variation in the grain size distribution are shown for the cases of C(s) (blue lines), dirty silicates (black lines) and iron-free silicates (red lines). The solid lines show the opacities for the grain size distribution of the ISM in its standard range of values (stnd in the figure): $x_g = 3.5$, $a_{\rm min} = 0.005$ and $a_{\rm max} = 0.25$ μm. The case of an almost flat distribution, $x_g = 0.1$, is illustrated for three choices of the minimum and maximum grain sizes: $a_{\rm min} = 0.1$ and $a_{\rm max} = 0.15$ μm (dotted line), $a_{\rm min} = 0.2$ and $a_{\rm max} = 0.25$ μm (dashed line), $a_{\rm min} = 0.3$ and $a_{\rm max} = 0.35$ μm (dashed-dotted line). The total mass of dust is fixed by the abundance of the key-element, $\epsilon_{k,i}$, according to Eq. 3.17. The key-element is assumed to be completely condensed in the dust species i ($f_i = 1$). Notice that, under this hypothesis, the total volume occupied by the grains for different choices of the grain-size distribution remains the same. In other words, the smaller are the grains, the higher is their number.

For the flat grain-size distribution, the opacity around 1 μm tends to become flatter for increasing values of the grain-sizes. Even if the maximum peak of the opacity is higher for distributions with a prevalence of small grains (stnd case), for larger grains the opacity remains higher in a broader range of wavelength.

For wavelength between 0.5 and 2 μm the opacity of iron-free silicates becomes comparable to the dirty silicate one for the flat grain size distribution peaked around 0.2 and 0.3 μm, whereas it deviates from the dirty silicate one around 3 μm.

3.3 Opacity average over the incident radiation field

As already anticipated in Chapter 2 the dynamical model adopted is based on a gray atmosphere computed by means of suitable frequency averaged opacities: the Rosseland and Planck opacities.

In order to compute these mean opacities for each dust species i, the wavelength-dependent opacity obtained from Eq. 3.15 is averaged over the wavelength-dependent incident radiation energy density approximated by a black body.

The final opacities are thus expressed as a function of the temperature of the black body that provides the incident radiation field.

Following Lamers & Cassinelli (1999) I consider two limiting cases, the optically thin and the optically thick regimes.

The first regime is typically valid at the very beginning of dust condensation, when the condensed fraction of dust is very low. In fact, before dust is formed, the opacity, entirely provided by gas, is very low, according to Bell & Lin (1994),

$$\kappa_{\rm gas} = 10^{-8}\rho^{2/3}T^3, \tag{3.21}$$

where ρ is in g cm^{-3} and T is in K.

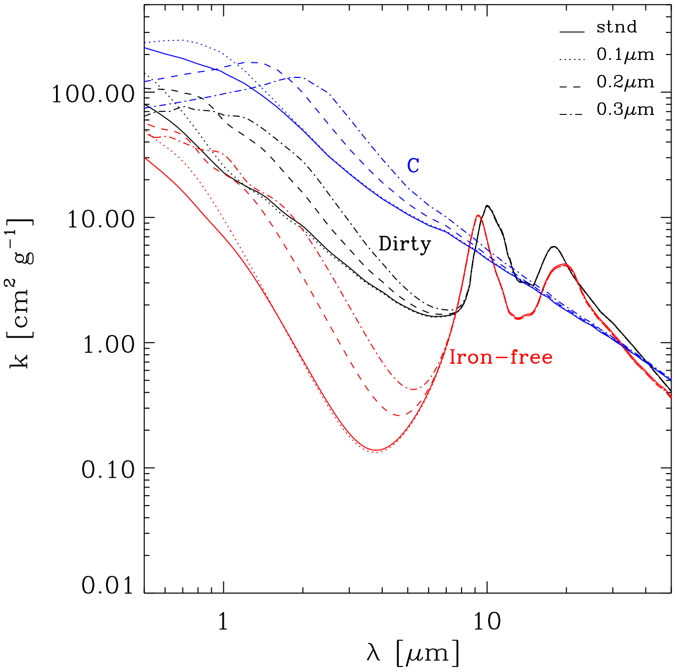

Figure 3.4: Opacities of various dust species: C(s) (blue lines), dirty silicates (black lines) and iron-free silicates (red lines) as a function of the wavelength, for different grain size distributions given by Eq. 3.16: $x_g = 3.5$, $a_{\rm min} = 0.005$ and $a_{\rm max} = 0.25\ \mu$m (stnd-solid lines), or for almost flat grain size distribution ($x_g = 0.1$) with $a_{\rm min} = 0.1$ and $a_{\rm max} = 0.15\ \mu$m (0.1 μm-dotted lines), $a_{\rm min} = 0.2$ and $a_{\rm max} = 0.25\ \mu$m (0.2 μm dashed lines), $a_{\rm min} = 0.3$ and $a_{\rm max} = 0.35\ \mu$m (0.3 μm dashed-dotted lines). For each of the choices, the normalization is computed for the abundances of the key-element $\epsilon_{k,i}$ taken from Anders & Grevesse (1989) and computed through Eq. 3.20.

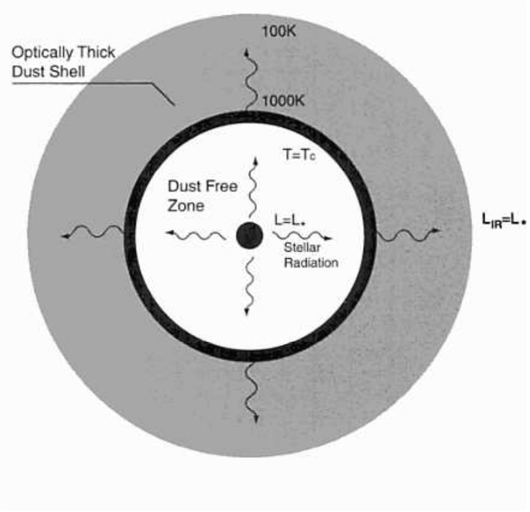

Figure 3.5: Schematic view of optically thin and optically thick regimes (before and after the dust formation zone). When dust is not yet formed the incident radiation is the one of a black body at the effective temperature, outside of the dust formation shell the light is heavily absorbed and the incident radiation field corresponds to a black body at the local temperature. The figure is taken from Lamers & Cassinelli (1999).

As can be seen by comparing the above formula with the dust opacities shown in Fig. 3.3, $\kappa_{\rm gas}$ is several orders of magnitude lower than the value of the dust opacities around 1μm.

Already when the first dust grains condense (e.g. Al_2O_3 in M-stars) the opacity gets much larger and, as soon as dust is formed, the medium becomes optically thick and the dust thermalizes at local temperature.

A schematic representation is sketched in Fig. 3.5. When the optically thin regime holds, the radiation energy density perceived by a shell around the star is that of a black body at the effective temperature of the star. On the other hand, when the dust shell is formed and the optically thick regime is dominant, the external shells perceive the radiation energy density of a black body at the local temperature. In the two regimes the opacity is evaluated with two different methods.

As long as the medium remains optically thin, the photon mean-free path is so long that the diffusion approximation of photons is not valid. In these circumstances, a straight arithmetic average of the monochromatic absorption coefficient, designated with $\kappa_{P,i}$ for each dust species i, over a black body at the effective temperature of the star, $T_{\rm eff}$, is suitable to represent the absorption properties of the gas in a simplified version of the radiation transport equation (Helling et al., 2000). This average is known as "Planck mean opacity":

$$\kappa_{{\rm P},i}(T_{\rm eff}) = \frac{\int_0^\infty \kappa_{\nu,i} B_\nu d\nu}{\int_0^\infty B_\nu d\nu}. \tag{3.22}$$

In the optically thick regime, local thermal equilibrium and the diffusion approximation of the radiative transport equation are valid, because photons mean-free path is much shorter than the typical scale length (R_*) and collisions dominate the thermodynamic state of matter. In such conditions the black body distribution is computed at the local gas temperature, T, assuming local thermal equilibrium. In the diffusion approximation the frequency-independent Rosseland mean opacity $\kappa_{{\rm R},i}$ turns out to be the harmonic average over the frequencies:

$$\frac{1}{\kappa_{{\rm R},i}(T)} = \frac{\int_0^\infty \frac{1}{\kappa_{\nu,i}} \frac{\partial B_\nu}{\partial T} d\nu}{\int_0^\infty \frac{\partial B_\nu}{\partial T} d\nu}. \tag{3.23}$$

This average emphasizes spectral regions of weak absorption, across which the energy flux is most efficiently transported.

Both Rosseland and Planck opacities are frequency-integrated averages, so that they finally depend on the temperature, density and chemical composition of the gas.

Figure 3.6 shows the comparison between Planck (black lines) and Rosseland (red lines) mean opacities as a function of the black body temperature in the range between 500 and 3000 K for the most relevant dust species present in the CSEs: olivine (solid line), iron (dotted), amorphous carbon (dashed) and SiC (dashed-dotted). The computation is performed for the maximum of dust fractional condensation and for the standard ISM grain size distribution ($x_g = 3.5$, $a_{\rm min} = 0.005$ μm and $a_{\rm max} = 0.25$ μm in Eq. 3.16).

For the Planck average, the most opaque species above 700 K is carbon dust, whereas, for temperatures between 150 and 700 K, corresponding to a range of wavelengths between ~4.4 and ~20 μm, both dirty and iron-free olivine opacities are higher than the carbon one. In this range of wavelengths, in fact, the characteristic double peak of silicate species at 9.8 and 18 μm tends to increase the opacity.

For the Rosseland average, the dirty olivine opacity is comparable to the amorphous carbon one above 200 K.

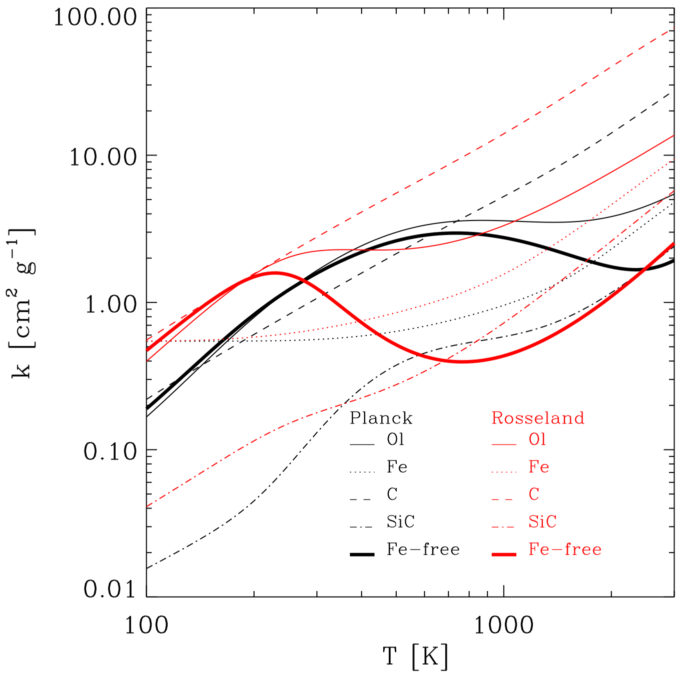

Figure 3.6: Planck mean opacities (black lines) are compared with Rosseland ones for different dust species (with $\epsilon_{k,i}$ values taken from Anders & Grevesse, 1989). Olivine (solid lines), pyroxene (dotted lines) and iron (dashed line). The computation is performed assuming $x_g = 3.5$ and $a_{\rm min} = 0.005$ μm and $a_{\rm max} = 0.25$ μm in Eq. 3.16 for all the dust species considered.

The comparison between the dirty silicate and iron-free opacities shows that the Planck averages of the two sets are comparable between 150 and 700 K, while they diverge at higher temperatures. The range of temperatures in which the two Planck opacities are comparable corresponds to wavelengths between ~4.4 and ~20 μm. From the comparison in Fig. 3.3, it follows that the two opacities are very similar above 7 μm, while below 7 μm the iron-free opacity is much lower than the one of dirty silicates. The Planck averages remain similar up to 20 μm because the average computed in this way weights more those regions in which κ_λ is higher (Eq. 3.22). Thus, the Planck averages of the two different sets remain similar up to 700 K.

On the other hand, the Rosseland averages of dirty and iron-free silicates are similar only below 200 K, whereas above this temperature the iron-free opacity is highly depressed with respect to the dirty one. The reason why this happens is that the Rosseland average weights more those regions in which the term κ_λ is lower, as shown in Eq. 3.23. As a consequence, it is heavily affected by the large difference between iron-free and dirty silicates opacities below 7 μm.

3.4 Average opacity for the computations of wind models

As already stated in Section 3.2 the opacity is computed for each dust species under the hypothesis of complete condensation of the key-element for the dust compound under consideration. In particular, the resulting averaged opacities $\kappa_{{\rm P},i}$ and $\kappa_{{\rm R},i}$ are proportional to its abundance.

However, to obtain the current dust opacities, the quantities $\kappa_{{\rm P},i}$ and $\kappa_{{\rm R},i}$ are multiplied by the fraction of dust effectively condensed, f_i, defined by Eq. 2.8. The corresponding opacities for each i are proportional to the amount of key-element effectively condensed in that specific dust species.

The total Planck opacity is therefore,

$$\kappa_{\rm P} = \sum_i f_i \kappa_{{\rm P},i}, \tag{3.24}$$

and the correspondent Rosseland one is

$$\kappa_{\rm R} = \sum_i f_i \kappa_{{\rm R},i}. \tag{3.25}$$

As discussed in GS99, this approximation is accurate enough if the opacity of one of the dust species is dominant. In M-stars the opacity is dominated by silicate dust, while, in C-stars, most of the opacity is provided by amorphous carbon.

To account for the transition from the optically thin to the optically thick regime that happens when dust is forming, I use a combination of the Planck and Rosseland opacities, by means of an appropriate weighting factor related to the vertical optical depth of the layers where dust is forming (τ_d):

$$\kappa_{\rm av} = \kappa_{\rm gas}(T) + \kappa_{\rm P}(T_{\rm eff}) \exp(-\tau_d) + \kappa_R(T)(1 - \exp(-\tau_d)]. \tag{3.26}$$

The quantity τ_d is computed integrating from the dust condensation radius (R_c) outwards

$$\tau_d = \int_{R_c}^{r} \rho \kappa_{\rm av} dr'. \tag{3.27}$$

3.5 Different opacity sets for silicates

In the literature different data sets for silicate opacity are adopted.

As the opacity is a critical quantity that affects the wind structure and dynamics, it is worth investigating the properties of the different data sets, listed in Table 3.1. The abbreviations used in the figures are also given.

They are described briefly in the following.

- *Oxygen-rich and oxygen-deficient dirty silicates (Ossenkopf et al., 1992).*
  In these two data sets, the constants n and k are estimated through observations of circumstellar silicates relative to the peak value near 10 μm. This evaluation is based on the following assumptions. The grain size distribution is a power-law with $x_g = 3.5$ and the grains form a continuous distribution of ellipsoidal shape in the Rayleigh limit. These data sets include in silicates some impurities. In particular, silicates have 6.3% of Fe_3O_4 and 3.1% of Fe. The oxygen-deficient set is representative of warm oxygen-deficient circumstellar silicate dust, if silicates have not yet reached their stoichiometric proportion. On the other hand, the second set is representative of OH/IR stars and the diffuse ISM. As pointed out by the authors, the optical constants of the two sets of this mixture are nearly independent of the type of silicate (oxygen-deficient or oxygen-rich).

- *Olivine with* $x_{\rm ol} = 0.5$ *(Dorschner et al., 1995).*
  This data set is derived from the study of the optical properties of silicate glasses prepared in laboratory. Glasses of olivine have stoichiometric formula $Mg_{2x_{\rm ol}}Fe_{2(1-x_{\rm ol})}SiO_4$ and with $x_{\rm ol} = 0.5$.

Table 3.1: Different data sets for silicate dust.

Silicate	Reference	Abbreviation
Dirty O-rich	Ossenkopf et al. (1992); Le Sidaner & Le Bertre (1996)	Orich, LL
Dirty O-deficient	Ossenkopf et al. (1992)	Odef
Olivine $x_{\rm ol} = 0.5$	Dorschner et al. (1995) GS99	Dorsch, GS99
Iron-free olivine	Jäger et al. (2003)	iron-free

- *Dirty silicates (Le Sidaner & Le Bertre, 1996).*
  In this opacity set the silicates cross-section is derived by selected stellar sources with energy distribution between 1 and 20 μm. The resulting spectra are interpreted by means of a radiative transfer model applied to each object. The range of temperature of grain formation is assumed to be between 800–950 K, depending on the pressure of the region of dust formation and the effective temperature is $T_{\rm eff} \sim 1800-2800$ K. The condensation radius, outflow expansion velocity and drift velocity are assumed. The cross-sections are recovered under the assumption that the grains have all the same size of 0.1 μm.

- *Olivine (GS99).*
  In GS99 an analytic fit of the opacity of amorphous olivine as a function of the temperature is computed. The authors evaluated the Rosseland average (Eq. 3.23) from the data set by Dorschner et al. (1995) under the assumption that the medium is always optically thick. The analytic fit as a function of the temperature is provided by the following formula

$$\begin{aligned} K_{\rm ol}(T) &= \Big[(6.147\times10^{-7}T^{2.444})^{-2} + \Big((6.957\times10^{4}T^{-2.329})^{2} + \qquad (3.28)\\ &+ \sqrt{(3.505\times10^{-4}T^{0.755})^{4} + (1.043\times10^{-9}T^{2.523})^{4}}\Big)^{-1}\Big]^{-1/2}. \qquad (3.29)\end{aligned}$$

- *Iron-free olivine (forsterite) (Jäger et al., 2003).*
  This set of optical constants are derived from transmission measurements in the wavelength range between 0.2 and 500 μm for pure amorphous forsterite prepared in laboratory.

The different approaches by which the silicate optical constants are derived, affect the final opacities, and therefore the wind dynamics.

In the upper panel of Fig. 3.7 the different data sets are plotted as a function of the wavelength. In particular, the radiation pressure cross-section is averaged over an almost flat grain size distribution for which $x_g = 0.1$, $a_{\rm min} = 0.005$, $a_{\rm max} = 0.18$ μm. The only exception is the set of data by Le Sidaner & Le Bertre (1996) in which the authors assumed that the grains have all the same size (0.1 μm).

For this latter data set, I compute the normalization constant starting from a grain size distribution of Dirac delta function:

$$\frac{d\epsilon_{\rm sil}}{da} = A_{\rm sil}\delta(a - a_0), \qquad (3.30)$$

and finally using Eq. 3.18 I get

$$A_i = \frac{3\epsilon_{k,i} m_{d,i}}{n_{k,i} 4\pi\rho_{d,i} a_0^3}. \qquad (3.31)$$

In the lower panel of Fig. 3.7 the opacities averaged over the black body radiation energy density are plotted against temperature, for the Planck (black) and Rosseland (red) averages.

The behaviours of the oxygen-deficient and the oxygen-rich data sets from Ossenkopf et al. (1992) and Le Sidaner & Le Bertre (1996) are very similar for both the Planck and Rosseland averages.

In the data set from Dorschner et al. (1995) the Planck opacity of olivine is similar to the previous quoted data sets, but it diverges in the Rosseland average.

This trend can be understood by looking at the upper panel of Fig. 3.7 in which opacities as a function of the wavelength are compared. For the three data sets of oxygen-deficient (Ossenkopf et al., 1992) and oxygen-rich (Ossenkopf et al., 1992; Le Sidaner & Le Bertre, 1996) silicates, the behaviour of the opacity as a function of the wavelength is very similar, and therefore this is reflected in the final mean opacities.

On the other hand, both the data set by Dorschner et al. (1995) and Jäger et al. (2003) show a minimum in the opacity as a function of the wavelength around 7 and 3-4 μm, respectively. These two wavelengths correspond to temperatures of $\sim$400 K and $\sim$700-1000 K, respectively.

In the case of the Planck mean opacities the corresponding averages are not greatly affected by these two minima and the resulting curves are quite similar to the other data sets. In fact, the Planck average weights more the regions where the term κ_λ is high than the regions of low absorption.

On the other hand, the correspondent Rosseland mean opacities are well below the results obtained from the other data sets. The Rosseland average, in fact, weights more the regions in which the opacity is low than the ones of high absorption.

Finally, the fitting formula for olivine Rosseland opacity provided by GS99 is drawn with the thick solid line. As this formula is based on the data set from Dorschner et al. (1995) the resulting curve has the same shape as I obtain from the data but with a slightly different normalization constant.

Some caution is necessary in the use of this fitting formula. In fact, if the opacity obtained is used as it is given, the results can be very different from the one obtained by using the average opacity provided by Eq. 3.26. In particular, between 1000 and 2000 K this opacity is about one-third with respect to the other data sets.

The usually adopted data set, that is the one I chose for the computations that will be presented in the following chapters, is the oxygen-rich data set by Ossenkopf et al. (1992). This data set is representative of the chemical composition of silicates (olivine and pyroxene) in the CSEs of M-stars which are mostly amorphous and might include iron impurities. Moreover, differently from the data set by Le Sidaner & Le Bertre (1996), which is limited to dust grains of 0.1 μm, the selected data set allows the computation of the opacities in the range of sizes adopted for the grain size distribution.

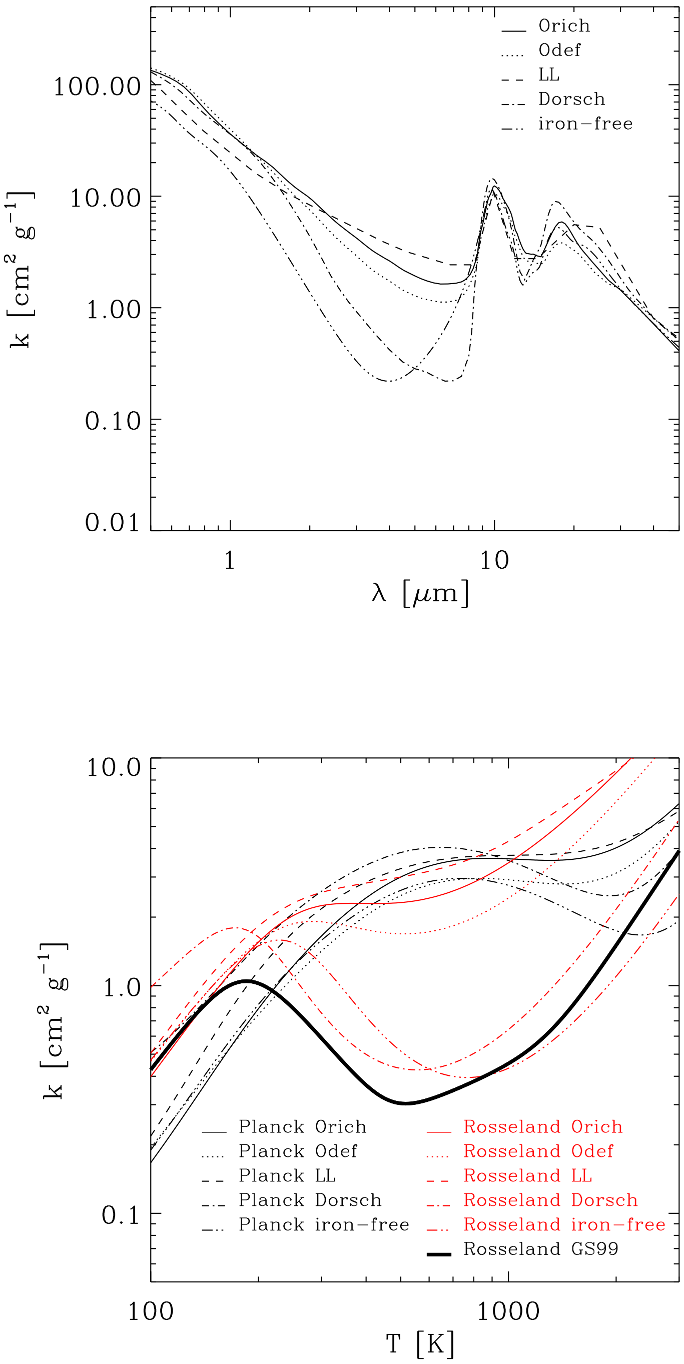

Figure 3.7: *Upper panel*: opacities as a function of the wavelength computed for a grain size distribution with $x_g = 0.1$, $a_{\rm min} = 0.005$ and $a_{\rm max} = 0.18$ μm. The opacities are computed for different data sets: oxygen-rich (thin-solid lines) and oxygen-deficient silicates opacities (dotted lines) from Ossenkopf et al. (1992), from Dorschner et al. (1995) (dashed lines) and data from Le Sidaner & Le Bertre (1996) (dot-dashed lines). *Lower panel*: Planck and Rosseland mean opacities (black and red lines, respectively) as a function of the temperature of the black body radiation computed for the same data sets.

Chapter 4

Dust growth

From a microscopic point of view, dust formation is an extension of the gas phase chemistry from the first critical clusters of molecules up to fully-grown grains. The most general description of this process consists of following the network of the relevant chemical reactions including, at the same time, molecules, clusters and dust grains.

Another kind of approach describes dust growth in relatively simpler terms based on the fact that the proprieties of molecules and dust grains are quite different. In the molecular domain, in fact, the chemical reactions between molecules critically depend on their size. On the other hand, in the macroscopic regime, typical of seed nuclei and dust grains, the description of the reactions between molecules and grains can be treated in an approximated way.

In particular, dust formation in the expanding CSE of a TP-AGB star can be modeled as a two-step process. After the so-called "nucleation process" from which the first, most refractory, stable compounds (seed nuclei) are formed, accretion of dust grains proceeds by addition of other molecules from the gas phase through a given chemical reaction.

The seed nuclei are usually defined as aggregates of about 100 atoms, corresponding to cluster sizes of 10^{-7} cm.

From the seeds, dust grains can grow in different ways:

- homogeneous growth of homogeneous grains. In this case in each growth process the same identical monomer is added to the grain;
- growth of the grain by a variety of molecules.

Nucleation and accretion are processes that occur far from chemical equilibrium condition. However, before describing the detailed dust growth based on non-equilibrium chemistry, it is useful to investigate equilibrium chemistry for two reasons. First of all, the results of equilibrium chemistry provide an interesting insight about which are the most refractory dust species that firstly form in CSE. Second, destruction rates are determined by considering that their values are, by definition, equal to their growth rates, in chemical equilibrium conditions.

The equilibrium chemistry is described in the following section.

4.1 Equilibrium chemistry in Circumstellar envelopes

In the two different classes of TP-AGB stars (C- and M-type) the molecules observed in the gas phase are very different. In C-stars, the carbon over oxygen ratio is $C/O > 1$ and all the oxygen atoms are locked into the very stable CO molecules. In this condition, the most abundant free element in the gas phase able to form molecules is usually carbon. The chemistry of C-stars

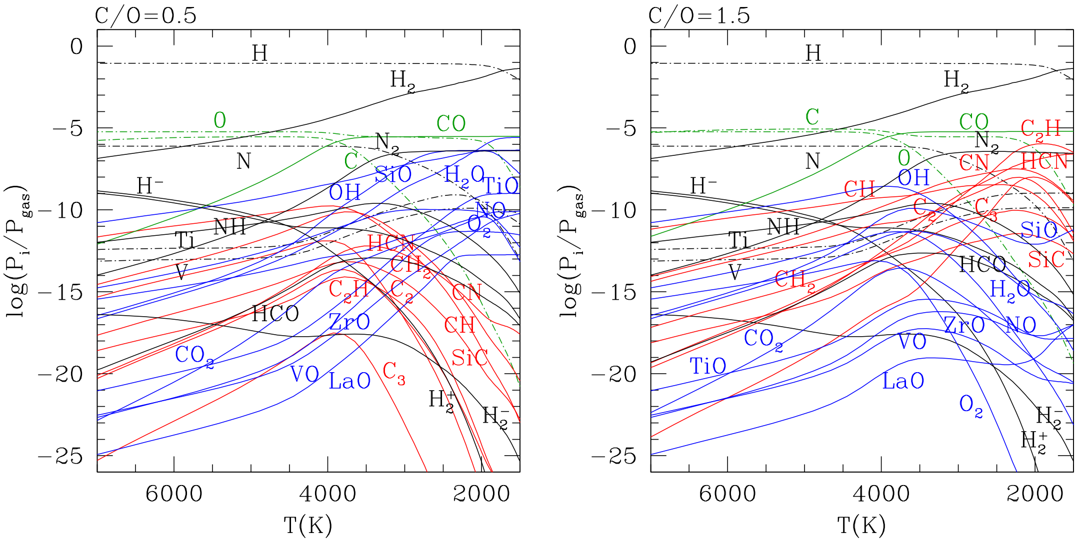

Figure 4.1: Partial pressures of a subset of atomic and molecular species computed with the ÆSOPUS code (Marigo & Aringer, 2009) according to the temperature-pressure stratification of a complete envelope-atmosphere model with $\log(T_{\rm eff}) = 3.45$, $\log(L/L_\odot) = 3.7$, $M_* = 2\ {\rm M}_\odot$, and solar metallicity $Z = Z_\odot = 0.0152$ following the revision by Caffau et al. (2011). Two values of the C/O ratio have been considered, i.e. C/O = 0.5 (left panel) and C/O = 1.5 (right panel). Note the abrupt change in the molecular equilibria of the O-bearing (blue) and C-bearing (red) molecules between the two cases, as well as the almost invariance of the abundance of the highly stable CO molecule.

dust is therefore based on carbon chemistry and it is mainly composed of Silicon Carbide (SiC), amorphous carbon and iron.

On the other hand, in M-stars the chemistry of dust grains is determined by the presence of oxygen excess in the gas phase ($C/O < 1$) and the dust species formed are mainly amorphous silicates, quartz (SiO_2), periclase (MgO), corundum (Al_2O_3) and iron.

The intermediate case of S-stars with $C/O \sim 1$ is not here considered as these objects are rare and their contribution to the total dust production is very low. Thus, in this thesis I assume that, when $C/O > 1$, the dust species formed are the ones typical of C-stars CSEs, whereas, when $C/O < 1$, the dust species produced are the ones of M-stars CSEs.

The relative abundances of the different molecules in the gas phase in stellar atmospheres are plotted in Fig. 4.1 where their partial pressures over the total gas pressure are shown as a function of the temperature for two values of the C/O, 0.5 (left panel), and 1.5 (right panel).

The partial pressures correspond to the equilibrium abundances of the molecules in the stellar atmosphere according to the temperature-pressure stratification of a complete envelope-atmosphere model with $\log(T_{\rm eff}) = 3.45$, $\log(L/L_\odot) = 3.7$, $M_* = 2\ {\rm M}_\odot$, and solar metallicity $Z = Z_\odot = 0.0152$, following the revision by Caffau et al. (2011). Of course at the highest abundances in the atmosphere, correspond the highest values of the partial pressures in the plot.

For M-stars in the range of temperature between 2000 and 4000 K the partial pressure of oxygen-bearing molecules such as SiO, H_2O, OH and TiO are several orders of magnitude larger than the carbon-based molecules such as HCN, CH_2 and CN. The opposite occurs for C-stars for which CH_2, CN and HCN are much more abundant than SiO, H_2O and OH.

Notwithstanding the complexity of the starting molecular chemistry in the gas phase shown in Fig. 4.1, not all the molecules are able to stick on the grain surface. The stable molecule CO

Table 4.1: Dust formation reactions for M- and C-stars. The starting gas molecules and atoms from which each dust species is formed are also given.

Species	Reactions	Molecules
M-stars	dust formation	
ol	$2x_{ol}Mg + 2(1 - x_{ol})Fe + SiO + 3H_2O$ $\rightarrow Mg_{2x_{ol}}Fe_{2(1-x_{ol})}SiO_4(s) + 3H_2$	Mg, Fe, SiO, H_2O
py	$x_{py}Mg + (1 - x_{py})Fe + SiO + 2H_2O$ $\rightarrow Mg_{x_{py}}Fe_{(1-x_{py})}SiO_3(s) + 2H_2$	Mg, Fe, SiO, H_2O
qu	$SiO + H_2O \rightarrow SiO_2(s) + H_2$	SiO, H_2O
pe	$Mg + H_2O \rightarrow MgO(s) + H_2$	Mg, H_2O
co	$Al_2O + 2H_2O \rightarrow Al_2O_3(s) + 2H_2$	Al_2O, H_2O
Fe(s)	$Fe \rightarrow Fe(s)$	Fe
M-stars	cation exchange	
ol	$Fe_2SiO_4(s) + 2Mg(g) \rightarrow Mg_2SiO_4(s) + 2Fe(g)$	Mg, Fe
py	$FeSiO_3(s) + Mg(g) \rightarrow MgSiO_3(s) + Fe(g)$	Mg, Fe
C-stars	dust formation	
C(s)	$C_2H_2 \rightarrow 2C(s) + H_2$	C_2H_2
SiC	$2Si + C_2H_2 \rightarrow 2SiC(s) + H_2$	C_2H_2, Si
Fe(s)	$Fe \rightarrow Fe(s)$	Fe

is not chemically active, as its high bond dissociation energy (1072 kJ/mol) prevents the chemical reaction at the dust grain surface for which the bond breaking of the molecule is required. In addition to that, some molecules are not abundant enough to form a considerable amount of dust. In fact, the molecular abundances are limited by the initial atmospheric elemental abundances in the stellar atmosphere and by the complexity of the molecules that might be difficult to form.

In the dust formation scheme here adopted, only the most abundant molecules in the gas phase are assumed to form and dust growth is assumed to proceed by addition of molecules in the gas phase on the starting seeds through a given chemical reaction for each dust species. The reactions of dust formation are listed in Table 4.1 and are taken from FG06, excepting for corundum (Gail & Sedlmayr, 1998).

By definition, a reaction is in chemical equilibrium when the rate at which products are formed equals the rate at which they are destroyed through the inverse reaction. In this status the net variation of the products (that in the specific case is dust) is zero.

Let us consider a generic formation reaction of the solid dust species S and a gas species D from the starting molecules and atoms A, B, C in the gas phase

$$aA + bB + cC \rightarrow sS + dD. \tag{4.1}$$

At a given temperature and pressure, the reaction considered is spontaneous if the variation of the free energy per mole (Gibbs energy) is negative $\Delta G_i(p, T) < 0$ (Atkins & de Paula, 2010). The free energy changes during the reaction until a minimum value is reached. At this point, no more reactants can be converted into products and the reaction reaches its equilibrium.

I indicate with $G^\circ_j(T)$ the free energy of formation of the species $j = A, B, C, S, D$ formed from their free gaseous atoms at the temperature T in the standard state pressure of $p^\circ = 1$ bar: $G^\circ_j(T) = G_j(p^\circ, T)$. In other words, the quantity $G^\circ_j(T)$ is the free energy variation between the free atoms and the molecule, j.

At a given temperature, for any of the species j the free energy changes if the pressure is different from p°. At a pressure of p, the correspondent molar free energy $G_j(p, T)$ is

$$G_j(p, T) = G^\circ_j(T) + RT \ln p, \tag{4.2}$$

where R is the ideal gas constant. If the considered species is solid (S), as in the case of dust formation, the variation of free energy due to the change of pressure is zero and $G_{\rm S}(p, T) = G^\circ_{\rm S}(T)$.

Finally, the variation of the free energy of formation, ΔG, for the generic reaction in Eq. 4.1 at a given temperature and pressure is

$$\begin{aligned} \Delta G &= {\rm s}G^\circ_{\rm S} + {\rm d}G^\circ_{\rm D} + {\rm d}RT \ln p_{\rm D} + \\ &- {\rm a}G^\circ_{\rm A} - {\rm a}RT \ln p_{\rm A} - {\rm b}G^\circ_{\rm B} - {\rm b}RT \ln p_{\rm B} - {\rm c}G^\circ_{\rm C} - {\rm c}RT \ln p_{\rm C}, \end{aligned} \tag{4.3}$$

$$\tag{4.4}$$

and finally,

$$\Delta G = \Delta G^\circ + RT \ln \frac{p^{\rm d}_{\rm D}}{p^{\rm a}_{\rm A} p^{\rm b}_{\rm B} p^{\rm c}_{\rm C}}, \tag{4.5}$$

where ΔG° is the variation of free energy of the reaction at pressure p° and is a function of the temperature. If the reaction is at its equilibrium point, then $\Delta G = 0$ and the relation between the free energy of formation, ΔG°, and the equilibrium partial pressures is,

$$\frac{p^{\rm d}_{\rm D,eq}}{p^{\rm a}_{\rm A,eq} p^{\rm b}_{\rm B,eq} p^{\rm c}_{\rm C,eq}} = \exp\Big(- \frac{\Delta G^\circ}{RT} \Big) = K_p. \tag{4.6}$$

The quantity K_p is the constant for the formation reaction and it is computed for each dust species i by means of ΔG°_i that is a function of the gas temperature.

The ratio between the product of the partial pressures of products and the product of reactants is called "mass-action ratio" and it equals K_p only if the partial pressures are obtained when the reaction is at its equilibrium.

The law of mass action says that, a system with certain initial partial pressures determined by the abundances of the gas species, reacts in such a way that the mass-action ratio tends to approach the constant value K_p. In other words, this means that the system tends to its equilibrium condition.

Consequently, the products of a chemical reaction are produced or destroyed if the mass-action ratio is smaller or greater than K_P, respectively. In the former case, the system tends to produce more products in order to enhance the mass-action ratio, while in the latter case, the system tends to destroy the products in favour of the reactants in order to decrease the ratio.

If some of the partial pressures of the species in the chemical reaction increase, the system tend to re-balance in order to restore the equilibrium so that the mass-action ratio equals again K_p. If the concentrations, and therefore the partial pressures, of the reactants increase, the chemical reaction moves from reactants to products (from left to right) to increase the pressures of the products. Conversely, if the partial pressures of products increase, the chemical reaction moves in the opposite direction, from the products to the reactants (from right to left) increasing the pressures of the reactants.

Without taking into account for now the kinetics of the reactions, I can simply assume that dust is produced or destroyed accordingly to the law of mass action.

For each dust species i the quantity ΔG_i° is computed by means of the fitting formulae provided by Sharp & Huebner (1990),

$$\Delta G_i^\circ = \alpha T^{-1} + \beta + \gamma T + \delta T^2 + \epsilon T^3, \tag{4.7}$$

where T is the temperature and the coefficients $\alpha, \beta, \gamma, \delta$ and ϵ are determined by fitting the data in JANAF table (Chase, 1986) by Duschl et al. (1996). For the dust species not available in this latter reference, I fitted the data from Barin & Platzki (1995) with Eq. 4.7 finding the correspondent coefficients. In the range of temperatures considered the species included in my model never undergo a phase transition and therefore the tabulated values provided by Barin & Platzki (1995) are smooth and regular without the typical discontinuities due to the occurrence of a phase transition.

If the abundances of the species in the gas phase are fixed by the initial chemical composition, the correspondent partial pressures, p_j, are determined by $\epsilon_{g,j}$ through the relation

$$p_j = \epsilon_{g,j} N_{\mathrm{H}} k_B T. \tag{4.8}$$

The partial pressure of a given gas species j can be expressed in terms of the partial pressure that the hydrogen molecules would have if they were present as free atoms in the gas phase, $P_{\mathrm{H}} = N_{\mathrm{H}} k_B T$:

$$p_j = \epsilon_j P_{\mathrm{H}}. \tag{4.9}$$

Assuming that the total pressure, P, is entirely provided by H_2 molecules and He atoms, one gets

$$P_{\mathrm{H}} = \frac{2}{1 + 2\epsilon_{\mathrm{He}}} P. \tag{4.10}$$

Therefore, Eq. 4.9 becomes

$$p_j = \epsilon_j \frac{2}{1 + 2\epsilon_{\mathrm{He}}} P. \tag{4.11}$$

By substituting 4.11 in 4.6 I finally obtain

$$P = \frac{1 + 2\epsilon_{He}}{2} \left[K_p \frac{\epsilon_{\mathrm{A}}^{\mathrm{a}} \epsilon_{\mathrm{B}}^{\mathrm{b}} \epsilon_{\mathrm{C}}^{\mathrm{c}}}{\epsilon_{\mathrm{D}}^{\mathrm{d}}} \right]^{1/(\mathrm{d-a-b-c})}. \tag{4.12}$$

This general relation provides, for each dust species, the locus of the points in the pressure-temperature (P-T) diagram for which the chemical reaction of dust formation is at its equilibrium given the abundances, ϵ_j where $j = \mathrm{A, B, C, D}$. The dependence of total pressure on the gas temperature is in the term K_p.

These loci are denominated “stability curves” and divide the P-T plane in two regions for each chemical reaction: below the curve the dust species grows, above the curve the inverse reaction is so efficient that the specific dust species cannot be formed.

The resulting curve depends on the chemical reaction considered, and gives an indication of which dust species form first, given the formation reactions. This study is useful, for example, in order to investigate which species are good candidates to form the first seed nuclei.

In the following section, I will explicitly provide the quantities $\epsilon_{j,g}$, where g refers to the actual abundance in the gas phase. This computation takes into account the fact that the starting abundance ϵ_j is in general different from the actual abundance in the gas phase $\epsilon_{j,g}$ as j is progressively depleted from the gas phase to form dust. As, by definition, the condensation fraction of an element into a certain dust species is the ratio between the condensed number of atoms and the total initial one, then, the number of condensed atoms of the key-element, $f_{k,i}^{\rm cond}$, is

$$f_{k,i}^{\rm cond} = f_i \epsilon_{k,i}. \tag{4.13}$$

In order to compute how many atoms of a generic element j are condensed into the dust species i, $f_{j,i}^{\rm cond}$, one needs to multiply $f_{k,i}^{\rm cond}$ by the ratio between the number of atoms of the considered element, $n_{j,i}$, within a monomer of dust, and the number of atoms of the key-element in that monomer, $n_{k,i}$:

$$f_{j,i}^{\rm cond} = \frac{n_{j,i}}{n_{k,i}} f_{k,i}^{\rm cond} \tag{4.14}$$

The condensation fraction is defined by Eq. 2.8. The explicit relations 4.6 and 4.12 will be also provided for each dust species considered in M- and C-stars.

The considered molecules and atoms are listed in Table 4.1 and their abundances in the gas phase are computed as follows.

4.1.1 M-stars

For the most abundant gas species present in the CSEs of M-stars (H_2, CO, SiO, Mg, Fe, H_2O, and Al_2O), I assume that:

- all the available hydrogen is present as H_2 molecules;
- magnesium and iron are present in the gas phase only as free atoms;
- silicon is present in the gas phase only as SiO, and the small fraction of SiS is neglected;
- aluminium is present as Al_2O;
- oxygen is present in the gas phase as CO, SiO, Al_2O and H_2O.

The explicit form of $\epsilon_{j,g}$ are given in the following.

- H_2
  As almost all the hydrogen available is in the form of H_2 I get by definition that

$$\epsilon_{\rm H_2} = \frac{\epsilon_{\rm H}}{2} = 0.5 \tag{4.15}$$

- SiO
  The abundance of SiO molecules is limited by the number of silicon atoms initially available in the gas phase which is usually lower than the oxygen one (see, for example, Table 2.2). In this case, from the initial abundance of silicon, I need to subtract the number of silicon atoms locked into dust grains of Si-bearing species (olivine, pyroxene and quartz). For these species, silicon is the key-element, and the condensed fraction is computed through Eq. 4.13.

$$\epsilon_{{\rm SiO},g} = (1 - f_{\rm ol} - f_{\rm py} - f_{\rm qu})\epsilon_{\rm Si}, \tag{4.16}$$

- Al_2O
  The abundance of these molecules is limited by the initial abundance of aluminium atoms that are much less abundant than oxygen (Table 2.2). Aluminium can moreover be partially condensed in corundum dust. As aluminium is the key-element for corundum, the fraction condensed is given by Eq. 4.13. The abundance of free aluminium atoms in the gas phase is finally converted into Al_2O abundance dividing by two, as two aluminium atoms are needed for one Al_2O molecule:

$$\epsilon_{\mathrm{Al_2O},g} = \frac{1}{2}(1 - f_{\mathrm{co}})\epsilon_{\mathrm{Al}}, \tag{4.17}$$

- H_2O
  This molecule forms from the oxygen that remains available from the formation of CO, SiO and Al_2O which are limited by the less abundant carbon, silicon and aluminium. From the initially available abundance of oxygen atoms I first have to subtract the abundances of carbon, needed to form CO, the abundance of SiO (Eq. 4.16), and, similarly, the abundance of Al_2O (Eq. 4.17) molecules. The available number of oxygen atoms obtained can be partially condensed into the oxygen-bearing dust species. All the dust species considered for M-stars with the exception of iron dust contain oxygen atoms.

  In this regard I have that:

  - For periclase: for each magnesium atom condensed, where magnesium is the key-element, one atom of oxygen is consumed. Therefore the total number of oxygen atoms locked into periclase is, according to Eq. 4.14:

$$f^{\mathrm{cond}}_{\mathrm{O,pe}} = f_{\mathrm{pe}}\epsilon_{\mathrm{Mg}}. \tag{4.18}$$

  - For corundum: for every two aluminium atoms condensed, where aluminium is the key-element, three atoms of oxygen are consumed. The total number of oxygen atoms locked into corundum is, from Eq. 4.14:

$$f^{\mathrm{cond}}_{\mathrm{O,co}} = \frac{3}{2} f_{\mathrm{co}}\epsilon_{\mathrm{Al}}. \tag{4.19}$$

  - For olivine, pyroxene and quartz: if the key-element is silicon, for each silicon atom condensed, the number of oxygen atoms condensed into olivine, pyroxene and quartz are four, three and two, respectively. Thus, the total number of oxygen atoms locked into olivine, pyroxene and quartz are, according to Eq. 4.14:

$$f^{\mathrm{cond}}_{\mathrm{O,ol,py,qu}} = (4 f_{\mathrm{ol}} + 3 f_{\mathrm{py}} + 2 f_{\mathrm{qu}})\epsilon_{\mathrm{Si}}. \tag{4.20}$$

  Combining Eqs. 4.18, 4.19 and 4.20 I finally get

$$\epsilon_{\mathrm{H_2O},g} = \epsilon_{\mathrm{O}} - \epsilon_{\mathrm{C}} - \left(\frac{1}{2} - f_{\mathrm{co}}\right)\epsilon_{\mathrm{Al}} - f_{\mathrm{pe}}\epsilon_{\mathrm{Mg}} - (1 + 3 f_{\mathrm{ol}} + 2 f_{\mathrm{py}} + f_{\mathrm{qu}})\epsilon_{\mathrm{Si}}, \tag{4.21}$$

- Mg
  The amount of free magnesium available in the gas phase is conditioned by the number of atoms locked into olivine, pyroxene and periclase monomers.

  - For periclase: as magnesium is the key-element the number of atoms locked into this dust species is, according to Eq. 4.13:

$$f^{\mathrm{cond}}_{\mathrm{Mg,pe}} = f_{\mathrm{pe}}\epsilon_{\mathrm{Mg}}. \tag{4.22}$$

  - For olivine and pyroxene: for each silicon atom condensed, where silicon is the key-element, the number of magnesium atoms condensed into olivine and pyroxene are $2x_{\mathrm{ol}}$ and x_{py} respectively. Thus, the total number of magnesium atoms locked into these dust species are, according to Eq. 4.14:

$$f^{\mathrm{cond}}_{\mathrm{Mg,ol,py,qu}} = (2x_{\mathrm{ol}}\, f_{\mathrm{ol}} + x_{\mathrm{py}}\, f_{\mathrm{py}})\epsilon_{\mathrm{Si}}. \tag{4.23}$$

By combining Eqs. 4.22 and 4.23, it follows that

$$\epsilon_{\mathrm{Mg},g} = \epsilon_{\mathrm{Mg}}(1 - f_{\mathrm{pe}}) - (2x_{\mathrm{ol}}\, f_{\mathrm{ol}} + x_{\mathrm{py}}\, f_{\mathrm{py}})\epsilon_{\mathrm{Si}}. \tag{4.24}$$

- Fe
  All the iron atoms not locked into iron dust grains or olivine and pyroxene in the form of impurities remain in the form of free iron atoms.

  - For iron dust: as iron is the key-element the number of atoms locked into this dust species is, from Eq. 4.13:

$$f^{\mathrm{cond}}_{\mathrm{Fe,Fe(s)}} = f_{\mathrm{Fe(s)}}\epsilon_{\mathrm{Fe}}. \tag{4.25}$$

  - For olivine and pyroxene: for each silicon atom condensed, where silicon is the key-element, the number of iron atoms condensed into olivine and pyroxene are $2(1 - x_{\mathrm{ol}})$ and $(1 - x_{\mathrm{py}})$ respectively. Thus, the total number of magnesium atoms locked into these dust species are, from Eq. 4.13:

$$f^{\mathrm{cond}}_{\mathrm{Fe,ol,py}} = [2(1 - x_{\mathrm{ol}})\, f_{\mathrm{ol}} + (1 - x_{\mathrm{py}})\, f_{\mathrm{py}})]\epsilon_{\mathrm{Si}}. \tag{4.26}$$

From Eqs. 4.25 and 4.26 one gets,

$$\epsilon_{\mathrm{Fe},g} = \epsilon_{\mathrm{Fe}}[(1 - f_{\mathrm{Fe(s)}}) - 2(1 - x_{\mathrm{ol}})\, f_{\mathrm{ol}} + (1 - x_{\mathrm{py}})\, f_{\mathrm{py}}]. \tag{4.27}$$

By explicitly expressing the law of mass action in Eq. 4.6 for the reactions listed in Table 4.1, I obtain the following stability curves from relation 4.12.

- Olivine

$$\frac{p^3_{\mathrm{H_2}}}{p^{2x_{\mathrm{ol}}}_{\mathrm{Mg}}\, p^{2(1-x_{\mathrm{ol}})}_{\mathrm{Fe}}\, p_{\mathrm{SiO}}\, p^3_{\mathrm{H_2O}}} = \exp\Big(-\frac{\Delta G^\circ_{\mathrm{ol}}}{RT}\Big) = K_p(\mathrm{ol}), \tag{4.28}$$

where K_p(ol) is the constant of the reaction of olivine formation and $\Delta G^\circ_{\mathrm{ol}}$ is

$$\begin{array}{rcl} \Delta G^\circ_{\mathrm{ol}} & = & 2x_{\mathrm{ol}}G^\circ_{\mathrm{Mg_2SiO_4}} + 2(1 - x_{\mathrm{ol}})G^\circ_{\mathrm{Fe_2SiO_4}} + 3G^\circ_{\mathrm{H_2}} + G^\circ_{\mathrm{ol,mix}} + \\ & - & 2x_{\mathrm{ol}}G^\circ_{\mathrm{Mg}} - 2(1 - x_{\mathrm{ol}})G^\circ_{\mathrm{Fe}} - G^\circ_{\mathrm{SiO}} - 3G^\circ_{\mathrm{H_2O}}, \end{array} \tag{4.29}$$

where it is assumed that olivine can be imagined as composed of $2x_{\mathrm{ol}}$ moles of forsterite and $2(1 - x_{\mathrm{ol}})$ moles of fayalite. The mixing term $G^\circ_{\mathrm{ol,mix}}$ is added to the free energy variation. For olivine the mixing term is

$$G^\circ_{\mathrm{ol,mix}} = 2RT[x_{\mathrm{ol}} \ln x_{\mathrm{ol}} + (1 - x_{\mathrm{ol}}) \ln(1 - x_{\mathrm{ol}})], \tag{4.30}$$

because the Mg^{2+} and Fe^{2+} ions are distributed over two moles of cation sites.

From Eq. 4.12, the final P-T relation is

$$P = \frac{1+2\epsilon_{\rm He}}{2}\left[\frac{\epsilon^3_{\rm H_2}}{\epsilon^{2x_{\rm ol}}_{{\rm Mg},g}\epsilon^{2(1-x_{\rm ol})}_{{\rm Fe},g}\epsilon_{{\rm SiO},g}\epsilon^3_{{\rm H_2O},g}K_p({\rm ol})}\right]^{1/3}, \tag{4.31}$$

where $\epsilon_{\rm H_2}$, $\epsilon_{{\rm Mg},g}$, $\epsilon_{{\rm Fe},g}$, $\epsilon_{{\rm SiO},g}$ and $\epsilon_{{\rm H_2O},g}$ are given by Eqs. 4.15, 4.24, 4.27, 4.16 and 4.21, respectively.

- Pyroxene

$$\frac{p^2_{\rm H_2}}{p^{x_{\rm py}}_{\rm Mg}p^{(1-x_{\rm py})}_{\rm Fe}p_{\rm SiO}p^2_{\rm H_2O}} = \exp\Big(-\frac{\Delta G^\circ_{\rm py}}{RT}\Big) = K_p({\rm py}), \tag{4.32}$$

where K_p(py) is the constant of the formation reaction of pyroxene and similarly to the previous case

$$\begin{aligned}\Delta G^\circ_{\rm py} &= x_{\rm py}G^\circ_{\rm MgSiO_3} + (1-x_{\rm py})G^\circ_{\rm FeSiO_3} + 2G^\circ_{\rm H_2} + G^\circ_{py,mix} + \\ &- x_{\rm py}G^\circ_{\rm Mg} - (1-x_{\rm py})G^\circ_{\rm Fe} - G^\circ_{\rm SiO_3} - 2G^\circ_{\rm H_2O},\end{aligned} \tag{4.33}$$

where pyroxene can be imagined as formed by $x_{\rm py}$ moles of enstatite and $(1-x_{\rm py})$ moles of ferrosilite. Also in this case the adequate mixing term has to be added:

$$G^\circ_{\rm py,mix} = RT[x_{\rm py}\ln x_{\rm py} + (1-x_{\rm py})\ln(1-x_{\rm py})] \tag{4.34}$$

because the Mg^+ and Fe^+ ions are distributed over one mole of cation sites.

The final P-T relation is

$$P = \frac{1+2\epsilon_{\rm He}}{2}\left[\frac{\epsilon^2_{\rm H_2}}{\epsilon^{x_{\rm py}}_{{\rm Mg},g}\epsilon^{(1-x_{\rm py})}_{{\rm Fe},g}\epsilon_{{\rm SiO},g}\epsilon^2_{{\rm H_2O},g}K_p({\rm py})}\right]^{1/2}, \tag{4.35}$$

where $\epsilon_{\rm H_2}$, $\epsilon_{{\rm Mg},g}$, $\epsilon_{{\rm Fe},g}$, $\epsilon_{{\rm SiO},g}$ and $\epsilon_{{\rm H_2O},g}$ are given by Eqs. 4.15, 4.24, 4.27, 4.16 and 4.21, respectively.

- Quartz

$$\frac{p_{\rm H_2}}{p_{\rm SiO}p_{\rm H_2O}} = \exp\Big(-\frac{\Delta G^\circ_{\rm qu}}{RT}\Big) = K_p({\rm qu}) \tag{4.36}$$

where K_p(qu) is the constant of the reaction of formation for quartz and

$$\Delta G^\circ_{\rm qu} = G^\circ_{\rm SiO_2} + G^\circ_{\rm H_2} - G^\circ_{\rm SiO} - G^\circ_{\rm H_2O} \tag{4.37}$$

The final P-T relation is

$$P = \frac{1+2\epsilon_{\rm He}}{2}\frac{\epsilon_{\rm H_2}}{\epsilon_{{\rm SiO},g}\epsilon_{{\rm H_2O},g}K_p({\rm qu})} \tag{4.38}$$

where $\epsilon_{\rm H_2}$, $\epsilon_{{\rm SiO},g}$ and $\epsilon_{\rm H_2O,g}$ are given by Eqs. 4.15, 4.16 and 4.21, respectively.

- Periclase

$$\frac{p_{H_2}}{p_{Mg}p_{H_2O}} = \exp\Big(-\frac{\Delta G^\circ_{pe}}{RT}\Big) = K_p(\mathrm{pe}) \tag{4.39}$$

where K_p(pe) is the constant for the formation reaction of periclase and

$$\Delta G^\circ_{pe} = G^\circ_{MgO} + G^\circ_{H_2} - G^\circ_{H_2O} - G^\circ_{Mg}. \tag{4.40}$$

The final P-T relation is

$$P = \frac{1 + 2\epsilon_{He}}{2}\frac{\epsilon_{H_2}}{\epsilon_{Mg,g}\epsilon_{H_2O,g}K_p(\mathrm{pe})} \tag{4.41}$$

where ϵ_{H_2}, $\epsilon_{Mg,g}$ and $\epsilon_{H_2O,g}$ are given by Eqs. 4.15, 4.24 and 4.21, respectively.

- Corundum

$$\frac{p^2_{H_2}}{p_{Al_2O}p^2_{H_2O}} = \exp\Big(-\frac{\Delta G^\circ_{co}}{RT}\Big) = K_p(\mathrm{co}) \tag{4.42}$$

where K_p(co) is the constant for the formation reaction of corundum and

$$\Delta G^\circ_{co} = G^\circ_{Al_2O_3} + 2G^\circ_{H_2} - 2G^\circ_{H_2O} - G^\circ_{Al_2O}. \tag{4.43}$$

The final P-T relation is

$$P = \frac{1 + 2\epsilon_{He}}{2}\frac{\epsilon^2_{H_2}}{\epsilon_{Al_2O,g}\epsilon^2_{H_2O,g}K_p(\mathrm{co})} \tag{4.44}$$

where $\epsilon_{Al_2O,g}$ and $\epsilon_{H_2O,g}$ are given by 4.17 and 4.21, respectively.

- Iron

$$\frac{1}{p_{Fe}} = \exp\Big(-\frac{\Delta^\circ G_{Fe(s)}}{RT}\Big) = K_p[\mathrm{Fe(s)}] \tag{4.45}$$

where K_p[Fe(s)] is the constant of the formation reaction of iron and the correspondent variation in the free energy is given by the transition between the vapour (v) and the solid phase(s):

$$\Delta^\circ G_{Fe(s)} = G^\circ(\mathrm{Fe, s}) - G^\circ(\mathrm{Fe, v}). \tag{4.46}$$

Finally, the P-T relation is

$$P = \frac{1 + 2\epsilon_{He}}{2}\frac{1}{\epsilon_{Fe,g}K_p[\mathrm{Fe(s)}]}, \tag{4.47}$$

where $\epsilon_{Fe,g}$ is given by Eq. 4.27.

4.1.2 C-stars

In C-stars the gas contains carbon-rich elements and the most abundant carbon-bearing species in the gas phase besides CO is C_2H_2. On the other hand, silicon atoms are bound in SiS molecules and any excess of silicon is present in the form of free atoms. Other Si-bearing species like SiC_2 have small abundances and are neglected in this calculation.

The explicit form of the abundances $\epsilon_{j,g}$ are listed in the following

- Si
  From the initial abundance of silicon atoms I subtract the abundance of S atoms taking into account the formation of SiS molecules. In addition to that, silicon atoms can be locked into SiC dust. As silicon is the key-element of SiC, the number of silicon atoms condensed in this dust species is given by Eq. 4.13.

  The final abundance of silicon in the gas phase is

$$\epsilon_{\mathrm{Si},g} = (1 - f_{\mathrm{SiC}})\epsilon_{\mathrm{Si}} - \epsilon_{\mathrm{S}}. \tag{4.48}$$

- C_2H_2
  In this case the carbon atoms can be locked in CO molecules or in carbon and SiC dust. The fraction of carbon condensed in amorphous carbon is given by Eq. 4.13, whereas in SiC, for each atom of silicon condensed, a carbon atom is consumed and therefore the fraction of condensed carbon is provided by Eq. 4.14.

  The final abundance of C_2H_2 is obtained by dividing the abundance of the available carbon atoms in the gas phase by the number of atoms needed to form the considered molecule:

$$\epsilon_{\mathrm{C_2H_2},g} = \frac{1}{2}(1 - f_{\mathrm{C(s)}})\epsilon_{\mathrm{C}} - \epsilon_{\mathrm{O}} - f_{\mathrm{SiC}}\epsilon_{\mathrm{Si}}. \tag{4.49}$$

- Fe
  Iron atoms are depleted from the gas phase only because of the formation of iron dust. The number of condensed iron atoms is given by Eq. 4.13, and finally the abundance in the gas phase is:

$$\epsilon_{\mathrm{Fe},g} = \epsilon_{\mathrm{Fe}}(1 - f_{\mathrm{Fe(s)}}). \tag{4.50}$$

As for M-stars, I express the explicit form for the locus of the points in the P-T diagram for which the formation reaction of each dust species is at its equilibrium

- Amorphous carbon
  The formation of carbon dust is assumed to proceed just in one direction below a certain critical threshold temperature without considering the backward reaction. The reason of this will be fully explained in Section 4.2. The equilibrium curve of this species is therefore not illustrated in the P-T diagram. For the purposes of this first investigation, it is sufficient to know that the condensation gas temperature assumed for this species is between 1100 and 1300 K.

- For SiC I obtain

$$\frac{p_{\mathrm{H_2}}}{p_{\mathrm{Si}}^2 p_{\mathrm{C_2H_2}}} = K_p(\mathrm{SiC}) \tag{4.51}$$

  where $K_p(\mathrm{SiC})$ is the constant for the formation reaction of silicon carbide and

$$\Delta G^\circ_{\mathrm{SiC}} = 2G^\circ_{\mathrm{SiC}} + G^\circ_{\mathrm{H_2}} - G^\circ_{\mathrm{C_2H_2}} - 2G^\circ_{\mathrm{Si}}. \tag{4.52}$$

  The final P-T relation is therefore

$$P = \frac{1 + 2\epsilon_{\mathrm{He}}}{2}\left[\frac{\epsilon_{\mathrm{H_2}}}{\epsilon^2_{\mathrm{Si},g}\epsilon_{\mathrm{C_2H_2},g}K_p(\mathrm{SiC})}\right]^{1/2}, \tag{4.53}$$

  where $\epsilon_{\mathrm{H_2}}$ $\epsilon_{\mathrm{Si},g}$ and $\epsilon_{\mathrm{C_2H_2},g}$ are given by 4.15, 4.48 and 4.49, respectively.

- For iron dust I obtain

$$\frac{1}{p_{\mathrm{ir}}} = \exp\Big(-\frac{\Delta^{\circ}G_{\mathrm{Fe(s)}}}{RT}\Big) = K_p[\mathrm{Fe(s)}], \tag{4.54}$$

where $K_p[Fe(s)]$ is the constant for the formation reaction of iron, and the correspondent variation in the free energy is given by the transition between the vapour and the solid phase:

$$\Delta^{\circ}\mathrm{G}_{\mathrm{Fe(s)}} = \mathrm{G}^{\circ}[\mathrm{Fe(s)}] - \mathrm{G}^{\circ}[\mathrm{Fe(v)}]. \tag{4.55}$$

$$P = \frac{1+2\epsilon_{He}}{2}\frac{1}{K_p[\mathrm{Fe(s)}]\epsilon_{Fe,g}}, \tag{4.56}$$

where $\epsilon_{\mathrm{Fe,g}}$ is given by Eq. 4.50.

4.1.3 Condensation sequence

The stability curves for M- and C-stars dust species are drawn in Fig. 4.2 and define the so-called "condensation sequence", starting from the most refractory dust species, formed at the highest temperatures, to the ones formed at lower temperatures. As this study is performed when dust is not yet formed, the condensation fractions of all the dust species, f_i, are set equal to zero. Data of the abundances of the elements are taken from Anders & Grevesse (1989) and are listed in Table 2.2. However, for SiC I assumed $\epsilon_{\mathrm{C}} = 2 \times 10^{-3}$ in order to have $\epsilon_{\mathrm{C}}/2 > \epsilon_{\mathrm{O}}$ as required in the computation of $\epsilon_{\mathrm{C_2H_2},g}$ computed by Eq. 4.49.

For the two different starting chemical compositions (oxygen- or carbon-rich) the results can be summarized as follows.

- M-stars
  In the considered range of pressures, corundum is the first aggregate that forms. At the characteristic gas pressures of CSEs $P \sim 10^{-3} - 10^{-2}$ dyne cm^{-2}, the typical temperature is about 1500 K. This value is well above the temperatures of olivine and pyroxene, between 900 and 1100 K, according to the fraction of iron present in the dust grain. In particular, the higher the iron content is, the lower the typical temperatures at which silicate dust is expected to form are. An intermediate case for $x_g = 0.5$ is shown in Fig. 4.2. The stability curves of olivine and pyroxene are very close because the gas species needed for their formation are the same, and the final dust chemical compositions are very similar.

  As far as iron, periclase and quartz are concerned, their typical condensation temperatures are around 1000 K, close to the condensation temperature of iron-free silicates.

- C-stars
  The condensation temperature of SiC is well above the condensation temperature of iron dust and is around 1200 K for pressures between 10^{-3} and 10^{-2} dyne cm^{-2}. The formation of SiC is expected to occur before the formation of carbon dust if this latter species condenses at 1100 K. On the other hand, the condensation sequence is reversed for these two species if the condensation of amorphous carbon is assumed to happen at 1300 K.

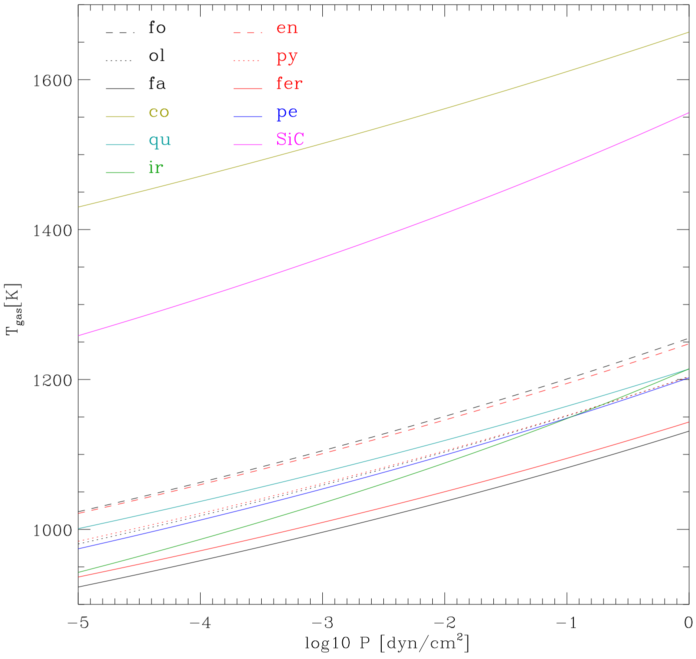

Figure 4.2: Stability curves for the various dust species. The reactions of formation are listed in Table 4.1. The curves are drawn when the condensation fraction is still zero for all the dust compounds ($f_i = 0$).

4.2 Seed nuclei

As already anticipated, the growth of dust grains is assumed to proceed through the addition of molecules and atoms from the gas phase on the first aggregates.

The theoretical treatment of the initial cluster formation requires data about the thermodynamic and the energetic properties of the chemical reactions involved. For this purpose, some fundamental pieces of information are the Gibbs free energy of formation and the binding energies of the clusters in the gas phase that are often not provided by experimental data.

There have been several attempts to model the formation of these first aggregates in order to determine both their chemical composition and their initial number.

In spite of these attempts the nucleation process remains still unknown and there is a general agreement on the fact that the first seed nuclei should be formed at high temperatures and need to be made up of elements abundant enough to form a certain number of initial clusters.

Thus, because of the uncertainties that affect the computations of the nucleation process (Goumans & Bromley, 2012), it is reasonable to keep the number of seeds as an adjustable parameter.

In the following I summarize the current picture for M- and C-stars.

4.2.1 M-stars

In M-stars, the formation of critical clusters occurs at a high supersaturation, defined as the ratio between the growth and destruction rates, $S >> 1$, whereas the accretion proceeds already at $S > 1$.

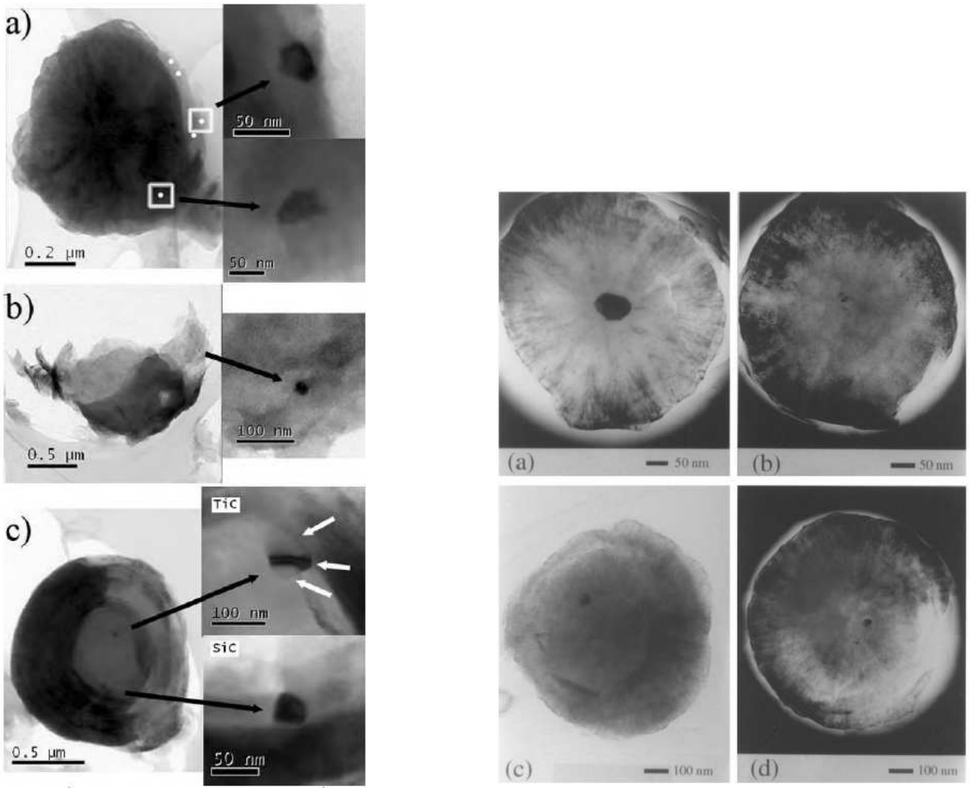

Figure 4.3: *Left panel*: a) graphite with SiC positions indicated (white dots) and inset of faceted SiCs; b) graphite with small internal SiC; and c) graphite showing twinned TiC and SiC (white arrows indicate separate twin domains). The figure is taken from Hynes et al. (2007). *Right panel*: images of ultrathin sections of selected circumstellar graphite spherules with internal crystals. (a) Spherule with a large (100 nm) central iron-rich crystal (iron or iron carbide). (b) Spherule, with a central cluster of 4 (Ti, Zr, Mo)C crystals. (c) Spherule with a 50 nm noncentral TiC crystal with minor Zr and Mo, and a core of nanocrystalline carbon just interior to this crystal; this spherule section contains nine other smaller crystals that are not visible in this orientation. (d) Spherule with two noncentral Ru-, Zr-, and Mo-bearing TiC internal crystals. The figure is taken from Bernatowicz et al. (1996).

According to the elemental abundances in CSEs and to the expected condensation temperatures, possible seed candidates are SiO, SiO_2, MgO, Fe, Al_2O_3, TiO, and TiO_2.

For silicates, a rough estimate of the abundance of seeds can be obtained integrating Eq. 3.16, assuming the number of seeds to be equal to the number of fully-grown grains needed to reproduce the observed local ISM extinction.

Adopting an exponent $x_g = 3.5$, $\log A_{\rm ol} = -15.21$, suitable for olivine (Mathis et al., 1977), and integrating between $a_{\rm min} = 0.005\ \mu$m and $a_{\rm max} = 0.25\ \mu$m, one gets

$$\epsilon_s = \int_{a_{\rm min}}^{a_{\rm max}} A_{\rm ol} a^{-3.5} da \sim 10^{-10}. \tag{4.57}$$

In preliminary investigations, made adopting this initial number of seeds, I obtain grain sizes of about $a \sim 0.01\ \mu$m, never succeeding in reproducing the largest observed grain size $a \geq 0.1\ \mu$m (Sargent et al., 2010; Norris et al., 2012).

On the other hand, assuming that the number of seeds is the number of fully-grown grains needed to reproduce the total dust mass observed (Eq. 3.17), I get:

$$\epsilon_s = \frac{M_i}{m_g}\frac{1}{N_{\rm H}} \sim 10^{-13}, \tag{4.58}$$

where the fully-grown grains have typical size $a = 0.1\ \mu$m and mass $m_g = (4/3)\pi a^3 \rho_d$ (Jones & Merrill, 1976).

The quantity $M_i/N_{\rm H} = M_{\rm ol}/N_{\rm H}$ is derived assuming $\rho_{d,\rm ol} = 3.75$ g cm^{-3}, $n_{\rm Si,ol} = 1$, $\epsilon_{\rm Si,ol} = 3.55 \cdot 10^{-5}$ (Table 2.2), and $m_{d,\rm ol} = 172.23\ m_{\rm H}$

The seeds abundance obtained is much lower than that of Eq. 4.57, and it is the same as the one assumed by GS99. This value appears also to be consistent with detailed nucleation computations by Jeong et al. (2003), as well as in very good agreement with the value inferred by Knapp (1985) for a sample of Galactic M-giants. Adopting $\epsilon_s = 10^{-13}$ in the models, the grains reach typical sizes of $\sim 0.15\ \mu$m, in agreement with the observations and consistent with the value of the grain size used to compute the seed number.

At varying metallicity it is natural to expect that the number of seeds depends on the abundance of the elements forming them. Because of the uncertainties on the process of seed formation I assume that in M-giants the number of seeds scales with the gas metallicity:

$$\epsilon_{s,\rm M} = \epsilon_s \Big(\frac{Z}{Z_{\rm ISM}}\Big), \tag{4.59}$$

where $Z_{\rm ISM} = 0.017$ is the local metallicity of the ISM.

4.2.2 C-stars

As far as C-stars are concerned, the formation of the first aggregates has been extensively studied by Cherchneff (2000). In this scenario the formation of carbonaceous dust starts with the formation of the polycyclic aromatic hydrocarbons (PAHs) from the abundant acetylene, C_2H_2, which is able to react with hydrogen atoms and start an active hydrocarbon chemistry.

In particular, the growth of aromatic rings needed to form PAHs is described by three reactions: addition of acetylene, H abstraction to form a radical and second addition of acetylene followed by the ring closure (Cherchneff et al., 1992).

This chain of reactions is efficient at gas temperatures between 900 and 1100 K and nucleation is active in this temperature window. The further growth of the amorphous carbon dust grain therefore proceeds through the subsequent deposition of carbon atoms via acetylene surface reaction and the coagulation of PAH products.

Assuming that the mentioned process is the one through which carbon seeds are formed, I compute the number of seeds for C-stars in analogy of M-stars, scaling their number with the abundance of carbon not locked into CO molecules, $\epsilon_{(\mathrm{C-O})} = \epsilon_{\mathrm{C}} - \epsilon_{\mathrm{O}}$ (Cherchneff, 2006)

$$\epsilon_{s,\mathrm{C}} = \epsilon_s \Big[\frac{\epsilon_{(\mathrm{C-O})}}{\epsilon_{(\mathrm{C-O})_{\mathrm{ISM}}}} \Big]. \tag{4.60}$$

The present value of $\epsilon_{(\mathrm{C-O})_{\mathrm{ISM}}}$ is less than one (Table 2.2), but now an extinction that is produced by carbon grains is observed. Therefore, I can conclude that $\epsilon_{(\mathrm{C-O})_{\mathrm{ISM}}} > 0$ when carbon grains formed.

The value of $\epsilon_{(\mathrm{C-O})_{\mathrm{ISM}}}$ at the moment of carbon grains formation is evaluated from Eq. 3.20. The obtained value gives the C-excess that formed the total mass of carbon grains, needed to reproduce the extinction now observed.

For this computation I assume $\log A_{\mathrm{C(s)}} = -15.24$ (Mathis et al., 1977), $\rho_{d,\mathrm{C(s)}} = 2.2$ g cm^{-3}, $m_{d,\mathrm{C(s)}} = 12.011\ m_{\mathrm{H}}$, x_g=3.5 and $a_{\min} = 0.005\ \mu$m, $a_{\max} = 0.25\ \mu$m. Note that $\rho_{d,\mathrm{C(s)}}$ needs to be converted from g cm^{-3} to g μm^{-3} because the grain sizes are given in μm. The value obtained is

$$\epsilon_{(\mathrm{C-O})_{\mathrm{ISM}}} \sim 3.8 \times 10^{-4}. \tag{4.61}$$

This value is very similar to the solar abundance presently observed $\epsilon_{\mathrm{C}} = 3.63{\cdot}10^{-4}$ (Table 2.2).

The quantity ϵ_s is estimated, similarly to the M-stars case, from Eq. 3.17 where $M_i/N_{\mathrm{H}} = M_{\mathrm{C(s)}}/N_{\mathrm{H}}$, with $n_{\mathrm{k,C(s)}} = 1$ and $\epsilon_{k,C(s)} = \epsilon_{(\mathrm{C-O})_{\mathrm{ISM}}}$. The value of $\epsilon_{s,C}$ is finally $\epsilon_s \sim 10^{-13}$, very close to the one obtained for M-stars and in agreement with the value adopted by FG06.

On the other hand, the study of pre-solar graphitic spherules, whose origin is attributed to C-stars in the TP-AGB, can give important insight about the condensation process of amorphous carbon dust. One fraction of the studied pre-solar graphitic contains internal crystals of metal carbides with composition from nearly pure TiC to nearly pure Zr-Mo carbide (Bernatowicz et al., 1996) and only rarely SiC (Hynes et al., 2007). An image of pre-solar grains is shown in Fig. 4.3.

These carbides, with the exception of SiC that is assumed to condense separately, might have served as heterogeneous nucleation centers for condensation of carbon, opening an alternative path with respect to the homogeneous accretion described above (Croat et al., 2005).

In this scenario, the number of seeds is estimated in a different way.

Let us first assume that the typical seed observed in pre-solar grains is made up with TiC monomers and that it has a typical size of about $a_s = 50 \cdot 10^{-7}$ cm. If M_s is the correspondent mass of the seed nuclei and $\mathrm{m_{TiC}}$=59.88 m_{H} is the mass of one monomer of TiC, the number of monomers in the seed nuclei is

$$n_{\mathrm{TiC}} = \frac{M_s}{m_{\mathrm{TiC}}} = 1.67 \times 10^4, \tag{4.62}$$

where the mass of the monomer is given by $M_s = 4\pi/3 a_s^3 \rho_{\mathrm{TiC}}$ and $\rho_{\mathrm{TiC}} = 0.08$ g cm^{-3}.

For solar abundances partition and solar metallicity, the abundance of the titanium atoms over N_{H} is $\epsilon_{\mathrm{Ti}} = 9.77 \times 10^{-8}$ (Table 2.2). Therefore, the number of seed nuclei given this initial elemental abundance is

$$\epsilon_s = \frac{\epsilon_{\mathrm{Ti}}}{n_{\mathrm{TiC}}} \sim 6 \times 10^{-12}. \tag{4.63}$$

Since this is just a rough estimation and the observed value of a_s for metal carbides is in the range $5 - 200 \cdot 10^{-7}$ cm, I consider values of the number of seeds between 10^{-13} and 10^{-11}

at solar metallicity. However, preliminary analysis with different values of ϵ_s shows that the produced final grain size reaches values above 0.1 μm only for $\epsilon_s < 10^{-13}$ which is the standard adopted value. This value has to be scaled with the metallicity in analogy to M-stars

$$\epsilon_{s,\mathrm{C,TiC}} = \epsilon_s \Big(\frac{Z}{Z_{\mathrm{ISM}}} \Big). \tag{4.64}$$

In this thesis I will consider the homogeneous growth as the main mechanism for carbon dust formation.

4.3 Accretion of dust grains

The second step considered in the process of dust formation is the addition of molecules and atoms from the gas phase to the dust grain.

The particles impinging onto a solid surface may experience chemical bond formation called chemisorption (Ertl, 2010). This bond formation may keep the molecular entity intact (nondissociative chemisorption) or it may be associated with bond breaking and separation of the fragments on the surface (dissociative chemisorption). The inverse process is called desorption.

The addition of the molecules and atoms from the gas phase goes through the chemical reactions listed in Table 4.1. They provide important pieces of information about how the dust formation proceeds (i.e. how many molecules or atoms from the gas phase are needed to form one monomer of dust).

The computation of the variation of the grain size is performed by explicitly evaluating the sticking rate of molecules or atoms impinging on the grain surface and their evaporation rate due to the destruction processes.

The accretion of dust grains, and their final sizes, depends on the CSE conditions such as the density and the temperature profile, and on the adopted assumptions in the dust grow model (e.g. the evaporation process at work).

It is possible to define a generic equation describing the variation of the grain size. The increase or decrease of the dust sizes occur, respectively, when accretion or destruction processes dominate.

The differential equation governing the variation of the grain volume per unit time can be written as

$$\frac{1}{V_{0,i}} \frac{d}{dt} \frac{4\pi a_i^3}{3} = 4\pi a_i^2 (J_i^{\mathrm{gr}} - J_i^{\mathrm{dec}}), \tag{4.65}$$

here $V_{0,i}$ is the volume of the monomer in the solid, a_i is the size of the grain of species i and J_i^{gr},J_i^{dec} are the growth and destruction rates, respectively. $V_{0,i}$ can be expressed in terms of the atomic weight of the monomer A_i and of the mass density of the dust species i, $\rho_{d,i}$.

$$V_{0,i} = \frac{A_i m_{\mathrm{H}}}{\rho_{d,i}}. \tag{4.66}$$

The quantity J_i^{gr} is derived as described in Section 4.3.1, whereas J_i^{dec} depends on the dominant destruction processed described in the following sections.

The variation of the the grain size a_i comes naturally by differentiating Eq. 4.65

$$\frac{da_i}{dt} = V_{0,i} (J_i^{\mathrm{gr}} - J_i^{\mathrm{dec}}). \tag{4.67}$$

In the context of TP-AGB stars, I am interested in the dust growth process. At the beginning, the condition in the CSE prevents dust from growing, because the destruction term remains dominant within few stellar radii (depending on the destruction process assumed to be at work). Therefore, the numerical integration of Eq. 4.67 starts when the condition $(J_i^{\mathrm{gr}} - J_i^{\mathrm{dec}}) > 0$ is satisfied, whereas the derivative is kept equal to zero when J_i^{dec} dominates.

The dust condensation radius $R_{\mathrm{C},i}$ is the distance from the star at which the condition $da_i/dt > 0$ is verified. The dust condensation radius is in general different for the different dust species i, and depends on the decomposition process assumed to be at work.

In the following section I will describe how the growth term, J_i^{gr}, is derived.

4.3.1 The growth rate

The rate at which the reaction proceeds is determined by the flux of molecules or atoms in the gas phase per unit time, able to stick on the dust grain. Each dust grain is considered to be at rest and the flux of incident particles collides on its surface.

The total rate of collisions of each gas species is given by the product between their number density, given by Eq. 2.21, and their mean thermal velocity, $v_{th,j}(T_{\mathrm{gas}})$, where the gas temperature T_{gas} is given by Eq. 2.13. More specifically, the quantity $v_{th,j}(T_{\mathrm{gas}})$ is the mean velocity of the particles moving towards the grain surface and it is given by

$$v_{th,j} = \sqrt{\frac{k_B T_{\mathrm{gas}}}{2\pi m_j}}, \tag{4.68}$$

where k_B is the Boltzmann constant, and m_j the mass of the particle in the gas phase.

The final rate of molecules or atoms that are adsorbed by the dust grain is computed by multiplying the flux of particles per unit time by the so-called “sticking coefficient”. This quantity, generally provided by experimental determinations, is by definition the ratio between the number of the particles adsorbed by the grain surface, J_{ad}, over the total number of incident particles, J_{in} (MacNaught et al., 1997)

$$\alpha_i = \frac{J_{\mathrm{ad}}}{J_{\mathrm{in}}}. \tag{4.69}$$

Finally, the rate of the sticking particles, $J_{i,j}^{\mathrm{gr}}$, for each of the gas species j, is

$$J_{i,j}^{\mathrm{gr}} = \alpha_i n_{j,g} v_{th,j}(T_{\mathrm{gas}}). \tag{4.70}$$

The sticking coefficient, α_i, is assumed to be the same for all the particles forming the dust species i. This quantity is a function of surface temperature (dust temperature), surface coverage and structural details. The sticking coefficient provides an indirect measure of the degree of the kinetic barrier or the efficiency of condensation. Its value is between 0 to 1, zero implying infinite kinetic barrier and no condensation, and unity representing no kinetic barrier where all the impinging gas atoms or molecules are incorporated into the solid (see also Chapter 5).

The quantity $J_{i,j}^{\mathrm{gr}}$ is expected to decrease along the CSE. First of all, the gas density decreases as r^{-2} and is even more diluted because of the outflow acceleration. Second, $n_{j,g}$ is depleted from the gas phase because of dust condensation.

Once the rate of effective collisions for all the gas species j involved in the formation reaction is given by Eq. 4.70, it is possible to derive the growth rate of the dust grain by taking into account the following considerations:

- In order to form s_i monomers of the dust species i, the number of gas particles that should stick on the grain surface is equal to their stoichiometric coefficient s_j. The values of s_i and s_j are given by the specific formation reaction.
- The rate at which new monomers of dust are formed, and therefore the rate at which the dust grain is accreted, is determined by the rate at which the particles j stick on the dust grain, $J^{\mathrm{gr}}_{i,j}$ and on the stoichiometric coefficient, s_j. For each dust species i, the gas species for which the quantity $J^{\mathrm{gr}}_{i,j}/s_j$ is the lowest determines how fast the chemical reaction of dust accretion proceeds. This computation relies on the assumption that, when the slowest step of the chemical reaction occurs, the number of the other gas species that have stuck on the grain is already equal to their own s_j. The atom or molecule determining the slowest step in the dust formation reaction is called "rate-determining species".
- If the addition of s_j molecules or atoms of the rate-determining species forms s_i monomers of dust (with $s_i > 1$) the growth rate needs to be multiplied by s_i.

The growth rate for each dust species, J^{gr}_i, therefore reads

$$J^{\mathrm{gr}}_i = \min\left\{\frac{s_i}{s_j} J^{\mathrm{gr}}_{i,j}\right\}. \tag{4.71}$$

The gas species corresponding to this minimum is, by definition, the rate-determining species. It could change during the dust formation process within the CSE, as the abundances of the starting molecules and atoms change along the CSE.

The growth rate of the dust species listed in Table 4.1 are explicitly given in the following.

4.3.2 M-stars

- Olivine
  In order to form one monomer of olivine, two atoms of either magnesium or iron, one of SiO and three of H_2O are needed.

$$J^{\mathrm{gr}}_{\mathrm{ol}} = \min\left\{\frac{1}{2}\left(J^{\mathrm{gr}}_{\mathrm{ol,Mg}} + J^{gr}_{\mathrm{ol,Fe}}\right), \frac{1}{3} J^{\mathrm{gr}}_{\mathrm{ol,H_2O}}, J^{\mathrm{gr}}_{\mathrm{ol,SiO}}\right\} \tag{4.72}$$

  Since olivine can be conceived as an ideal solution of forsterite (Mg_2SiO_4) and fayalite (Fe_2SiO_4), each site for a cation can either be occupied by an Fe^{2+} or Mg^{2+} ion. For this reason the growth rates of iron and magnesium atoms are added, rather than considered separately in the computation of the growth.

- Pyroxene
  One monomer of pyroxene needs one atom of either magnesium or iron, one of SiO and two of H_2O.

$$J^{\mathrm{gr}}_{\mathrm{py}} = \min\left\{J^{\mathrm{gr}}_{\mathrm{py,Mg}} + J^{\mathrm{gr}}_{\mathrm{py,Fe}}, \frac{1}{2} J^{\mathrm{gr}}_{\mathrm{py,H_2O}}, J^{\mathrm{gr}}_{\mathrm{py,SiO}}\right\}. \tag{4.73}$$

  Analogously to olivine dust, pyroxene can be considered as an ideal solution of enstatite ($MgSiO_3$) and ferrosilite ($FeSiO_3$). Each cation site can either be occupied by an Fe^+ or Mg^+ ion.

- Quartz
  To form one monomer of quartz dust, one molecule of SiO and one of H_2O are needed.

$$J^{\mathrm{gr}}_{\mathrm{qu}} = \min\left\{J^{\mathrm{gr}}_{\mathrm{qu,H_2O}}, J^{\mathrm{gr}}_{\mathrm{qu,SiO}}\right\}. \tag{4.74}$$

- Periclase
  To form one monomer of periclase, one atom of magnesium and one molecule of H_2O are needed.
$$J^{\mathrm{gr}}_{\mathrm{pe}} = \min\left\{J^{\mathrm{gr}}_{\mathrm{pe,Mg}}, J^{\mathrm{gr}}_{\mathrm{pe,H_2O}}\right\}. \tag{4.75}$$
- Corundum
  For one monomer of corundum, one molecule of Al_2O and two of H_2O need to be added.
$$J^{\mathrm{gr}}_{\mathrm{co}} = \min\left\{J^{\mathrm{gr}}_{\mathrm{co,Al_2O}}, \frac{1}{2}J^{\mathrm{gr}}_{\mathrm{co,H_2O}}\right\}. \tag{4.76}$$
- Iron
  Iron dust directly condenses from the gas phase. Therefore one monomer of dust, corresponds to one atom of iron.
$$J^{\mathrm{gr}}_{\mathrm{Fe(s)}} = J^{\mathrm{gr}}_{\mathrm{Fe(s),Fe}} \tag{4.77}$$

4.3.3 C-stars

- Amorphous carbon
  For this dust species, just one molecule of acetylene, C_2H_2, is needed to produce two monomers of dust.
$$J^{\mathrm{gr}}_{\mathrm{C(s)}} = 2J^{\mathrm{gr}}_{\mathrm{C(s),C_2H_2}}. \tag{4.78}$$
- Silicon carbide
  In order to form two monomers of SiC, two atoms of silicon and one molecule of C_2H_2 are needed
$$J^{\mathrm{gr}}_{\mathrm{SiC}} = \min\left\{\frac{1}{2}J^{\mathrm{gr}}_{\mathrm{SiC,Si}}, J^{\mathrm{gr}}_{\mathrm{SiC,C_2H_2}}\right\}. \tag{4.79}$$
- Iron
  The formation of iron dust is treated with the same formalism of M-stars.

4.3.4 The destruction rate

As already mentioned, the dust grain growth is calculated from the balance between the growth and the destruction rates in Eq. 4.67. The destruction process goes through the inverse process of the molecules or atom absorption namely the desorption. As for any reactions, also desorption is characterized by its own activation energy. This is particularly important in order to determine which destruction processes are efficient in the typical conditions of CSE and it will be treated extensively in Chapter 5.

In the typical conditions of CSEs two main destruction mechanisms can be distinguished: pure sublimation, due to dust heating by stellar radiation and, for dust species that can react with H_2 molecules, such as olivine and pyroxene, the inverse reaction of the formation ones, listed in Table 4.1, occurring at the grain surface (Helling & Woitke, 2006).

The latter process is a reduction reaction and it is sometimes named chemisputtering (GS99).

In the former case the desorption reaction is activated by the energy provided by the stellar heating and depends on the equilibrium temperature reached by the dust grain surface (see Eq. 4.83). On the other hand, as far as chemisputtering is concerned, the reaction can be triggered by the kinetic energy of H_2 molecules, if they are energetic enough to break the bond Si-O or Mg-O. In this kind of reaction, H_2 molecules destroy the structure of an oxide to form H_2O molecules that are released in the gas phase (Nagahara & Ozawa, 1996).

The total destruction rate is given by the sum the two contributions

$$J_i^{\mathrm{dec}} = J_i^{\mathrm{sub}} + J_i^{\mathrm{cs}}. \tag{4.80}$$

The two destruction mechanisms are separately discussed in the following.

- *Destruction by sublimation*
  Sublimation is the natural evaporation process of molecules from the surface of the dust grain. The evaporation rate is a function of the temperature reached by the grain surface.

  It is also known that the sublimation process does not always work in a simple way. In the case of silicate dust the nominal molecule that evaporates does not exist as a single entity in the gas phase and does not vaporize in the usual sense. Instead the dust grain decomposes into molecules that exist in the gas phase (incongruent evaporation) (Duschl et al., 1996). The way in which the molecules desorb determines the rapidity of the grain decomposition.

  The evaporation rate, J_i^{sub}, is determined by considering that, in chemical equilibrium, it must equal the growth rate. Then, since the sublimation process depends only on the specific properties of the grain under consideration, the rate determined in this way must hold also outside equilibrium. I thus obtain from Eq. 4.70, after eliminating $n_{j,g}$ with the partial pressure and the temperature,

  $$J_i^{\mathrm{sub}} = \alpha v_{th,j}(T_{\mathrm{dust}}) \frac{p(T_{\mathrm{dust}})}{k_B T_{\mathrm{dust}}}, \tag{4.81}$$

  where T_{dust} is the dust equilibrium temperature (see Eq. 4.83), $v_{th,j}(T_{\mathrm{dust}})$ is the thermal velocity of the molecule ejected from the grain surface. The quantity $p(T_{\mathrm{dust}})$ is the saturated vapour pressure at the dust temperature, that can be expressed with the Clausius-Clapeyron equation

  $$p(T_{\mathrm{dust}}) = \exp\Big(-\frac{c_1}{T_{\mathrm{dust}}} + c_2\Big), \tag{4.82}$$

  where c_1 and c_2 are sublimation constants, characteristics of the species under consideration. The constant c_1 contains the latent heat of sublimation of the dust species and the constant c_2 actually is slightly dependent on the temperature. Both quantities may be obtained either directly from thermodynamical data (Duschl et al., 1996), or by fitting with Eq. 4.82 the results of sublimation experiments (Kimura et al., 2002; Kobayashi et al., 2009, 2011).

  The dust equilibrium temperature in Eq. 4.81 is evaluated in the following way. The radiation field is able to heat the dust up to a certain equilibrium temperature at any distances from the photosphere. Absorption and re-emission of photons by the dust particles is proportional to the absorption coefficient Q_{abs}, defined in Chapter 3, which in turn is a function of the grain size and of the wavelength of the incident radiation.

  Initially, when dust is not yet formed or the opacity is negligible, the medium can be approximated as optically thin and the equation describing the energy balance between the radiation absorbed by the dust grains and the one which is re-irradiated is

  $$T_{\mathrm{dust}}^4 Q_{\mathrm{abs,P}}(a, T_{\mathrm{dust}}) = {T_{\mathrm{eff}}}^4 Q_{\mathrm{abs,P}}(a, T_{\mathrm{eff}}) W(r). \tag{4.83}$$

$Q_{\mathrm{abs,P}}$ is the Planck averaged absorption coefficient, computed analogously to Eq. 3.22. This quantity is explicitly expressed as a function of the temperature and grain size, and the dilution factor $W(r)$ is defined in Eq. 2.14. The dust equilibrium temperature depends on optical properties and, therefore, on the chemical composition.

The dust condensation temperature, T_{cond}, is defined as the dust equilibrium temperature at the point where dust of a given type effectively condenses. The dust equilibrium temperature, T_{dust}, computed through Eq. 4.83 is only a virtual quantity, i.e. it is the temperature that the dust would have if it could begin to form at a given radial distance.

- *Destruction by chemisputtering*
  The H_2 molecules in the gas phase may be adsorbed by the solid surface and may accelerate the evaporation with respect to pure sublimation. In particular, the presence of H_2 molecules changes the destruction reaction with respect to free evaporation by means of a process that, as already anticipated, is given by the inverse reaction with respect to the formation one (Table 4.1).

  The chemisputtering destruction rate, J_i^{cs}, is determined in an analogous way, assuming that the growth and destruction rates at equilibrium must balance, and using the law of mass action to determine the partial equilibrium pressure of the rate-determining species, $p_{j,\mathrm{eq}}$ (Eq. 4.85), determined as described in Duschl et al. (1996). In analogy to Eq. 4.67 the destruction rate is finally expressed by

$$J_i^{\mathrm{cs}} = s_i \frac{\alpha v_{th,j}(T_{\mathrm{gas}})}{s_j} \frac{p_{j,i\mathrm{eq}}}{k_B T_{\mathrm{gas}}}. \tag{4.84}$$

  where j is the rate-determining species of each dust species i. Note that I replaced $n_{j,i} v_{th,j} = p_{j,i}/k_B T_{\mathrm{gas}}$ (for the equilibrium abundances).

  In Section 4.3.1 the partial pressure of the rate-determining species is uniquely determined by the partial pressures of the other species in the gas phase. The partial pressures change along the CSE according to the variations of $n_{j,i}$ (Eqs. from 4.16 to 4.27 for M-stars and from 4.48 to 4.50 for C-stars). If the rate determining species is the gas species A, I obtain that the correspondent equilibrium partial pressure is

$$p_{A,\mathrm{eq}} = \left[\frac{p_{\mathrm{D}}^{\mathrm{d}}}{p_{\mathrm{B}}^{\mathrm{b}} p_{\mathrm{C}}^{\mathrm{c}}} \exp\left(\frac{\Delta G^\circ}{RT_{\mathrm{gas}}} \right) \right]^{1/\mathrm{a}}. \tag{4.85}$$

  The thermodynamical data for the computation of chemisputtering rates are taken from Sharp & Huebner (1990) with the exception of $FeSiO_3$ and SiC for which I adopt the data taken by Barin & Platzki (1995).

  The explicit form of the term $p_{\mathrm{A,eq}}$, for the different dust species, is provided as follows.

4.3.5 M-stars

- Olivine: assuming that the rate-determining species of olivine is SiO, I obtain

$$p_{\mathrm{SiO,eq}} = \frac{p_{\mathrm{H_2}}^3}{p_{\mathrm{Mg}}^{2x_{\mathrm{ol}}} p_{\mathrm{Fe}}^{2(1-x_{\mathrm{ol}})} p_{\mathrm{H_2O}}^3 K_p(\mathrm{ol})}, \tag{4.86}$$

- Pyroxene: assuming that its rate-determining species to be SiO, I finally have

$$p_{\mathrm{SiO,eq}} = \frac{p_{\mathrm{H_2}}^2}{p_{Mg}^{x_{\mathrm{py}}} p_{\mathrm{Fe}}^{(1-x_{\mathrm{py}})} p_{\mathrm{H_2O}}^2 K_p(\mathrm{py})}, \tag{4.87}$$

- Quartz: analogously to the previous two cases,

$$p_{\mathrm{SiO,eq}} = \frac{p_{\mathrm{H_2}}}{p_{\mathrm{H_2O}} K_p(\mathrm{qu})} \tag{4.88}$$

- Periclase: if its rate-determining species is magnesium

$$p_{\mathrm{Mg,eq}} = \frac{p_{\mathrm{H_2}}}{p_{\mathrm{H_2O}} K_p(\mathrm{pe})} \tag{4.89}$$

- Corundum. If the rate-determining species is Al_2O the correspondent partial pressure is

$$p_{\mathrm{Al_2O,eq}} = \left[\frac{p_{\mathrm{H_2}}^2}{p_{\mathrm{H_2O}}^2 K_p(\mathrm{co})} \right]^{1/2} \tag{4.90}$$

- Iron. As this species is directly formed from iron atoms I get

$$p_{\mathrm{Fe,eq}} = K_p[\mathrm{Fe(s)}]^{-1} \tag{4.91}$$

4.3.6 C-stars

Analogously to M-stars, I list in the following the explicit forms of the partial pressures of the rate-determining species of C-stars.

- Amorphous carbon. As already mentioned, for this species I do not take into account the backward reaction because carbon dust is assumed to form below a threshold temperature (1100 or 1300 K according to the model adopted in Section 5).
- Silicon carbide. If the rate determining species is Si one has

$$p_{\mathrm{Si,eq}} = \left(\frac{p_{\mathrm{H_2}}}{p_{\mathrm{C_2H_2}} K_p(\mathrm{SiC})} \right)^{1/2} \tag{4.92}$$

- Iron. This dust species is treated with the same formalism adopted for M-stars.

4.3.7 Modification in the composition of Olivine and Pyroxene

In this final subsection the possible modification of the magnesium over iron plus magnusium fraction of olivine and pyroxene composition is discussed.

Following FG06, the probability x that a surface site for a magnesium or iron atom during particle growth is occupied by magnesium is given by the ratio of the deposition rates from the gas phase (where $i = \mathrm{ol,py}$)

$$x_{g,i} = \frac{J_{i,\mathrm{Mg}}^{\mathrm{gr}}}{J_{i,\mathrm{Mg}}^{\mathrm{gr}} + J_{i,\mathrm{Fe}}^{\mathrm{gr}}}. \tag{4.93}$$

$x_{g,i}$ is in general different from the abundance in the grain.

Following GS99 I will denote with N_{Si} the number of silicon atoms within a silicate grain, and with M the number of sites occupied by Mg^{2+} (for olivine) and Mg^{+} (for pyroxene). The aim is to study how the fraction

$$x_i = \mathrm{Mg}/(\mathrm{Mg} + \mathrm{Fe}), \tag{4.94}$$

changes in the grain. If N_{Si} sites are occupied by silicon atoms, a number equal to $N_{\mathrm{ol}} = 2N_{\mathrm{Si}}$ and $N_{\mathrm{py}} = N_{\mathrm{Si}}$ sites will be occupied by Mg+Fe atoms, for olivine and pyroxene, respectively.

The change of the quantity x_i is

$$\begin{aligned} \frac{dx_i}{dt} &= \frac{d}{dt}\frac{M}{N} = && (4.95)\\ &= -\frac{M}{N^2}\frac{dN}{dt} + \frac{1}{N}\frac{dM}{dt}, && (4.96)\\ & && (4.97) \end{aligned}$$

and finally by means of the definition given by Eq. 4.94:

$$\frac{dx_i}{dt} = -\frac{x_i}{N}\frac{dN}{dt} + \frac{1}{N}\frac{dM}{dt} \tag{4.98}$$

The term dM/dt, is given by the sum of two terms. One describes the variation of the number of sites occupied by magnesium atoms, newly created in the growth process, $dM_{\mathrm{gd},i}/dt$. The other, describes the variation of M due to a possible exchange between a magnesium atom, in the grain, and a iron atom, in the gas phase, $dM_{\mathrm{ex},i}/dt$ (cation exchange):

$$\frac{dM}{dt} = \frac{dM_{\mathrm{gd},i}}{dt} + \frac{dM_{\mathrm{ex},i}}{dt}. \tag{4.99}$$

The quantity dN/dt is the variation of the total number of sites newly created in the growth process, that can be occupied by either magnesium or iron.

I will consider the terms dN/dt and dM/dt separately.

4.3.8 Variation of the total number sites N=Mg+Fe

The number of silicon sites N_{Si} changes with time because of the dust growth. Considering that in each monomer of silicate dust there is one silicon atom, the number variation of N_{Si} is

$$\frac{dN_{\mathrm{Si}}}{dt} = \frac{d}{dt}\frac{4\pi a_i^3}{3V_{0,i}} = \frac{4\pi a_i^2}{V_{0,i}}\frac{da_i}{dt}. \tag{4.100}$$

By means of Eq. 4.67 one finally gets

$$\frac{dN_{\mathrm{Si}}}{dt} = 4\pi a_i^2 (J_i^{\mathrm{gr}} - J_i^{\mathrm{dec}}). \tag{4.101}$$

Moreover, the volume of a grain of radius a_i can be expressed as a function of $V_{0,i}$ as

$$\frac{4\pi a_i^3 \rho_{d,i}}{3} = N_{\mathrm{Si}} V_{0,i}, \tag{4.102}$$

so that

$$4\pi a^2 = N_{\mathrm{Si}} \frac{3V_{0,i}}{a_i}, \tag{4.103}$$

therefore, by eliminating from Eq. 4.101 the term $4\pi a_i^3$ through 4.103, one gets

$$\frac{dN_{\mathrm{Si}}}{dt} = N_{\mathrm{Si}} \frac{3V_{0,i}}{a_i}(J_i^{\mathrm{gr}} - J_i^{\mathrm{dec}}). \tag{4.104}$$

4.3.9 Variation of sites occupied by magnesium

As already mentioned, the variation of M can occur through two processes. On the other hand, a newly created site can be occupied by magnesium with a certain probability, on the other hand, some direct exchanges between magnesium on the grain and iron atoms in the gas can occur. This process is described through a chemical reaction given in Table 4.1. This means that if a magnesium atom collides on the surface of a grain at a site which is occupied by an iron cation, the particles may exchange. This process is regulated by the energetics of the exchange reaction, as it will be outlined in the following.

The variation of M due to the first mechanism is expressed by

$$\frac{dM_{\mathrm{gd},i}}{dt} = 4\pi a_i^2 s_{i,\mathrm{Mg}}(x_{g,i}J_i^{\mathrm{gr}} - x_i J_i^{\mathrm{dec}}). \tag{4.105}$$

This relation takes into account the fact that for each monomer of dust formed, a number equal to $s_{i,\mathrm{Mg}}$ of magnesium atoms are added to the grain.

In analogy to Eq. 4.101 one gets

$$\frac{dM_{\mathrm{gd},i}}{dt} = N_{\mathrm{Si}}\frac{3V_{0,i}}{a_i}(x_{g,i}J_i^{\mathrm{gr}} - x_i J_i^{\mathrm{dec}}), \tag{4.106}$$

The cation exchange is expressed by an analogous equation:

$$\frac{dM_{\mathrm{ex},i}}{dt} = N_{\mathrm{Si}}\frac{3V_{0,i}}{a_i}(J_+^{\mathrm{ex}} - J_-^{\mathrm{ex}}), \tag{4.107}$$

where J_+^{ex} is the rate of exchange between an iron atom in the grain and a magnesium atom in the gas, and J_-^{ex} is the correspondent rate of exchange between a magnesium atom in the grain and an iron atom in the gas and will be specified later. Therefore, by inserting Eqs. 4.101, 4.106 and 4.107, where $N_{\mathrm{Si}} = N_{\mathrm{ol}}/2$, for olivine, and with $N_{\mathrm{Si}} = N_{\mathrm{py}}$, one gets

- Olivine.

$$\frac{dx_{\mathrm{ol}}}{dt} = \frac{3V_{0,\mathrm{ol}}}{a}[(x_g - x_{\mathrm{ol}})J_{\mathrm{ol}}^{gr} + \frac{1}{2}(J_{+,\mathrm{ol}}^{\mathrm{ex}} - J_{-,\mathrm{ol}}^{\mathrm{ex}})], \tag{4.108}$$

- Pyroxene.

$$\frac{dx_{\mathrm{py}}}{dt} = \frac{3V_{0,\mathrm{py}}}{a_{\mathrm{py}}}[(x_g - x_{\mathrm{py}})J_{\mathrm{py}}^{\mathrm{gr}} + (J_{+,\mathrm{py}}^{\mathrm{ex}} - J_{-,\mathrm{py}}^{\mathrm{ex}})]. \tag{4.109}$$

While the term J_i^{gr} has already been defined, the terms $J_{+,i}^{\mathrm{ex}}$ and $J_{-,i}^{\mathrm{ex}}$ need to be specified.

The rate of collisions of magnesium atoms is defined similarly to the growth rate (Eq. 4.71). The flux of the colliding magnesium atoms that succeed in the exchange with a corresponding iron atom is given, per unit time, by

$$J_{+,i}^{\mathrm{ex}} = \alpha_{i,\mathrm{ex}} n_{\mathrm{Mg},g} v_{th,\mathrm{Mg}}, \tag{4.110}$$

where the coefficient $\alpha_{i,\mathrm{ex}}$ is the probability of exchange of a magnesium atom with an iron one.

The rate of the inverse reaction, J_-^{ex}, is given by the iron atoms able to exchange with a magnesium one. Therefore one has that

$$J_{-,i}^{\mathrm{ex}} = \beta_{i,\mathrm{ex}} n_{\mathrm{Fe},g} v_{th,\mathrm{Fe}} \tag{4.111}$$

where $\beta_{i,\mathrm{ex}}$ is the probability of exchange of an iron atom with a magnesium one.

The coefficient $\beta_{i,\mathrm{ex}}$ is related to $\alpha_{i,\mathrm{ex}}$. This relation can be determined by considering the cation exchange reactions at their chemical equilibrium. For a given partial pressure of iron atoms, determined by its abundance, the correspondent Mg partial pressure at the equilibrium is determined, by the law of mass action, in analogy to Eq. 4.85

$$p_{\mathrm{Mg,eq}} = [p_{\mathrm{Fe}}^{s_{\mathrm{Fe}}} K_p(T, x_i)]^{1/s_{\mathrm{Mg}}}, \tag{4.112}$$

where s_{Mg} and s_{Fe} are the stoichiometric coefficients of magnesium and iron, respectively, and $K_p(T, x_i)$ is the constant of the exchange reaction. In particular, at the chemical equilibrium $J_{+,i}^{\mathrm{ex}} = J_{-,i}^{\mathrm{ex}}$, and thus

$$\beta_{\mathrm{ol,ex}} = \alpha_{\mathrm{ol,ex}} \frac{v_{th,\mathrm{Mg}}}{v_{th,\mathrm{Fe}}} \frac{n_{\mathrm{Mg,eq}}}{n_{\mathrm{Fe}}} \tag{4.113}$$

Through Eq. 4.113 it is possible to express $J_{-,i}^{\mathrm{ex}}$ in Eq. 4.111 as

$$J_{-,i}^{\mathrm{ex}} = \alpha_{i,\mathrm{ex}} n_{\mathrm{Mg,eq}} v_{th,\mathrm{Mg}}, \tag{4.114}$$

and therefore, after eliminating the partial pressures in Eq. 4.112,

$$J_{-,i}^{\mathrm{ex}} = \alpha_{i,\mathrm{ex}} [n_{\mathrm{Fe}}^{s_{\mathrm{Fe}}} K_p(T, x_i)]^{1/s_{\mathrm{Mg}}} v_{th,\mathrm{Mg}}, \tag{4.115}$$

The rate of exchange of cations in Eqs. 4.108 and 4.109 is therefore

$$J_{+,i}^{\mathrm{ex}} - J_{-,i}^{\mathrm{ex}} = v_{th,\mathrm{Mg}} \alpha_{\mathrm{ex},i} [n_{\mathrm{Mg,eq}} - n_{\mathrm{Fe}} K_p(T, x_i)^{1/s_{\mathrm{Mg}}}] \tag{4.116}$$

According to the reactions listed in Table 4.1, the constants of the reactions for olivine and pyroxene are computed as follows

- Olivine

  $$K_p(\mathrm{ol}) = \exp\left[-\frac{\Delta G_{\mathrm{fa}}^{\circ} - \Delta G_{\mathrm{fo}}^{\circ}}{2RT} - \frac{G_{\mathrm{ol,mix}}^{\circ}}{2(1 - x_{\mathrm{ol}})RT} \right] \tag{4.117}$$

  $\Delta G_{\mathrm{fa}}^{\circ}$ and $\Delta G_{\mathrm{fo}}^{\circ}$ are the free energies of formation of fayalite and forsterite from the free atoms, and $G_{\mathrm{ol,mix}}^{\circ}$ is the entropy of mixing for two moles of cations specified in Eq. 4.30.

- Pyroxene

  $$K_p(\mathrm{py}) = \exp\left[-\frac{\Delta G_{\mathrm{en}}^{\circ} - \Delta G_{\mathrm{fer}}^{\circ}}{RT} - \frac{G_{\mathrm{py,mix}}^{\circ}}{(1 - x_{\mathrm{py}})RT} \right] \tag{4.118}$$

  $\Delta G_{\mathrm{en}}^{\circ}$ and $\Delta G_{\mathrm{fer}}^{\circ}$ are the free energies of formation of enstatite and ferrosilite, respectively, from the free atoms and $G_{\mathrm{py,mix}}^{\circ}$ is the entropy of mixing for one mole of cations specified in Eq. 4.34.

Chapter 5

Circumstellar Envelopes Models

In this Chapter I present the basic assumptions underlying the dust growth schemes. Section 5.1 is devoted to the case of M-stars while, in Section 5.2 I consider the case of C-stars. In Section 5.3, I outline the effects brought by changing the main assumptions of the dust growth schemes by comparing a few models of both M-giant CSEs and C-star CSEs.

5.1 M-stars CSE models

In Chapter 4 I discussed how the growth of silicate dust grains is determined by the balance between their accretion and their destruction rates. Two destruction processes can be at work: pure sublimation and chemisputtering. From the standard computations, based on the calculation of the Gibbs energies, it follows that chemisputtering rates are much larger than the sublimation ones. Therefore, many authors assume that the former process is the one that inhibits the growth of dust grains (GS99, FG06).

However, these computations are only based on energetics considerations and miss the important role of the activation energies in chemical reactions. This is the aim of chemical kinetics that should be preferred in the analysis of the chemisputtering efficiency.

In this respect experimental studies are fundamental to quantify the kinetics of reactions. Indeed, experimental measurements of the evaporation rates in presence of H_2 molecules provide important results in order to determine if, at the typical conditions of pressure and temperature characterizing the CSEs, chemisputtering is efficient.

Some basic definitions of chemical kinetics are briefly recalled in Section 5.1.1, to help the reader to interpret the experimental results outlined in Section 5.1.2. Direct condensation experiments are briefly reviewed in Section 5.1.3. The comparison between the condensation temperatures obtained when chemisputtering is included and the ones derived when only pure sublimation is at work, is performed in Section 5.1.4.

5.1.1 Chemical kinetics

Given the simple reaction

$$\mathrm{A} \rightarrow \mathrm{B}, \tag{5.1}$$

an infinitesimal increase in the product $B = d\xi$ corresponds to a decrease in the reactant $A = -d\xi$. The quantity ξ is know as "extent of reaction".

For a more general chemical reaction,

$$\mathrm{s_A A + s_B B \rightarrow s_C C + s_D D}, \tag{5.2}$$

the extent of reaction is defined in such a way that, if it changes by $\Delta\xi$, then the change in the amount of any species, j = A, B, C, D, is $s_j\Delta\xi$, for the products, and $-s_j\Delta\xi$ for the reactants.

It is now possible to define the "rate of reaction", v, as the rate of change of the extent of reaction

$$v = \frac{d\xi}{dt}. \tag{5.3}$$

The quantity ξ is related to the variation of the amount of the substances involved in the reaction. If dj is the infinitesimal variation of the species j, one gets by definition that

$$s_j d\xi = dj. \tag{5.4}$$

Therefore, by differentiating, from Eq. 5.3 it follows that

$$v = \frac{1}{s_j}\frac{dj}{dt}. \tag{5.5}$$

The rate of reaction is often found to be proportional to the concentrations of the reactants raised to a certain power. Considering reactions of the form 5.2 one has that

$$v = k[A]^a[B]^b, \tag{5.6}$$

where the square brackets indicate the molar concentration of the species and k is called "rate constant" of the reaction. The rate constant does not depend on the concentrations, but is a function of the temperature, whereas a and b are experimentally determined for the specific reaction considered. Equation 5.6 is called "rate law" of the reaction. The power at which the concentration of a species is raised in the rate law is the *order* of the reaction with respect to that species. The *overall order* of a reaction is the sum of the individual orders (a + b). The rate constant is governed by the Arrhenius equation

$$k = k_0 \exp\Big(-\frac{E_a}{RT}\Big), \tag{5.7}$$

where k_0 is a constant and E_a is the activation energy of the reaction. To activate the reaction, the reactants need to have a minimum kinetic energy, equal to E_a in order to form the products. The exponential factor in Eq. 5.7 can be interpreted as the fraction of collisions with enough kinetic energy to lead to the reaction. In fact, the number of gas particles, N_j, that have energy in excess of E_a is given by the Boltzmann distribution

$$N_j = N \exp-\Big(\frac{E_a}{RT}\Big), \tag{5.8}$$

where N is the total number of particles.

If the gas temperature is much lower than

$$T = \frac{E_a}{R}, \tag{5.9}$$

the reaction slows down, because only a tiny fraction of the particles are more energetic than E_a.

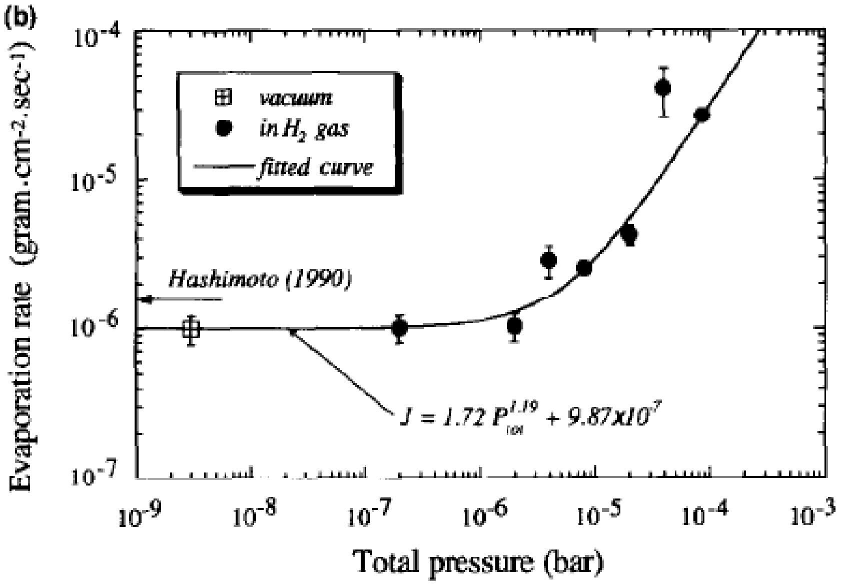

Figure 5.1: Evaporation rate as a function of the total pressure at the fixed temperature of 2000 K. The figure is taken from Nagahara & Ozawa (1996).

5.1.2 Laboratory experiments of silicates evaporation

The experiments by Nagahara & Ozawa (1996) consider the evaporation of a crystal of forsterite (Mg_2SiO_4) in presence of H_2 at temperature of about 2000 K. The evaporation fraction is defined as the difference between the initial and the final weights, divided by the initial one. The evaporation rate is fitted by the formula

$$J = 1.72 P_{\rm tot}^{1.19} + 9.87 \times 10^{-7} [\mathrm{g \cdot cm^{-2} s^{-1}}], \tag{5.10}$$

where $P_{\rm tot}$ is given in bar. The data fit is shown in Fig. 5.1. When the pressure is low, less than 10^{-6} bar (1 dyne cm^{-2}) the first term of the right hand side is negligible, the evaporation rate is independent of the pressure and it is the same as the one measured in vacuum. On the other hand, for pressures above 10^{-6} bar, the evaporation rate depends linearly on the pressure. At the typical pressure of the CSE (10^{-2} dyne $\mathrm{cm}^{-2} = 10^{-8}$ bar) the relation is independent of the pressure and the sublimation rate is the same as in vacuum. The evaporation rate, in fact, is almost constant for total pressures between 0.1 and 1 dyne cm^{-2}, where the partial pressure of H_2 molecules is too low to affect the evaporation rate significantly.

From this kind of experiment the authors were also able to determine the value of the sticking coefficient for olivine α_{ol} that varies from 0.06 (in the vacuum) up to 0.2 at pressures of 10^2 dyne cm^{-2}. This quantity is estimated by dividing the maximum theoretical evaporation rate (obtained with $\alpha_{\rm ol} = 1$) to the measured one. This corresponds to Eq. 4.69.

Another experiment in which quartz glass (SiO_2) erosion in presence of hydrogen gas is studied, was performed by Tso & Pask (1982) in the range of temperature between 1500 and 1700 K. In particular, they determined the activation energy barrier of the reaction

$$\mathrm{SiO_2(s) + H_2(g) \rightarrow SiO(g) + H_2O(g)}, \tag{5.11}$$

from the relation between the sublimation rates and the term $1/T$, obtaining a value of 343±33 kJ mol^{-1}.

An analogous experiment was performed by Gardner (1974) for the same chemical reaction (Section 5.11) in the range of temperatures between $\sim$ 1400 and 1900 K finding an activation energy barrier of about 355 kJ mol^{-1}.

In the work of Massieon et al. (1993) the experiment of the olivine reduction by H_2 molecules was performed in the range of pressure between 4.6×10^4 and 1.4×10^5 dyne cm^{-2} and for temperatures between 1070 and 1370 K. They considered two types of solid olivine, pure fayalite (Fe_2SiO_4) and olivine that includes a fraction of magnesium in place of iron, called Fa93 ($Fe_{1.86}Mg_{0.14}SiO_4$). The kinetics of the reaction that was studied is

$$2H_2 + Fe_2SiO_4 \rightarrow 2H_2O + 2Fe + SiO_2 \tag{5.12}$$

They found that the activation energy barrier of the Fa93 compound is 205 kJ mol^{-1} and that of Fe_2SiO_4 is equal to 260 kJ mol^{-1}.

The results of all these experiments can be interpreted in the following way.

First of all, in order to activate chemisputtering, the kinetic energy of H_2 molecules has to be high. The lowest measured value of the activation energy is the one of Fa_{93} compound and is 205 kJ mol^{-1} (Gardner, 1974), corresponding to a kinetic temperature of $T \sim 25000$ K (Eq. 5.9). This means that, at the temperature at which Nagahara & Ozawa (1996) performed their experiment, 2000 K, the reaction is slowed down by a factor 10^5. Second, the chemisputtering efficiency depends on the total pressure. In fact, the decomposition rate measured by Nagahara & Ozawa (1996) is found to be the same as in vacuum at the typical pressures found in CSEs (10^{-2} dyne cm^{-2}), while the pressure-dependent regime is for $P > 10^2$ dyne cm^{-2}. The increase in the decomposition rate at higher pressures, can be explained by the fact that the fraction of particles more energetic than the activation energy increases proportionally to their total number, according to Eq. 5.8.

In conclusion, the critical dependence of the chemisputtering on the temperature and pressure and the key-role played by the chemical kinetics, indicate that the chemisputtering destruction rate cannot be simply evaluated on the basis of energetic requirements because the chemisputtering reaction rate is likely to be highly suppressed in the typical conditions of the CSEs.

5.1.3 Laboratory experiments of silicates condensation

In another important experiment, Nagahara et al. (2009) performed a laboratory study of the inverse process of evaporation: condensation. The insights derived by this study, as for instance the typical condensation temperature of silicates, are of great importance for the purposes of this thesis.

The experiments were performed in an evacuated tube in which a gas source and a substrate are set up. The gas source is a synthesized single crystal of forsterite (Mg_2SiO_4), which is heated from the outside. Forsterite evaporates to generate gas species of Mg, SiO, and O with the ratio of 2:1:3. The species in the gas phase move downward along the tube, finally hitting the substrate surface.

The substrate is either Al_2O_3 or Mo, both of which are highly refractory, and no reaction between impinging gas is expected at any temperature. The heating system that controls the temperature of the substrate is independent of the one that generates atoms and molecules.

In this particular case, the substrate temperature is lower than the gas one. This condition is of particular interest because it resembles the conditions of dust grains in CSEs. While the temperature of the substrate changes, different dust species can form from the initial gas composition. In this way, the condensation temperature can be controlled by changing that of the substrate, because the gas particles instantaneously acquire that temperature.

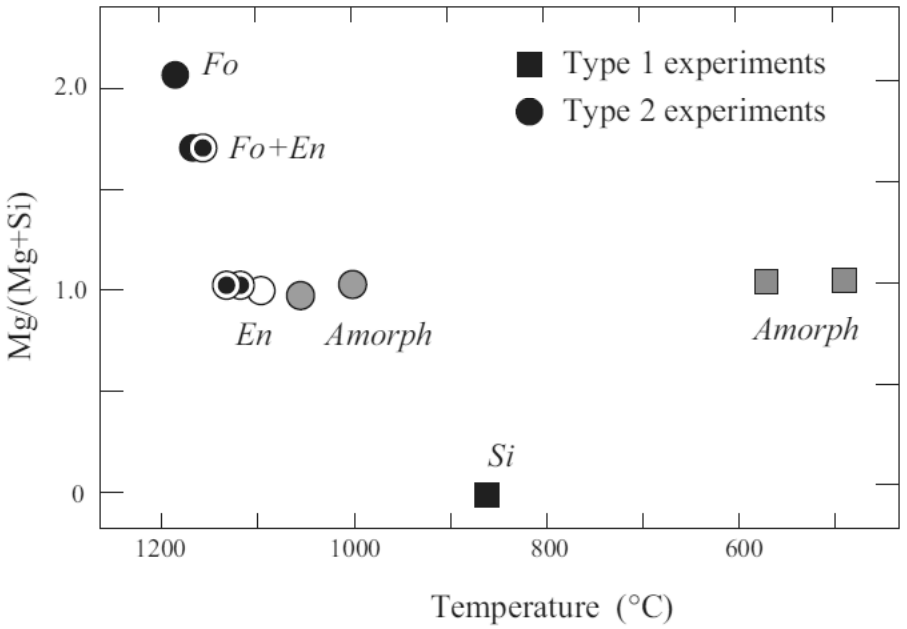

Figure 5.2: Mg/(Mg+Si) ratio as a function of the condensation temperature. The figure is taken from Nagahara et al. (2009).

Mutual interactions among gas atoms and molecules are negligible because their mean free path is larger than the size of the tube.

Two types of experiments were performed, that differ only in the final flux of gas particles hitting the substrate surface.

The so called “type 1 experiments” were performed in a silica glass tube. The inner wall is characterized by a temperature lower than that of the gas particles. For this reason, the particles that hit the tube surface remain attached to it and there is no reflection. The net effect of this process is that the particle flux hitting the substrate is much lower than the initial flux coming from the source. The pressure during experiments is as low as 10^{-4} dyne cm^{-2}.

On the other hand, the so-called “type 2 experiment” was performed in a vacuum chamber with a vertical alumina tube in the center. The gas source is set at the bottom of the tube, and the substrate is inserted from the top. In this experimental set up, a fraction of gas particles directly arrives at the substrate, whereas the fraction that collides with the alumina tube can either be reflected and thus attach to the substrate, or can react with alumina to form $MgAl_2O_4$ (spinel) due to the high temperature of the tube. The formation of spinel results in chemical fractionation of gas. The condensation flux of gas onto the substrate is calculated to be Mg:Si=1:1. The main difference with respect to type 1 experiment is that the gas atoms and molecules that collide with the tube can be reflected maintaining approximately the original flux. The pressure measured at a port attached to the vacuum chamber is about 10^{-3}-10^{-2} dyne cm^{-2}.

As shown in Fig. 5.2, the results of the two experiments can be summarized as follows.

In type 1 experiment dust does not condense above 1270 K, whereas at lower temperatures (720 K), amorphous Mg-silicates are formed. The chemical composition of the silicates obtained is Mg:Si=1:1 which means that about one half of magnesium was lost from the bulk source composition (Mg:Si=2:1).

During type 2 experiment the gas flow was fractionated from forsterite-like composition (Mg:Si =2:1) to close to enstatite-like composition (Mg:Si=1:1) due to the reaction with the alumina tube.

The highest condensation temperature is found for crystalline forsterite at 1450 K, while the condensation of amorphous forsterite and enstatite is around 1320 K.

A significant difference between type 1 and type 2 experiments is that in the latter case the gas pressure is higher and with a larger flux than the former. Thus, this result is an indication of the fact that the final condensation temperature of amorphous silicates, expected to be the most abundant one in the CSEs of M-stars, depends on the flux of the particles. This fact can be interpreted thinking about the condensation process in terms of the competition between the growth and destruction rates and that at sufficiently high growth rates condensation temperatures of silicates can be as high as $T \sim 1400$ K. This will be discussed in the following section.

5.1.4 Evaluation of the condensation temperature of silicates in CSEs

The condensation temperature is defined to be the temperature at which the condition $da_i/dt = 0$ is met. From Eq. 2.19 this means that at this point $(da_i/dt)^{\rm gr} = (da_i/dt)^{\rm dec}$. In particular, from Eq. 4.80, it follows that, if chemisputtering is at work, $J_i^{\rm gr} = J_i^{\rm cs}$ and the condensation temperature $T_{\rm cond}$ refers to the *gas* temperature; on the other hand, if only sublimation is included, $J_i^{\rm gr} = J_i^{\rm sub}$ and the condensation temperature refers to the *dust* temperature.

The condensation temperatures of silicates is here studied as a function of $(da_i/dt)^{\rm gr}$ and the destruction by sublimation and chemisputtering are considered separately. The condensation temperatures are shown in Fig. 5.3. The solid and dotted lines refer to the case of the olivine and pyroxene, respectively, with $J_i^{\rm sub}$ computed following the method by Kimura et al. (2002) (see also Kobayashi et al., 2011). For olivine, Kimura et al. (2002) determine, from experimental results, $c_1 = 6.56 \times 10^4$ K and $\exp(c_2) = 6.72 \times 10^{14}$ dyne cm^{-2}. With these values I obtain condensation temperatures between 1200 K and 1400 K.

The olivine curve obtained with this approach can be compared with that derived for forsterite (dashed line) using, instead, the analytical fits to theoretical calculations of c_1 and c_2 provided by Duschl et al. (1996), from calculations of decomposition equilibria. The two methods give comparable condensation temperatures for olivine-type silicates. The values shown in the figure are also consistent with those derived by Kobayashi et al. (2009) and Kobayashi et al. (2011), in the different context of sublimation of dust grains in comets.

Furthermore, this method provides condensation temperature for olivine in very good agreement with the recent experimental values by Nagahara et al. (2009), who have found $T_{\rm cond}$ from ~1350 K (amorphous silicates) to $T_{\rm cond}$ ~1450 K (crystalline silicates).

For the evaporation of pyroxene some authors have considered that the preferential mode is through SiO_2 molecules (Tachibana et al., 2002) and have empirically derived $c_1 = 6.99 \times 10^4$ K and $\exp(c_2) = 3.13 \times 10^{11}$ dyne cm^{-2}. With these values I obtain condensation temperatures that lie between 1500 K and 1600 K. However, the result for pyroxene is not very reliable and must be considered only as un upper limit for the following reason. It is assumed that pyroxene evaporates preferentially incongruently through SiO_2 but without taking into account that this incongruent sublimation is followed by the production of forsterite (Tachibana et al., 2002) which, at these temperatures, immediately evaporates. Moreover, as pointed out in the work by Nagahara et al. (2009), forsterite is the phase that condenses first from gas at a wide range of Mg/Si ratios different from 1.

Thus, in the following, I will consider the condensation temperature of the olivine as representative of all other silicates, when just sublimation is considered.

The condensation temperatures derived if just pure sublimation is at work, $T_{\rm cond}$, are compared with the gas temperatures at which olivine and pyroxene are expected to form when

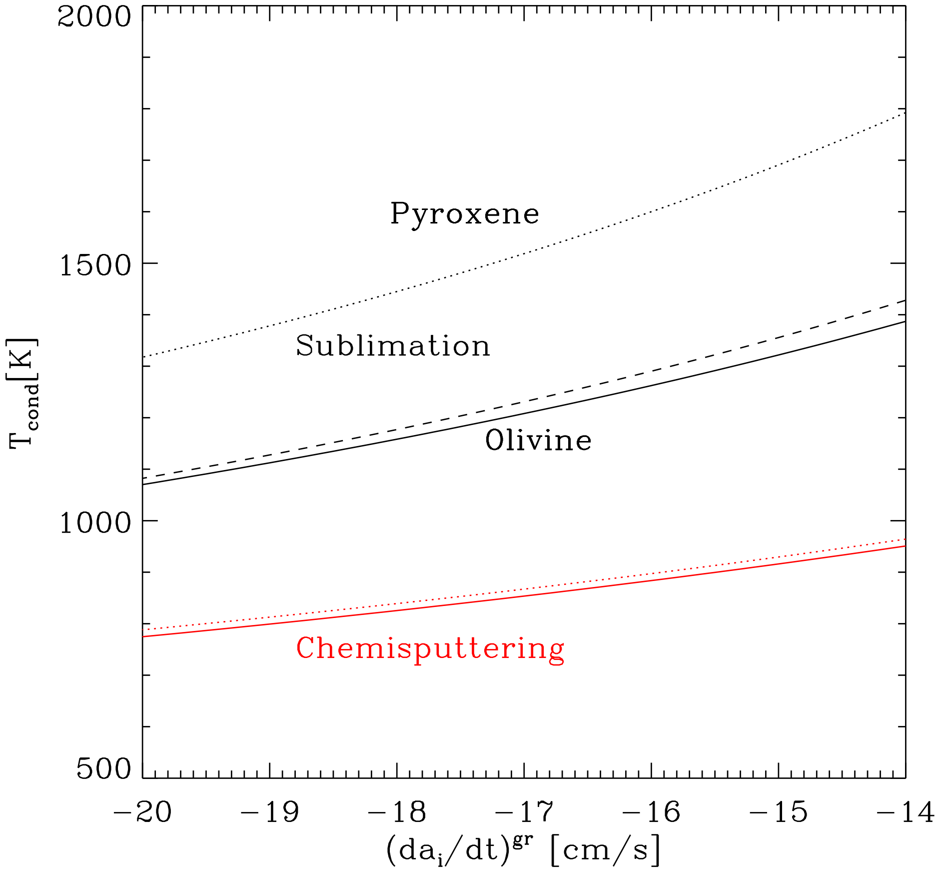

Figure 5.3: Condensation temperatures of olivine and pyroxene as a function of the growth rate given by Eq. 2.19 with $J_i^{dec} = 0$. For the pure sublimation case ($J_i^{cs} = 0$) the curves for olivine (black solid and dashed lines) are obtained from the models of Kimura et al. (2002) and Duschl et al. (1996) respectively, while pyroxene curve is from Kimura et al. (2002) (black dotted line). For the pure chemisputtering case ($J_i^{sub} = 0$) the curves from olivine (red solid line) and pyroxene (red dotted line) are obtained from Eqs. 4.28 and 4.32 respectively, for the abundances given by Anders & Grevesse (1989).

chemisputtering is included (red lines). These latter temperatures are very close to each other, and are significantly lower (by about 200 K) than the condensation temperatures, $T_{\rm cond}$, obtained when only sublimation is considered. In fact, silicate destruction by chemisputtering is very efficient above $T_{\rm gas}$ ~1100 K (see also Fig. 4.2), also in agreement with other authors (Gail & Sedlmayr, 1999; Helling & Woitke, 2006; Gail, 2010). Note that this latter value refers to the *gas* temperature, and it is improperly referred by some authors as the condensation temperature of silicates, that, on the other hand, regards the *dust* temperature ($T_{\rm cond}$). The corresponding value of $T_{\rm cond}$ when chemisputtering is included can be significantly lower than the gas temperature, $T_{\rm cond}$ ~900 K.

In conclusion, the experimental measurements of the high activation energy required for chemisputtering reaction support a scenario in which this mechanism is completely inhibited in the conditions of pressure and temperatures characterizing the CSEs. A further support of this scenario, comes from the determination of the condensation temperatures of silicates, that are in agreement with the ones found in condensation experiments when chemisputtering is neglected and only sublimation is at work.

For these reasons, two classes of models are presented in the following sections. In the first one chemisputtering is included, as normally considered in the models of GS99 and FG06, in the second, chemisputtering is neglected, and only pure sublimation due to dust heating is taken into account.

5.1.5 M-star models with efficient chemisputtering

From the analysis of experimental results by Nagahara & Ozawa (1996), Gail & Sedlmayr (1999) concluded that the chemisputtering process should be fully efficient within the CSEs of TP-AGB stars. They have shown that, in this case, the destruction rate by chemisputtering is always much larger than that of sublimation, so that one can assume that $J_i^{\rm dec} = J_i^{\rm cs}$. The term $J_i^{\rm cs}$ is given by Eq. 4.84.

I thus assume that chemisputtering is fully efficient for the species that can react with hydrogen molecules. For the species that do not react with hydrogen molecules, such as iron, I consider only the sublimation rate.

In the following I will refer to this scheme as *low-condensation temperature (LCT) scheme*, because, as already pointed out in Section 5.1.4 the condensation temperature of silicates is lower than the one obtained by only including pure sublimation.

5.1.6 M-star models with inhibited chemisputtering

In this class of models chemisputtering is completely inhibited for silicates and sublimation is the only destruction process at work. For the computation of these models some approximations are needed.

First of all, in these models I neglect the chemisputtering process at any pressure (Kobayashi et al., 2011) on the basis of the discussion in Section 5.1.4. Thus, the evolution of the grain size is described by Eq. 2.19, with the destruction rate given only by the sublimation term, $J_i^{\rm dec} = J_i^{\rm sub}$, computed from Eq. 4.81.

Second, the condensation temperature found by this method for olivine is considered to be representative also for pyroxene, for which the condensation temperature computed is affected by uncertainties (Section 5.1.4).

Third, the sublimation rate depends on the dust equilibrium temperature $T_{\rm dust}$ (Eq. 4.83) which assumes that the medium is optically thin. In principle, one should take into account that, if different dust species form at different radial distances, Eq. 4.83 should hold only for that species which forms first because thereafter the medium might be no more optically thin. However, this approximation is applied only to the silicate dust, that is by far the most important opacity source in the CSEs of M-stars and for which it has been assumed that the condensation temperature is independent of composition (olivine or pyroxene).

Thus, instead of integrating the full Eq. 2.19, I first determine the condensation point within the CSE by comparing the growth rate with the maximum sublimation rate, i.e. the sublimation rate obtained by setting $\alpha_i = 1$ in Eq. 4.81. This point is defined by the condition $J_i^{\rm gr} = J_{i,\rm max}^{\rm dec}$ and provides also the condensation temperature. Beyond this point, I compute the evolution of the grain size by assuming that the sublimation process is negligible in the right-hand side of Eq. 2.19. In this way, the condensation temperature depends, on the one hand, on the dust species which determines $J_{i,\rm max}^{\rm dec}$ and, on the other, on the physical conditions of the CSE, which determine $J_i^{\rm gr}$. Since the real sublimation rate is only α_i times the maximum sublimation rate, the above condition implies that condensation begins when the growth rate is $\sim 1/\alpha_i$ (~10 for silicates) the real sublimation rate. The corresponding super-saturation ratio is also $\sim 1/\alpha_i$ (~10 for silicates). Considering also that, beyond the condensation point, the sublimation rate decreases almost exponentially with the temperature, retaining only the growth term in Eq. 2.19 does not affect the accuracy of the results. This method is similar to the procedure usually followed in the literature, but for the fact that, instead of assuming a fixed condensation temperature, I derive it from the comparison of the growth and destruction rates.

In the following I will refer to this scheme as *high-condensation temperature (HCT) models*.

5.2 C-stars CSE models

5.2.1 Low temperature models

For amorphous carbon, I take into account that its growth can initially proceed through complex reactions of C_2H_2 addition, forming isolated chains that subsequently coalesce into larger cores. Further growth of carbon mantles on these initial seeds can continue through vapor condensation (GS99). This homogeneous accretion is consistent with the microanalyses of pre-solar graphitic spherules extracted from meteorites, revealing the presence of nanocrystalline carbon cores consisting of randomly oriented graphene sheets, from PAH-sized units up to sheets 3-4 nm in diameter (Bernatowicz et al., 1996). According to Cherchneff et al. (1992), the chain of C_2H_2 addition reactions have a bottleneck in the formation of the benzene because it becomes effective only when the *gas* temperature is below $T_{\rm gas}$=1100 K. Therefore, while the sublimation temperature of solid carbon can exceed ~1600 K, its growth should be inhibited above $T_{\rm gas}$=1100 K. Thus, following FG06, I do not consider any destruction reaction in the case of amorphous carbon, but I assume that it can grow only when $T_{\rm gas} \leq 1100$ K.

In analogy to the case of M-star models with efficient chemisputtering, I will also refer to these C-star models as *low-condensation temperature (LCT) models*.

5.2.2 C-star models with modified condensation temperature

For the amorphous carbon I have already explained that the growth is not regulated by its sublimation temperature (~1500 K), but by the gas temperature window (900–1100 K) that allows an efficient chain of C_2H_2 addition reactions (Cherchneff et al., 1992). However, recent hydrodynamical investigations indicate that, during a pulsation cycle, gas that is initially at temperatures well above 1100 K, after being shocked may cool down and remain inside the effective temperature window long enough to enhance the rate of addition reactions (Cherchneff, 2011). In the detailed model of IRC+10216 this process allows the formation of amorphous carbon in inner regions of the CSE where the pre-shock gas temperature is significantly above the effective window, $T_{\rm gas}$ = 1300 K (Cherchneff, 2012). As a consequence, the growth rate of amorphous carbon can be significantly enhanced. To investigate the impact on the predicted ejecta of carbon dust, I explore the case of a higher temperature window, following the detailed results of Cherchneff (2012). In this case I simply assume that the amorphous carbon can condense below $T_{\rm gas}$ = 1300 K, which should set a fairly upper limit to the growth rate of amorphous carbon.

In the following I will refer to this scheme as *high-condensation temperature (HCT) models*.

5.3 Comparisons between selected models

5.3.1 M-stars

As already discussed in Chapter 2 the CSE structure, i.e. density, temperature and velocity profiles, is tightly coupled with the input parameters provided by the TP-AGB evolutionary models. In this section I compare some selected models for different choices of the input parameters (M_*, L_*, $\dot{M}$, $T_{\rm eff}$, $\epsilon_{\rm Si,ol-py}$) that change simultaneously during the TP-AGB phase. The models are selected in different phases along the TP-AGB track. The results are for both the LCT and the HCT models, and for M- and C-stars.

The input parameters of the selected models are summarized in Table 5.1 and are discussed below.

- *Model 1* (M1).
  This model is at the beginning of the TP-AGB of a star with an initial mass of 1.7 $M_\odot$ and Z = 0.02. Therefore, its stellar mass is close to its initial value. The low mass-loss rate is characteristic of this initial phase, as the highest mass-loss rates are typically reached during the final phase of the TP-AGB.

- *Model 2* (M2).
  With respect to M1, M2 is characterized by an intermediate value of the mass-loss rate. The actual stellar mass is slightly lower but it is still close to the starting value.

- *Model 3* (M3).
  This model is representative of the final phase of the TP-AGB of the same star. The actual stellar mass is only 40% of the initial stellar mass because almost all the stellar envelope has been ejected. The mass-loss rate is high as expected in these final stages. Note that the effective temperature of this model is higher than the ones in M1 and M2 because, at this stage, the star has already lost part of its envelope, showing regions at higher temperature.

The CSE structure of the above models (M1 to M3 from the left to the right) are shown in Fig. 5.4, 5.5 and 5.6.

In the three top panels of Fig. 5.4 I plot the condensation degrees of all the dust species that are formed in the CSE of M-stars. In the second row the contributions to the dust opacities due to the different dust species are illustrated. The opacity of each species is given by the product

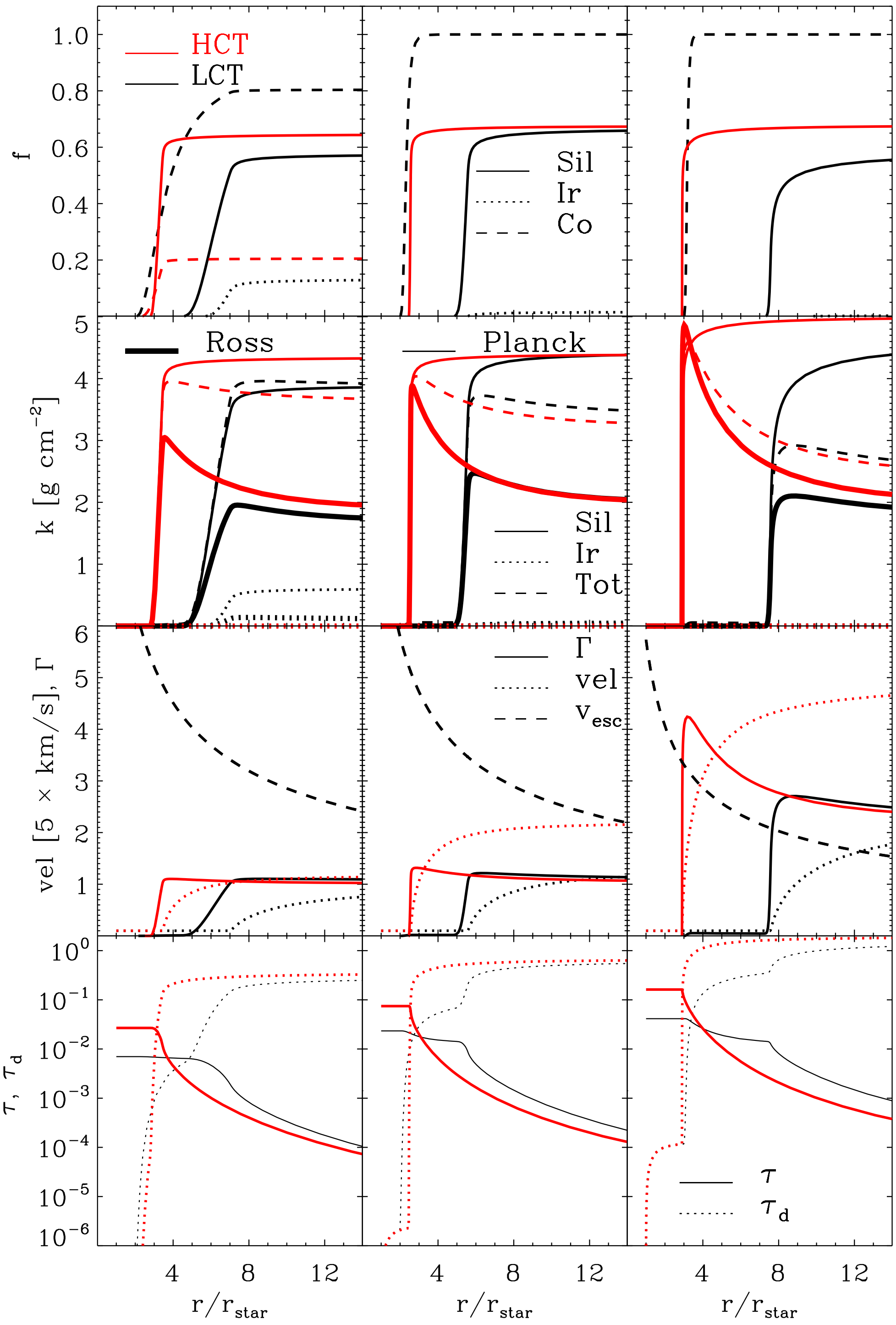

Figure 5.4: Some of the quantities characterizing M-star CSEs defined in Chapter 2 and 3 computed for the two different formalisms: HCT (red) and LCT (black). From left to right I consider from M1 to M3 listed in Table 5.1. *First row*: condensation fractions of the various dust species formed in M-star CSEs (Eq. 2.8). The different dust species are plotted with different linestyles specified in the plot. *Second row*: Rosseland (solid thick) and Planck (solid thin) opacities for the same dust species (Eqs. 3.23 and 3.22). The total average opacity for each model is computed according to Eq. 2.9 (dash-dotted). *Third row*: Γ (solid), expansion velocity (dotted) and escape velocity (dashed) profiles (Eqs. 2.3, 2.4 and 2.6). *Fourth row*: τ (solid) and τ_d (dotted) profiles (Eq. 2.15 and 2.10).

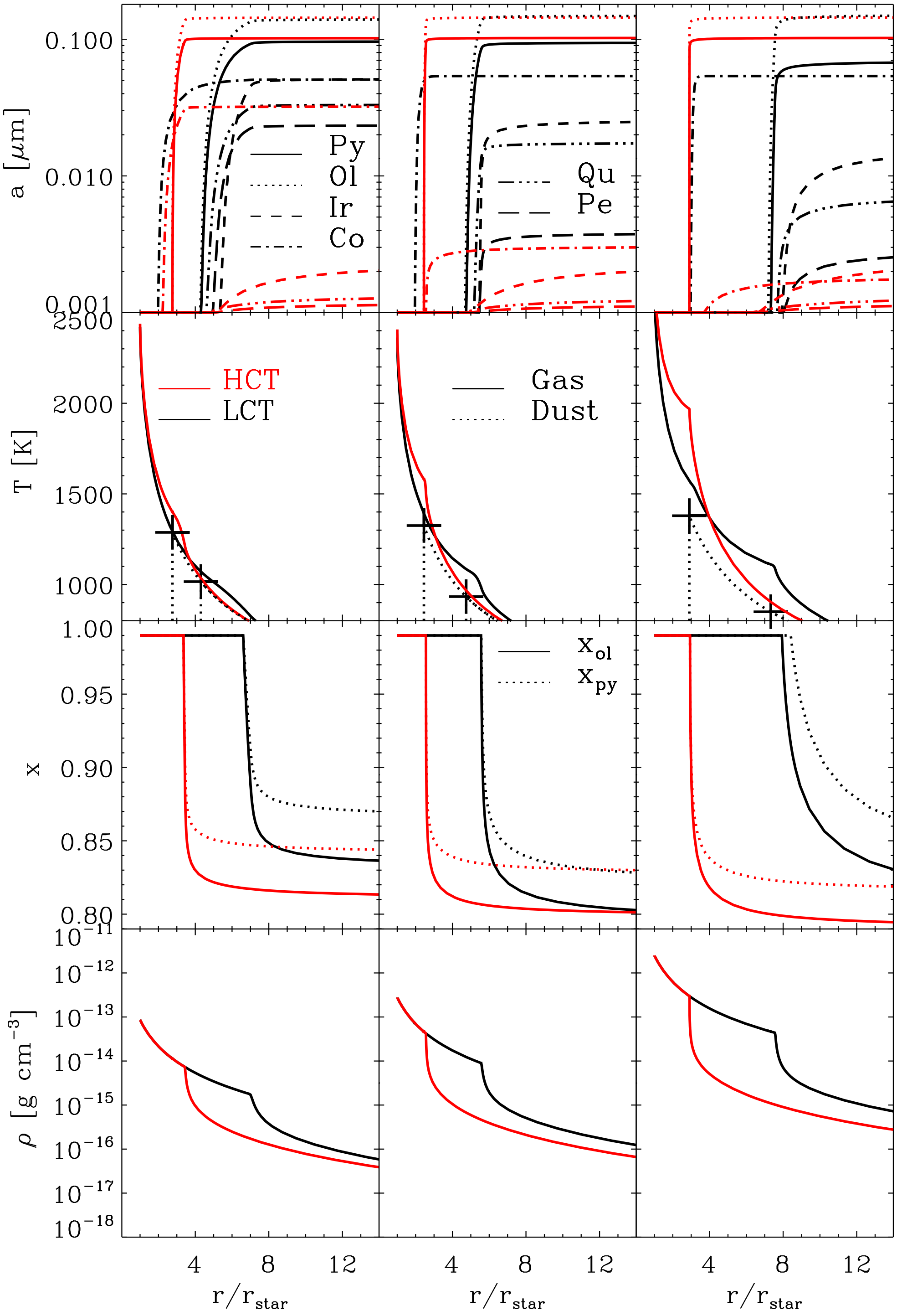

Figure 5.5: Some of the quantities characterizing M-star CSEs defined in Chapter 2 computed for the two different formalisms: HCT (red) and LCT (black). From left to right I consider from M1 to M3 listed in Table 5.1. *First row*: sizes of the various dust species formed in M-star CSEs (Eq. 2.19). The different dust species are plotted with different linestyles specified in the plot. *Second row*: gas (solid) and silicate dust (dotted) temperature profiles (Eq. 2.13 and 4.83). The condensation radii of silicates are indicated with a cross. *Third row*: variation of the fractional abundance of magnesium within olivine (solid) and pyroxene (dotted) (Eq. 2.22 and 2.23).

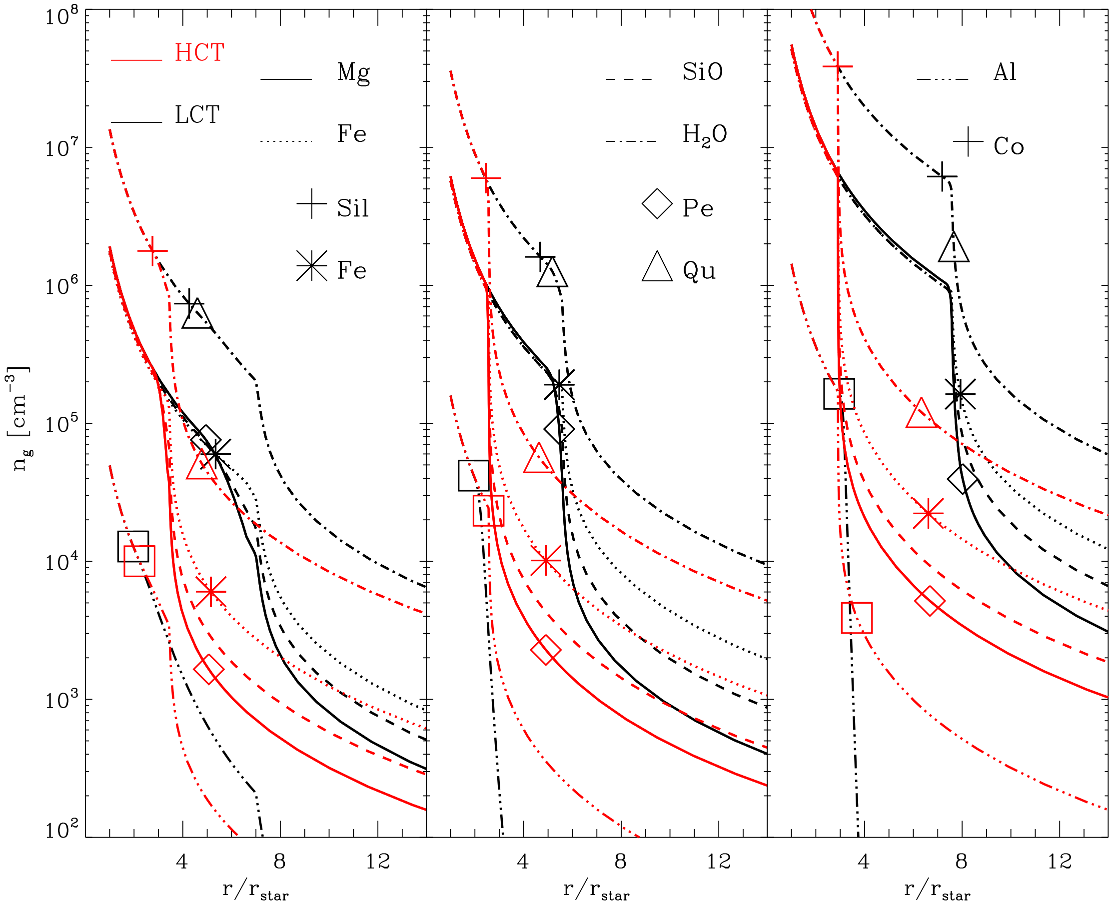

Figure 5.6: Number density profiles of the various molecules and atoms in the gas phase involved in the formation of the various dust species, listed in Table 2.1 (Eq. 2.21). Different colours are used for the two different schemes: HCT (red) and LCT (black). From left to right I plot from M1 to M3 listed in Table 5.1. The different gas species are plotted with different linestyles specified in the plot. The condensation radii of the different dust species are also indicated with different symbols.

Table 5.1: Input parameters M-stars CSE models.

Model	$M_{*,i}$ [$M_\odot$]	Z	M_* [$M_\odot$]	L_* [$L_\odot$]	$\dot{M}$ [$M_\odot$ yr^{-1}]	$T_{\rm eff}$ [K]	$\epsilon_{\rm Si,ol-py}$
1	1.7	0.02	1.62	5.9×10^3	4×10^{-7}	2900	5.1×10^{-5}
2	1.7	0.02	1.45	6.15×10^3	1.5×10^{-6}	2800	5.1×10^{-5}
3	1.7	0.02	0.63	7.65×10^3	10^{-5}	3100	5.1×10^{-5}

between its condensation fraction and its opacity computed as if all the available key-element is locked into that dust species. The opacities are plotted both for the Planck average (thin lines) and for the Rosseland one (thick lines). In the third row I plot the quantity Γ, the velocity profiles and the escape velocity, given by Eq. 2.6. In the fourth line the quantities τ and τ_d are shown.

In Fig. 5.5 I plot, for the same models, the radius of the different dust species (first row), the dust and gas temperatures profiles (second row), the variation of olivine and pyroxene compositions, $x_{\rm ol}$ and $x_{\rm py}$ (third row) and finally the density profiles (fourth row).

In Fig. 5.6 I show the number density profiles of the molecules and atoms needed to form the dust species. The condensation radii at which the various species form are indicated with different symbols. I remind that the condensation radius is defined, for each dust species, as the radius for which $da_i/dt = 0$, and depends on the destruction processes assumed to be at work.

From these figures I can sketch the following picture.

- *Condensation fractions*.
  In HCT scheme the only two relevant species able to condense are silicates for all the models listed in 5.1. The values of the condensation fractions, $\sim$ 60%, is the same for all the models. The silicate condensations show a rapid increase around 2-3 R_*. For M3 the condensation fraction of silicates obtained with the LCT scheme is lower than the ones obtained in M1 and M2. The reason why this happens is that in M3 the acceleration of the outflow is slighly higher than in the previous cases and, as a consequence, the density drops faster inhibiting the condensation.

  In LCT models, the bulk of the condensation for silicates occurs at larger radii ($\sim$7-8 R_*) than in the HCT models whereas corundum dust is able to condense already between $\sim$1-2 R_*. In agreement with the discussion in Chapter 4 this dust species is highly refractory and it is able to condense already around 1500 K (see Fig. 4.2).

- *Opacities*.
  In all models considered, the contribution to the total opacity of both HCT and LCT models, is essentially provided by silicates. Even for the case with a high condensation fraction of corundum, this dust species is too transparent to stellar radiation to provide an essential contribution to the total opacity.

  By construction the weighted opacities are between the Planck and Rosseland average.

  I remind that in Chapter 3 the Rosseland mean opacity is computed at the local gas temperature, which, at each radius, is given by Eq. 2.13. On the other hand, the Planck mean opacity is always computed at the stellar effective temperature, $T_{\rm eff}$.

  As shown in the plots, the Planck average, after the first strong rise, remains constant throughout the CSE, because the $T_{\rm eff}$ is fixed for a given TP-AGB model. On the other hand, the Rosseland opacity changes as a function of the distance from the photosphere because of the change in the local temperature.

  In the HCT scheme, the condensation fractions of silicates are almost the same in the different models, but the Rosseland mean opacity at the condensation radius increases from M1 to M3. The reason of this is that the gas temperature at the condensation radius increases from M1 to M3. The gas temperature at the condensation radius is plotted in the second row of Fig. 5.5, whereas the opacity as a function of the temperature is shown in Fig. 3.7.

In the LCT scheme, the situation is complicated by the slightly different condensation fractions and radii of the models and the differences between the Rosseland opacities from M1 to M3, are due to the combination of these two effects.

Within a single model, the differences between LCT and HCT for the Planck mean opacities are determined only by the different condensation fractions of silicates, as T_{eff} is fixed by the TP-AGB model considered. For the Rosseland mean opacity the most important difference between the LCT and HCT schemes is given by the different gas temperatures at the condensation radius. The latter value is much lower in the LCT case, as can be seen in the temperature profiles.

The weighted opacities tend to reach a maximum value when the silicates are formed, and then they decrease. In fact, the rapid formation of silicate dust increases the value of τ_d and, when it reaches values around 1, the opacity approaches the Rosseland average according to Eq. 2.9. This behaviour is particularly evident in M3 for the HCT case and it is due to the larger value (above 1) reached by τ_d, than in the other models considered.

The quantity τ_d is integrated, according to Eq. 2.10 from the condensation radius of the first species formed, outwards. As can be seen from this equation, τ_d is proportional to the density and to the opacity. As a consequence, this quantity increases as soon as the most opaque dust species are formed, and then tend to stabilize around a constant value.

For a fixed opacity, the higher the gas density at the condensation radius is, the higher will be the value of τ_d. As a consequence, within the same scheme (either LCT or HCT), and with comparable silicate condensation fractions, τ_d tends to increase from M1 to M3 because of the increasing values of the mass-loss rates (from $4{\times}10^{-7}$ to $\sim 10^{-5}$ $M_\odot$ yr^{-1}). The corresponding τ_d are, 0.25, 0.55 and 1.23, for the LCT case, and 0.33, 0.64 and 1.83, for the HCT one.

The values of τ_d reached in the HCT scheme tend to be slightly higher than those obtained adopting the LCT scheme. The integration in the two schemes starts almost at the same radius (and therefore density), as the condensation of corundum in the LCT scheme occurs almost at the same radius of silicates in the HCT one. However, in the former case the opacity of corundum dust is much lower with respect to the silicates one.

As the values of τ_d are similar in the LCT and HCT models, the corresponding opacities behave very similarly when silicates are condensed.

- *Wind dynamics*.
  The first general consideration regarding all the models is that, as the total opacity increases, Γ increases as well, as expected from Eq. 2.3, and the outflow is accelerated according to Eq. 2.4. As expected, the term Γ presents the same functional shape as κ on which it depends linearly according to Eq. 2.3.

  - Comparison between HCT and LCT models.
    In all the models considered, silicates condense at about the same radial distances that is around ~2-3 R_* for HCT models and ~7-8 R_* for LCT ones. The earlier condensation in HCT models directly affects the outflow velocity because of the r^{-2} dependence of the acceleration in Eq. 2.4.

    Condensation of silicate dust occurs at a distance that is a factor 2.5 less than when chemisputtering is included ($r \sim R_*$) and consequently the acceleration term is larger in HCT models, mainly because of the larger local acceleration of gravity in the inner regions. This produces final velocities in HCT models which are more than twice the terminal velocities reached in the LCT scheme.

  As a consequence of the larger acceleration in the HCT models, the expansion velocities reach the escape velocity closer to the stellar photosphere than in the corresponding LCT models.

  - Comparison between models at different evolutionary stages (from M1 to M3).
    Γ is proportional to the stellar luminosity, L_*, and inversely proportional to the current stellar mass, M_*. Therefore, it naturally follows that the quantity Γ tend to reach higher and higher values from M1 to M3, both for the effect of the higher opacity and because of the increasing value of the luminosity coupled with a decreasing value of the current stellar mass.

    Therefore, from M1 to M3, I find increasing expansion velocities.

    The escape velocity profiles show the behaviour, $v_{\rm esc} \propto r^{-1}$, but are systematically shifted toward lower escape velocities from M1 to M3. This is due to the fact that the escape velocity is proportional to the actual value of the stellar mass that in M3 is about half the value it has in M1.

    In all the models considered, the expansion velocity finally exceeds the escape velocity, but at different distances from the stellar atmosphere.

    M3 is the most favourable case for a dust-driven wind.

- *Densities*.
  The number density of molecules and atoms in the gas phase is particularly important because it directly affects the growth rate of the different dust species (see Chapter 4).

  The initial density increases from M1 to M3, according to the fact that this quantity is directly proportional to the mass-loss rate (Eq. 2.11), and I assume a constant initial velocity independent of the mass.

  The acceleration of the outflow affects the density profile of the CSE, as expected from Eq. 2.11. As can be seen from the plots in the fourth row of Fig. 5.5, the gas density first decreases with the radius according to the r^{-2} law and then it drops when the velocity increases.

  The number densities of the molecules and atoms in the gas phase decrease proportionally. The ability of different dust species to condense at different distances from the photosphere, combined with this drop of the density is what mostly determines the relative final condensation fractions of the various species. The further depletion of the molecules and atoms from the gas phase due to dust condensation is a secondary effect, as shown in Fig. 5.6.

  As a consequence, when a certain dust species is able to form, the number density of the molecules or atoms necessary to build it might be already too low if the wind acceleration has already occurred.

  In particular, because silicates form earlier in HCT models than in the LCT ones, dust species different from olivine and pyroxene cannot condense. On the other hand, in the LCT scheme, various dust species can form. For example, in M1, iron dust is able to condense partially. In the LCT scheme, as quartz forms from the same molecules (SiO and H_2O), its formation can be in competition with that of olivine and pyroxene. However, quartz finally condenses in negligible amounts because olivine and pyroxene condense at slightly higher temperatures, depleting the gas from these molecules. Analogously, periclase is not condensed because the species required for its formation (Mg and H_2O) are depleted from the gas phase because of the formation of silicates at higher temperature.

- *Temperature*.
  In the second row of Fig. 5.5 I plot the gas and dust temperature profiles for the HCT and LCT models from M1 to M3. The crosses denote the points where silicate dust starts to condense.

  In the LCT scheme dust condensation starts at a *gas* temperature of about $T_{\rm gas}$ ~1100 K, (see also Helling & Woitke, 2006) and in agreement with the condensation curves drawn in Fig. 4.2 (see also GS99). The corresponding dust condensation temperatures are between $T_{\rm cond} \sim 800$ K, in M3, and $T_{\rm cond} \sim 1000$ K, in M1. As already mentioned in Section 5.1.4 the condensation temperatures are generally lower than the gas temperatures.

  In the HCT formalism, for M3, silicate dust begins to condense at a dust temperature of $T_{\rm cond} \sim 1350$ K, well above the limit obtained with chemisputtering and in very good agreement with experimental determinations (Nagahara et al., 2009) (see Section 5.1.3). The corresponding gas temperature, $T_{\rm gas} \sim 2000$ K, is comparable with the one at which Nagahara & Ozawa (1996) performed their experiments. The corresponding gas pressure is relatively low, $P \sim 5 \times 10^{-2}$ dyne cm^{-2}, and falls in the regime where the decomposition rate measured by Nagahara & Ozawa (1996) is independent of the pressure (Section 5.1.2).

  For M1 in the HCT scheme the dust condensation temperature is $T_{\rm cond} \sim 1300$ K, whereas the correspondent gas temperature is around 1400 K. The correspondent total pressure is lower than in M3, $P \sim 7 \times 10^{-3}$ dyne cm^{-2}, again in the regime for which the decomposition rate can be considered as given by pure sublimation.

- *Compositional variation of silicates*.
  The variation of the fractional magnesium content of olivine and pyroxene is followed starting from an initial value of $x_{\rm ol} = x_{\rm py} = 0.99$, i.e. assuming that silicates are initially iron-free. This choice is made to investigate the possibility that some iron atoms can be included in initially iron-free silicate grains through cation-exchange processes or during the grain growth as expressed by Eqs. 4.108, for olivine, and 4.109, for pyroxene. This assumes that the chemical composition of silicates, initially iron-free, can be rearranged according to the energetics of the exchange reactions between magnesium atoms, on the grain surface, and iron atoms, in the gas phase, and according to the probability that a newly formed monomer of dust, through the accretion process, can contain iron atoms.

  For all the models considered, the value of $x_{\rm ol}$ and $x_{\rm py}$ stabilizes around a value of 0.8. These simulations show that a certain amount of iron can be included in the silicates, even if pure iron dust always condenses at temperatures lower than those of silicates. The percentage of iron atoms included is of the same order as the one observed (Tielens et al., 1998) and is in agreement with the adopted opacity data set (Ossenkopf et al., 1992).

  As I already discussed in Chapter 3, the inclusion of impurities in silicate dust grains has very important effects on the opacity and on the wind dynamics. In the light of the above results, it is worth noticing that in models that need only iron-free silicates (Höfner, 2009), the exchange and capture processes responsible for the inclusion of iron atoms have to be fully inhibited.

The inclusion of iron in silicate dust can inhibit the formation of iron dust that is, however, already limited by the effects induced by the wind dynamics as the outflow is usually accelerated before iron dust is formed.

- *Grain sizes*.
  The final grain sizes for the various dust species are determined by the initial abundances of the key-element in the gas phase, by the number of the seed nuclei and by the wind dynamics.

  Pyroxene and olivine are the dust species that reach the highest grain size dimensions, around 0.1 μm. The final grain sizes of pyroxene and olivine are almost independent of the scheme adopted (LCT or HCT).

  In the LCT scheme periclase and quartz dust grain are smaller than 0.02 μm, whereas iron size is between 0.04 and 0.01 from M1 to M3. These grain sizes correspond to negligible condensation fractions.

  In the HCT scheme the grain size of periclase, quartz and iron are always very small and their fraction is negligible.

In summary, in M-stars the bulk of condensation is made of silicate dust that provides most of the opacity needed to accelerate the outflow.

The condensation of silicate dust occurs at different distances from the atmosphere, according to the condensation scheme adopted (LCT or HCT). In spite of that, their condensation fractions and sizes are almost constant and do not greatly depend on the scheme adopted and on the variation of the various input parameters as the mass-loss rate, the luminosity, the effective temperature and the actual stellar mass that, on the other hand, affect the wind dynamics. The main reason why this happens, is that silicates are the only dust species able to accelerate the outflow and therefore the number densities of the atoms and molecules needed for their production do not drop significantly before their condensation. As soon as dust is formed, the opacity increases, the wind is triggered and then the density drops and the dust growth stops. This mechanism is “self-regulating” in such a way that the final condensation fraction reached by silicates is almost constant.

On the other hand, the condensation fractions of all the other dust species do depend on the underlying assumptions of the CSEs.

Also considering the different models, M1 M2 and M3, one sees that the condensation fraction of silicates does not change significantly. Indeed in the cases in which the formation of silicates initially proceeds at low rates, as in M1, silicate dust has a longer time available to grow. On the other hand, in the models in which the densities are higher (M2 and M3), the formation of silicates is very rapid but this immediately produces a drop in density that self regulates the dust growth.

An important result is that iron-free silicates are likely to modify their initial chemical composition with the inclusion of iron atoms. This follows from the combined effects of cation exchange reactions and direct formation of monomers with iron atoms. This has important consequences for the opacity of the silicates and for wind dynamics as it will be extensively discussed in Chapter 6.

5.3.2 C-stars

In analogy to M-stars, I select a few models of C-stars to study the relevant quantities of their CSEs. The input parameters of the selected models are summarized in Table 5.2.

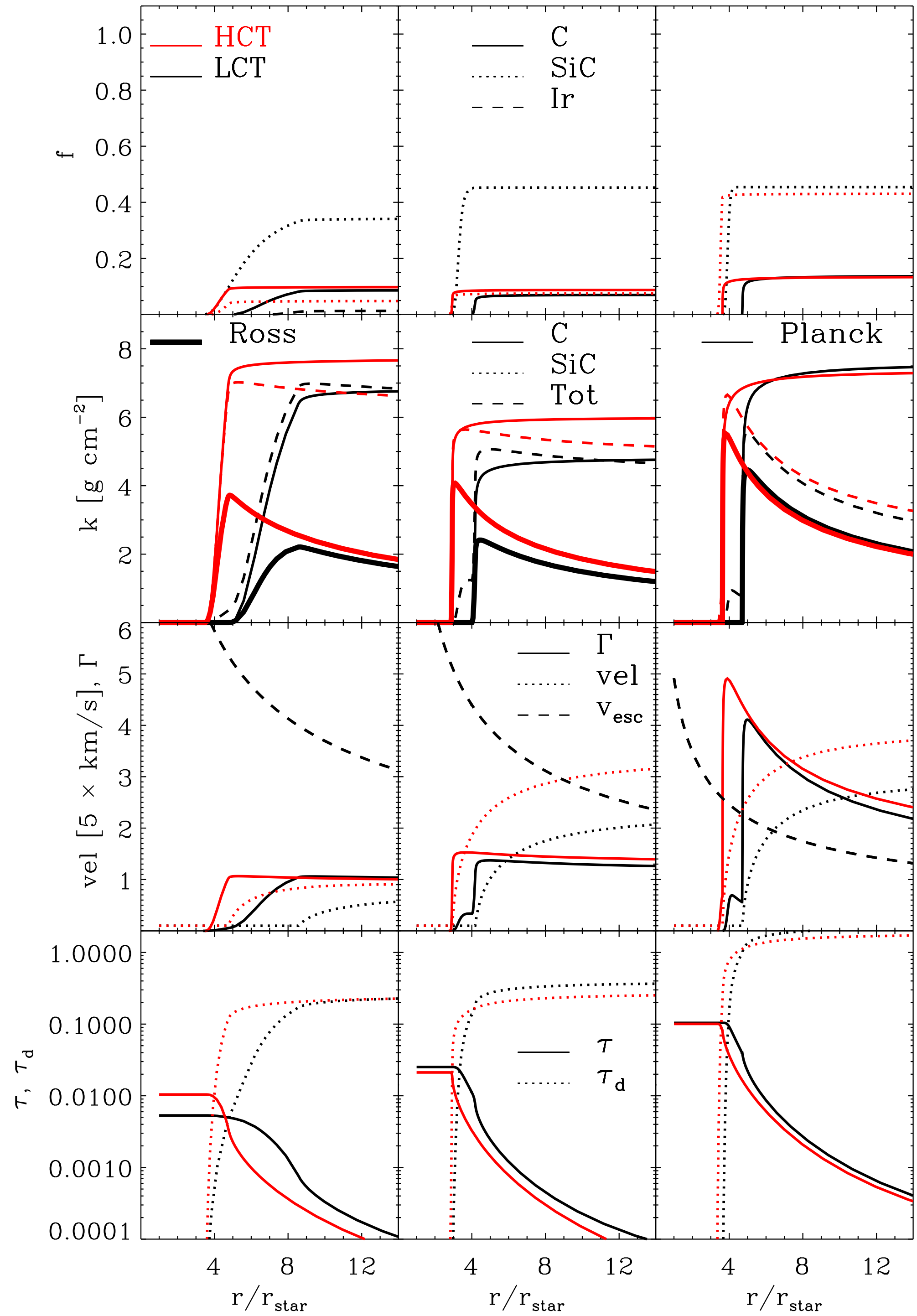

Figure 5.7: The same as in Fig. 5.4 but from M4 to M6, listed in Table 5.2.

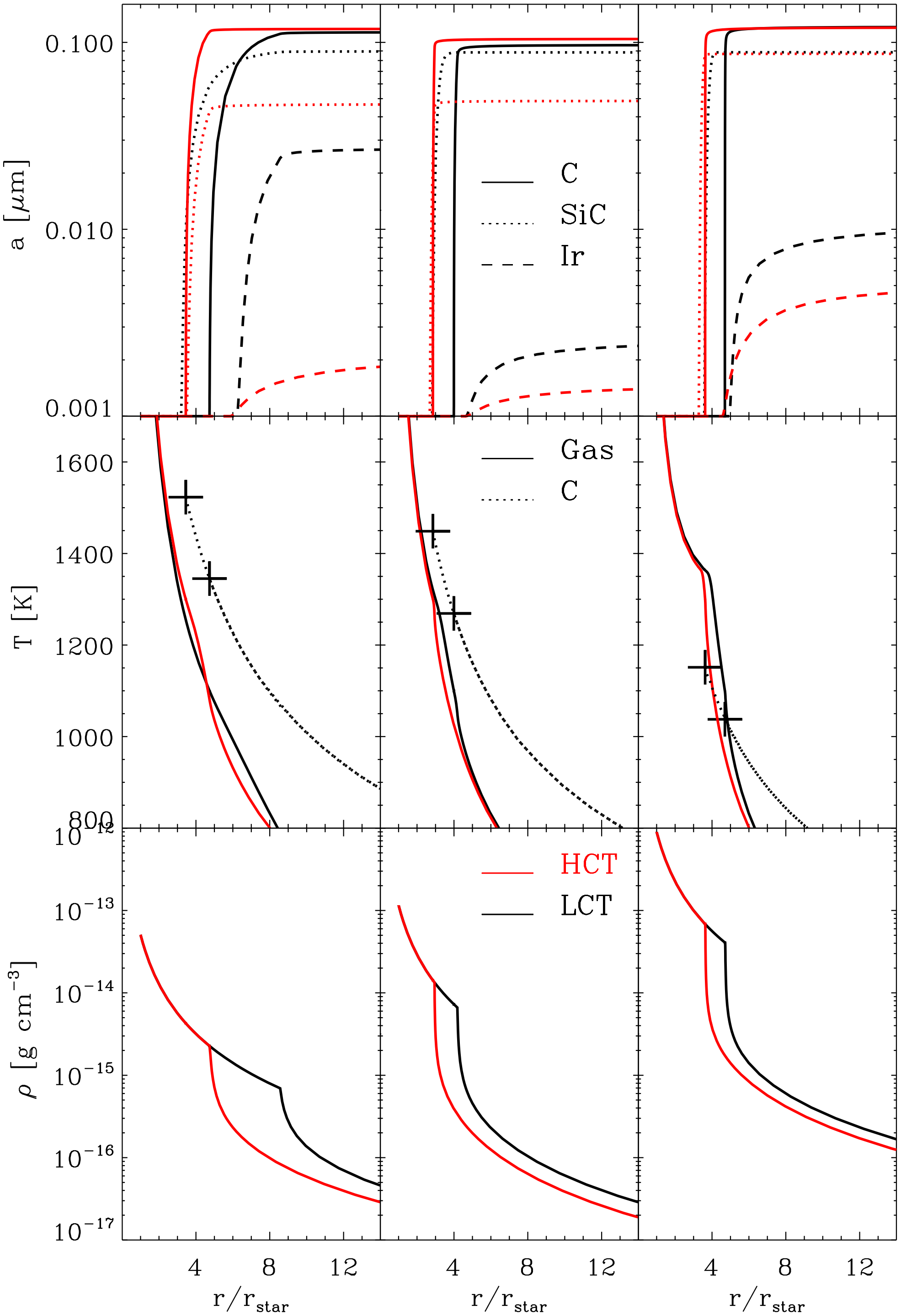

Figure 5.8: For the first two rows from the top: the same as in Fig. 5.5. For the third row: the same as the fourth row of Fig. 5.5. The models considered are from M4 to M6 in Table 5.2.

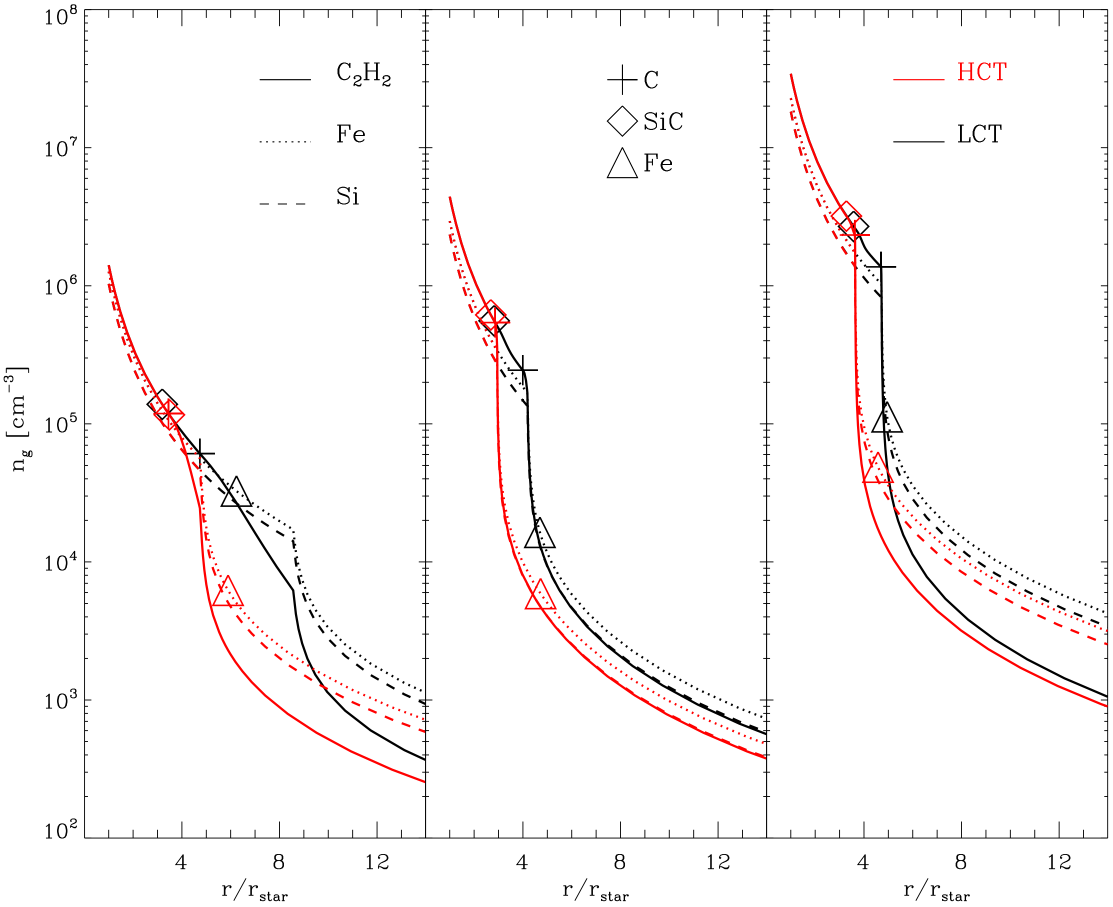

Figure 5.9: The same as in Fig. 5.4 but from M4 to M6, listed in Table 5.2.

Table 5.2: Input parameters C-stars CSE models.

Model	$M_{*,i}$ [$M_\odot$]	Z	M_* [$M_\odot$]	L_* [$L_\odot$]	$\dot{M}$ [$M_\odot$ yr^{-1}]	$T_{\rm eff}$ [K]	$(\epsilon_C - \epsilon_O)/\epsilon_C$	$(\epsilon_{Si} - \epsilon_S)/\epsilon_{Si}$
4	2	0.02	1.8	3.56×10^3	$\sim 10^{-7}$	~ 3100	0.46	0.15
5	2	0.02	1.7	5.905×10^3	$\sim 6 \times 10^{-7}$	~ 2800	0.45	0.19
6	2	0.02	0.76	7.29×10^3	$\sim 10^{-5}$	~ 2400	0.45	0.19

In Figs. 5.7, 5.8 and 5.9 I show the relevant quantities that characterize the CSE structure. In the mentioned figures, the plots refers to models from M4 to M6 from the left column to the right one.

The quantities plotted are the same as in M-stars: in Fig. 5.7 I plotted the condensation fractions in the first row, the opacities (second row), Γ, the expansion velocities and the escape velocities (third row) and τ, τ_d (fourth row).

In Fig. 5.8 I draw the grain sizes (first row), the dust and gas temperature profiles (second row) and the density profiles (third row).

Finally in Fig. 5.9 I plot the number densities of the molecules and atoms in the gas phase.

The models are representative of different phases along the TP-AGB tracks. The models have similar values of the carbon excess, as its variation would complicate even more the interpretation of the results.

They are briefly described in the following.

- *Model 4* (M4).
  This is a model at the beginning of the TP-AGB of a star of initial mass $M_* = 2\ \mathrm{M}_\odot$ and $Z = 0.02$. Therefore its stellar mass is close to its initial value. The low mass-loss rate is characteristic of this initial phase.

- *Model 5* (M5).
  With respect to M4, M5 is characterized by an intermediate value of the mass-loss rate. The actual stellar mass is lower than M4 but it is still close to the starting value.

- *Model 6* (M6).
  This model is representative of the final phase of the TP-AGB of the same star. The actual stellar mass is only 40% of the initial stellar mass because almost all the stellar envelope has been ejected. The mass-loss rate is high as expected in these final stages.

From these plots it is possible to get to the following conclusions in analogy with the previous discussion for M-stars.

- *Condensation fractions*.
  With the HCT formalism, carbon dust condenses closer to the star ($r \sim 3 - 4\ \mathrm{R}_*$) than the cases of LCT ($r \sim 4 - 5\ \mathrm{R}_*$).

  In M5 and M6, SiC shows the highest condensation fraction in both the HCT and LCT formalisms. M4 shows a similar behaviour in the LCT formalism, but, when the HCT formalism is adopted, amorphous carbon has the highest condensation fraction.

  I remind that, by definition, the condensation fraction of a given dust species is computed with respect to the initial abundance of the key-element, irrespective of being partially locked into gas molecules (Eq. 2.8).

  Therefore, the reason why the condensation fraction of SiC is usually higher than that of carbon, is that, in these models, most of the carbon atoms are locked into CO molecules, while the condensation of silicon carbide is computed with respect to the abundance of silicon. The condensation fraction of carbon is almost constant (~ 10%) from M4 to M6 and both in the HCT and LCT cases.

  The condensation fraction of SiC is instead variable. In particular, in HCT models its value is lower than in LCT models. This difference is due to the different wind dynamics in the two schemes which affects the number densities of the species in the gas phase. This will be extensively discussed in the Section dedicated to the density profiles.

- *Opacities*.

  In all the models considered, the opacity is essentially provided by carbon dust and therefore the outflow is accelerated when it is formed. This is due to the fact that even if the condensation fraction of carbon is lower than that of SiC, the former species is much more opaque than the latter.

  As discussed for M-stars, the Rosseland opacities shown for the different models, from M4 to M6, are shaped by the temperature at the condensation radius and also depend on the condensation fractions of carbon dust. The higher is the condensation temperature, the higher tends to be the Rosseland opacity, if the condensation fractions are kept fixed.

  As the effective temperature is constant within a single model, the differences between LCT and HCT in the Planck opacities for a given dust species are just due to the small variation in the condensation fractions. The differences in the Rosseland opacities between LCT and HCT schemes at the condensation radius are primarily due to the different gas local temperatures more than the differences in the condensation fractions. In fact, the two curves get closer when the local gas temperature becomes similar.

  The weighted opacities increase when amorphous carbon is formed and, when τ_d reach values around 1, the opacities tend to approach the Rosseland mean (Eq. 2.9). The value of τ_d is higher when condensation happens in regions of higher ρ. In M6 and with the HCT formalism, this characteristic trend of the opacity is particularly pronounced: after a peak the opacity decreases. The sudden increase in the opacity caused by the carbon formation, in fact, is followed by an increase of τ_d that reaches values that are higher than those of all the other models.

  In M5 and M6 the values of τ_d reached in the LCT scheme, encompass the ones reached in the HCT case. This can be explained by the higher contribution by SiC dust in the former class of models than in the latter. In fact, in the HCT case the condensed fraction of SiC is highly reduced.

  Moreover, from M4 to M6 the values reached by τ_d are higher because of the larger gas densities at the condensation radius due to the increasing value of the mass-loss rate.

  From M4 to M6 the values of τ_d are 0.37 , 0.51 and 2.18, for the LCT, and 0.25, 0.35 and 1.71 for the HCT.

  Once carbon dust is formed, the opacity shows similar behaviour in HCT and LCT schemes. In fact, in both formalisms, the models reach very similar condensation fractions and, consequently, τ_d.

- *Wind dynamics*.

  The comparison between the models obtained assuming the HCT or the LCT schemes shows that in the former case the outflow velocities are higher. Since Γ reaches comparable values in the two cases, it is possible to conclude that the difference in the velocity profiles is mainly due to the higher local acceleration of gravity in the inner regions, according to Eq. 2.4.

  Similarly to the M-stars models, from M4 to M6 Γ increases because of the combined effects of larger values of the opacity κ and of the decreasing values of the current stellar mass, coupled with higher luminosities (see Eq. 2.3).

  At the same time, the variation of the input parameters during the TP-AGB phase, has the effect of decreasing systematically the curves of the escape velocities from M4 to M6 according to Eq. 2.6.

From M4 to M6, for both formalisms, the outflows are finally accelerated up to expansion velocities that exceed the correspondent escape velocities. In particular, the most favourable case of an efficient dust-driven wind is M6.

- *Densities*.
  The density profiles behave as expected from Eq. 2.11. After the initial r^{-2} they suddenly drop as a consequence of the outflow acceleration.

  The number densities of the molecules and atoms in the gas phase decrease proportionally. This drop affects the final condensation degrees of the various dust species according to their condensation radii.

  In LCT models carbon dust condenses after SiC and the number density of C_2H_2 and of silicon atoms remain high for long enough to form SiC. On the other hand, in the HCT models the condensation of SiC occurs after the acceleration of the outflow, preventing SiC from condensing in large fractions. The gap in the condensation fractions of SiC between HCT and LCT is particularly exacerbated for low mass-loss rates. In the HCT model, the condensation fraction of SiC in M4 is lower than the ones obtained in M5 and M6 because of the lower number densities of silicon atoms and C_2H_2. Finally, iron dust is never formed because it condenses when the number density of iron atoms is already much lower than the initial one.

- *Temperature*.
  In C-stars carbon dust reaches temperatures higher than the gas ones because of the high absorption capacity of carbon grains. However, the maximum dust temperature reached by carbon grains after the condensation radius is always below its sublimation temperature that is about 1500 K.

- *Grain sizes*.
  The highest value of the grain sizes is reached by amorphous carbon both in LCT and HCT schemes and has the same value from M4 to M6 around 0.1 μm.

  In the LCT scheme, the size of SiC dust is constant from M4 to M6 and its value is around 0.1 μm. In the HCT scheme SiC grain sizes are generally smaller than those obtained adopting the LCT scheme. In the former formalism, in fact, the wind accelerates just before SiC can form. The only exception in HCT models is for M6 in which SiC dust is formed just before carbon dust (and therefore wind acceleration).

  Carbon dust has larger grain sizes than SiC, but the condensation fraction of SiC is larger than the carbon one. The low condensation fraction of carbon is due to the fact that the key-element of carbon dust is C that is mostly condensed into CO molecules and the fraction of carbon initially available is only $(\epsilon_C - \epsilon_O)/\epsilon_C$. On the other hand, the key-element of SiC is silicon and therefore the fraction of silicon available is higher, $(\epsilon_{Si} - \epsilon_S)/\epsilon_{Si}$. The values are shown in Table 5.2

  Finally, the grain sizes reached by iron dust grains change from model to model and are different in LCT and HCT formalisms within the same model. This again is an effect of the wind dynamics.

In conclusion, in C-stars the carbon condensation fraction depends on the available carbon not locked into CO molecules. In the cases investigated, its condensation fraction is usually below the one of SiC.

However, carbon dust is the species that provides the needed opacity to accelerate the outflow.

The different temperatures assumed in the HCT and LCT schemes naturally imply that the carbon condensation radii are different in the two classes of models. In LCT models the typical condensation radius for carbon dust is between 4-5 R_*, whereas for HCT computations it is between 3-4 R_*. The different choice of the condensation temperature affects the wind dynamics (larger expansion velocities) and the condensation fractions of SiC and iron dust.

As previously noticed for M-stars, the condensation fractions and sizes for carbon dust are almost constant also for the different schemes adopted and it is always around 0.1 μm.

Finally I remark that, for C-stars, the HCT scheme has been included only to test the possible effects of a higher gas condensation temperature and it will not be assumed as the preferred dust formation scheme.

Chapter 6

AGB dust formation from low to solar metallicity

With the formalism outlined in Chapter 5 I follow the growth and evolution of dust in the CSEs of selected evolutionary TP-AGB tracks, extracted from the set of Marigo et al. (2013). This chapter is based on the paper by Nanni et al. (2013).

I consider three values of the initial metallicity, $Z = 0.001, 0.008, 0.02$, which are representative of low, intermediate and solar metallicity, respectively, and a few selected values of the initial stellar mass, between 1 $M_\odot$ and 6 $M_\odot$, as listed in Table 6.4.

I exclude from the calculations the models for mass-loss rates below 10^{-8} $M_\odot$ yr^{-1}, because dust formation is already negligible at those values (FG06).

The opacities adopted are listed in Table 6.1 and are computed as described in Chapter 3. For some dust species I use the fitting formula provided by GS99 (indicated as “fit” in the table). I remind that these species are very transparent to the stellar radiation and condensed in very low fractions (see Chapter 5) and therefore do not affect the wind dynamics. The references are also shown in the table.

The properties of dust adopted in the computations of dust growth and variation in the chemistry of silicates (Eqs. 2.19, 4.108 and 4.109), i.e. the mass number, A_i, the dust density, $\rho_{d,i}$, the sticking coefficients, α_i, and the cation exchange coefficients, $\alpha_{\mathrm{ex},i}$, are are specified in Table 6.2.

Table 6.1: Data for the opacity and dust temperature calculations.

species	opacity
M-stars	
olivine	O-rich (Ossenkopf et al., 1992)
pyroxene	O-rich (Ossenkopf et al., 1992)
iron	(Leksina & Penkina, 1967)
periclase	GS99 (fit)
quartz	GS99 (fit)
corundum	(Begemann et al., 1997)
C-stars	
carbon	(Hanner, 1988)
SiC	(Pégourié, 1988)

Table 6.2: Data used in the calculation of growth and vaporization rates A and $\rho_{d,i}$ are taken from Lide (1995).

species	A_i	$\rho_{d,i}$	α_i	$\alpha_{\mathrm{ex},i}$
M-stars				
corundum	101.961	3.97	1.0 (Nanni et al., 2013)	
iron	55.845	7.87	1.0 (Landolt-Börnstein, 1968)	
quartz	60.085	2.196	0.01 (Landolt-Börnstein, 1968), 0.1 (FG06)	
olivine	172.23	3.75	0.1 [LCT] (Nagahara & Ozawa, 1996), 0.1-0.2 [HCT]	0.06 (GS99,FG06)
pyroxene	116.16	3.58	0.1 [LCT] (FG06), 0.1-0.2 [HCT]	0.06 (FG06)
periclase	40.304	3.6	0.2 (FG06)	
C-stars				
carbon	12.011	2.2	1.0 (FG06)	
SiC	40.097	3.16	1.0 (Råback, 1999)	

Table 6.3: Data for the opacity and condensation temperature calculations for the LCT and HCT schemes in M-stars.

ϵ_s	10^{-13}	Eq. 4.58, Ch. 4
v_0 [km s^{-1}]	0.5	Eq. 2.4, Ch. 2
x_g	3.5 [LCT], 0.1 [HCT]	Eq. 3.16, Ch. 3
a_{min} [μm]	0.005	Ch. 3
a_{max} [μm]	0.25 [LCT], 0.18 [HCT]	Ch. 3
a_0 [μm]	10^{-3}	Eq. 2.19, Ch. 2
x_{ol}	0.99	Eq. 2.22, Ch. 2
x_{py}	0.99	Eq. 2.23, Ch. 2

The values of the sticking coefficients are taken from laboratory measurements, when available, or theoretical computations. For some of the dust species considered it is not possible to rely on experimental measurements of the sticking coefficient and some assumption are needed. For pyroxene I adopt the same value as that used for olivine. For corundum the maximum possible value, i.e. $\alpha_{\rm co} = 1$ was chosen. Finally, for amorphous carbon the usual assumption is to adopt $\alpha_{\rm C} = 1$ because, once the C_2H_2 addition reactions are activated, the gas temperature $T_{\rm gas} \sim 1100$ K is so much below the typical sublimation temperature ~ 1600 K of carbon, that the latter is supposed to grow at the maximum efficiency (Gail & Sedlmayr, 1988; Cherchneff et al., 1992; Krueger et al., 1996). I thus adopt the standard assumption $\alpha_{\rm C} = 1$, but I also check the effects of adopting a lower sticking coefficient $\alpha_{\rm C} = 0.5$ and $\alpha_{\rm C} = 0.1$. All the references are also indicated in the table.

Finally the initial data, i.e. initial velocity, v_0, abundance of seeds ϵ_s, slope of the grain size distribution x_g, minimum and maximum grain dimension, $a_{\rm min}$ and $a_{\rm max}$, initial grain size, a_0, and the fractions of magnesium over magnesium plus iron atoms, $x_{\rm ol}$ and $x_{\rm py}$, are provided in Table 6.3. For these latter quantities I also recall the corresponding equations and chapters ("Ch." in the table) in which they are first mentioned. Different assumptions have been made for the two schemes (LCT or HCT). In the LCT case, the values adopted are the same as in FG06, Ventura et al. (2012a) and Ventura et al. (2012b). This choice allows a comparison with the results of these authors, in which the standard LCT scheme is adopted. In the HCT case, I assume an almost flat grain size distribution, in a range more suitable for the typical final sizes obtained in the computations, that predict a maximum grain size of about 0.15 μm.

6.1 Expansion velocities

A straightforward quantity predicted by these models is the terminal velocity of the expanding envelope. that can be compared with the observed values. Contrary to more sophisticated hydrodynamical models, the presented model does not provide the mass-loss rate, which must be assumed. The meaning of this comparison is thus to check whether, given the stellar parameters and the corresponding mass-loss rates, the model is able to reproduce the terminal velocities of the wind, over the entire range of observational data.

6.1.1 M-stars

For Galactic M-type TP-AGB stars the comparison is shown in Fig. 6.1. Mass-loss rates and expansion velocities are taken from Loup et al. (1993) (black triangles), González Delgado et al. (2003) (black pentagons) and Schöier et al. (2013) (black squares). Data from Loup et al. (1993) and Schöier et al. (2013) are derived from observations of ^{12}CO and HCN rotational transitions, whereas González Delgado et al. (2003) obtained their values from the interpretation of SiO rotational transition lines. The mass-loss rates range from $\sim 10^{-7}$ $M_\odot yr^{-1}$ to a few 10^{-5} $M_\odot yr^{-1}$, including also dust-enshrouded TP-AGB stars, while the wind velocities range from a few km s^{-1} to 20 km s^{-1}. For the models I adopt an initial metallicity $Z = 0.02$, assumed to be typical of the solar environment (Lambert et al., 1986). I remind that, though the current solar metallicity is estimated to be $Z_\odot \approx 0.0154$ (Caffau et al., 2011) and its derived initial metallicity is $Z_\odot \approx 0.017$ (Bressan et al., 2012), Lambert et al. (1986) compared their observations with model atmospheres based on the old (Lambert, 1978) solar abundances for which $Z_\odot \approx 0.021$. In Fig. 6.1, as well as in Figs. from 6.2 to 6.4 where I compare predictions with observations, the evolutionary tracks of TP-AGB stars of various masses are represented with a discrete number of points, selected from a randomly generated uniform distribution of

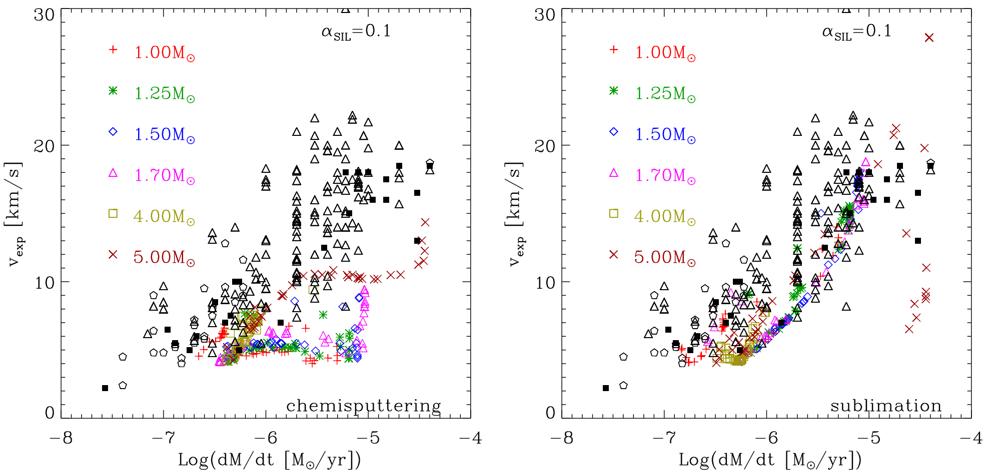

Figure 6.1: Expansion velocities of circumstellar outflows against mass-loss rates of variable M-stars. Observations of Galactic M-stars by Loup et al. (1993) (black triangles), González Delgado et al. (2003) (black pentagons) and Schöier et al. (2013) (black squares) are compared with predicted expansion velocities for a few selected TP-AGB tracks with Z = 0.02 for the values of initial stellar masses listed in upper left of each figure. *Left panel*: comparison with simulations that assume fully efficient chemisputtering. *Right panel*: comparison with HCT models.

ages that samples the entire TP-AGB phase of each star. The number of points is not set equal to the total number of observed objects because the aim of this comparison is only to highlight the regions where TP-AGB stars are expected to spend most of their evolutionary time, and not that of performing a population synthesis analysis. This latter investigation would require the convolution with the initial mass function and the star formation rate, which is beyond the goal of this thesis.

In the left panel of Fig. 6.1 I compare the data with the results obtained from adopting the LCT scheme while, in the right panel, I adopted the HCT scheme (see Chapter 5). From this comparison, it immediately follows that the models with efficient chemisputtering cannot reproduce the observed velocities. Indeed, the predicted velocities never exceed 10 km s^{-1}, and, after an initial rise, they saturate or even decrease at increasing mass-loss rate, failing to reproduce the observed trend. This long-standing discrepancy has challenged many theoretical investigations (Ireland & Scholz, 2006; Woitke, 2006, e.g.). As also discussed by FG06 this problem is largely insensitive to the adopted opacities. Indeed, even using different opacity data set, (Jones & Merrill, 1976; Ossenkopf et al., 1992; Dorschner et al., 1995) I cannot reproduce the observed relation.

Recently a solution to this discrepancy has been advanced by Höfner (2008a). In this model the condensation temperature of silicates is fixed, $T_{\rm cond} = 1000$ K, which implies that dirty silicates condense at about $r \sim 5$ R$_*$. In this case, the acceleration term (Eq. 2.2) is not large enough to reproduce the observed expansion velocities. The solution adopted to overcome this impasse is to assume that large iron-free silicates are produced. Indeed, as already discussed in Chapter 3, at the typical wavelengths at which stellar emission peaks, iron-free silicate grains are characterized by lower absorption efficiency than dirty silicate ones. This implies that, at a given distance from the photosphere, the former species reaches lower equilibrium temperature, $T_{\rm dust}$, than the latter, and thus iron-free dust grains become thermally stable in inner regions of the CSE ($r \sim 2$ R$_*$). However, the opacity of iron-free silicates becomes comparable to the

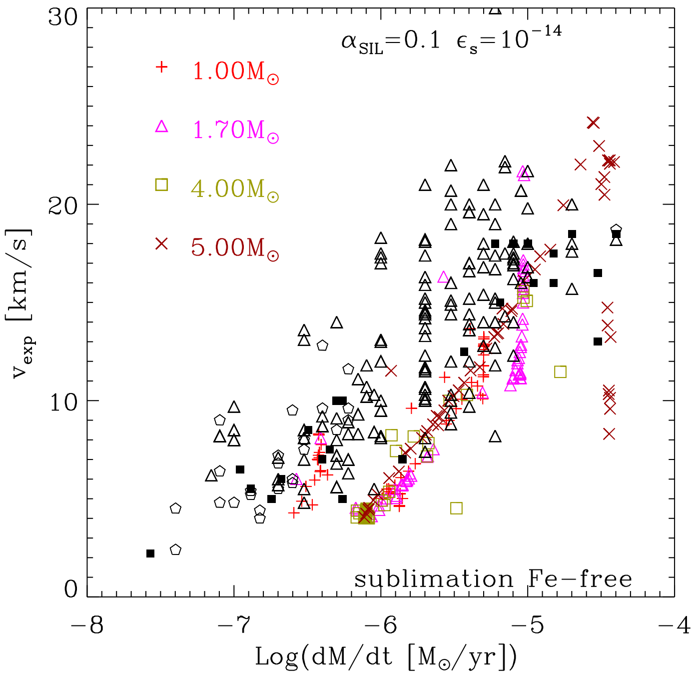

Figure 6.2: The same as in Fig. 6.1, but using HCT models and large iron-free grains (~0.3 μm) obtained by decreasing the number of seeds to $\epsilon_s = 10^{-14}$.

dirty silicates ones for grain sizes above 0.1 μm. In particular, in Höfner (2008a) the grain size needed to produce the opacity required to accelerate the outflow is ~ 0.3 μm (Bladh et al., 2013). A high sticking coefficient ($\alpha_{sil} = 1$) is also assumed in this model.

An alternative explanation of the discrepancy between observed and predicted terminal velocities is naturally provided by the HCT scheme, as can be seen in the right panel of Fig. 6.1. With a higher condensation temperature for silicates, dust formation can take place in inner regions of the CSE, where the acceleration term is larger, without the need of assuming that only iron-free grains are formed. The observed trend of velocity with mass-loss rate is now satisfactorily reproduced, with the predicted values only slightly lower than observations. In order to further improve the comparison, other important input parameters could be varied such as, the average dust size and the sticking coefficients. Moreover, the computations performed in Chapter 5 indicate that iron can be included in silicates and therefore it is reasonable to adopt the dirty silicates opacities.

In order to investigate the effects of adopting large grains in the HCT scheme, I compute a few models decreasing the number of seeds to $\epsilon_s = 10^{-14}$ for which the final grain size is around 0.3 μm. In these runs I adopt opacities suitable for iron-free silicates (forsterite and enstatite) taken from Jäger et al. (2003). With a lower number of seeds I obtain grain sizes larger than ~ 0.3 μm. The models are plotted in Fig. 6.2. The comparison with the observed velocities is clearly improved with respect to the results shown in the right panel of Fig. 6.1.

The effects of changing only the sticking coefficient are shown in Fig. 6.3. Here I use HCT models with standard sizes and opacity but with a modest variation of the sticking coefficient, from 0.1 to 0.2. This variation is reasonable given that the sticking coefficients for circumstellar conditions are not experimentally well constrained (Nagahara et al., 2009). The agreement with the data is also good, indicating that with a larger condensation temperature it may not be necessary to invoke iron-free grains.

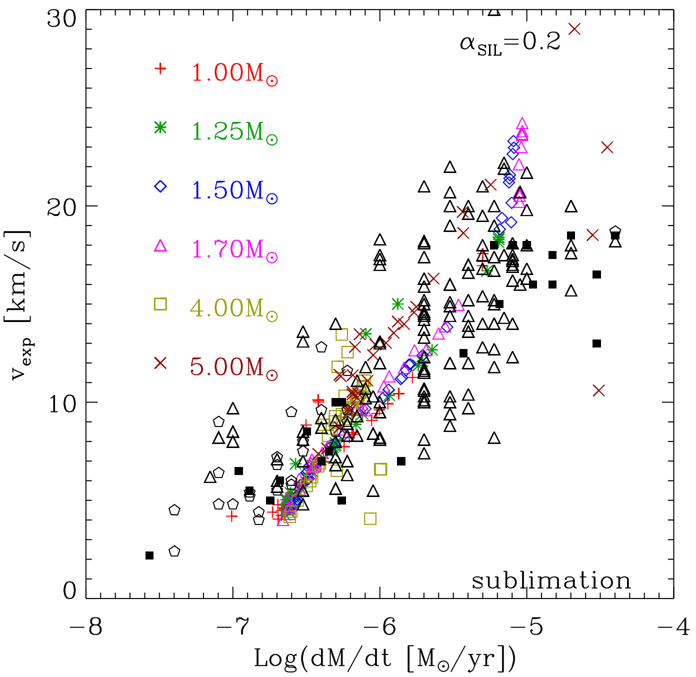

Figure 6.3: The same as in Fig. 6.1, but using HCT models and a sticking coefficient of silicates of 0.2.

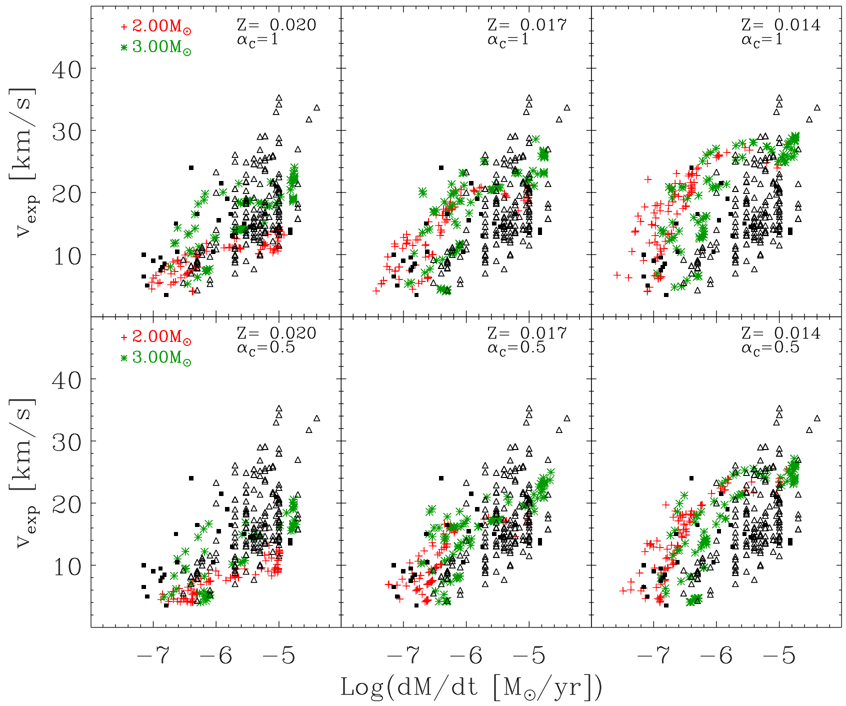

Figure 6.4: Expansion velocities of circumstellar outflows against mass-loss rates of variable C-stars. Observations of Galactic C-stars by Loup et al. (1993) (black triangles) and Schöier et al. (2013) (black squares) are compared with predicted expansion velocities for a few selected TP-AGB tracks of different initial metallicity, Z = 0.02, Z = 0.017 and Z = 0.014. The adopted sticking coefficient of amorphous carbon dust is specified in each panel.

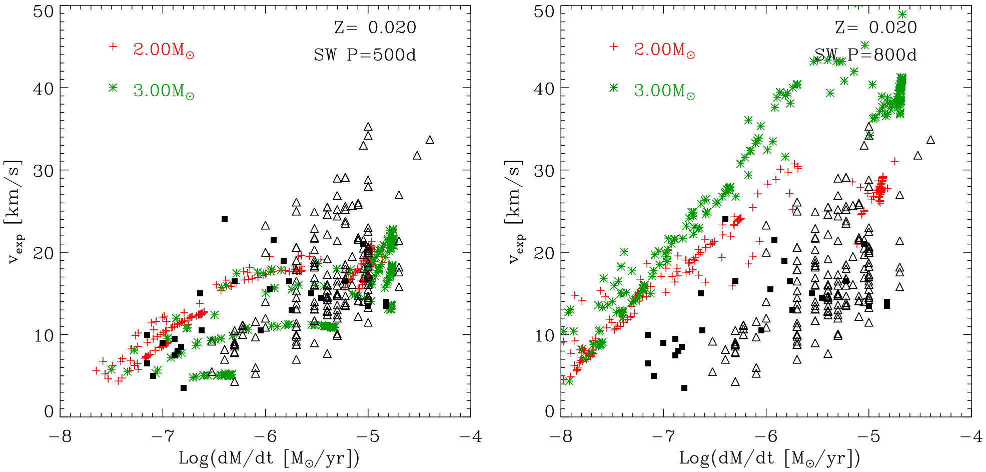

Figure 6.5: Impact of different laws of mass-loss rate on the expansion velocities of CSEs of C-stars. Observations of Galactic C-stars by Loup et al. (1993) (black triangles) and Schöier et al. (2013) (black squares) are compared with those predicted by models of $Z = 0.02$ for two other different mass-loss rate recipes. *Left panel*: the Vassiliadis & Wood (1993) mass-loss law in its original formulation. *Right panel*: the Vassiliadis & Wood (1993) mass-loss law but delaying the onset of the super-wind to a pulsation period $P = 800$ days (Kamath et al., 2011).

6.1.2 C-stars

The comparison with C-stars is shown in Fig. 6.4. Observed terminal velocities and mass-loss rates of Galactic C-giants are taken from Loup et al. (1993) (black triangles) and Schöier et al. (2013) (filled black squares). The observed velocities range from a few km s^{-1} to about 35 km s^{-1} for mass-loss rates between $\sim 10^{-7}$ M$_\odot$yr^{-1} and $\sim 10^{-5}$ M$_\odot$yr^{-1}. The results obtained by adopting the LCT scheme of C-stars with initial mass between 2 M$_\odot$ and 3 M$_\odot$, $Z = 0.02$, and sticking coefficient of amorphous carbon $\alpha_C = 1$ (top left panel) reproduce fairly well the observed diagram. This result is already known because the opacity of amorphous carbon is by far larger than that of silicate dust (Chapter 3).

The other two upper panels in Fig. 6.4 show the effects of lowering the initial metallicity from $Z = 0.02$ to $Z = 0.017$ and to $Z = 0.014$. At a given mass-loss rate, the predicted terminal velocities increase at decreasing metallicity and while for $Z = 0.02$ the models perform fairly well, at lower metallicity there is a tendency to run above the region occupied by the bulk of the data.

In particular, for $Z = 0.014$ many models fall in a region with detectable mass-loss rates but with velocities significantly higher than observed. This effect can be explained by considering that, as shown in Figs. 1.6, 1.7 and 1.8, at decreasing metallicity C-stars of the same mass not only reach a higher C/O ratio, but also a larger carbon excess, ϵ_C-ϵ_O. Indeed, for the metallicities considered in Fig. 6.4, the maximum C/O attained in the models of 2 M$_\odot$ and 3 M$_\odot$ are C/O = 1.24 and 1.46 for $Z = 0.02$, C/O = 1.52 and 1.70 for $Z = 0.017$, C/O = 1.95 and 2.06 for $Z = 0.014$, while the maximum carbon excess is 1.92×10^{-4} and 3.52×10^{-4} for $Z = 0.02$, 3.63×10^{-4} and 4.57×10^{-4} for $Z = 0.017$ and 5.39×10^{-4} and 5.58×10^{-4} for $Z = 0.014$, respectively. With a larger carbon excess, the amount of amorphous carbon that can be produced in the adopted scheme is also larger and the wind experiences a higher acceleration. To see how this result depends on the adopted value of the sticking coefficient of the amorphous carbon I have recomputed the above dust evolution sequences with both

$\alpha_C = 0.5$ and $\alpha_C = 0.1$. With the latter value I could not reproduce realistic expansion velocities in the range of C/O ratios expected to accelerate the outflow (Mattsson et al., 2008, 2010). With the intermediate value $\alpha_C = 0.5$ one can still get a good agreement with the data, as shown by the lower panels of Fig. 6.4. With $\alpha_C = 0.5$ the best agreement between data and simulations is achieved for $Z = 0.017$ and, as in the case with sticking coefficient $\alpha_C = 1$, $Z = 0.014$ seems to be a too low metallicity for the Galactic C-stars. Clearly, there is a degeneracy between the carbon excess and the sticking coefficient, so that I expect that even for $Z = 0.014$ there will be a value of the sticking coefficient, $0.1 < \alpha_C < 0.5$, that is able to reproduce the observed data. Nevertheless, given that a metallicity between $Z = 0.02$ and $Z = 0.017$ is fairly representative of the possible values for C-stars of the Galactic disk and in absence of more accurate experimental determinations, I consider $0.5 \leq \alpha_C \leq 1$ the most plausible range for the sticking coefficient of amorphous carbon.

It is also interesting to see the effects of adopting different mass-loss prescriptions, but maintaining the same prescription for the efficiency of the third dredge-up (Karakas et al., 2002). In the left panel of Fig. 6.5 I show the effects of adopting the mass-loss rate prescription of Vassiliadis & Wood (1993) in its original formulation, with a superwind phase starting at a pulsation period $P = 500$ days. The general agreement is satisfactory, similar to the results in Fig. 6.4 (top panel).

Instead, delaying the onset of the superwind to $P = 800$ days as suggested by Kamath et al. (2011) (right panel), I predict expansion velocities that are too high compared to the bulk of the observed data, for $10^{-6} < \dot{M} < 10^{-5}$ $M_\odot$ yr^{-1}. In this case, TP-AGB models suffer more third dredge-up events, which lead to larger C/O ratios, i.e. 1.77 and 2.47 for the 2 $M_\odot$ and 3 $M_\odot$ models, respectively. Lower velocities may be obtained with models of higher metallicity, but this would conflict with the observed oxygen abundances of the Galactic C-stars which are slightly sub-solar. Within the adopted scheme for C-dust formation, a delayed super-wind can still produce a reasonable agreement with observations, but invoking a lower efficiency of the third dredge-up at the same time.

It is also worth mentioning that there is observational evidence that C-stars in the Small Magellanic Cloud (SMC), despite having very similar molecular C_2H_2 and HCN NIR band strengths compared to C-stars in the Large Magellanic Cloud (LMC), show a lower intrinsic dust attenuation (van Loon et al., 2008). This would confirm earlier suggestions that also for C-stars the dust-to-gas ratio should decrease with the initial metallicity, and this would directly affect the predicted velocities. In particular van Loon (2000), combining scaling laws provided by spherically symmetric stationary dusty winds with other observational evidence, derived a linear relation between the dust-to-gas ratio and the initial metallicity of C-stars. While in M-giants a correlation with metallicity is naturally explained by the secondary nature of the dust key-elements such as silicon and magnesium, for C-stars this would mean that the efficiency of converting C-molecules into C-grains decreases with the initial metallicity (van Loon et al., 2008).

In summary, I can draw the following conclusions: expansion velocities of C-stars depend on the interplay between mass-loss and third dredge-up, and are affected by the uncertainties in the sticking coefficients and the details of the underlying nucleation process. As a result, some degree of degeneracy affects the predictions. At the same time, the observed velocities may offer a powerful tool to calibrate the above processes, provided that other independent observational constraints are considered jointly (e.g. measurements of C/O ratios, effective temperatures, mass-loss rates, lifetimes from star counts, etc.).

6.2 Dust mass-loss rates, condensation fractions and sizes

Figures 6.6, 6.7 and 6.8 show the evolution of the dust mass-loss rates, the dust sizes, the dust-to-gas mass ratios and the condensation fractions of the three different metallicities considered and of several initial masses. I only show the results of the HCT scheme computed with $\alpha_{\rm sil} = 0.2$, which provides the best agreement with observations in terms of expansion velocities for M-stars. For sake of simplicity, the mass-loss rates and the dust-to-gas ratios are shown only for silicates, amorphous carbon and SiC. As for grain sizes and condensation fractions, I distinguish between pyroxene and olivine.

Referring back to Figs. 1.6, 1.7 and 1.8, it is clear that all these quantities are modulated by the thermal pulse cycles, over which significant changes in L_*, $T_{\rm eff}$, and $\dot{M}$ are expected to take place. The chemical type of the main dust species (either silicates of carbonaceous dust) is essentially controlled by the C/O ratio, hence it depends on the interplay between the third dredge-up, which tends to increase the carbon excess, and HBB, that converts carbon, and even oxygen at lower metallicities, into nitrogen. Stars with mass $M_* \leq 1.5 - 2$ $M_\odot$, corresponding to item a) in Chapter 1, will produce mainly olivine and pyroxene.

At the lower metallicity the condensation fractions are very low and these stars are able to give rise to a dust driven wind only during the peak luminosity associated with the thermal pulses. At increasing metallicity, the condensation fractions become larger and the stars are able to produce a dust driven wind also during the inter-pulse phase. The dust composition of the stars with masses of $\sim 2 - 3$ $M_\odot$, whose evolution has been described in item b) in section Chapter 1, is initially that of an M-giant, i.e. mainly composed of silicates. During this phase the C/O ratio increases because of the third dredge-up, while remaining below unity. Therefore, the excess of oxygen ($\epsilon_O - \epsilon_C$), available to be locked into silicates progressively decreases. However, since the key-element is silicon, the dust-to-gas ratio is not affected by this variation until eventually C/O ~1. At this stage there is a visible drop in silicate production. Once the C/O ratio becomes larger than 1, carbonaceous dust is produced, initially in the form of SiC. In fact, SiC condenses at a higher gas temperature than amorphous carbon, but its abundance is limited either by the silicon abundance or by the carbon excess if ϵ_C-$\epsilon_O \leq \epsilon_{\rm Si}$. When this latter condition is fulfilled, almost all the carbon available condenses into SiC, as it can be seen at the first thermal pulse of the C-star phase of the 2 $M_\odot$ and 3 $M_\odot$ models at solar metallicity. As soon as $\epsilon_C - \epsilon_O > \epsilon_{\rm Si}$, amorphous carbon becomes the dominant species as the abundance of the SiC is now controlled by the abundance of silicon. Note that the mass-loss rate during the C-star phase is about two orders of magnitude larger than in the previous M-star phase, so that the integrated dust ejecta are mainly in the form of amorphous carbon. The dust evolution of the more massive stars at low and intermediate metallicity is similar to the previous case but, because of the very efficient HBB, there is a rapid initial decrease of the C/O ratio. Since the key-element of silicate dust is silicon, the dust-to-gas ratio is unaffected by this variation. The stars evolve at higher luminosities and cooler effective temperatures and the mass-loss rates, in both gas and dust, increase significantly. In the case of intermediate metallicity the star becomes carbon-rich in its last evolutionary stages when HBB is extinguished. Since at this stage only few more third dredge-up episodes may still take place, the contribution of carbonaceous dust to the integrated ejecta is negligible compared to that of silicates. In the case of the model of $M_* = 5$ $M_\odot$ and $Z = 0.001$, that may be considered representative of the more massive TP-AGB stars of low metallicity corresponding to item c) in Chapter 1, the HBB is so efficient that also the ON cycle is active, causing the partial conversion of oxygen into nitrogen. Thus, after an initial drop of both C and O, the C/O ratio quickly becomes larger than unity. As a consequence, silicate dust production is negligible and the main product is

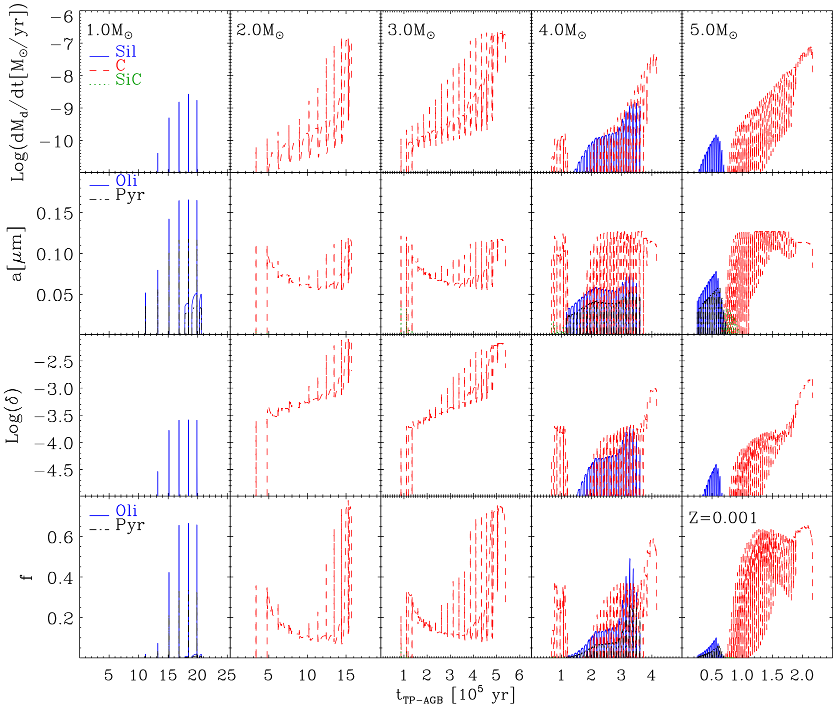

Figure 6.6: Dust properties of selected models of initial metallicity $Z = 0.001$, for various initial masses, as shown in the upper panels. From top to bottom I depict the dust mass-loss rates in $\mathrm{M_{\odot}yr^{-1}}$, the dust sizes in μm, the dust-to-gas ratios δ, and the dust condensation fractions f, respectively. The main dust species are silicates (blue lines), amorphous carbon (red lines) and SiC (green lines). In some panels silicates are separated into olivine type dust (blue lines) and pyroxene type dust (black lines) as indicated in the insets.

amorphous carbon. SiC dust is also minor in this model. Finally the model with $M_{*} = 4\ \mathrm{M_{\odot}}$ and $Z = 0.001$ presents several characteristics at a time. It begins as an M-giant but its silicate condensation fraction is not high enough to power a dust driven wind. It then becomes a C-star, item b), but, after a while, the HBB is efficient enough to convert it back again into an M-giant, this time with a dust driven wind, item d) in Chapter 1. After this stage its dust evolution is characterized by the quasi-periodic transitions across C/O = 1 from both directions, caused by the alternating effects of the third dredge-up (C/O ↑) and HBB (C/O ↓), corresponding to item e). Accordingly, the main characteristics of this star are the concomitant presence of both silicate and carbonaceous dust in the same thermal pulse cycle, because the two crossings are experienced within the same cycle. During the C-star phase the main product is amorphous carbon even if C/O ∼1, because of the very low silicon abundance.

In summary, on the basis of the above results, the emerging picture concerning dust production in single stars is as follows. At $Z = 0.001$ silicates dominate dust production only at the lowest masses ($M_{*} \sim 1\ \mathrm{M_{\odot}}$) where the third dredge-up process is absent. However the corresponding dust mass-loss rates are very low. At larger masses, amorphous carbon is the main dust species, though its amount may change depending on the relative efficiencies of the third dredge-up and HBB. At increasing metallicity, the third dredge-up and HBB combine in such a way that the mass range for carbon dust production becomes narrower. At $Z = 0.02$, carbon dust is produced between $2\ \mathrm{M_{\odot}}$ and $4\ \mathrm{M_{\odot}}$ whereas, in all other masses, silicate dust is the main product. This result is almost independent of whether chemisputtering is included or not but, obviously, in the case without chemisputtering, silicates tend to condense more effi-

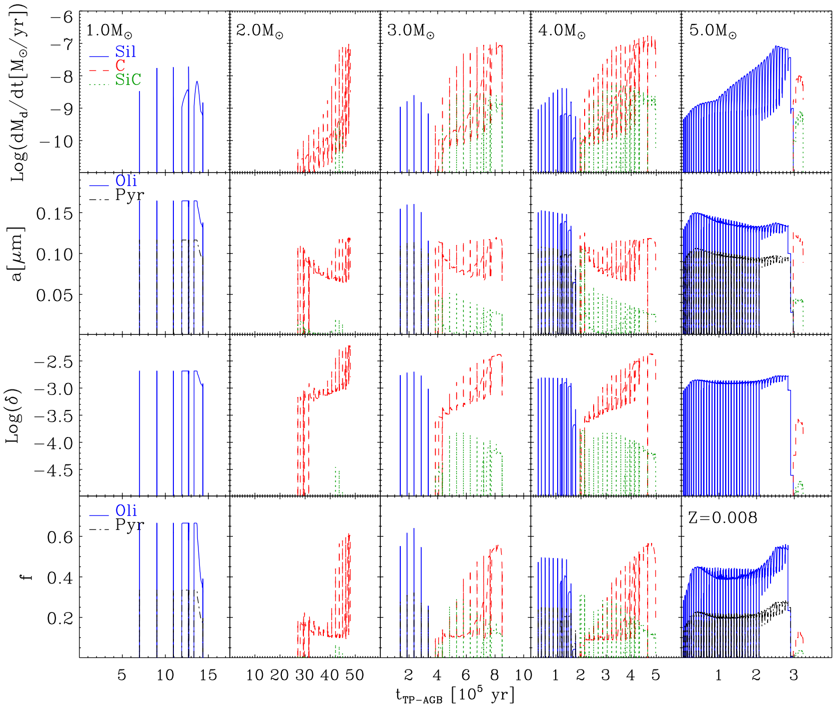

Figure 6.7: The same as in Fig. 6.6, but for initial metallicity $Z = 0.008$.

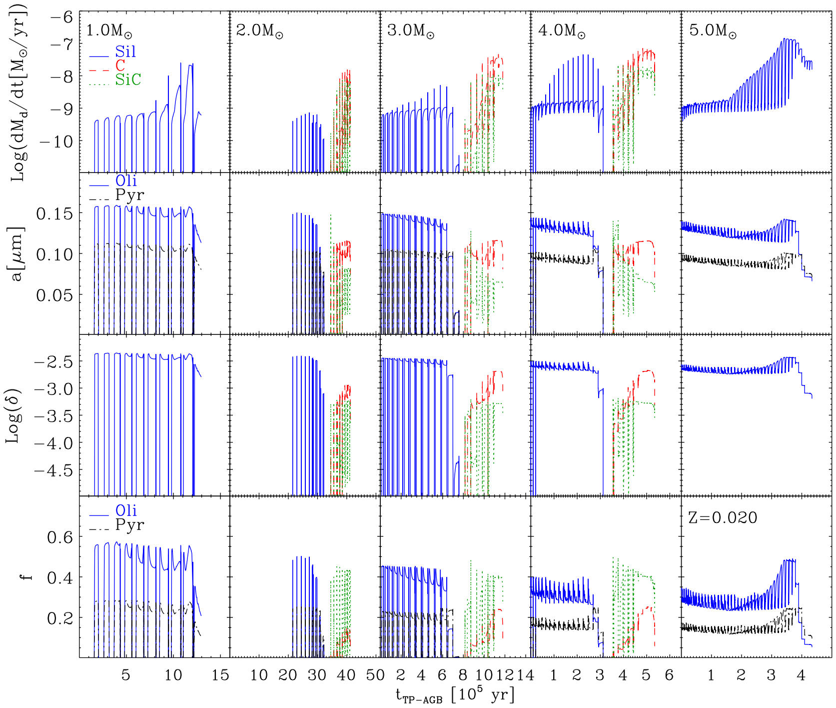

Figure 6.8: The same as in Fig. 6.6, but for initial metallicity $Z = 0.02$.

ciently. The differences between the condensation fractions of silicates computed by the LCT and the HCT schemes are more pronounced at mass-loss rates below 10^{-6} $M_{\odot}$ yr^{-1} while, at higher mass-loss rates, the models reach approximately the same condensation degrees. These are also the phases that dominate the total dust production.

The sizes a of dust grains span a wide range of values during the TP-AGB evolution, from a few hundredths of a micron up to a maximum, typically around 0.15 μm, for all stellar masses and metallicities, as shown in Figs. 6.6, 6.7 and 6.8. The broad range of a spanned during the TP-AGB phase depends mainly on the efficiency of mass-loss, as this latter determines the volume density of the key-elements which, in turn, regulate the growth rates. Interestingly, the maximum value of the size is almost independent from the metallicity of the star. This is due to the fact that both the initial number of seeds and the total amount of dust that may condense, scale linearly with the metallicity or with the carbon excess (Eqs. 4.59 and 4.60). Indeed, by decreasing the number of seeds to $\epsilon_s = 10^{-14}$ in a few test models, I obtain a maximum size ≥ 0.3 μm, as expected from the above simple scaling.

6.3 Dust-to-gas ratios and composition

The lower panels in Figs. 6.6, 6.7 and 6.8 show the dust-to-gas ratios δ, and the condensation fractions f, respectively. The dust-to-gas ratios of CSE models can be compared with observations when independent data exist for both the dust mass-loss and the gas mass-loss rates. Unfortunately, the dust-to-gas ratio is difficult to measure mainly due to the difficulties of obtaining accurate measurements of the gas mass-loss rates. For example, for the extragalactic C-stars, for which CO observations are challenging, the dust-gas-ratio is almost always assumed and used to derive the total mass-loss rate from MIR observations. An important issue is whether and how this ratio depends on metallicity and chemistry. There are indications that for M-giants it decreases almost linearly with the metallicity (Marshall et al., 2004), while for the C-stars the situation is more intriguing because carbon is enhanced by the third dredge-up, and so dust production may not reflect the initial metallicity as in M- giants. If also carbon formed from heterogenous nucleation on metal carbides, as suggested by some recent observations (van Loon et al., 2008), then a behaviour similar to that shown by M-giants should be expected. If a significant fraction of carbon formed from homogeneous growth, as suggested by the absence of metallic seeds in the nuclei of several meteoritic graphite spherules (Bernatowicz et al., 1996), then the behaviour of the dust-to-gas ratio may be more dependent on the evolution along the TP-AGB. Typical values assumed for the CSE dust-to-gas ratios are 1/200 for the Galaxy, 1/500 for the LMC and 1/1000 for the SMC (Groenewegen et al., 1998; van Loon et al., 2005). Dust-to-gas ratios twice the quoted values are also quite common (Groenewegen et al., 2009; Woods et al., 2012).

A noticeable effect that can be already seen in Figs. 6.6, 6.7 and 6.8 is that in M-giants the dust-to-gas ratio (δ) shows only a mild dependence on the evolutionary status of the star. Of course, there are strong variations near the peak luminosity after each thermal pulse but, during the inter-pulse phase, its value is almost constant. In contrast, in the case of C-stars, δ generally increases during the evolution both at the peak luminosity and at each inter-pulse cycle. This may be an effect of the choice of adopting a homogeneous growth process for carbon. The comparison with Galactic M-giants (right panel) and with LMC data (left panel) is shown in Fig. 6.9. For Galactic M-stars I use the sample by Knapp (1985) providing both dust and gas mass-loss rates. For LMC M-stars there exist only very few data in the literature that can be used to determine δ. From OH observations of a small sample of M-giants by Marshall et al. (2004), I derive the gas mass-loss rates using the prescription presented by van der Veen &

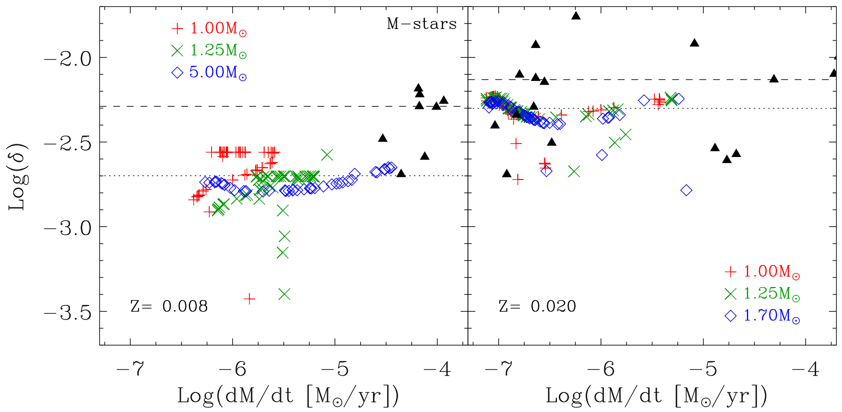

Figure 6.9: Observed and predicted dust-to-gas ratios of Galactic and LMC M-stars. *Left panel*: LMC data from Marshall et al. (2004) are compared with models of $Z = 0.008$ and initial masses of 1, 1.25, 5 M$_\odot$. The dashed line indicates the median value of the data (1/194), whereas the dotted line represents the usually assumed value of the dust-to-gas ratio 1/500 (van Loon et al., 2005). *Right panel*: comparison between models of $Z = 0.02$ and initial masses of 1, 1.25, 1.7 M$_\odot$ with Galactic data from Knapp (1985). The dashed line indicates the median value of the data (1/135), whereas the dotted line represents the usually assumed value of the dust-to-gas ratio 1/200 (Groenewegen & de Jong, 1998). See text for details.

Rugers (1989)

$$\dot{M} = f_{\rm OH}/f_{{\rm OH}_\odot} \times 1.8 \times 10^{-7}\sqrt{F_{\rm OH}}\,v_{\rm exp}D \tag{6.1}$$

where D is the distance in kpc, assumed $D = 50$ for the LMC, $F_{\rm OH}$ is the OH 1612-MHz maser peak intensity in Jy and $v_{\rm exp}$ is the wind expansion velocity in km s^{-1}. The latter two quantities are provided by Marshall et al. (2004) while the factor $f_{\rm OH}$, representing the conversion factor from OH to H_2 abundances, is scaled with the metallicity, i.e. $f_{\rm OH}$= 0.02/0.008× $f_{{\rm OH}_\odot}$ ($f_{{\rm OH}_\odot} = 1.6 \times 10^{-4}$) in Eq. 6.1. The dust mass-loss rates are derived from the total mass-loss rates provided by van Loon et al. (2005) for common stars, which are based on MIR spectral fitting. I re-normalize the values to the velocities by Marshall et al. (2004) and multiply by the dust-to-gas ratio assumed by van Loon et al. (2005), $\delta = 1/500$. These data are compared with selected HCT models with $Z = 0.02$ and $Z = 0.008$ and initial stellar masses of 1, 1.25, 1.7 and 5 M$_\odot$, the latter only for the lower metallicity. Like in the comparison with the velocities, the models are drawn from a uniform randomly generated set of TP-AGB ages, for each mass. Furthermore, I also take into account that the H_2 abundance in the TP-AGB models considered is ≈75% of the total gas mass and, accordingly, I multiply the total mass-loss rates by the same factor. The dashed line in the right panel of Fig. 6.9 represents the median value for the Knapp (1985) data, $\delta = 1/135$. I adopt the median value of the data since, in the case of such a range of values covering about one order of magnitude because of different physical conditions, the mean value would be biased toward the highest values ($\delta = 1/106$). The resulting value is larger than that usually assumed, $\delta = 1/200$ shown by the dotted line. The models cluster around $\delta = 1/200$ and systematically underestimate the observed median value by ≈50%. Note that in these models the total fraction of silicon that is condensed into dust is already high, typically ∼0.7 (see also lower panels of Figs. 6.6, 6.7 and 6.8) and that, in order to reproduce the observed values at solar metallicity, all the silicon should be locked into silicate dust, as already noticed by Knapp (1985), unless the adopted metallicity is too low. Furthermore, as already anticipated, the models show only a small dependence on the evolutionary phase along the TP-AGB, represented here by the value of the total mass-loss rate. Concerning the

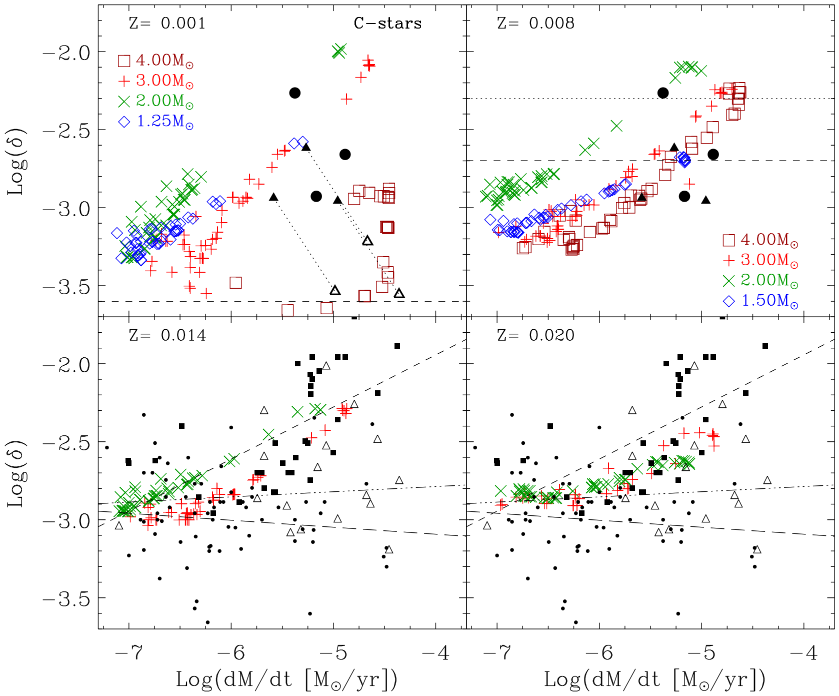

Figure 6.10: Observed and predicted dust-to-gas ratios of C-stars. *Upper panels*: comparison between models with $Z = 0.001$ and 0.008 and initial masses of 1.25, 1.5, 2, 3, 4 $\mathrm{M}_\odot$ with thick disk C-stars (filled triangles) and Galactic Halo C-stars (filled circles) from Lagadec et al. (2012). Empty thick triangles are obtained adopting an H_2/CO factor four times larger than that used by Lagadec et al. (2012) for Halo C-stars. In the left panel the dashed line represents $\delta = 1/4000$. In the right panel, the dotted line represents $\delta = 1/200$ and the dashed line is the median value of stars. *Lower panels*: comparison between models of $Z = 0.014$ and $Z = 0.02$ and initial masses of 2 and 3 $\mathrm{M}_\odot$ with Galactic data from Knapp (1985) (open triangles) by Groenewegen et al. (1998) (filled boxes) and Bergeat & Chevallier (2005) (small dots). In these panels the lines are best fits to the logarithmic values of δ and mass-loss rates. Short-dashed line represents the fit for Groenewegen et al. (1998), dot-dashed line is for Knapp (1985) and long-dashed line for Bergeat & Chevallier (2005).

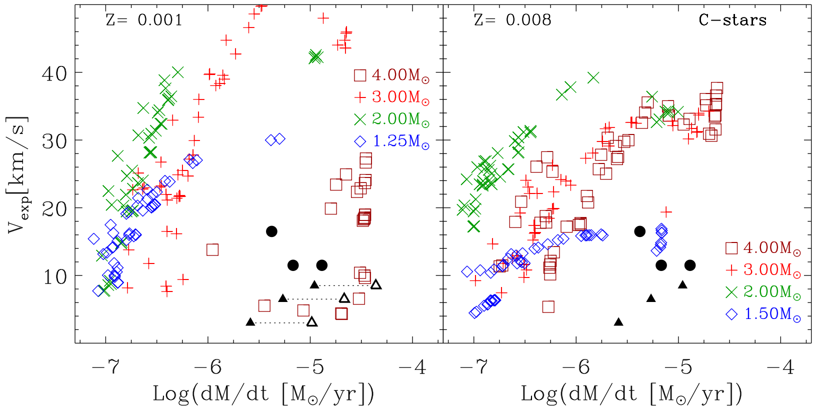

Figure 6.11: Predicted expansion velocities of C-stars at low and intermediate metallicities for selected models with $Z = 0.001$ and $Z = 0.008$ and initial masses of 1.25, 1.5, 2, 3, 4 M$_\odot$. Data for thick disk stars (filled triangles) and Galactic Halo stars (filled circles), are taken from Lagadec et al. (2012). At the lower metallicity I show the effect of accounting for a H_2/CO conversion factor equal to four times that used by Lagadec et al. (2012) for the Halo stars. See text for more details.

LMC (left panel), the median value of the data ($\delta = 1/194$, dashed line) is ~40% lower than that of Galactic M-giants. On the other hand, the presented models cluster around $\delta = 1/500$ (dotted line), the value usually adopted for the LMC. Marshall et al. (2004) already noticed that, in order to reproduce the total mass-loss rates derived from infrared observations assuming $\delta = 1/500$ (van Loon et al., 2005), they had to use a conversion factor for the LMC stars $f_{\rm OH}/f_{\rm OH_\odot} = 5$. Had I used this higher conversion factor, the median of the data would have been very near to ~ 1/500. However, unless the adopted metallicities for the Galactic and LMC stars are grossly in error, my scaling seems more robust because oxygen is a very good tracer of the metallicity, even for non standard elemental partition. I finally notice that the models do not reproduce the highest observed mass-loss rates, in both Galactic and LMC M-giants. In the latter case, the mismatch is more evident because the observations are likely biased toward the highest mass-loss rates. Because also at this metallicity the trend with the total mass-loss rate (if any) is modest, pushing the models toward higher mass-loss rates would not solve the discrepancy with the observed dust-to-gas ratios.

Predicted dust-to-gas ratios for C-stars are compared with the observed data in Fig. 6.10. Data for Galactic C-stars are shown in the lower two panels of Fig. 6.10. Open triangles refer to the data by Knapp (1985) (median value 1/693, $\log\delta = -2.84$), filled boxes to Groenewegen et al. (1998) (median value 1/370, $\log\delta = -2.57$), and small dots to the revised compilation by Bergeat & Chevallier (2005) (median value 1/909, $\log\delta = -2.96$). C-stars LCT models with initial masses of 2 and 3 M$_\odot$ are shown in the lower right panel for $Z = 0.02$ and in the lower left panel for $Z = 0.014$, respectively. In contrast with M-giants, the models show a clear trend of increasing dust-to-gas ratio with mass-loss rate, that becomes more evident at decreasing metallicity. In order to judge whether this trend is real I have fitted with a least square routine the logarithmic values of δ and mass-loss rates. Only the data from Groenewegen et al. (1998) (short-dashed line) show a similar trend while in both the sample from Knapp (1985) (dot-dashed line) and in that from Bergeat & Chevallier (2005) (long-dashed line) this trend is not observed. Overall the models are in fairly good agreement with the observations of Galactic C-stars though they cannot reproduce the highest observed ratios. The predictions of the models at intermediate and low metallicities are shown in the upper right and left panels of

Fig. 6.10, respectively. At metallicities lower than those of the Galactic disk, the comparison with observations is challenged by the lack of gas mass-loss observations in typical subsolar environments rich in C-stars, such as the Magellanic Clouds. I plot in Fig. 6.10 only the recent observations of a few metal poor C-stars toward the Galactic Halo by Lagadec et al. (2012). From radial velocities, distances and Galactic coordinates (Lagadec et al., 2012) place their memberships in the thick disk (filled triangles in Fig. 6.10) or in the Halo (filled circles). The nature of the Halo stars is still a matter of debate. In low metallicity models the minimum mass for a star to become C-star is $M_{*} \sim 1.2$ M$_{\odot}$, while the typical turn-off mass for an old metal poor population like that of the Halo is $M_{*} \sim 0.9$ M$_{\odot}$. Since the lack of an efficient third dredge-up at low masses is a common feature of all the models of C-stars and assuming that they are correct, these stars do not belong to the Halo population and they could have formed either in the thick disk or outside the Galaxy (e.g. in the Sagittarius dSph Galaxy). Furthermore, the Halo stars show strong C_2H_2 molecular absorption bands, typical of low metallicity stars (van Loon et al., 2008) and strong SiC emission, characteristic of more metal rich stars. Since the metallicity of these stars cannot be firmly constrained, I compare their dust-to-gas ratios with the predictions of both the intermediate and low metallicity models. The median value of their dust-to-gas ratios, $\delta = 1/456$ ($\log \delta = -2.66$), is very similar to that assumed for intermediate metallicity stars, $\delta = 1/500$, which I show as a dashed line in the upper right panel. In the same panel the dotted line represents $\delta = 1/200$, typical of solar metallicity but sometimes taken as reference also for intermediate metallicities. For $Z = 0.008$ I plot the models of initial masses 1.5, 2, 3 and 4 M$_{\odot}$. For $Z = 0.001$ the dashed line represents $\delta = 1/4000$, obtained by scaling the $Z = 0.008$ usual reference value linearly with the metallicity. For $Z = 0.001$ I plot the models of 1.25, 2, 3 and 4 M$_{\odot}$. At these metallicities the trend of increasing δ with increasing mass-loss rate becomes more evident. Notice also that, at decreasing metallicity, the dust-to-gas ratios at low mass-loss rates decreases while the maximum value, reached at the highest mass-loss rates, increases with a global spread of about one order of magnitude. Thus a constant dust-to-gas ratio is not supported by the presented models.

Furthermore the simple random selection process adopted, indicates that at low metallicity lower values of δ are preferred, but these values are still significantly higher than those predicted by a linear scaling with the metallicity. I also recall that at the lowest metallicity the most massive TP-AGB stars undergo a very efficient HBB which inhibits the growth of the carbon excess to large values. This explains why, at $Z = 0.001$, the maximum value reached by the model of 4 M$_{\odot}$ is significantly lower than those of less massive stars. If I assume an intermediate metallicity for C-stars by Lagadec et al. (2012), I find that their dust-to-gas ratios can be fairly well reproduced by the models though, for most of them, there is a significant degeneracy with the initial mass. However at this same metallicity I cannot reproduce the velocities of the Halo stars, while thick disk stars could be compatible with the model of $M_{*} = 1.5$ M$_{\odot}$, as shown in Fig. 6.11. Halo stars expansion velocities can be reproduced at the lower metallicity only by those models in which the HBB is very efficient, such as that with $M_{*} = 4$ M$_{\odot}$. At this metallicity one should also correct for a H_2/CO conversion factor higher than that used by Lagadec et al. (2012). This would shift the data toward higher gas mass-loss rates and lower values of δ as shown by the empty thick triangles in Figs. 6.10 and 6.11, obtained adopting an H_2/CO factor four times larger than that used by Lagadec et al. (2012). Notice that with this correction the Halo stars are fully compatible, in dust-to-gas ratio, velocities and mass-loss rates, with low metallicity models where the growth of carbon excess is inhibited by an efficient HBB. Whether this is a real effect or if it mimics a more general need of reducing the efficiency of carbon dust formation at low metallicity, as suggested by other authors, must be analyzed by means of models that take fully into account the heterogeneous growth of amorphous carbon on metal seeds (van Loon et al., 2008).

The dust composition of the models can be derived from the condensation fractions plotted in the lower panel of Figs. 6.6, 6.7 and 6.8. For amorphous silicates, the most abundant dust species in M-giants, I consider the two main components, olivine and pyroxene. Crystalline silicates have also been detected from their MIR features but their abundances are by far less than the corresponding amorphous phase. Though the condensation fractions are plotted separately for olivine and pyroxene, it is not yet possible to quantify their relative abundances observationally.

On the contrary, in the case of C-stars it is possible to derive the relative abundances of the two different main components, SiC an amorphous carbon. Fig. 6.12 shows the comparison between existing observations of the SiC/C mass ratio and the predictions of models, for different metallicities. I plot the data for Galactic stars (filled squares) from Groenewegen et al. (1998) together with the models at $Z = 0.02$ in the lower right panel and at $Z = 0.014$ in the lower left panel, respectively. Data for LMC C-stars (filled small dots) from Groenewegen et al. (2007) are compared with models at $Z = 0.008$ in the upper right panel. Finally, the data from Lagadec et al. (2012) (filled triangles for the Halo memberships and large filled dots for the thick disk memberships) are compared with models of low and intermediate metallicity in the upper left and upper right panels, respectively. As can be seen from the figure the models overestimate the observed SiC/C ratios at solar metallicity. Galactic data are mostly concentrated around 0.05-0.1 while the models may reach also SiC/C=1, as shown by the dust-to-gas ratios in Figs. 6.6, 1.7 and 6.8. Though the comparison improves if I consider a slightly lower metallicity for the Galactic data, $Z = 0.014$, there is an evident over-production of SiC. At $Z = 0.008$ the agreement with the observations is only partially better. The majority of the stars have $\mathrm{SiC}/\mathrm{C} = 0.02$ but also a high uncertainty (Groenewegen et al., 2007). These data are consistent with TP-AGB stars with initial mass $M_{*} \sim 2$ $\mathrm{M}_{\odot}$. On the other hand data with values larger than 0.02 are well reproduced by all the other models. In particular the putative thick disk members in the sample from Lagadec et al. (2012) (large filled dots) are well reproduced by stars with initial mass $M_{*} = 1.5$ $\mathrm{M}_{\odot}$. At the lowest metallicity considered here the predicted SiC/C ratios become negligibly small. A decreasing SiC/C ratio with metallicity is indeed observed through the measure of the strength of the SiC spectral features at 11.3 μm. This feature decreases going from the Galaxy to the LMC and to the SMC and other metal poor galaxies of the Local Group (Sloan et al., 2009). In this respect the location of the Halo stars in the $Z = 0.001$ panel are surprising, as already noticed by Lagadec et al. (2012).

A noticeable feature emerging from the Galactic sample is that, at increasing mass-loss rates, the SiC/C ratios decrease. This trend is also shown by the models. Their inspection also highlights that while carbon dust-to-gas ratio, δ_{C}, continuously increases with the mass-loss rate, δ_{SiC} initially increases and then it remains constant or even decreases. Furthermore, the maximum value reached by the models decreases with the metallicity. While the latter effect is expected if silicon is the key element for the formation of SiC, the global decrease with the mass-loss rate is rather an effect of the internal structure and wind dynamics of the CSE. This is even more evident if I increase the temperature of carbon dust. For the HCT models, where carbon condenses at T_{gas}=1300 K, the picture becomes quite different, as can be seen in Fig. 6.13. At low mass-loss rates the predicted SiC/C ratios are significantly lower than those of LCT models while at high mass-loss rates the value remains almost unchanged. This behaviour is due to the fact that, at low mass-loss rates, the condensation process is very sensitive to the details of the internal structure, because the overall density is lower. Indeed, the large opacity rise due to the condensation of carbon is always accompanied by a strong acceleration of the wind and thus by a significant temperature and a density drop. At lower mass-loss

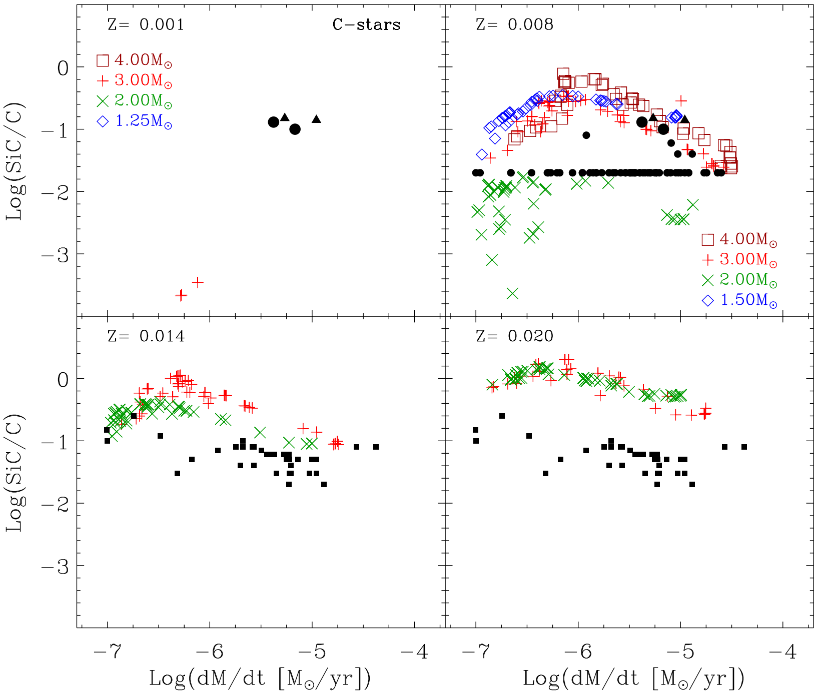

Figure 6.12: Observed and predicted SiC/C ratios as a function of the metallicity. *Lower panels*: data for Galactic stars (filled squares), from Groenewegen et al. (1998), are compared to models of 2 and 3 M$_\odot$ for $Z = 0.02$ (right) and $Z = 0.014$ (left), respectively. *Upper-right panel*: LMC C-stars (filled small dots), from Groenewegen et al. (2007), and Halo stars (filled triangles) and thick disk stars (large filled dots), from Lagadec et al. (2012), are compared with of $Z = 0.008$ and masses of of 1.5, 2, 3 and 4 M$_\odot$. *Upper-left panel*: models of 1.25, 2, 3 and 4 M$_\odot$ and $Z = 0.001$ are compared with the data from Lagadec et al. (2012).

rates the global density is lower and an earlier condensation of carbon is enough to inhibit the formation of SiC. On the contrary at high mass-loss rates the structure is self-regulating and less dependent on the details of the condensation process. In this case an increase of the carbon condensation temperature has an almost negligible impact on the SiC/C ratios.

6.4 Dust ejecta

By integrating the dust mass-loss rate along the entire TP-AGB phase I compute dust ejecta for the different masses and metallicities. The ejecta refer to individual stars and they may not be representative of the corresponding dust yields obtained after convolving with the initial mass function. They are provided in Table 6.4 for both the LCT models and for the HCT models (Chapter 5). The above integration is performed irrespective of the ability of dust to drive or not the stellar wind. In fact, as already discussed, in M-stars, and in particular in models with chemisputtering, dust cannot always drive an outflow consistent with the adopted mass-loss rate. In these cases I must assume that there exist other possible ways to accelerate the wind, that may finally deliver the material into the ISM (Harper, 1996). However, these phases are characterized by a low dust mass-loss rate so that they do not contribute significantly to the total ejecta.

Figure 6.14 shows the total dust ejecta of the main condensed compounds, i.e. silicates, amorphous carbon, iron and SiC, as a function of the initial stellar mass and for the three

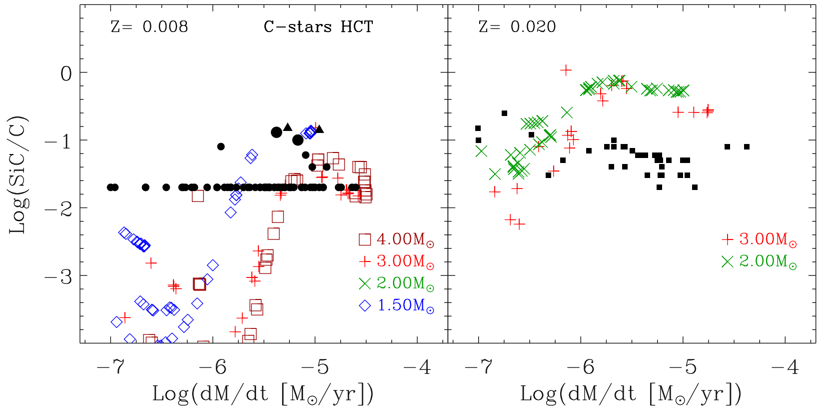

Figure 6.13: The same as in Fig. 6.12 for Z = 0.008 and Z = 0.02, but for HCT models.

metallicities considered here.

I first compare the results of models, obtained with the two different formalisms (either LCT or HCT). I remind that, in the case of C-stars, the chemisputtering process is neglected in both schemes (see also FG06) but, as a test case, I recompute the models with a higher gas condensation temperature (= 1300 K instead of 1100 K) to check its effect on the total ejecta. These models are plotted as asterisks in the figure and are referred in Table 6.4 as HCT models. I notice also that, in the case of SiC and Fe, possible differences in the ejecta, between LCT and HCT models, are only an indirect consequence of the variations of the condensation temperatures of silicates and amorphous carbon, because their dust growth schemes do not change.

As for the C-stars, the final dust ejecta mainly consist of amorphous carbon (C in Table 6.4) and there are no significant differences between LCT and HCT models, at any metallicity. As far as the variation of α_C is concerned, its largest effect is on the ejecta of amorphous carbon but the maximum variation between the models computed with $\alpha_C = 1$ and $\alpha_C = 0.5$, at solar metallicity, is only 5%.

Differently, in the case of M-stars, I find that the silicate ejecta of HCT models can be as much as 50% higher compared to the LCT ones. These differences tend to vanish towards the largest mass models, since the condensation fraction of silicates is quite high in both classes of models, mostly due to the large mass-loss rates.

Thus I may conclude that, in spite of the differences in velocity, density and temperature profiles brought about by the adoption of either of the two formalisms, their effect on the final dust ejecta is, instead, rather weak.

In the same figure I also plot the results of FG06, Ventura et al. (2012a) and Ventura et al. (2012b), that can be compared to the LCT scheme. I remark that TP-AGB models by FG06 are based on a compilation of analytic relations partly taken from Marigo et al. (1996) while, in Ventura et al. (2012a) and Ventura et al. (2012b) full numerical calculations along the AGB are used. The latter models also include the super-AGB stars between 6 $M_\odot$ and 8 $M_\odot$, that have developed an electron-degenerate O-Ne core after the C-burning phase (Siess, 2010).

At low metallicity the results obtained are qualitatively in good agreement with those of FG06, since both studies predict that the bulk of dust produced by low and intermediate mass stars is amorphous carbon. In the models presented the carbon dust production is even larger than in FG06, by up to a factor of two in some cases.

I emphasize that the TP-AGB models computed by FG06 neglect two important aspects of stellar evolution, namely: the break-down of the core mass-luminosity relation due to HBB in stars with masses $M_* > 4\ \mathrm{M}_\odot$, and the drastic changes in molecular opacities, hence in the effective temperatures, as soon as the C/O ratio increases above unity as a consequence of the third dredge-up. Both factors concur to a likely overestimation of the TP-AGB lifetimes, hence to an over-exposure of the stellar mantle to nucleosynthesis and mixing processes.

Therefore, the FG06 TP-AGB models are, by construction, quite different from the most recent ones of Marigo et al. (2013). The latter models are based on accurate numerical integrations of a complete envelope model in which the HBB energetics and nucleosynthesis are properly taken into account, the initial conditions at the first thermal pulse are extracted from the stellar evolutionary tracks (Bressan et al., 2012), and more importantly, they use new and accurate equation of state and molecular opacities that account for the continuous changes in the surface chemical composition (Marigo et al., 2013).

In the models of Ventura et al. (2012a) at $Z = 0.001$, the dust production is about ten times less than in the presented models. Furthermore, while Ventura et al. (2012a) predict that the dust ejecta are dominated by silicates for stars with $M_* > 3\ \mathrm{M}_\odot$, in the presented models the main dust species is amorphous carbon. This latter difference is likely due, from one side, to a more efficient third dredge-up in the adopted TP-AGB models, and, on the other hand, to the higher mass-loss rate in the models by Ventura et al. (2012a), where the C-star phase is highly reduced with respect Marigo et al. (2013) models.

At $Z = 0.008$ I am again in qualitatively good agreement with FG06 because both studies predict that stars with mass below 1.5 $\mathrm{M}_\odot$ produce silicate dust, while at higher masses the main dust species is amorphous carbon.

However, while in FG06 models for stars more massive than 5 $\mathrm{M}_\odot$ the carbonaceous and silicate dust ejecta are comparable, in the presented models the ejecta are dominated by silicates. This difference is likely due to a more efficient HBB in the discussed models. I also note that for $M_* > 5\ \mathrm{M}_\odot$, dust ejecta predicted by the presented models are roughly five times larger than those of FG06.

The comparison with Ventura et al. (2012b) shows again that, for $1.5 < M_* < 4\ \mathrm{M}_\odot$, the presented models produce about ten times more dust. Only for $M_* \geq 4.5\ \mathrm{M}_\odot$ their dust ejecta become comparable (and sometimes slightly higher) to those of our models. In Ventura et al. (2012b) silicate dust production becomes efficient above $M_* = 3.5\ \mathrm{M}_\odot$ whereas, in the presented models this happens at about $M_* = 4.7\ \mathrm{M}_\odot$. At solar metallicity I can compare my results only with those of FG06. The production of carbon dust is limited to the mass range between 2 $\mathrm{M}_\odot$ and 4 $\mathrm{M}_\odot$, with a peak at around 3 $\mathrm{M}_\odot$, both in the presented models and in those of FG06. The larger dust ejecta predicted by FG06 are probably due to the larger C/O ratios reached by their TP-AGB models. In fact, FG06 do not account for the cooling effect of the TP-AGB tracks (for C/O > 1), produced by the C-rich molecular opacities, with consequent shortening of the C-star lifetimes (Marigo, 2002).

Moreover, for $M_* > 5\ \mathrm{M}_\odot$, silicate ejecta of the presented models are roughly a factor of three larger than the ones obtained by FG06. This may be related to a more efficient HBB in the former models, that lowers significantly the carbon content in the CSEs.

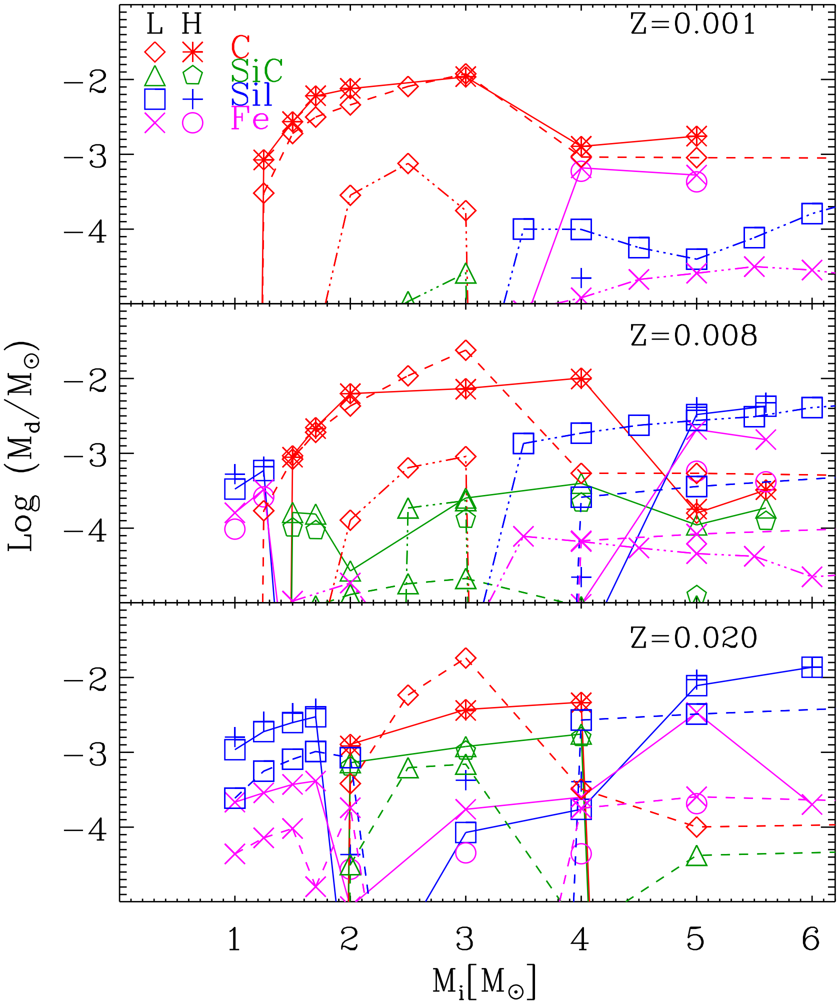

Figure 6.14: Total dust ejecta as a function of the initial stellar mass and for different initial metallicity. For low-(LCT) and high-(HCT) condensation temperature models, I use different symbols, as indicated in the upper panel. To facilitate the comparison with other authors, the LCT scheme are connected with solid lines while, for the models with chemisputtering by FG06 I use dashed lines and, for those of Ventura et al. (2012a) (Z = 0.001) and Ventura et al. (2012b) (Z = 0.008), I use dotted-dashed lines. For the HCT scheme I use only the corresponding symbols.

Table 6.4: Dust ejecta for LCT and HCT models.

$M_{*,i}$ [$M_\odot$]	log (age/yr)	Sil		Fe		Al_2O_3		C		SiC	
					log ($M/M_\odot$)						
$Z = 0.001$		LCT	HCT	LCT	HCT	LCT	HCT	LCT	HCT	LCT	HCT
1.00	9.7	−6.53	−5.66	−6.48	−6.63	−7.44	−7.74	-	-	-	-
1.25	9.5	-	-	−8.62	−8.87	-	-	−3.07	−3.08	-	-
1.50	9.3	-	-	−8.03	−8.27	-	-	−2.56	−2.56	-	-
1.70	9.1	-	-	−7.69	−7.92	-	-	−2.22	−2.22	-	-
2.00	8.9	-	-	−7.57	−7.80	-	-	−2.12	−2.12	-	-
3.00	8.5	-	-	−7.40	−7.62	-	-	−1.97	−1.96	−8.94	−9.01
4.00	8.2	−6.92	−4.65	−3.18	−3.23	−6.03	−6.29	−2.89	−2.89	-	−8.55
5.00	8.0	-	−5.75	−3.28	−3.37	-	−7.22	−2.76	−2.76	-	−8.45
$Z = 0.008$		LCT	HCT	LCT	HCT	LCT	HCT	LCT	HCT	LCT	HCT
1.00	9.9	−3.48	−3.28	−3.79	−4.01	−4.53	−5.24	-	-	-	-
1.25	9.6	−3.23	−3.18	−3.48	−3.58	−4.28	−6.31	-	-	-	-
1.50	9.4	−7.98	−7.34	−6.66	−7.03	−8.56	−8.74	−3.03	−3.05	−3.79	−4.00
1.70	9.3	-	-	−6.90	−7.64	-	-	−2.66	−2.67	−3.81	−4.03
2.00	9.1	-	-	−7.16	−7.50	-	-	−2.20	−2.20	−4.57	−6.99
3.00	8.6	−6.65	−5.95	−6.14	−6.37	−7.49	−7.91	−2.13	−2.14	−3.60	−3.88
4.00	8.3	−5.69	−4.66	−5.02	−5.13	−6.43	−6.60	−1.99	−2.01	−3.40	−3.66
5.00	8.0	−2.48	−2.39	−2.68	−3.24	−3.48	−5.48	−3.80	−3.75	−3.96	−4.90
5.60	7.9	−2.37	−2.32	−2.82	−3.38	−3.39	−5.73	−3.49	−3.49	−3.73	−3.91
$Z = 0.02$		LCT	HCT	LCT	HCT	LCT	HCT	LCT	HCT	LCT	HCT
1.00	10	−2.99	−2.80	−3.68	−5.42	−4.04	−5.23	-	-	-	-
1.25	9.7	−2.73	−2.59	−3.55	−5.60	−3.80	−5.13	-	-	-	-
1.50	9.5	−2.63	−2.48	−3.46	−5.33	−3.69	−5.06	-	-	-	-
1.70	9.4	−2.54	−2.42	−3.40	−5.28	−3.60	−5.03	-	-	-	-
2.00	9.2	−6.73	−4.37	−5.06	−4.56	−7.29	−6.07	−2.89	−2.92	−3.14	−3.20
3.00	8.7	−4.07	−3.37	−3.76	−4.34	−4.75	−5.06	−2.43	−2.44	−2.92	−2.98
4.00	8.3	−3.76	−3.40	−3.60	−4.36	−4.38	−4.94	−2.33	−2.34	−2.76	−2.80
5.00	8.1	−2.11	−2.03	−2.47	−3.69	−2.94	−4.76	-	-	-	-
6.00	7.9	−1.86	−1.86	−3.70	−6.96	−2.84	−5.12	-	-	-	-

Chapter 7

Dust formation at super-solar metallicity

7.1 The TP-AGB models

I extend the formalism presented in the previous chapters to the case of super-solar metallicity stars. The dust growth model (wind equations, method of solution and initial values) has been already described in Chapter 2. I consider here only the results obtained with the preferred schemes of dust growth according to which in M-stars chemisputtering of silicates by H_2 molecules is neglected (HCT), whereas for C-stars the standard LCT scheme is adopted (see Chapter 5). The initial stellar masses are the same ones used in the lower metallicity cases, as listed in Table 7.1.

Stellar evolution from the pre-main sequence up to the first thermal pulse is calculated with the `PARSEC` code (Bressan et al., 2012), while the following evolution along the the whole TP-AGB phase is computed with the `COLIBRI` code (Marigo et al., 2013). The main features of the stellar evolutionary tracks have been already discussed in Chapter 1. Some examples of low- and intermediate-mass stars are shown in Figs. 7.1 and 7.2, for different choices of the initial metallicity, $Z = 0.04$ and 0.06, respectively. A first important difference with respect to the solar and sub-solar metallicity models is that, as shown in Figs. 7.3 and 7.4, only the model of $M_* = 5$ $M_\odot$ with $Z = 0.04$ is able to reach a C/O ratio slightly larger than unity while, in all other cases this ratio remains below the unity. Thus, at super-solar metallicity, the C-star phase is practically absent and I will focus the discussion on the M-giant stars. Concerning the M-giant stars I also notice that, as expected, their effective temperatures decrease on average, as the metallicity increases. On the other hand their predicted mass-loss rates do not change significantly with the metallicity.

7.1.1 The dust condensation temperature of silicates, $T_{\rm cond}$

A noticeable difference in the physical prescription at super-solar metallicity concerns the computation of the dust equilibrium temperature of silicates (Eq. 4.83).

Preliminary computations show that silicates can form significantly closer to the star, where gas temperatures and densities are higher than in the models of solar or lower metallicity, described in Chapter 6. In such conditions, the hypothesis of thermal decoupling between gas and dust, which forms the basis of the simple treatment presented, becomes questionable and dust heating due to collisions may become important. To account for this effect, I need to modify Eq. 4.83, used to compute the dust equilibrium temperature, considering also a col-

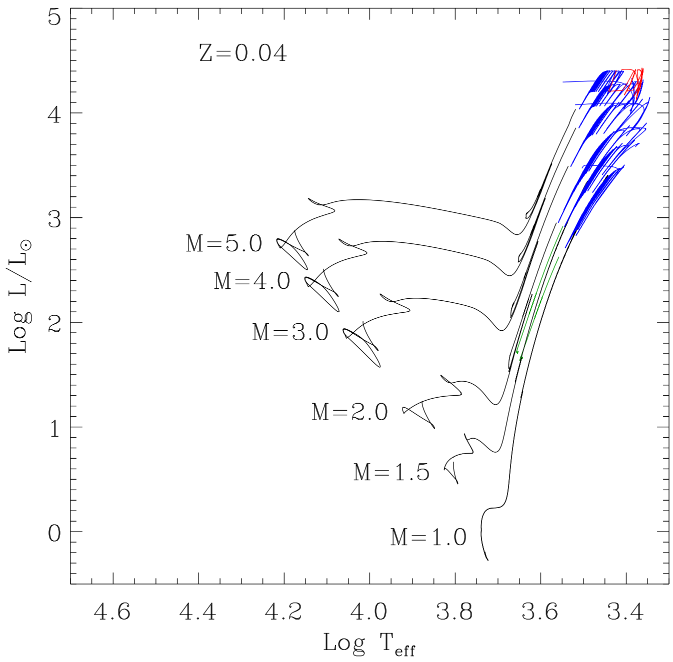

Figure 7.1: Evolutionary tracks for stars with $Z = 0.04$ and initial masses $M_* = 1, 1.5, 2$ $3, 4, 5$ M$_\odot$. The tracks are computed by means of `PARSEC` code up to the TP-AGB phase, and by means of `COLIBRI` until the entire envelope of the star is lost by stellar winds. The thermal pulses developed when C/O$<$1 are plotted with blue lines. On the other hand, the thermal pulses plotted in red correspond to C/O$>$ 1. The He-burning phase of low-mass stars is plotted in green color.

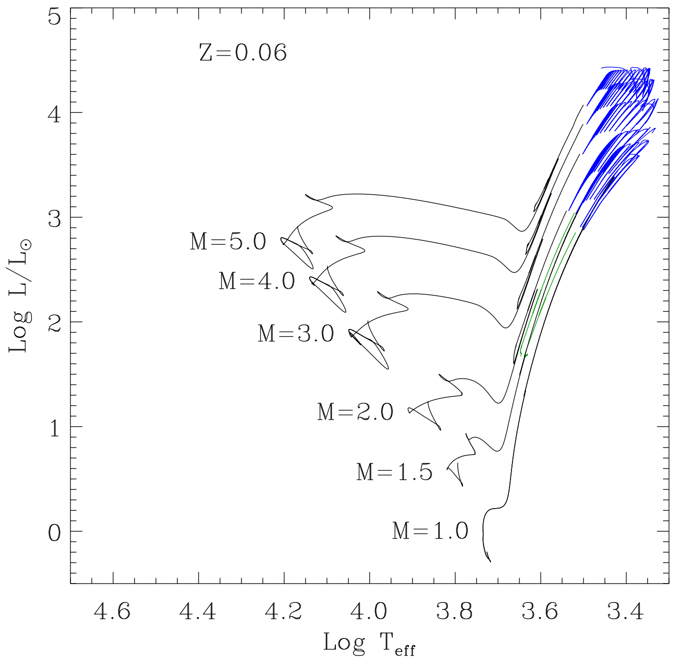

Figure 7.2: The same as in Fig. 7.1, but at $Z = 0.06$.

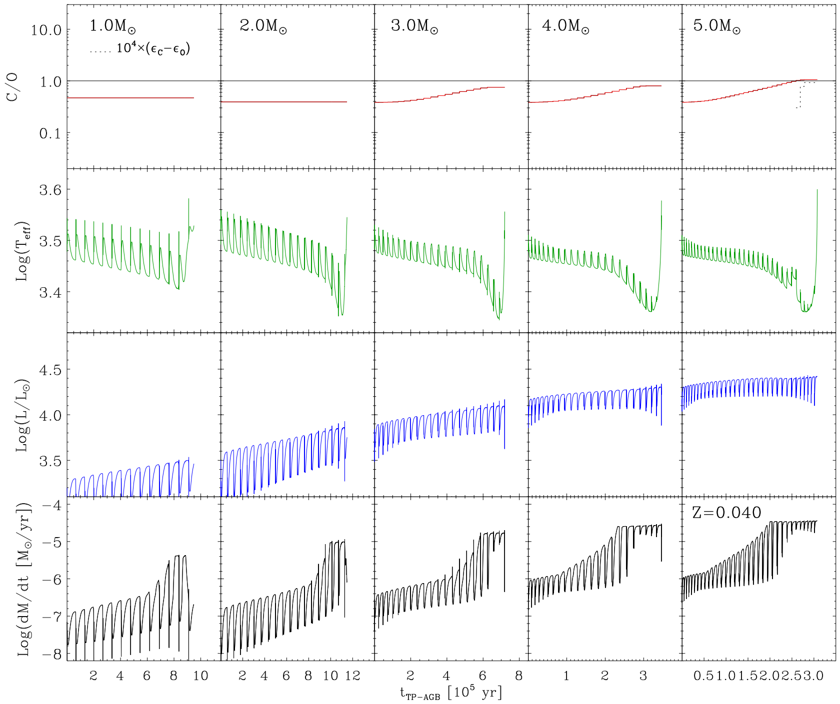

Figure 7.3: Evolution of surface C/O, carbon excess $\epsilon_C - \epsilon_O$ (only when positive), effective temperature, luminosity, and mass-loss rate during the whole TP-AGB phase of a few selected models with initial metallicity $Z = 0.04$, computed with the `COLIBRI` code (Marigo et al., 2013). These quantities are the key input stellar parameters for the presented dust growth model. Time is counted from the first thermal pulse. Note that effective temperature and luminosity are obtained from the solution of the full set of the stellar structure equations, and not from fitting relations as usually done in synthetic TP-AGB models. The value of the C/O ratio is always below unity. See the text for more details.

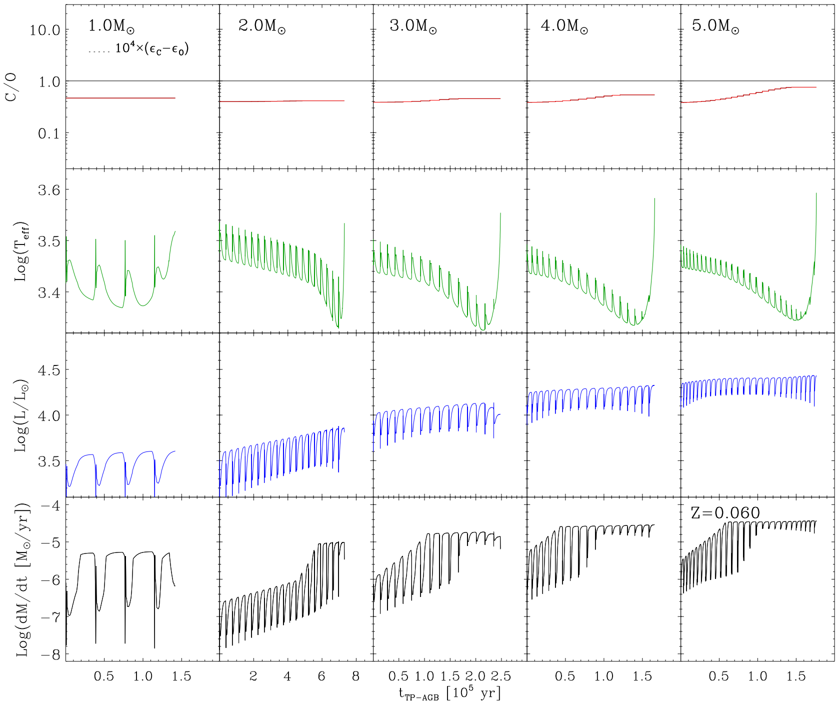

Figure 7.4: The same as in Fig. 7.3, but for initial metallicity $Z = 0.06$.

lisional heating term. The heating rate is computed by considering only collisions with H_2 molecules, which are by far the most abundant species and, that at each collision, the amount of energy gained by a dust grain is equal to $[3/2k_B(T_{\rm gas} - T_{\rm dust})]$ (Lucy, 1976). Therefore, the dust collisional heating rate (in erg s^{-1}) can be expressed as

$$H_{\rm collision} = 4\pi a^2 \frac{3}{2} k_B (T_{\rm gas} - T_{\rm dust}) N_{\rm H_2} v_{th,\rm H_2} \tag{7.1}$$

Correspondingly, the energy balance Eq. 4.83, becomes

$$\sigma\, T^4_{\rm dust} Q_{\rm abs,P}(a, T_{\rm dust}) = \sigma\, {T_{\rm eff}}^4 Q_{\rm abs,P}(a, T_{\rm eff}) W(r) + \frac{H_{\rm collision}}{4\pi a^2}, \tag{7.2}$$

where $N_{\rm H_2}$ is the number density of H_2 molecules that is approximately equal to $N_{\rm H}/2$. It is worth to remind here that the effect of heating by collisions is different from that of chemisputtering by H_2 molecules, because the latter involve the activation of a chemical reaction.

7.2 Results

7.2.1 Expansion velocities

Before presenting the results of super-solar metallicity stars, I discuss the role of the collision heating term, Eq. 7.1 and 7.2, in the models of solar and of lower metallicity. In particular, to check whether this effect is important also at lower metallicity, I compute two sets of the TP-AGB tracks of $Z = 0.02$, one neglecting and the other taking into account the collisional heating. The corresponding expansion velocities are plotted against the mass-loss rates in Fig. 7.5. The case in which collisional heating is neglected is shown in the left panel, while the

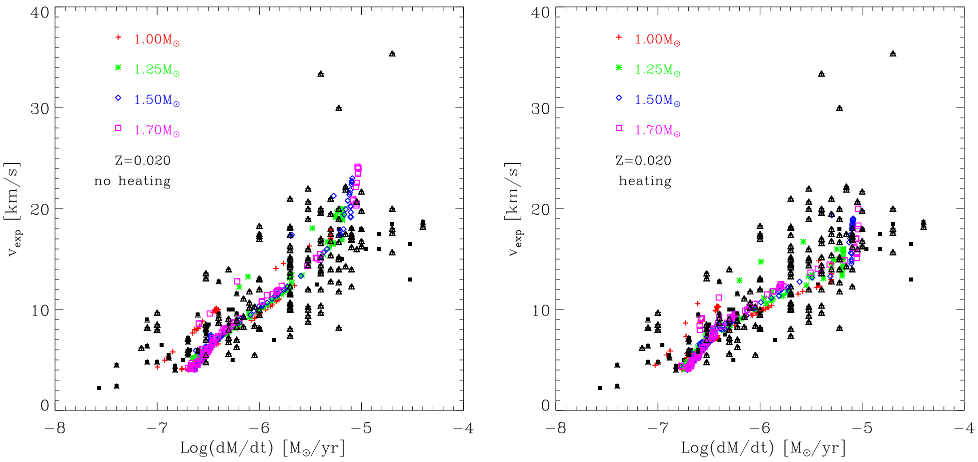

Figure 7.5: Expansion velocities of circumstellar outflows against mass-loss rates of variable M-stars. Observations of Galactic M-stars by Loup et al. (1993) (black triangles), González Delgado et al. (2003) (black pentagons) and Schöier et al. (2013) (black squares) are compared with predicted expansion velocities for a few selected TP-AGB tracks with $Z = 0.02$ for the values of initial stellar masses listed in upper left of each figure. *Left panel*: comparison with simulations that do not include the heating effect due to H_2 collisions. *Right panel*: comparison with models that include the effect of the heating. For this metallicity the results do not not change significantly.

case that accounts for collisional heating is presented in the right panel. In both cases I show TP-AGB tracks of masses $M_* = 1, 1.25, 1.5, 1.7$ M$_\odot$, represented with a discrete number of points selected from a randomly generated uniform distribution of ages that samples the entire TP-AGB phase. The models are compared with the velocities observed in Galactic M-type TP-AGB stars. Mass-loss rates and expansion velocities are taken from Loup et al. (1993) (black triangles), González Delgado et al. (2003) (black pentagons) and Schöier et al. (2013) (black squares), as in Chapter 6. As can be seen, the effects of collisions become important only at the highest mass-loss rates, where the expansion velocities decrease by about 10%. Thus, neglecting the collisional heating term at solar and sub-solar metallicity can be considered a fair approximation.

On the contrary, at super-solar metallicities, the models obtained neglecting collisional heating are often characterized by too large initial optical depths, inconsistent with the gray atmosphere models adopted, and the corresponding results cannot be considered reliable. As already anticipated, this is related to the condensation radii of these models which, at these high metallicities, are too close to the photospheres. This is likely caused by the larger growth rates that characterize more metal rich CSEs at the same mass-loss rates and, at the same time, by the lower dust radiation heating due to the lower effective temperatures of more metal rich M-giants. At these radii, the collisional heating rates turn out to be important, and including this term into the energy balance equation rises the dust equilibrium temperature and the corresponding sublimation rate, at a given radius. As a consequence, the condensation points shift outwards, at radii comparable to those of less metal rich stars of the same mass-loss rates.

We stress that this term does not affect significantly the dust condensation temperature, which I obtain through the energy balance, but the radius at which this condensation temperature is reached.

The expansion velocities of the super-metal rich models are plotted in Fig. 7.6, with the

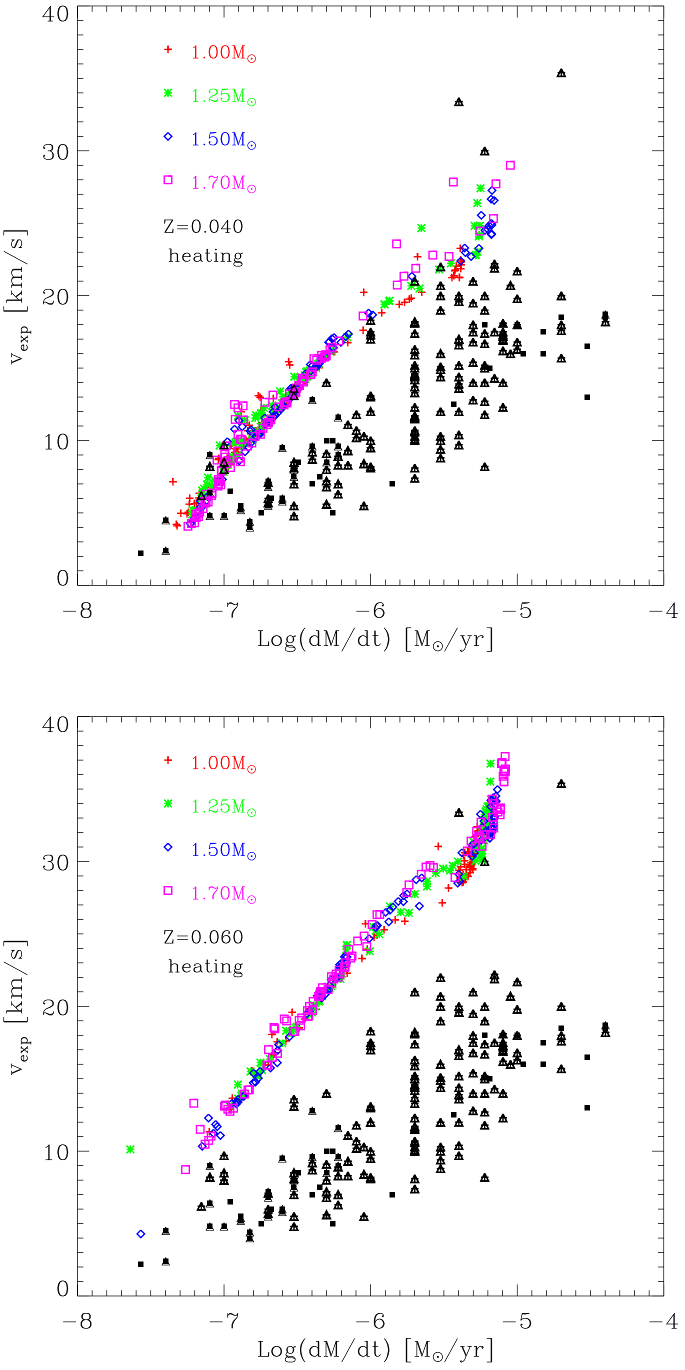

Figure 7.6: The same as right panel of Fig. 7.5 for Z = 0.04 and Z = 0.06.

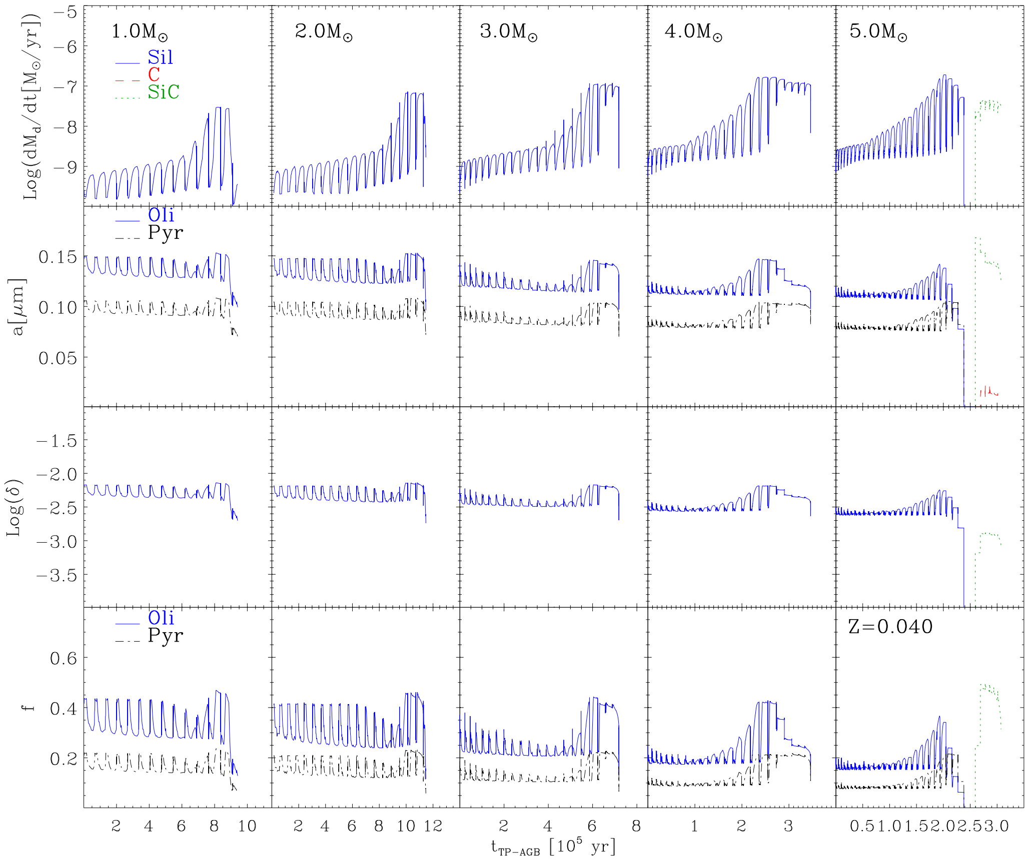

Figure 7.7: Dust properties of selected models of initial metallicity $Z = 0.04$, for various initial masses, as shown in the upper panels. From top to bottom I depict the dust mass-loss rates in $M_\odot yr^{-1}$, the dust sizes in μm, the dust-to-gas ratios δ, and the dust condensation fractions f, respectively. The main dust species are silicates (blue lines). For $M_* = 5\,M_\odot$ amorphous carbon (red lines) and SiC (green lines) are also produced. In some panels silicates are separated into olivine type dust (blue lines) and pyroxene type dust (black lines) as indicated in the insets.

same method adopted for Fig. 7.5. At increasing metallicity the velocity at a given mass-loss rate are higher as a result of the larger opacity of the medium in CSEs (see Chapter 3). A few observed M-type TP-AGB stars, along the highest envelope of the data, could be compatible with low mass super-metal rich stars ($Z \sim 0.04$).

7.2.2 Condensation fractions, composition, dust sizes and dust mass-loss rates

As already mentioned, super metal rich stars are dominated by silicate dust production as shown in Fig. 7.7, for $Z = 0.04$, and in Fig. 7.8, for $Z = 0.06$.

The sizes of dust grains are typically between $a = 0.1\,\mu$m and $a = 0.15\,\mu$m, for all the stellar masses and metallicities. These values are similar to those obtained at solar metallicity and, because of the assumptions of the presented models, the maximum value of the size remains almost independent from the metallicity of the star up to the most metal rich case considered. The reason is that both the initial number of seeds, given by Eq. 4.59, and the total amount of dust that may condense, scale linearly with the metallicity.

Old super metal rich stars of this kind could populate the nuclear regions of passively evolved elliptical galaxies (Bertola et al., 1995) and it is interesting to notice that at a typical

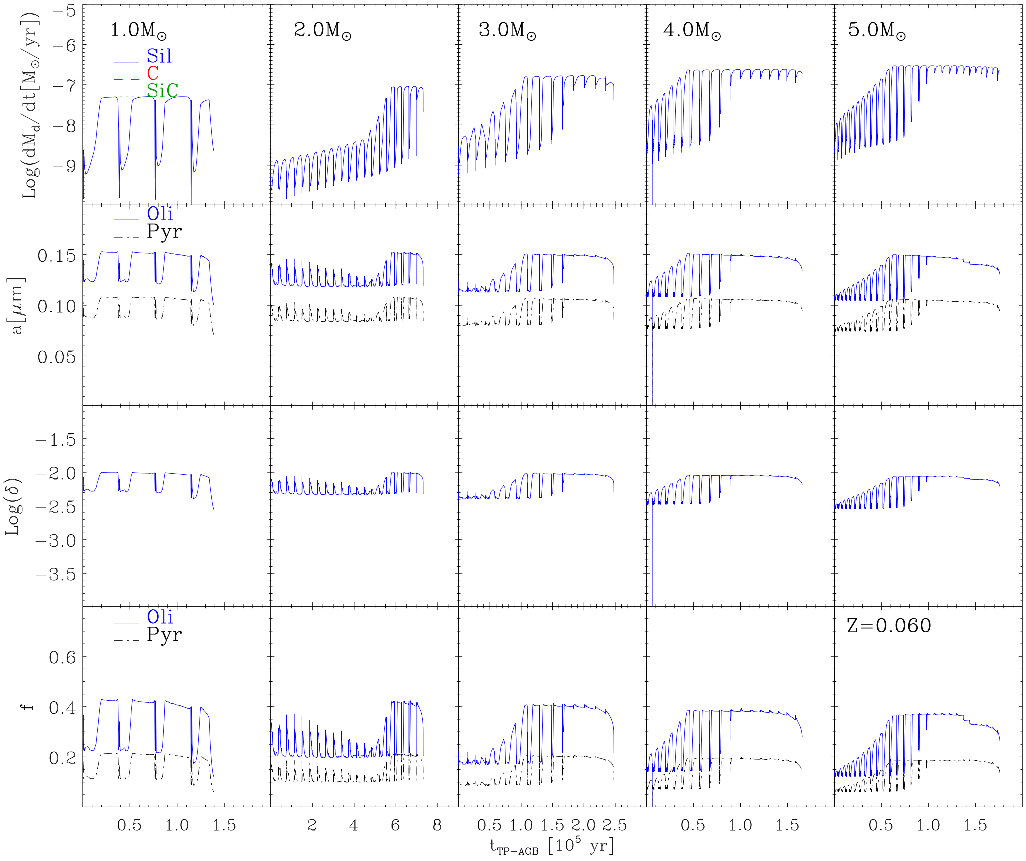

Figure 7.8: The same as in Fig. 7.7, but for initial metallicity $Z = 0.06$.

age of 10 Gyr, the turn-off mass is slightly larger than $M_* = 1.1$ M$_\odot$ (see Table 7.1). These stars can reach high dust mass-loss rates ejecting silicate dust, which could be responsible of the 9.7μm silicate features discovered by Spitzer in the nuclear regions of nearby elliptical galaxies (Bressan et al., 2006). The observed MIR spectral features are quite broad and could be consistent with a size distribution peaked toward large grains, as the ones shown in Figs. 7.7 and 7.8.

The lower panels in Figs. 7.7 and 7.8 show the dust-to-gas ratios δ, and the condensation fractions f, respectively. As discussed in Chapter 6, typical values of the silicate dust-to-gas ratios in the models of solar metallicity are around $\delta \sim$1/200-1/300 while, at $Z = 0.04$, $\delta \leq$1/200 and, at $Z = 0.06$, $\delta \leq$1/100. Thus the predicted dust-to-gas ratios do not increase linearly with the metallicity. In agreement with this results, the condensation fractions, plotted in the lowest panels of the figures, decreases at increasing metallicity. Considering for comparison the $M_* = 1$ M$_\odot$ model, the condensation fraction of olivine decreases from $f_{\rm ol} \sim 0.45 - 0.55$, at $Z = 0.02$, to $f_{\rm ol} \sim 0.3 - 0.4$, at $Z = 0.04$, and to $f_{\rm ol} \sim 0.2 - 0.4$, at $Z = 0.06$. A similar decrease at increasing Z occurs for the condensation fraction of the pyroxene. This is likely due to the larger expansion velocity, at a given mass-loss rate, reached by the more metal rich envelopes, as a consequence of an initially larger dust opacity. For comparison, I remind that the average value assumed for the CSE dust-to-gas ratios in Galactic M-giants is $\delta \sim$1/200 (Groenewegen et al., 1998; van Loon et al., 2005), but in some M-giants, it can exceed the value of 1/100.

7.3 Dust ejecta

The integrated ejecta along the entire TP-AGB phase of the main condensed compounds, i.e. silicates, amorphous carbon, iron and SiC, are plotted in Fig. 7.9 for the different masses and metallicities, and are provided in Table 7.1. They refer to individual stars and they may not be representative of the corresponding dust yields obtained after convolving with the initial mass function.

I remind that the integration is performed irrespectively of the ability of dust to drive or not the stellar wind, similarly to Chapter 6, but, at super-solar metallicity, only in a few models the dust-driven wind is not efficient. For comparison, I plot in the same figure also the results obtained in Chapter 6 for $Z = 0.02$. At a given mass, the dust ejecta increase with the metallicity, albeit not linearly but proportionally to $Z^{0.7}$ on average. The silicate ejecta at a given metallicity increase with the mass, but tend to saturate at high masses or even decrease for the case of $M_* = 5$ M$_\odot$ at $Z = 0.04$. In the latter case the decrease is due to a C/O ratio that reaches unity toward the end of the evolution (see Fig. 7.7).

The models presented here and in Chapter 6, make it possible to draw a consistent picture of how dust production evolves over a wide range of metallicities. Particularly useful are the ratios between the total dust ejecta and the gas ejecta, which, after being convolved with the stellar initial mass function and the star formation rate, outline the theoretical picture of galactic dust evolution (Dwek et al., 2007; Valiante et al., 2009; Dwek & Cherchneff, 2011). Often, in such models the dust-to-mass ratio is scaled with the metallicity, i.e. $\delta(Z)/\delta_\odot = Z/Z_\odot$, skipping all the details of the dust production processes.

Different values of $\delta_\odot$ can be found in the literature but the most common one is $\delta_\odot$=1/200. A value $\delta_\odot = Z_\odot$ is sometimes assumed as an extreme case, where all the metals are supposed to condense into dust, $\delta(Z) = Z$.

In Fig. 7.10 I compare the predictions of the integrated dust-to-gas ratios, i.e. the ratios between the total dust and gas ejecta $M_{\rm d}/M_{\rm g}$ after integration along the TP-AGB tracks of several stellar masses, as a function of the metallicity. I show separately the sum of the silicates

Z	0.04						0.06			
$M_{*,i}$ [$M_\odot$]	Age log (yr)	Sil	Fe	Al_2O_3	C	SiC	Age log (yr)	Sil	Fe	Al_2O_3
		log ($M/M_\odot$)						log ($M/M_\odot$)		
1.00	10.136	−2.59	−6.41	−4.21	-	-	10.095	−2.46	−7.08	−4.82
1.25	9.793	−2.39	−6.43	−4.13	-	-	9.765	−2.25	−6.87	−4.62
1.50	9.551	−2.27	−6.26	−4.03	-	-	9.528	−2.11	−6.69	−4.05
1.70	9.392	−2.19	−6.00	−3.94	-	-	9.372	−2.07	−6.74	−3.87
2.00	9.226	−2.09	−6.20	−3.84	-	-	9.188	−1.96	−6.63	−3.71
3.00	8.697	−1.92	−6.40	−3.75	-	-	8.647	−1.71	−6.36	−3.89
4.00	8.323	−1.81	−6.05	−3.77	-	-	8.273	−1.58	−6.23	−4.06
5.00	8.057	−2.17	−2.67	−3.72	−6.06	−2.77	8.001	−1.50	−6.09	−3.82

Table 7.1: Dust ejecta at $Z = 0.04$ and $Z = 0.06$.

plus the iron ejecta, and the sum of these ejecta plus the carbon ejecta (the global ejecta), all normalized to the gas ejecta. This codification allows one to recognize at once the overall dust contribution and the main dust species. In the figure, the solid line represents the extreme case, for which $\delta_\odot = Z_\odot$ while, the dotted line, represents the standard assumption $\delta_\odot$=1/200.

A striking impression from this figure is that the global dust-to-gas ejecta are much less dependent from the metallicity than what is usually assumed. There is of course a modulation with the initial mass but, considering for example the cases of the models of $M_* = 1.5, 2, 3\,M_\odot$, one can see that the ratios M_d/M_g, at super-solar metallicity are mainly composed by silicates and that, after an initial decrease at decreasing metallicity, they rise again due to the overproduction of carbon at lower metallicities. The models of $M_* = 1, 4, 5\ M_\odot$ show a similar behaviour down to $Z = 0.008$ and they thereafter decline. In any case, in the models of $M_* = 4, 5\ M_\odot$ at the lowest metallicity considered, $Z = 0.001$, the ratios are slightly larger than the extreme case $\delta(Z) = Z$.

In summary, I can conclude that, at the lowest metallicity, the global dust-to-gas ejecta may reach, or even encompass by an order of magnitude, the extreme ratio $\delta(Z) = Z$, due to the efficient carbon dust production while, at the highest metallicities, the ratios saturate, possibly due to the abrupt decrease in density produced by the large accelerations of the dust-driven winds.

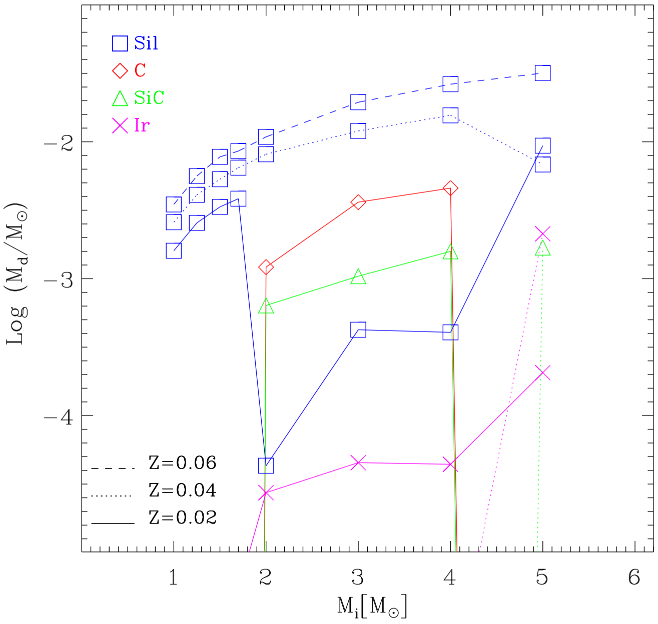

Figure 7.9: Total dust ejecta as a function of the initial stellar mass and for different initial metallicity, $Z = 0.06$ (dashed lines), $Z = 0.04$ (dotted lines) and, for comparison, $Z = 0.02$ from Nanni et al. (2013) (solid lines).

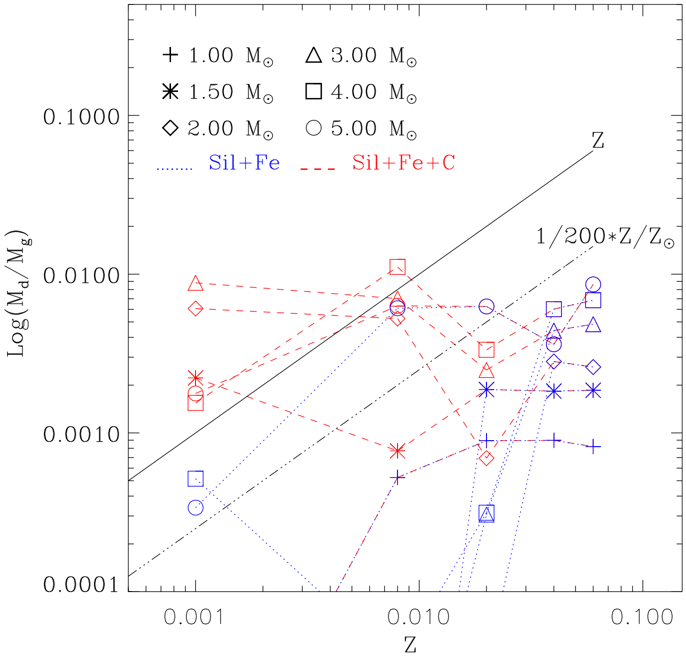

Figure 7.10: Dust-to-gas ejecta ratios as a function of the initial stellar mass and initial metallicity.

Chapter 8

Conclusions

In this thesis I investigate the evolution and mineralogy of the dust grains that are expected to form in the outflows of TP-AGB stars. For this purpose a dust-growth model coupled to a simplified description of the wind dynamics, is applied to a large set of TP-AGB evolutionary tracks computed by Marigo et al. (2013). These TP-AGB tracks rely on an accurate treatment of the molecular chemistry and opacities across the stellar envelope and the atmosphere, which are consistently linked to the changes in the chemical abundances caused by the third dredge-up and HBB nucleosynthesis.

Using the formalism developed by FG06, I find that the models of M-giants fail to reproduce the measured expansion velocities of the CSEs around Galactic M-stars, and their correlations with the mass-loss rates.

The above discrepancy is independent of the adopted opacity set (Chapters 3) because the cause lies in the inability of iron-rich silicates to form and remain thermally stable in the inner regions of the CSE, so that the acceleration imparted to the gas only starts at larger distances and it is insufficient to account for the observed expansion velocities. The discrepancy between predicted and measured expansion velocities for M-stars is a well-known fact, and it stems from a more dramatic issue, inherent to the severe inability of detailed dynamical wind models to even generate an outflow from O-rich TP-AGB stars, i.e. to reach dust radiative accelerations larger than the gravitational one (Woitke, 2006).

This challenging problem has been more recently tackled by Höfner (2008b) and Bladh et al. (2013). These studies point out that the only possible way to produce a wind in M-stars relies on photon scattering by large iron-free silicate grains. Since these grains are transparent to radiation at shorter wavelengths, they can survive in the inner zones of CSE, where they give an efficient boost to the gas thanks to their high scattering opacity (Chapters 3 and 6).

From all these indications, it is clear that in any case, i.e. for any model, the critical process that should be inhibited is dust destruction in the inner regions of the CSE.

Guided by this premise, I have revisited the two mechanisms that are able to efficiently destroy dust grains, i.e. in order of importance, chemisputtering by H_2 molecules and sublimation (Gail & Sedlmayr, 1999).

Concerning chemisputtering, I take into account the suggestion of several authors that, considering the activation energy barrier of the reduction reaction of silicates by H_2 (Gardner 1974; Tso & Pask 1982; Massieon et al. 1993; Tielens, private communication) the process could be strongly inhibited at the temperatures and pressures of the regions where dust is predicted to form (Chapter 5).

There is also experimental evidence that, at the pressures typical of a CSE ($P \leq 10^{-2}$ dyne cm^{-2}), chemisputtering may not be efficient (Nagahara & Ozawa, 1996; Tachibana et al., 2002).

Furthermore, in recent experiments condensation temperatures of amorphous silicates as high as 1350 K have been measured (Nagahara et al., 2009).

Therefore, I consider it instructive examining the case in which the evolution of dust grains is only determined by growth and free sublimation, hence switching chemisputtering off. The rate of sublimation in vacuum, computed following Kobayashi et al. (2011), is used to determine the critical temperature below which dust can grow, as explained in Chapter 5. In this way, I am able to follow the evolution of the condensation temperature in response to changes in the physical properties of the CSEs.

A key point is that, without chemisputtering, the sublimation rates of silicates exceed their growth rates at dust equilibrium temperatures significantly higher than previously assumed. I find that the condensation temperature of silicates is always between 1200 K and 1400 K and the corresponding gas pressure is always between $P \sim 10^{-4}$dyne cm^{-2} and $P \sim 10^{-2}$dyne cm^{-2} (Chapter 5). These values are in very good agreement with the recent experimental measurements by Nagahara et al. (2009). Moreover the value of the pressure corresponds to the conditions where chemisputtering should not be efficient (Nagahara & Ozawa, 1996).

In Chapter 6 I compared the predictions of the models with the measured expansion velocities and the dust-to-gas ratios of the expanding CSEs around Galactic M-stars, and their observed correlations with the mass-loss rates.

By neglecting chemisputtering and including a consistent determination of the condensation temperature, I find that, even assuming an opacity typical of dirty silicates, grains can form and survive in the inner regions of the CSEs ($r \sim 2$ R$_*$). In these regions the grains quickly grow to large sizes, and provide the gas with the needed acceleration. The models computed adopting the HCT scheme are able to reproduce fairly well the trend of the velocity with the mass-loss rate observed in Galactic M-giants (Fig. 6.1).

At the lower mass-loss rates, a small mismatch remains that may require further investigation. A possibility is that those measured in laboratory evaporation experiments may not represent the effective sticking coefficients that regulate the dust growth in CSEs. For instance, Nagahara & Ozawa (1996) noticed that the measured sticking coefficients refer to the crystalline structure used in the experiments, and that different structures could have different energy barriers for the formation reactions, implying different values of the sticking coefficient. Other authors have investigated the effects of increasing this coefficient up to 0.5 (Ventura et al. 2012a) for pyroxene, or even 1.0 for olivine (Höfner, 2008a). I find that just increasing the sticking coefficient of silicates to 0.2 is enough to eliminate the residual discrepancy between observed and predicted terminal velocities of M-giants. Another possibility could be that of decreasing the number of initial seeds in order to reach larger grain sizes that provide a higher opacity. Lowering the seed number from 10^{-13} to 10^{-14}, the maximum grain sizes increase from 0.1 μm to 0.3 μm, succeeding in reproducing the observed terminal velocities also for iron-free silicates, as shown in Fig. 6.2.

The predicted dust-to-gas ratios of M-giants are within the observed range. However, though the models cluster around $\delta = 1/200$, which is the value usually adopted for Galactic TP-AGB stars, the observed sample has a median value about 50% larger, $\delta = 1/135$. Furthermore the presented models never reach the highest measured values. They also follow the usual linear scaling at decreasing metallicity, clustering around $\delta = 1/500$ for $Z = 0.008$ but again, the few direct data available for LMC M-giants, indicate that their dust content is more than twice that the ones obtained from the models.

As far as C-star models are concerned, they reproduce fairly well the observed expansion velocities of Galactic C-stars. In the homogeneous growth scheme, at the basis of the adopted carbon dust formation model, the key role is played by the carbon over oxygen excess $\epsilon_{\rm C} - \epsilon_{\rm O}$

(Mattsson et al., 2010). This parameter is mainly determined by the complex interplay between mass-loss, third dredge-up and HBB. For example, I have shown that delaying the super-wind phase without suitably lowering the efficiency of the third dredge-up, the carbon enrichment at the surface would be larger, and consequently the terminal velocities would be higher. I have also shown that varying the sticking coefficient of carbon can induce some degeneracy with the metallicity but, unless one assumes a very low value (~0.1), the velocities of Galactic C-stars can be well reproduced. I compare the dust-to-gas ratios of the C-star models with three different Galactic samples. Contrary to those of M-giant models which show little dependence on the mass-loss rates, those of C-stars increase at increasing mass-loss rates. This trend is present only in one of the three samples (Groenewegen et al., 1998) while it is absent in the other two. At low mass-loss rates the median values of the three samples are similar and they are reproduced by models. At the high mass-loss rates the models are not able to reproduce the largest observed values. I also notice that the maximum mass-loss rate obtained in the presented models is about 2-3 times lower than the maximum observed one.

The coupling of the homogeneous growth scheme to TP-AGB models gives rise to the following trends with decreasing metallicity. The velocities at a given mass-loss rate increase, the dependence of the dust-to-gas ratios on the mass-loss rate becomes stronger, but their values at low mass-loss rates decrease. Unfortunately, in spite of the huge literature on C-stars at metallicities lower than solar, there is a severe lack of *direct* measurements of dust-to-gas ratio and terminal velocities. The velocities of six C-stars toward the Galactic Halo (Lagadec et al., 2012) are clearly significantly lower than those of the bulk of the models at $Z = 0.001$ and even at $Z = 0.008$. However, for the three objects likely belonging to the thick disk, I reproduce dust-to-gas ratios and velocities with C-stars of $Z = 0.008$ and $M_* = 1.5\ \mathrm{M}_\odot$. For the other three stars, that were classified as Halo members, the data can be reconciled with models with $Z = 0.001$ and $M_* \sim 4\ \mathrm{M}_\odot$, where the carbon excess is lowered by an efficient HBB. This value for the mass is somewhat higher than that estimated by Lagadec et al. (2012), on the basis of their luminosity ($M_* \sim 2\text{-}3\ \mathrm{M}_\odot$). Furthermore, and perhaps more important, the particularly strong equivalent width of their 7.5 μm C_2H_2 feature is difficult to reconcile with a relatively lower carbon excess. This could be an indication that the efficiency of carbon dust formation decreases at decreasing metallicity as suggested by van Loon et al. (2008).

For C-stars I also compared the predicted abundance ratios of SiC relative to carbon, with the observations. At solar metallicity, the LCT scheme predicts values that are significantly higher than those observed among Galactic C-stars while at intermediate metallicity the agreement is fairly good. The three Halo stars at low metallicity have measured SiC/C ratios that are too high compared to the ones obtained in the models. But this is more likely an intriguing problem related to their origin because the mid infrared SiC feature is observed to decrease significantly at decreasing metallicity. In any case the SiC/C ratio may depend on effects other than the global metallicity or the carbon excess. For example, I have shown that increasing the condensation temperature of carbon, lowers significantly the SiC/C ratios of models with moderate and low mass-loss rates.

The models presented provide a powerful check of the internal processes that regulate the evolution of TP-AGB stars, that should be added to all other existing observable tests used to calibrate this important phase of stellar evolution.

In Chapter 7 I applied the HCT scheme to the study of dust formation at super-solar metallicities, $Z = 0.04, 0.06$. In these models, it is necessary to take into account the coupling between dust and gas particles when computing the dust equilibrium temperature. In fact, at these metallicities, dust can form in regions where the temperature and density are so high that the collisional heating of dust grains produced by H_2 molecules can significantly affect the dust equilibrium temperature. At these high metallicities the expansion velocities are larger than those predicted by the models presented in Chapter 6. However, I notice that some of the Galactic stars with the largest observed velocities could be consistent with the ones obtained from the super metal-rich models.

In this thesis I also present dust ejecta of TP-AGB stars, computed from low to high metallicities, $Z = 0.001$, 0.008, 0.02, 0.04, 0.06

At low metallicity, the bulk of the dust consists of amorphous carbon, whereas, at increasing metallicity, the range of initial stellar masses producing this dust species is limited between 2 $M_{\odot}$ and 4 $M_{\odot}$ at $Z = 0.02$. Silicate dust production dominates at lower masses due to weak or absent dredge-up and, at higher masses, because of efficient HBB. On the other hand, at super-solar metallicity, the dust chemistry is essentially that of M-stars and the dust ejecta are mainly in the form of silicates.

I remark that the ejecta weakly depend on the details of the adopted condensation prescriptions. This is true not only for silicate dust, but also for carbon dust as demonstrated with the aid of test calculations in which I artificially increased the gas temperature threshold for the activation of the C_2H_2 chains.

At $Z = 0.001$, 0.008, 0.02 the predicted dust ejecta were compared with the ones found in the literature (FG06; Ventura et al., 2012a; Ventura et al., 2012b). From this comparison it emerged that the results do depend on the underlying TP-AGB evolutionary models. In particular, a sizeable discrepancy affects the predictions for the carbon dust production at low metallicity, between Ferrarotti & Gail (2006) the results based on the `COLIBRI` code on one side, and the ones obtained by Ventura et al. (2012a), on the other side. Furthermore, silicate ejecta computed with the `COLIBRI` code are significantly larger than those of Ferrarotti & Gail (2006) and Ventura et al. (2012a). For C-stars these differences are related to our poor understanding of the mass-loss and third dredge-up processes, since their ill-determined efficiency affects dramatically the surface C/O ratio. Differences in silicate ejecta are more subtly related also to initial metal partitions and adopted opacities, so that it is difficult to trace back their origin.

In both full evolutionary TP-AGB models (Ventura et al., 2012a), and TP-AGB models based on numerical envelope integrations (Marigo et al., 2013) mass-loss and third dredge-up are described by means of suitable parameters. For mass-loss, both models use empirical laws taken from the literature, while the third dredge-up is regulated by a parameterized efficiency of convective overshoot in full models, or directly described by its efficiency parameter in envelope-based models. How these parameters depend on the ambient metallicity is one of the far-reaching questions, that are crucial for the interpretation of extragalactic observations up to high redshift.

By dividing the dust ejecta by the total mass lost by the star during the TP-AGB phase, I obtain the total dust-to-gas ejecta ratios. The wide range of initial metallicity values, from $Z = 0.001$ to 0.06, outlines the following striking picture. The total dust-to-gas ejecta of intermediate mass stars are much less dependent on the metallicity than usually assumed. At the lowest metallicity the total dust-to-gas ejecta may reach and even exceed the value of the initial metallicity by even an order of magnitude, due to the efficient carbon dust production. At the highest metallicities, the ratios saturate, possibly due to the abrupt decrease in density produced by the large accelerations of the dusty driven winds. While I do think that the picture at the high metallicities is correct, I warn the reader that the issue of the large carbon dust production at the lowest metallicities is still open and awaits for direct observational confirmations as previously mentioned.

Finally I stress that the major aim of this work when coupled with `COLIBRI` code, is to provide a fast and flexible tool able to put different observations inside a common interpretative framework. In this respect, the dust formation scheme described here will be soon applied to study the emission properties of the circumstellar dusty envelopes.

Bibliography

Alongi M., Bertelli G., Bressan A., Chiosi C., 1991, A&A, 244, 95

Anders E., Grevesse N., 1989, Geochim. Cosmochim. Acta, 53, 197

Atkins P., de Paula J., 2010, Atkins' Physical Chemistry. OUP Oxford

Barin I., Platzki G., 1995, Thermochemical data of pure substances. No. v. 1 in Thermochemical Data of Pure Substances, VCH

Bedijn P. J., 1988, A&A, 205, 105

Beelen A., Cox P., Benford D. J., Dowell C. D., Kovács A., Bertoldi F., Omont A., Carilli C. L., 2006, ApJ, 642, 694

Begemann B., Dorschner J., Henning T., Mutschke H., Guertler J., Koempe C., Nass R., 1997, ApJ, 476, 199

Bell K. R., Lin D. N. C., 1994, ApJ, 427, 987

Bergeat J., Chevallier L., 2005, A&A, 429, 235

Bernatowicz T. J., Cowsik R., Gibbons P. C., Lodders K., Fegley Jr. B., Amari S., Lewis R. S., 1996, ApJ, 472, 760

Bertelli G., Bressan A., Chiosi C., Fagotto F., Nasi E., 1994, A&AS, 106, 275

Bertola F., Bressan A., Burstein D., Buson L. M., Chiosi C., di Serego Alighieri S., 1995, ApJ, 438, 680

Bertoldi F., Cox P., Neri R., Carilli C. L., Walter F., Omont A., Beelen A., Henkel C., Fan X., Strauss M. A., Menten K. M., 2003, A&A, 409, L47

Bladh S., Höfner S., Nowotny W., Aringer B., Eriksson K., 2013, A&A, 553, A20

Bloecker T., Schoenberner D., 1991, A&A, 244, L43

Boothroyd A. I., Sackmann I.-J., 1992, ApJ, 393, L21

Bowen G. H., Willson L. A., 1991, ApJ, 375, L53

Bressan A., Fagotto F., Bertelli G., Chiosi C., 1993, A&AS, 100, 647

Bressan A., Granato G. L., Silva L., 1998, A&A, 332, 135

Bressan A., Marigo P., Girardi L., Salasnich B., Dal Cero C., Rubele S., Nanni A., 2012, MNRAS, 427, 127

Bressan A., Panuzzo P., Buson L., Clemens M., Granato G. L., Rampazzo R., Silva L., Valdes J. R., Vega O., Danese L., 2006, ApJ, 639, L55

Caffau E., Ludwig H.-G., Steffen M., Freytag B., Bonifacio P., 2011, Sol. Phys., 268, 255

Calura F., Pipino A., Matteucci F., 2008, A&A, 479, 669

Chase M. W., 1986, JANAF thermochemical tables

Cherchneff I., 2000, in Wing R. F., ed., The Carbon Star Phenomenon Vol. 177 of IAU Symposium. p. 331

Cherchneff I., 2006, A&A, 456, 1001

Cherchneff I., 2011, A&A, 526, L11

Cherchneff I., 2012, A&A, 545, A12

Cherchneff I., Barker J. R., Tielens A. G. G. M., 1992, ApJ, 401, 269

Croat T. K., Stadermann F. J., Bernatowicz T. J., 2005, ApJ, 631, 976

Dorschner J., Begemann B., Henning T., Jaeger C., Mutschke H., 1995, A&A, 300, 503

Draine B. T., 2003, ARA&A, 41, 241

Draine B. T., 2009, in Henning T., Grün E., Steinacker J., eds, Cosmic Dust - Near and Far Vol. 414 of Astronomical Society of the Pacific Conference Series, Interstellar Dust Models and Evolutionary Implications. p. 453

Duschl W. J., Gail H.-P., Tscharnuter W. M., 1996, A&A, 312, 624

Dwek E., 1998, ApJ, 501, 643

Dwek E., Cherchneff I., 2011, ApJ, 727, 63

Dwek E., Galliano F., Jones A. P., 2007, Nuovo Cimento B Serie, 122, 959

Eales S., Lilly S., Webb T., Dunne L., Gear W., Clements D., Yun M., 2000, AJ, 120, 2244

Elitzur M., Ivezić Ž., 2001, MNRAS, 327, 403

Ertl G., 2010, Reactions at Solid Surfaces. Baker Lecture Series, Wiley

Ferrarotti A. S., Gail H.-P., 2006, A&A, 447, 553

Fleischer A. J., Gauger A., Sedlmayr E., 1991, A&A, 242, L1

Gail H.-P., 2010, in Henning T., ed., Lecture Notes in Physics, Berlin Springer Verlag Vol. 815 of Lecture Notes in Physics, Berlin Springer Verlag, Formation and Evolution of Minerals in Accretion Disks and Stellar Outflows. p. 61

Gail H.-P., Sedlmayr E., 1988, A&A, 206, 153

Gail H.-P., Sedlmayr E., 1998, Faraday Discussions, 109, 303

Gail H.-P., Sedlmayr E., 1999, A&A, 347, 594

Gall C., Andersen A. C., Hjorth J., 2011, A&A, 528, A14

Gardner R. A., 1974, Journal of solid state chemistry, 9, 336

Gehrz R., 1989, in Allamandola L. J., Tielens A. G. G. M., eds, Interstellar Dust Vol. 135 of IAU Symposium. p. 445

Girardi L., Bressan A., Bertelli G., Chiosi C., 2000, A&AS, 141, 371

Girardi L., Williams B. F., Gilbert K. M., Rosenfield P., Dalcanton J. J., Marigo P., Boyer M. L., Dolphin A., Weisz D. R., Melbourne J., Olsen K. A. G., Seth A. C., Skillman E., 2010, ApJ, 724, 1030

González Delgado D., Olofsson H., Kerschbaum F., Schöier F. L., Lindqvist M., Groenewegen M. A. T., 2003, A&A, 411, 123

Goumans T. P. M., Bromley S. T., 2012, MNRAS, 420, 3344

Grevesse N., Sauval A. J., 1998, Space Sci. Rev., 85, 161

Groenewegen M. A. T., de Jong T., 1998, A&A, 337, 797

Groenewegen M. A. T., Sloan G. C., Soszyński I., Petersen E. A., 2009, A&A, 506, 1277

Groenewegen M. A. T., Whitelock P. A., Smith C. H., Kerschbaum F., 1998, MNRAS, 293, 18

Groenewegen M. A. T., Wood P. R., Sloan G. C., Blommaert J. A. D. L., Cioni M.-R. L., Feast M. W., Hony S., Matsuura M., Menzies J. W., Olivier E. A., Vanhollebeke E., van Loon J. T., Whitelock P. A., Zijlstra A. A., Habing H. J., Lagadec E., 2007, MNRAS, 376, 313

Hanner M. S., 1988, NASA Conf. Publ., 3004, 22

Harper G., 1996, in Pallavicini R., Dupree A. K., eds, Cool Stars, Stellar Systems, and the Sun Vol. 109 of Astronomical Society of the Pacific Conference Series. p. 481

Helling C., Winters J. M., Sedlmayr E., 2000, A&A, 358, 651

Helling C., Woitke P., 2006, A&A, 455, 325

Höfner S., 2008a, Physica Scripta Volume T, 133, 014007

Höfner S., 2008b, A&A, 491, L1

Höfner S., 2009, in Henning T., Grün E., Steinacker J., eds, Cosmic Dust - Near and Far Vol. 414 of Astronomical Society of the Pacific Conference Series. p. 3

Höfner S., Gautschy-Loidl R., Aringer B., Jørgensen U. G., 2003, A&A, 399, 589

Hoyle F., Wickramasinghe N., 1991, The Theory of Cosmic Grains. Astrophysics and space science library, Kluwer Academic

Hynes K. M., Croat T. K., Bernatowicz T. J., 2007, in Lunar and Planetary Institute Science Conference Abstracts Vol. 38 of Lunar and Planetary Institute Science Conference Abstracts, Microstructure of Silicon Carbides Found Within Presolar Graphite. p. 1693

Iglesias C. A., Rogers F. J., 1996, ApJ, 464, 943

Ireland M. J., Scholz M., 2006, MNRAS, 367, 1585

Jäger C., Dorschner J., Mutschke H., Posch T., Henning T., 2003, A&A, 408, 193

Jeong K. S., Winters J. M., Le Bertre T., Sedlmayr E., 2003, A&A, 407, 191

Jones T. W., Merrill K. M., 1976, ApJ, 209, 509

Kamath D., Wood P. R., Soszyński I., Lebzelter T., 2011, in Kerschbaum F., Lebzelter T., Wing R. F., eds, Why Galaxies Care about AGB Stars II: Shining Examples and Common Inhabitants Vol. 445 of Astronomical Society of the Pacific Conference Series. p. 127

Karakas A. I., Lattanzio J. C., Pols O. R., 2002, PASA, 19, 515

Kimura H., Mann I., Biesecker D. A., Jessberger E. K., 2002, Icarus, 159, 529

Klotz D., Paladini C., Hron J., Aringer B., Sacuto S., Marigo P., Verhoelst T., 2013, ArXiv e-prints

Knapp G. R., 1985, ApJ, 293, 273

Kobayashi H., Kimura H., Watanabe S.-I., Yamamoto T., Müller S., 2011, Earth, Planets, and Space, 63, 1067

Kobayashi H., Watanabe S.-I., Kimura H., Yamamoto T., 2009, Icarus, 201, 395

Krueger D., Patzer A. B. C., Sedlmayr E., 1996, A&A, 313, 891

Lagadec E., Sloan G. C., Zijlstra A. A., Mauron N., Houck J. R., 2012, MNRAS, 427, 2588

Lambert D. L., 1978, MNRAS, 182, 249

Lambert D. L., Gustafsson B., Eriksson K., Hinkle K. H., 1986, ApJS, 62, 373

Lamers H. J. G. L. M., Cassinelli J. P., 1999, Introduction to Stellar Winds. Cambridge Univ. Press, Cambridge

Landolt-Börnstein 1968, In: Schäfer K. (ed.) Zahlenwerte und Funktionen.. No. v. 5b in Zahlenwerte und Funktionen, Springer-Verlag, Heidelberg

Le Bertre T., Winters J. M., 1998, A&A, 334, 173

Le Sidaner P., Le Bertre T., 1996, A&A, 314, 896

Leksina I., Penkina N., 1967, Fizik. Metall. Metalloved., 23, 344

Lide R. D., 1995, Handbook of Chemistry and Physics

Lilly S. J., Eales S. A., Gear W. K. P., Hammer F., Le Fèvre O., Crampton D., Bond J. R., Dunne L., 1999, ApJ, 518, 641

Lodders K., Fegley Jr. B., 1999, in Le Bertre T., Lèbre A., Waelkens C., eds, Asymptotic Giant Branch Stars Vol. 191 of IAU Symposium. p. 279

Loup C., Forveille T., Omont A., Paul J. F., 1993, A&AS, 99, 291

Lucy L. B., 1971, ApJ, 163, 95

Lucy L. B., 1976, ApJ, 205, 482

MacNaught A., Wilkinson A., of Pure I. U., Chemistry A., 1997, Compendium of Chemical Terminology: Iupac Recommendations. IUPAC Chemical Data Series, Blackwell Science

Maiolino R., Schneider R., Oliva E., Bianchi S., Ferrara A., Mannucci F., Pedani M., Roca Sogorb M., 2004, Nature, 431, 533

Marchenko S. V., 2006, in Lamers H. J. G. L. M., Langer N., Nugis T., Annuk K., eds, Stellar Evolution at Low Metallicity: Mass Loss, Explosions, Cosmology Vol. 353 of Astronomical Society of the Pacific Conference Series. p. 299

Marigo P., 2002, A&A, 387, 507

Marigo P., Aringer B., 2009, A&A, 508, 1539

Marigo P., Bressan A., Chiosi C., 1996, A&A, 313, 545

Marigo P., Bressan A., Nanni A., Girardi L., Pumo M. L., 2013, MNRAS, 434, 488

Marigo P., Girardi L., 2007, A&A, 469, 239

Marigo P., Girardi L., Bressan A., 1999, A&A, 344, 123

Marigo P., Girardi L., Bressan A., Groenewegen M. A. T., Silva L., Granato G. L., 2008, A&A, 482, 883

Marshall J. R., van Loon J. T., Matsuura M., Wood P. R., Zijlstra A. A., Whitelock P. A., 2004, MNRAS, 355, 1348

Massieon C. C., Cutler A. H., Shadman F., 1993, Industrial and Engineering Chemistry Research, 32, 1239

Mathis J. S., Rumpl W., Nordsieck K. H., 1977, ApJ, 217, 425

Matsuura M., Barlow M. J., Zijlstra A. A., Whitelock P. A., Cioni M.-R. L., Groenewegen M. A. T., Volk K., Kemper F., Kodama T., Lagadec E., Meixner M., Sloan G. C., Srinivasan S., 2009, MNRAS, 396, 918

Matsuura M., Woods P. M., Owen P. J., 2012, MNRAS, p. 434

Mattsson L., 2011, MNRAS, 414, 781

Mattsson L., Wahlin R., Höfner S., 2010, A&A, 509, A14

Mattsson L., Wahlin R., Höfner S., Eriksson K., 2008, A&A, 484, L5

Michałowski M. J., Murphy E. J., Hjorth J., Watson D., Gall C., Dunlop J. S., 2010a, A&A, 522, A15

Michałowski M. J., Watson D., Hjorth J., 2010b, ApJ, 712, 942

Nagahara H., Ogawa R., Ozawa K., Tamada S., Tachibana S., Chiba H., 2009, in Henning T., Grün E., Steinacker J., eds, Cosmic Dust - Near and Far Vol. 414 of Astronomical Society of the Pacific Conference Series, Laboratory Condensation and Reaction of Silicate Dust. p. 403

Nagahara H., Ozawa K., 1996, Geochim. Cosmochim. Acta, 60, 1445

Nanni A., Bressan A., Marigo P., Girardi L., 2013, MNRAS, 434, 2390

Norris B. R. M., Tuthill P. G., Ireland M. J., Lacour S., Zijlstra A. A., Lykou F., Evans T. M., Stewart P., Bedding T. R., Guyon O., Martinache F., 2012, in Society of Photo-Optical Instrumentation Engineers (SPIE) Conference Series Vol. 8445 of Society of Photo-Optical Instrumentation Engineers (SPIE) Conference Series

Nozawa T., Kozasa T., Umeda H., Maeda K., Nomoto K., 2003, ApJ, 598, 785

Ossenkopf V., Henning T., Mathis J. S., 1992, A&A, 261, 567

Pégourié B., 1988, A&A, 194, 335

Piovan L., Chiosi C., Merlin E., Grassi T., Tantalo R., Buonomo U., Cassarà L. P., 2011a, ArXiv e-prints

Piovan L., Chiosi C., Merlin E., Grassi T., Tantalo R., Buonomo U., Cassarà L. P., 2011b, ArXiv e-prints

Pipino A., Fan X. L., Matteucci F., Calura F., Silva L., Granato G., Maiolino R., 2011, A&A, 525, A61

Pipino A., Matteucci F., 2011, A&A, 530, A98

Renzini A., Voli M., 1981, A&A, 94, 175

Råback P., , Modeling of the Sublimation Growth of Silicon Carbide Crystals

Robson I., Priddey R. S., Isaak K. G., McMahon R. G., 2004, MNRAS, 351, L29

Sargent B. A., Srinivasan S., Meixner M., Kemper F., Tielens A. G. G. M., Speck A. K., Matsuura M., Bernard J.-P., Hony S., Gordon K. D., Indebetouw R., Marengo M., Sloan G. C., Woods P. M., 2010, ApJ, 716, 878

Schöier F. L., Ramstedt S., Olofsson H., Lindqvist M., Bieging J. H., Marvel K. B., 2013, A&A, 550, A78

Schröder K.-P., Cuntz M., 2005, ApJ, 630, L73

Sharp C. M., Huebner W. F., 1990, ApJS, 72, 417

Siess L., 2010, A&A, 512, A10

Sloan G. C., Matsuura M., Zijlstra A. A., Lagadec E., Groenewegen M. A. T., Wood P. R., Szyszka C., Bernard-Salas J., van Loon J. T., 2009, Science, 323, 353

Sugerman B. E. K., Ercolano B., Barlow M. J., Tielens A. G. G. M., Clayton G. C., Zijlstra A. A., Meixner M., Speck A., Gledhill T. M., Panagia N., Cohen M., Gordon K. D., Meyer M., Fabbri J., Bowey J. E., Welch D. L., Regan M. W., Kennicutt R. C., 2006, Science, 313, 196

Tachibana S., Tsuchiyama A., Nagahara H., 2002, Geochim. Cosmochim. Acta, 66, 713

Tielens A. G. G. M., Waters L. B. F. M., Molster F. J., Justtanont K., 1998, Ap&SS, 255, 415

Todini P., Ferrara A., 2001, MNRAS, 325, 726

Tso S. T., Pask J. A., 1982, Journal of the American Ceramic Society, 65, 457

Valiante R., Schneider R., Bianchi S., Andersen A. C., 2009, MNRAS, 397, 1661

Valiante R., Schneider R., Salvadori S., Bianchi S., 2011, MNRAS, 416, 1916

van der Veen W. E. C. J., Rugers M., 1989, A&A, 226, 183

van Loon J. T., 2000, A&A, 354, 125

van Loon J. T., Cioni M.-R. L., Zijlstra A. A., Loup C., 2005, A&A, 438, 273

van Loon J. T., Cohen M., Oliveira J. M., Matsuura M., McDonald I., Sloan G. C., Wood P. R., Zijlstra A. A., 2008, A&A, 487, 1055

Vassiliadis E., Wood P. R., 1993, ApJ, 413, 641

Ventura P., Criscienzo M. D., Schneider R., Carini R., Valiante R., D'Antona F., Gallerani S., Maiolino R., Tornambé A., 2012a, MNRAS, 424, 2345

Ventura P., di Criscienzo M., Schneider R., Carini R., Valiante R., D'Antona F., Gallerani S., Maiolino R., Tornambé A., 2012b, MNRAS, 420, 1442

Winters J. M., Le Bertre T., Jeong K. S., Helling C., Sedlmayr E., 2000, A&A, 361, 641

Woitke P., 2006, A&A, 460, L9

Wood P. R., 1990, in Cacciari C., Clementini G., eds, Confrontation Between Stellar Pulsation and Evolution Vol. 11 of Astronomical Society of the Pacific Conference Series, Mira variables - Pulsation, mass loss and evolution. pp 355–363

Wood P. R., Zarro D. M., 1981, ApJ, 247, 247

Woods P. M., Walsh C., Cordiner M. A., Kemper F., 2012, MNRAS, 426, 2689

Yamasawa D., Habe A., Kozasa T., Nozawa T., Hirashita H., Umeda H., Nomoto K., 2011, ApJ, 735, 44

Zhukovska S., Gail H.-P., Trieloff M., 2008, A&A, 479, 453

Zijlstra A. A., Lagadec E., Sloan G., Matsuura M., 2009, in Luttermoser D. G., Smith B. J., Stencel R. E., eds, The Biggest, Baddest, Coolest Stars Vol. 412 of Astronomical Society of the Pacific Conference Series, The AGB Superwind in Nearby Galaxies. p. 65

Acknowledgements

I would like to thank the referees, Jacco van Loon and Paolo Ventura, for carefully reading the manuscript and for giving me very good suggestions which significantly improved it.

I thank Luigi Danese, Alexander Tielens, Hiroshi Kobayashi, Isabelle Cherchneff and Laura Agostini for the fruitful discussions.

I would like to express my deep gratitude to my advisors, Alessandro Bressan and Paola Marigo, for their patience and for constantly following me during my entire PhD.

A particular thank is to my collaborator Léo Girardi for his constant help and support.

My gratitude is also to all the members of SISSA Physics Sector, to the scientific secretary Lorena Bencina and to the student secretaries Riccardo Iancer and Federica Tuniz.

Two special mentions are for my High School teacher Dario D'Orazi for the good preparation he provided me in scientific subjects (in particular chemistry) and for Prof. Alberto Credi for his amazing lectures about inorganic chemistry at the University and for his notes which I still look at from time to time.

Some others deserve my full gratitude: the kung fu TO'A group of Trieste, in particular Daniel, Zack, Paolo and Miscel and some very special people I had the honour to meet here in Trieste: Daniele, Claudia, Marco (the young one), Alessandra, Marko, Rita, Adriano, Matteo, Alessandro, Valeria, Maurizio, Antonella, Giorgio and all the other friends I met in SISSA during these four years. On top of that I would like to thank my special "putative grandfather" Eolo Di Casola, for his constant presence and LaTeXsupport and Aurora Meroni, for her encouragement in the draft of this thesis. I also thank my officemate, Matteo Calabrese, for supporting me with coffee, chocolate and tea.

A particular heartfelt thank is to my closest friends Rossella Aversa, that patiently read the manuscript with useful suggestions and Nicola Bassan, who helped me to solve any problem that my laptop came up with.

A special thank is to all those friends from Bologna who always and patiently supported me: Simona, Viola, Melissa and Virginia and naturally I cannot forget Silvia (Sissi) and Alessandro "il Maini".

On top of that, I would like to thank my beloved family, in particular my parents and my grandparents, for their constant encouragement and unconditioned love.